

POLITECNICO DI MILANO

School of Industrial and Information Engineering

Master's degree course in Biomedical Engineering



**A novel framework for EEG connectivity
analysis in resting state conditions.**

Supervisor: Riccardo Barbieri

Co-supervisors: Alessia Paglialonga

Alfonso Mastropietro

Author: Leonardo Andrés Góngora Velandia

ID: 918220

Academic Year 2020/2021

Table of contents

List of figures	4
List of Tables	7
List of annexes: Tables	7
Acknowledgments	8
Abstract	9
Summary	10
Sommario	13
1. Introduction.....	16
1.1. THE BRAIN	17
1.2. NEURAL ACTIVITY	20
1.3. ORIGIN OF ELECTROENCEPHALOGRAPHIC SIGNALS AND BRAIN RHYTHMS	21
2. Brain imaging techniques	24
2.1. TECHNOLOGIES FOR BRAIN IMAGING: A BRIEF DESCRIPTION	24
2.1.1. <i>Structural imaging methods:</i>	24
2.1.2. <i>Functional imaging methods</i>	25
2.2. EEG AS A BRAIN IMAGING TOOL	26
2.3. RELATIONSHIP BETWEEN EEG AND CONNECTIVITY	27
3. Effective Connectivity background, limitations, and improvements.	28
3.1. EFFECTIVE CONNECTIVITY.....	28
3.2. TYPICAL MEASURES.....	28
3.2.1. <i>Cross-Correlation and Coherence</i>	29
3.2.2. <i>Granger Causality (GS)</i>	30
3.2.3. <i>Multivariate Time Series</i>	31
3.2.4. <i>Dynamic Causal Modeling</i>	33
3.3. EFFECTIVE AND FUNCTIONAL CONNECTIVITY.....	33
3.4. APPLICATIONS OF EFFECTIVE CONNECTIVITY	34
3.5. WHAT DO THESE WORKS HAVE IN COMMON?	36
3.5.1. <i>Connectivity examples for resting state conditions</i>	37
3.6. LIMITATIONS AND POSSIBLE IMPROVEMENTS.....	39
3.6.1. <i>Characteristics of EEG signals</i>	41
4. Materials: EEG datasets and preprocessing	45
4.1. EEG DATASET	45
4.2. NOISE AND ARTIFACTS IN EEG SIGNALS.....	46
4.3. PREPROCESSING STAGE.....	48
5. Methods on Segmentation and Effective Connectivity	56
5.1. EEG SEGMENTATION	56
5.1.1. <i>Segment length analysis on EEG data</i>	56
5.1.2. <i>Stationary segments: The searching strategy</i>	71
5.2. THE EFFECTIVE CONNECTIVITY FRAMEWORK.....	80
5.2.1. <i>Effective Connectivity estimation</i>	81
6. Results and Analysis	87
6.1. RESULTS ON WINDOW LENGTH SELECTION	87

6.1.1.	<i>Selection of EEG recordings for processing</i>	87
6.1.2.	<i>Window selection approach</i>	88
6.1.3.	<i>Selected window durations</i>	114
6.2.	RESULTS ON EFFECTIVE CONNECTIVITY	115
6.2.1.	<i>Results from state-of-the-art methods</i>	115
6.2.2.	<i>Connectivity analysis from the ROIs point of view</i>	121
6.2.3.	<i>Connectivity in the sensor space: Graph Theory indexes</i>	127
7.	Discussion	145
8.	Conclusions	149
	Appendix A: Short-window duration analysis	152
	Annex	162
	References	178

List of figures

FIGURE 1. RELATIVE POSITION IDENTIFIERS OF THE BRAIN. IMAGE TAKEN FROM [6] HTTPS://WWW.THESCIENCEOFPSYCHOTHERAPY.COM/GLOSSARY/ROSTRAL/	18
FIGURE 2. DIVISION OF THE CEREBRUM INTO LOBES. IMAGE TAKEN FROM [7] HTTPS://MAYFIELDCLINIC.COM/PE-ANATBRAIN.HTM	19
FIGURE 3. SHAPES OF THE BRAIN RHYTHMS. A) DELTA FREQUENCY BAND, B) THETA FREQUENCY BAND, C) ALPHA FREQUENCY BAND, D) BETA FREQUENCY BAND. TAKEN FROM [13]	22
FIGURE 4. EFFECTIVE CONNECTIVITY PROCESSING SCHEME.	37
FIGURE 5. MODIFICATION ON THE E.C. STATISTICAL ANALYSIS TO ACCOUNT FOR THE WINDOW LENGTH.	41
FIGURE 6. CHANNEL LOCATIONS OVER THE SCALP USING THE EEG SYSTEM SYNAMPS 2/RT FROM NEUROSCAN. ONLY 62 OUT OF 70 CHANNELS ARE SHOWN SINCE APART FROM THE TWO HIGH-LEVEL ELECTRODES, THE CHANNELS M1, M2, LDA, LBIC, RDA, RBIC WERE NOT USED FOR RECORDING. (PLOT GENERATED USING EEGLAB [58])	46
FIGURE 7. A SEGMENT OF AN EEG SIGNAL RECORDED BY THE CHANNEL F8. TAKEN FROM THE EEG DATASET OF SUBJECT 10 (S10) DURING THE CLOSED EYES RESTING-STATE (R2).	47
FIGURE 8.A. SUBSET OF SIGNALS REGISTERED BY 11 OUT OF A TOTAL OF 68 CHANNELS. FIGURE 8.B. SAME SEGMENT OF THE SIGNAL FROM THE CHANNEL F8 CONTAINING ARTIFACTS.	48
FIGURE 9. PRE-PROCESSING BLOCK DIAGRAM FOR THE DATA CLEANING PROCESS.....	49
FIGURE 10. EEG SIGNALS AFTER PREPROCESSING. THE BOLD SIGNAL CORRESPONDS TO THE F8 RECORDING DURING THE TIME INTERVAL 127 TO 133.....	54
FIGURE 11. PROCESSING PIPELINE AFTER DATA CLEANING.....	56
FIGURE 12. THE GENERAL APPROACH FOR SEGMENTATION PERFORMED ON AN EEG SIGNAL.	57
FIGURE 13. SEGMENTATION BOUNDS OVER TIME FOR A SUBSET OF CHANNELS CONSIDERING.....	58
FIGURE 14. GRAPHICAL REPRESENTATION OF THE RESULT OF SEGMENTATION FOR $wl1 = 1$ S OF AN EEG SIGNAL COMING FROM THE CHANNEL F6.	59
FIGURE 15. SIGNAL SEGMENTATION CONSIDERING THE BASIS WINDOW LENGTH TO LOCATE IN TIME THE WINDOW.	60
FIGURE 16. KURTOSIS ESTIMATION FROM SEGMENT TO SEGMENT AND DISPOSITION OF.....	62
FIGURE 17. KURTOSIS DISTRIBUTIONS OF THE CHANNEL F1 OF SUBJECT 10 (S10) IN R2, ESTIMATED FROM DIFFERENT SEGMENT LENGTHS CONSIDERING $WL = 1$ S AND $Nw = 10$	63
FIGURE 18. KURTOSIS DISTRIBUTIONS OF THE CHANNEL F1 OF SUBJECT 10 (S10) IN R2, ESTIMATED FROM DIFFERENT SEGMENT LENGTHS CONSIDERING $WL = 50$ MS AND $Nw = 20$. SHOWN PDFS OF TENTHS OF A SECOND.	64
FIGURE 19. KURTOSIS DENSITIES ESTIMATED FROM SIGNALS OF DIFFERENT RECORDINGS.	66
FIGURE 20. KURTOSIS DISTRIBUTIONS CONSIDERING ALL THE SEGMENT ESTIMATIONS.	66
FIGURE 21. KURTOSIS DISTRIBUTIONS CONSIDERING ALL THE SEGMENT ESTIMATIONS.	67
FIGURE 22. KURTOSIS DISTRIBUTIONS FROM FRONTAL CHANNELS F1, F2, F3, F4, F5, AND Fz (S10 - R2).	68
FIGURE 23. KURTOSIS DISTRIBUTIONS FROM ALL THE SIGNALS ACQUIRED FROM S10 IN R2.	68
FIGURE 24. KURTOSIS VARIANCE PRESENTED AS A HEAT PLOT. FROM SIGNALS OF THE DATASET OF S10 IN R2.	69
FIGURE 25. KURTOSIS VARIANCE DENSITY ($K\sigma^2$ PDF), ESTIMATED BY CONSIDERING THE ARRAY OF KURTOSIS VALUES FROM THE 60 CHANNELS THAT COMPOSE THE S10 – R2 DATASET.....	70
FIGURE 26. KURTOSIS VARIANCE PDF. (S2 – R1).....	71
FIGURE 27. SEARCHING ALGORITHM AT DIFFERENT ITERATIONS.	74
FIGURE 28. KURTOSIS VARIANCE SEARCHING SPACE BOUNDS AND RELATIVE VARIANCES. (S2 – R1)	76
FIGURE 29. $K\sigma^2$ PDF OF THE S2 – R1 EEG RECORDING CONSIDERING THE SEARCHING INTERVALS AT DIFFERENT PERCENTAGE THRESHOLDS.	77
FIGURE 30. KURTOSIS DISTRIBUTIONS OF ALL THE CHANNELS COMPOSING THE S2 – R1 EEG RECORDING.....	79
FIGURE 31. MATRIX ORGANIZATION FOR THE CONNECTIVITY MEASURES OF SIZE $NChn \times NChn \times Frequency \times$ <i>Window</i>	83
FIGURE 32. DTF ADJACENCY MATRICES FOR EACH WINDOW DURATION (400MS, 2 s, 4 s, 20 s) DURING EYES OPEN (A, C, E, G) AND EYES CLOSED (B, D, G, H).....	85
FIGURE 33. HEAT PLOT DERIVED FROM 1 TO 10 SECONDS SEGMENTATION	89
FIGURE 34. KURTOSIS VARIANCE ($K\sigma^2$) SEARCHING DOMAIN FOR S2 – R1 (LEFT) AND S2 – R2 (RIGHT).	90
FIGURE 35. $K\sigma^2$ SEARCHING INTERVALS WITH RESPECT TO $MAX\sigma^2$ PROPORTION THRESHOLDS.....	91

FIGURE 36. THE NUMBER OF CHANNELS AS A FUNCTION OF THE SEGMENT LENGTH AND THE SEARCHING INTERVAL IN TERMS OF THE KURTOSIS VARIANCE. A. S2 – R1 B. S2 – R2.	92
FIGURE 37. KURTOSIS DISTRIBUTIONS CONSIDERING THE SELECTED CHANNELS FROM THE PERCENTAGE THRESHOLD.	94
FIGURE 38. HEAT PLOT DERIVED FROM 50 MS TO 1-SECOND SEGMENTATION	95
FIGURE 39. KURTOSIS VARIANCE ($K\sigma^2$) SEARCHING DOMAIN FOR S2 – R1 (LEFT) AND S2 – R2 (RIGHT).	95
FIGURE 40. $K\sigma^2$ SEARCHING INTERVALS WITH RESPECT TO $\text{MAX}\sigma^2$ PROPORTION THRESHOLDS.....	96
FIGURE 41. THE NUMBER OF CHANNELS AS A FUNCTION OF THE SEGMENT LENGTH AND THE SEARCHING INTERVAL IN TERMS OF THE KURTOSIS VARIANCE – SHORT WINDOW SEGMENTATION. A. S2 – R1 B. S2 – R2.	98
FIGURE 42. KURTOSIS DISTRIBUTIONS CONSIDERING THE SELECTED CHANNELS FROM THE PERCENTAGE THRESHOLD. A. S2 - R1 $wl = 250ms$ B. S2 – R2 $wl = 100ms$	98
FIGURE 43. KURTOSIS VARIANCE ($K\sigma^2$) SEARCHING DOMAINS FOR SEGMENTATIONS FROM 1 TO 10 SECONDS.....	101
FIGURE 44. $K\sigma^2$ PDFs AND THE CORRESPONDING SEARCHING INTERVALS WITH RESPECT TO $\text{MAX}\sigma^2$ PROPORTION THRESHOLDS. RESTING STATE CONDITIONS DEPICTED IN PAIRS: A, B) S5 – R1, R2. C, D) S6 – R1, R2. E, F) S8 – R1, R2. G, H) S9 – R1, R2. I, J) S10 – R1, R2.....	105
FIGURE 45. THE NUMBER OF CHANNELS AS A FUNCTION OF THE SEGMENT LENGTH AND THE SEARCHING INTERVAL IN TERMS OF THE KURTOSIS VARIANCE – LONG WINDOW SEGMENTATION.	110
FIGURE 46. KURTOSIS DISTRIBUTIONS CONSIDERING THE SELECTED CHANNELS FROM THE PERCENTAGE THRESHOLDS. – LONG WINDOW SEGMENTATION. RESTING STATE CONDITIONS DEPICTED IN PAIRS: A, B) S5 – R1, R2. C, D) S6 – R1, R2. E, F) S8 – R1, R2. G, H) S9 – R1, R2. I, J) S10 – R1, R2	113
FIGURE 47. VENN DIAGRAM OF THE COMMON CHANNELS ACROSS SUBJECTS AND TYPES OF SEGMENTS, DERIVED FROM TABLE 10. (DIAGRAM GENERATED USING THE WEB TOOL AT HTTP://BIOINFORMATICS.PSB.UGENT.BE/WEBTOOLS/VENN/).....	115
FIGURE 48. CONNECTIVITY DIAGRAMS OF THE WINDOW OF 20 SECONDS USING THE DTF AS CONNECTIVITY MEASURE - CONNECTIVITY DURING EYES CLOSED (R2) CONDITION. (LEFT) RESULTS BY [45] (RIGHT) RESULTS OBTAINED WITH OUR DATA.....	116
FIGURE 49. STRENGTH DIFFERENCE BETWEEN EYES CLOSED AND EYES OPEN. (LEFT) RESULTS BY [45] (RIGHT) RESULTS OBTAINED WITH OUR DATA.....	117
FIGURE 50. GRAPHS OF MEAN CLUSTER COEFFICIENT, GLOBAL EFFICIENCY, AND LOCAL EFFICIENCY AS A FUNCTION OF THE COST IN THE RANGE OF 8% - 20% AT EACH RESTING STATE CONDITION FOR THE ALPHA BAND. FIGURES ON THE LEFT ARE THE RESULTS OBTAINED BY [46], AND THE ONES ON THE RIGHT CORRESPOND TO THE RESULTS WITH THE IBFM DATA.....	118
FIGURE 51. GRAPHS OF MEAN CLUSTER COEFFICIENT, GLOBAL EFFICIENCY, AND LOCAL EFFICIENCY AS A FUNCTION OF THE COST IN THE RANGE OF 8% - 20% AT EACH RESTING STATE CONDITION FOR THE BETA BAND. FIGURES ON THE LEFT ARE THE RESULTS OBTAINED BY [46], AND THE ONES ON THE RIGHT CORRESPOND TO THE RESULTS WITH THE IBFM DATA.....	119
FIGURE 52. REGIONS OF INTEREST DEFINITION COMPRISING THE FRONTAL, POSTERIOR, LEFT-TEMPORAL, RIGHT-TEMPORAL AND CENTRAL REGIONS.	121
FIGURE 53. THREE-FACTOR ANOVA ANALYSIS AND THE POSSIBLE INTERACTIONS.	122
FIGURE 54. ROI CONNECTIVITY DIAGRAMS OBTAINED FOR THE EYES OPEN AND EYES CLOSED CONDITIONS FOR THE ALPHA FREQUENCY BAND	126
FIGURE 55. AVERAGE DEGREE (LEFT) AND STRENGTH (RIGHT) OF THE EFFECTIVE CONNECTIONS ESTIMATED FOR THE 62 CHANNELS COMPOSING THE NETWORK.....	130
FIGURE 56. GRAPHS OF MEAN LOCAL EFFICIENCY, MEAN CLUSTER COEFFICIENT AND BETWEENNESS CENTRALITY AS A FUNCTION OF THE COST FOR THE CHANNELS OF THE NETWORK AT EACH RESTING STATE CONDITION (A, C, D). AVERAGED VALUES OF THE NODAL PARAMETERS, THE THRESHOLDS AND THE CHANNELS SELECTED REPRESENTED BY THE MARKER 'O' (B, D, F). THE COLORS IN A, C, D REPRESENT THE PARAMETER AMPLITUDE AT EACH COST PERCENTAGE.	131
FIGURE 57. CONNECTIVITY DIAGRAMS OF THE WINDOW OF 20 SECONDS. (LEFT) CONNECTIVITY DURING EYES OPEN (R1) CONDITION. (RIGHT) CONNECTIVITY DURING EYES CLOSED (R2) CONDITION.....	132
FIGURE 58. CONNECTIVITY DIAGRAMS OF THE WINDOW OF 20 SECONDS. (LEFT) CONNECTIVITY DURING EYES OPEN (R1) CONDITION. (RIGHT) CONNECTIVITY DURING EYES CLOSED (R2) CONDITION.....	133
FIGURE 59. CONNECTIVITY DIAGRAMS FOR EYES OPEN AND EYES CLOSED STATES DURING THE ALPHA BAND FOR THE SELECTED WINDOWS.	136
FIGURE 60. CLUSTER DIAGRAMS FOR EYES OPEN AND EYES CLOSED STATES DURING THE ALPHA BAND FOR THE SELECTED WINDOWS.	137
FIGURE 61. GRAPH BASED PARAMETERS ESTIMATED FOR R1 AND R2 STATES DURING THE ALPHA BAND FOR THE SELECTED WINDOWS.	138

FIGURE 62. CONNECTIVITY DIAGRAMS FOR EYES OPEN AND EYES CLOSED STATES DURING THE BETA BAND FOR THE SELECTED WINDOWS.	141
FIGURE 63. CLUSTER DIAGRAMS FOR EYES OPEN AND EYES CLOSED STATES DURING THE ALPHA BAND FOR THE SELECTED WINDOWS.	142
FIGURE 64. GRAPH BASED PARAMETERS ESTIMATED FOR R1 AND R2 STATES DURING THE BETA BAND FOR THE SELECTED WINDOWS.	144
FIGURE 65. KURTOSIS VARIANCE ($K\sigma^2$) SEARCHING DOMAINS FOR SEGMENTATIONS FROM 50 MS TO 1 SECOND.	153
FIGURE 66. NUMBER OF CHANNELS AS A FUNCTION OF THE SEGMENT LENGTH AND THE SEARCHING INTERVAL IN TERMS OF THE KURTOSIS VARIANCE – SHORT WINDOW SEGMENTATION.	158
FIGURE 67. KURTOSIS DISTRIBUTIONS CONSIDERING THE SELECTED CHANNELS FROM THE PERCENTAGE THRESHOLDS. – SHORT WINDOW SEGMENTATION. RESTING-STATE CONDITIONS DEPICTED IN PAIRS: A, B) S5 – R1, R2. C, D) S6 – R1, R2. E, F) S8 – R1, R2. G, H) S9 – R1, R2. I, J) S10 – R1, R2	161

List of Tables

TABLE 1. SUBSTAGES IN THE PROCESSING OUTLINE CONSIDERED IN FIGURE 4.	39
TABLE 2. LIST OF WINDOW DURATIONS ON DIFFERENT WORKS THAT PERFORM CONNECTIVITY ANALYSIS.	40
TABLE 3. RECORDINGS' CHARACTERISTICS BEFORE AND AFTER THE CLEANING PROCESS	55
TABLE 4. SEGMENT DURATIONS AND NUMBER OF CHANNELS SHARING KURTOSIS VARIANCES	78
TABLE 5. SEGMENTATION CHARACTERISTICS FOR LONG AND SHORT SEGMENTS.	88
TABLE 6. KURTOSIS VARIANCE RANGE OF DIFFERENT PERCENTAGE THRESHOLDS, $wl = 1,2, \dots, 10$ SECONDS.....	106
TABLE 7. KURTOSIS VARIANCE RANGE OF DIFFERENT PERCENTAGE THRESHOLDS, $wl = 1,2, \dots, 10$ SECONDS.....	106
TABLE 8. SELECTED SEGMENT LENGTHS (IN GREEN) FOR EACH SUBJECT AND RESTING-STATE CONDITION.	111
TABLE 9. SEGMENT SELECTION FOR THE CONSIDERED EEG RECORDINGS.....	114
TABLE 10. COMMON CHANNELS OF ALL THE CONSIDERED SUBJECTS ACCORDING TO	114
TABLE 11. COMMON CHANNELS ACROSS SUBJECTS AND SEGMENT TYPES.....	115
TABLE 12. INTERACTION ANALYSIS BETWEEN CONDITION*BAND (EYES OPEN/EYES CLOSED * FREQUENCY BAND – ALPHA AND BETA).....	116
TABLE 13. SIGNIFICANCE OF INTERACTIONS FOR THE NORMALIZED DENSITY OF THE ALPHA BAND.....	124
TABLE 14. SIGNIFICANCE OF INTERACTIONS FOR THE AVERAGE STRENGTH OF THE ALPHA BAND.	124
TABLE 15. GRAPH THEORY MEASURES APPLIED TO THE ADJACENCY MATRICES OF SIGNIFICANT CONNECTIONS.	128
TABLE 16. KURTOSIS VARIANCE RANGE OF DIFFERENT PERCENTAGE THRESHOLDS, $wl = 50,100, \dots, 1000$ MILLISECONDS..	154
TABLE 17. KURTOSIS VARIANCE RANGE OF DIFFERENT PERCENTAGE THRESHOLDS, $wl = 50,100, \dots, 1000$ MILLISECONDS..	154
TABLE 18. SELECTED SEGMENT LENGTHS (IN GREEN) FOR EACH SUBJECT AND RESTING-STATE CONDITION – SHORT WINDOW SEGMENTATION.	159

List of annexes: Tables

TABLE AN 1. NUMBER OF CHANNELS, VARIANCE RANGE AND SEGMENT LENGTHS, $wl = 1, \dots, 10$ SECONDS. S2 – R1	168
TABLE AN 2. NUMBER OF CHANNELS, VARIANCE RANGE AND SEGMENT LENGTHS, $wl = 1, \dots, 10$ SECONDS. S2 – R2	168
TABLE AN 3. NUMBER OF CHANNELS, VARIANCE RANGE AND SEGMENT LENGTHS, $wl = 0.05, \dots, 1$ SECONDS. S2 – R1	168
TABLE AN 4. NUMBER OF CHANNELS, VARIANCE RANGE AND SEGMENT LENGTHS, $wl = 0.05, \dots, 1$ SECONDS. S2 – R2	169
TABLE AN 5. NUMBER OF CHANNELS, VARIANCE RANGE AND SEGMENT LENGTHS, $wl = 0.05, \dots, 1$ SECONDS. S5 – R1	169
TABLE AN 6. NUMBER OF CHANNELS, VARIANCE RANGE AND SEGMENT LENGTHS, $wl = 0.05, \dots, 1$ SECONDS. S5 – R2	170
TABLE AN 7. NUMBER OF CHANNELS, VARIANCE RANGE AND SEGMENT LENGTHS, $wl = 0.05, \dots, 1$ SECONDS. S6 – R1	170
TABLE AN 8. NUMBER OF CHANNELS, VARIANCE RANGE AND SEGMENT LENGTHS, $wl = 0.05, \dots, 1$ SECONDS. S6 – R2	171
TABLE AN 9. NUMBER OF CHANNELS, VARIANCE RANGE AND SEGMENT LENGTHS, $wl = 0.05, \dots, 1$ SECONDS. S8 – R1	171
TABLE AN 10. NUMBER OF CHANNELS, VARIANCE RANGE AND SEGMENT LENGTHS, $wl = 0.05, \dots, 1$ SECONDS. S8 – R2	172
TABLE AN 11. NUMBER OF CHANNELS, VARIANCE RANGE AND SEGMENT LENGTHS, $wl = 0.05, \dots, 1$ SECONDS. S9 – R1	172
TABLE AN 12. NUMBER OF CHANNELS, VARIANCE RANGE AND SEGMENT LENGTHS, $wl = 0.05, \dots, 1$ SECONDS. S9 – R2	173
TABLE AN 13. NUMBER OF CHANNELS, VARIANCE RANGE AND SEGMENT LENGTHS, $wl = 0.05, \dots, 1$ SECONDS. S10 – R1 ..	173
TABLE AN 14. NUMBER OF CHANNELS, VARIANCE RANGE AND SEGMENT LENGTHS, $wl = 0.05, \dots, 1$ SECONDS. S10 – R2 ..	174
TABLE AN 15. SIGNIFICANCE OF INTERACTIONS FOR THE NORMALIZED DENSITY OF THE BETA BAND.....	174
TABLE AN 16. SIGNIFICANCE OF INTERACTIONS FOR THE AVERAGE STRENGTH OF THE ALPHA BAND.....	174
TABLE AN 17. P-VALUES OF ALL THE WINDOWS FOR ALPHA AND BETA.....	177

Acknowledgments

I want to dedicate this thesis work to all the people that have been involved directly or indirectly in my formation as an engineer, those who have believed in me even when I have doubted myself.

This thesis is dedicated firstly and more importantly to my family who has supported me from Colombia. To my mom Martha who is the strongest person I know and the reason why I moved forward to follow my dreams. To my dad Jair who has always supported and believed in me. To my sisters who have been there when I needed them and Lesly who has cheered me up with her kind words. Thanks to my aunt Juana and my cousin Nana, without your help I would not be here working on my dreams.

I would like to also thank my dearest friends who have become the family I chose, who have supported and dealt with me even when I am annoying. Thanks to Laura and Paolo who opened me a space to share in which I feel so comfortable. To Sebastian who has dealt with me throughout these 2 years and who is always ready to help if I need it. To Greys, thank you for your support and understanding. To Mayra, thank you for listening to me when I needed it the most. And Kosara, who helped me so much in this thesis.

Finally, I would like to thank Professor Paglialonga and Professor Barbieri who have supported this work from the beginning and whose suggestions and opinions have really helped me to improve as an engineer and to become a better researcher. Also, thanks to all the people from the ITB research group at CNR for your kindness, support, and suggestions with this work.

Abstract

In this thesis work, we propose a new framework for effective connectivity analysis applied to EEG signals of resting-state conditions in the wakeful state. Our data consisted of 20 EEG recordings acquired during 5 minutes from 10 healthy subjects who were asked to maintain a relaxed state in two conditions, by keeping their eyes open, and eyes closed. First, a thorough analysis of the state of the art permitted to analyze and review the usual processing structure employed on the signals to find the effective connections that characterizes the connectivity patterns on the relaxation states.

To this extent we have implemented the standard processing framework fitting a Multivariate Autoregressive (MVAR) model to the signal samples and requiring the segmentation of the time-series into shorter blocks for an appropriate fitting of the model. The segment length for the MVAR fitting is a topic that is not usually addressed in the literature and is commonly selected based on basic assumptions of the characteristics of the signals under analysis. This is why a window selection step as an intermediate process is further implemented to find the window length that guarantees stationarity over the whole set of EEG channels from the dataset to perform the MVAR fitting process.

As result of this window selection approach, the windows of 400 milliseconds and 4 seconds were selected as the most stationary ones according to the analysis on the categories of short and long windows. These choices were employed to perform the effective connectivity analysis and were compared to other two windows of 2 seconds and 20 seconds in order to establish the results from them.

The connectivity patterns derived from these windows were compared first using the definition of regions of interest (ROIs). The estimated patterns indicated that the posterior area of the brain was the most involved one in the connectivity for the resting state conditions in all the windows, characterizing the influence of this area onto the frontal and lateral areas. However, this general point of view is not sufficient to characterize the connectivity networks, and the connectivity in the sensor space defined by using all the channels was employed for the final analysis of the data.

The connectivity analysis in the sensor space revealed similar connectivity patterns for the final choice of the 4 second windows. These patterns are in line with the currently most recognized definition of the default mode network (DMN) which involves the connections between specific channels in the posterior-central joint and the frontal-central area and that characterize the resting state connections between the Broadmann area 40 (precuneus) and Broadmann areas 8 and 10 (middle frontal regions). For this reason, the 4 seconds window was selected as the one explaining the effective connectivity according to the literature.

These results demonstrate that our framework is an efficient algorithm that provides correct results on connectivity according to the literature, this is achieved by selecting appropriate parameters for the fitting process and the model explains better the physiological characteristics of the neural activity under analysis.

Summary

Effective connectivity provides a way to analyze how the information flows across different nodes composing a network of sources. These sources are usually defined by a multivariate process like the electroencephalographic signals acquired by an array of EEG electrodes. The purpose of this thesis work is to analyze the effective connectivity on electroencephalographic signals that measure neural activity of resting-state conditions and propose possible improvements applied to the connectivity processing framework. This, to better explain the information flow according to the physiological characteristics of the signals under analysis and the observations from the state of the art.

Neural activity encodes the information transmission and the way how the different structures, organs, and systems communicate inside the complex machinery known as the human body. At the level of the brain, the neural activity can be tracked down considering different imaging techniques that measure the variation of electric and magnetic potentials, and the blood flow to obtain a representation of the functional activity produced in the brain. To understand what is happening in the brain, different strategies have been designed most of them based on digital signal processing considering the information acquired from brain structures. This information can have the form of a multivariate time series acquired from different sources (e.g., electrodes, BOLD signals). The techniques applied to these time-varying series range from the classical power spectral analysis, brain rhythms identification up to real-time applications of adaptive filtering and pattern recognition.

Considering electroencephalography (EEG), one of these processing techniques examines the causal relationships of the signals and provides a multivariate approach to measure if past samples of a signal exert some influence in the present information of another time-varying series. From this information, besides the anatomical relationships of the sensors that acquire the biopotentials in the scalp, it is possible to obtain a representation of the effective connections among the EEG channels, evaluating which channels exert influence onto other channels and to which extent. All of this is known as effective connectivity and provides a way to investigate the structures that are anatomically related or the hidden structures that participate in the transmission of information in the network that can be defined by the set of channels from the EEG system.

The effective connectivity analysis relies on a multivariate autoregressive (MVAR) model fitting process due to the nature of the EEG signals and their acquisition characteristics. The MVAR model implies that the signals under the fitting process need to have stationary characteristics, otherwise, the effective connectivity process will provide errors in the estimations. This is why there are needed stationary/quasi-stationary segments to provide an appropriate fitting of the MVAR model to then estimate the effective connectivity measures. Despite this obvious requirement, a big portion of effective connectivity works in the literature do not provide an evaluation of the stationary characteristics of the segment size considered for the MVAR fitting process, thus, they make some assumptions related to the brain activity task under analysis and select a window size from the minimum number of samples needed to capture the frequency components that are expected to explain the neural activity.

This is the reason why the design and implementation of an algorithm that looks for the stationary characteristics of different segment lengths of EEG signals is being proposed in

this thesis work. The EEG signals under analysis were acquired from 10 healthy subjects, from who 20 recordings were obtained. There were acquired 10 recordings under the open eyes resting-state condition and 10 more for the eyes-closed state. The recordings lasted in overall 5 minutes and were acquired at a sampling rate of 1000 Hz. These EEG datasets comprise the information of neural activity under a relaxation state in wakefulness.

The algorithm comprises the segmentation procedure, which is performed by considering different segment lengths, and from them, the kurtosis variance is employed to explain the stationarity exhibited by performing the segmentation under a specific segment duration. Then, a searching strategy by looking at the density function generated from the kurtosis variance values is employed to look for the segments that have less variability of kurtosis and that maximize the number of channels in the EEG dataset exhibiting the same characteristics.

As a result of this process, two windows (from two different kinds of segment length analysis, i.e., short, and long window length analysis), one of 400 milliseconds and one of 4 seconds are selected as the ones that explain most of the stationary characteristics across the channels for the subjects that participated in the experiment.

After this process, an evaluation of the effective connectivity was performed by considering the network characteristics explained by graph theory parameters. First, the adjacency matrices derived from the Directed Transfer Function matrices were generated by performing the statistical tests on surrogate data. From this process, the significant connections given the connectivity matrices are obtained and the connectivity diagrams are generated from them. The adjacency matrices are studied considering the parameters of centrality, segregation, clustering, and the basic measures that account for the connections related to a node and the amplitudes that explain the weights explained by the adjacency matrices. From these values, it is possible to characterize the network by looking at central nodes in the network and localizing regions of greater connectivity in the process under evaluation.

Some Regions of Interest (ROI) were also defined to have a bigger picture of the connectivity flow among larger areas that are being composed by different channels. In this way, it was possible to obtain general characteristics on the alpha and beta bands. Specifically, the posterior region showed to have a great influence on the frontal and lateral regions, as well as the central and frontal relationship. This was observed for all the windows under analysis; however, it was not enough to provide a detailed evaluation of the connectivity patterns for the resting state conditions. For this reason, the analysis on the sensor space considering the channels of the EEG system was performed and highlighted specific structures characterizing the neural activity.

As a result of this process, effective connectivity networks were found for windows larger than 1 second. Specifically, the windows of 2 seconds and 4 seconds exhibited similarities in the connectivity relationships which were supported by the graph-theoretical measures that explained their similarities concerning the number of connections present in the adjacency matrices.

In physiological terms, the networks exhibited by the windows are related to the so-called default mode network (DMN) which comprises the areas from the frontal-central joint and

the posterior-central areas which group the central nodes found in the windows of 2 seconds and 4 seconds. The connectivity patterns and the weights related to these connections highlighted a slight increment for the 2 seconds window for the alpha and beta bands compared to the other windows. The similarities of the results of the 4 seconds window to the connectivity diagrams of the 2 seconds segment, both in the connectivity structure and the graph-based parameters, permit to establish the relationship with the hypothesis of the involvement of the DMN in the characterization of the resting state conditions. The 20 seconds window showed a similar behavior only for the closed eyes condition in the alpha band case, differently from the other two segments. Finally, the case of the 400 ms window shows that very short segments are not necessarily a source of information for the effective connectivity framework even though they respect the stationary requirement for the MVAR fitting process.

Even though the 2 seconds window exhibited promising results to explain the connectivity relationships of the neural activity during resting states, it did not provide statistical significance for the degree measure that explains the connectivity behavior on the network and so the 4 seconds window was selected as an appropriate window length that explained the characteristics of the resting state condition in relaxation state during eyes open and eyes closed.

In conclusion, it is important to underline the main two novelties of this work that are the framework to select an appropriate window that considers the stationary characteristics of the signals under consideration and a way to highlight the central nodes in the sensor space according to the graph theory measures employed to characterize the effective connectivity network. From this framework, it was possible to obtain an algorithm that provides a way to evaluate the stationary characteristics of the EEG signals considering high-order statistics. Results applying our framework to an original dataset allows to compute the effective connectivity by employing the segment length that provides more stationary features for the EEG signal composing the datasets. Here, the window of 4 seconds selected from the searching strategy considering the algorithm was the one that explained better the physiological characteristics of the neural activity under analysis. This thesis work provides a tool that can be used to perform effective connectivity analysis on a much larger dataset considering also different setups and experiment conditions.

Sommario

Una connettività efficace fornisce un modo per analizzare il modo in cui le informazioni fluiscono attraverso i diversi nodi che compongono una rete di fonti. Queste sorgenti sono solitamente definite da un processo multivariato come i segnali elettroencefalografici acquisiti da una matrice di elettrodi EEG. Lo scopo di questo lavoro di tesi è analizzare la connettività effettiva su segnali elettroencefalografici che misurano l'attività neurale delle condizioni di stato di riposo e proporre possibili miglioramenti applicati al framework di elaborazione della connettività. Questo, per meglio spiegare il flusso di informazioni in base alle caratteristiche fisiologiche dei segnali in analisi e alle osservazioni dello stato dell'arte.

L'attività neurale codifica la trasmissione delle informazioni e il modo in cui le diverse strutture, organi e sistemi comunicano all'interno del complesso macchinario noto come corpo umano. A livello del cervello, l'attività neurale può essere rintracciata considerando diverse tecniche di imaging che misurano la variazione dei potenziali elettrici e magnetici e il flusso sanguigno per ottenere una rappresentazione dell'attività funzionale prodotta nel cervello. Per capire cosa sta succedendo nel cervello, sono state progettate diverse strategie, la maggior parte delle quali basate sull'elaborazione del segnale digitale, considerando le informazioni acquisite dalle strutture cerebrali. Queste informazioni possono avere la forma di una serie temporale multivariata acquisita da diverse fonti (ad esempio, elettrodi, segnali BOLD). Le tecniche applicate a queste serie variabili nel tempo vanno dalla classica analisi spettrale di potenza, all'identificazione dei ritmi cerebrali fino alle applicazioni in tempo reale di filtraggio adattivo e riconoscimento di pattern.

Considerando l'elettroencefalografia (EEG), una di queste tecniche di elaborazione esamina le relazioni causali dei segnali e fornisce un approccio multivariato per misurare se i campioni passati di un segnale esercitano una qualche influenza sulle informazioni presenti di un'altra serie variabile nel tempo. Da queste informazioni, oltre alle relazioni anatomiche dei sensori che acquisiscono i biopotenziali nel cuoio capelluto, è possibile ottenere una rappresentazione delle effettive connessioni tra i canali EEG, valutando quali canali esercitano influenza su altri canali e in che misura. Tutto ciò è noto come connettività efficace e fornisce un modo per indagare le strutture che sono anatomicamente correlate o le strutture nascoste che partecipano alla trasmissione di informazioni nella rete che possono essere definite dall'insieme di canali dal sistema EEG.

L'analisi della connettività efficace si basa su un processo di adattamento del modello autoregressivo multivariato (MVAR) a causa della natura dei segnali EEG e delle loro caratteristiche di acquisizione. Il modello MVAR implica che i segnali sotto il processo di adattamento devono avere caratteristiche stazionarie, altrimenti il processo di connettività efficace fornirà errori nelle stime. Questo è il motivo per cui sono necessari segmenti stazionari / quasi stazionari per fornire un adattamento appropriato del modello MVAR per poi stimare le misure di connettività effettive. Nonostante questo ovvio requisito, una gran parte dei lavori di connettività efficaci in letteratura non fornisce una valutazione delle caratteristiche stazionarie della dimensione del segmento considerata per il processo di adattamento MVAR, quindi, fanno alcune ipotesi relative al compito di attività cerebrale in analisi e selezionare una dimensione della finestra dal numero minimo di campioni necessari per acquisire i componenti di frequenza che dovrebbero spiegare l'attività neurale.

Questo è il motivo per cui in questo lavoro di tesi viene proposto il progetto e l'implementazione di un algoritmo che ricerca le caratteristiche stazionarie di diverse lunghezze di segmento di segnali EEG. I segnali EEG in analisi sono stati acquisiti da 10 soggetti sani, da cui sono state ottenute 20 registrazioni. Sono state acquisite 10 registrazioni in condizioni di stato di riposo ad occhi aperti e altre 10 per lo stato di occhi chiusi. Le registrazioni sono durate complessivamente 5 minuti e sono state acquisite a una frequenza di campionamento di 1000 Hz. Questi set di dati EEG comprendono le informazioni sull'attività neurale in uno stato di rilassamento durante la veglia.

L'algoritmo comprende la procedura di segmentazione, che viene eseguita considerando diverse lunghezze di segmento, e da esse, la varianza della curtosi viene impiegata per spiegare la stazionarietà esibita eseguendo la segmentazione sotto una durata di segmento specifica. Quindi, viene utilizzata una strategia di ricerca che esamina la funzione di densità generata dai valori di varianza della curtosi per cercare i segmenti che hanno meno variabilità della curtosi e che massimizzano il numero di canali nel set di dati EEG che presentano le stesse caratteristiche.

Come risultato di questo processo, due finestre (da due diversi tipi di analisi della lunghezza del segmento, ovvero analisi della lunghezza della finestra breve e lunga), una di 400 millisecondi e una di 4 secondi vengono selezionate come quelle che spiegano la maggior parte dello stazionario caratteristiche attraverso i canali per i soggetti che hanno partecipato all'esperimento.

Dopo questo processo, è stata eseguita una valutazione della connettività effettiva considerando le caratteristiche di rete spiegate dai parametri della teoria dei grafi. In primo luogo, le matrici di adiacenza derivate dalle matrici della funzione di trasferimento diretto sono state generate eseguendo i test statistici su dati surrogati. Da questo processo si ottengono le connessioni significative date le matrici di connettività e da esse si generano i diagrammi di connettività. Le matrici di adiacenza vengono studiate considerando i parametri di centralità, segregazione, clustering e le misure di base che tengono conto delle connessioni relative a un nodo e le ampiezze che spiegano i pesi spiegati dalle matrici di adiacenza. Da questi valori è possibile caratterizzare la rete osservando i nodi centrali della rete e localizzando le regioni di maggiore connettività nel processo in esame.

Sono state inoltre definite alcune regioni di interesse (ROI) per avere un quadro più ampio del flusso di connettività tra aree più ampie composte da canali diversi. In questo modo è stato possibile ottenere caratteristiche generali sulle bande alfa e beta. In particolare, la regione posteriore ha mostrato di avere una grande influenza sulle regioni frontale e laterale, nonché sulla relazione centrale e frontale. Questo è stato osservato per tutte le finestre in analisi; tuttavia, non era sufficiente fornire una valutazione dettagliata dei modelli di connettività per le condizioni di stato di riposo. Per questo motivo è stata eseguita l'analisi sullo spazio sensoriale considerando i canali del sistema EEG evidenziando strutture specifiche caratterizzanti l'attività neurale.

Come risultato di questo processo, sono state trovate reti di connettività efficaci per finestre di dimensioni superiori a 1 secondo. In particolare, le finestre di 2 secondi e 4 secondi mostravano somiglianze nelle relazioni di connettività che erano supportate dalle misure grafo-teoriche che spiegavano le loro somiglianze riguardo al numero di connessioni presenti nelle matrici di adiacenza.

In termini fisiologici, le reti esibite dalle finestre sono relative alla cosiddetta rete in modalità predefinita (DMN) che comprende le aree dall'articolazione frontale-centrale e le zone centro-posteriori che raggruppano i nodi centrali presenti nelle finestre di 2 secondi e 4 secondi. Gli schemi di connettività e i pesi relativi a queste connessioni hanno evidenziato un leggero incremento per la finestra di 2 secondi per le bande alfa e beta rispetto alle altre finestre. Le somiglianze dei risultati della finestra di 4 secondi con i diagrammi di connettività del segmento di 2 secondi, sia nella struttura di connettività che nei parametri basati su grafici, consentono di stabilire la relazione con l'ipotesi di coinvolgimento del DMN nella caratterizzazione di le condizioni di stato di riposo. La finestra di 20 secondi ha mostrato un comportamento simile solo per la condizione di occhi chiusi nel caso della banda alfa, a differenza degli altri due segmenti. Infine, il caso della finestra di 400 ms mostra che i segmenti molto brevi non sono necessariamente una fonte di informazioni per il framework di connettività efficace anche se rispettano il requisito stazionario per il processo di adattamento MVAR.

Anche se la finestra di 2 secondi ha mostrato risultati promettenti per spiegare le relazioni di connettività dell'attività neurale durante gli stati di riposo, non ha fornito significatività statistica per la misura del grado che spiega il comportamento di connettività sulla rete e quindi la finestra di 4 secondi è stata selezionata come lunghezza della finestra appropriata che spiegasse le caratteristiche della condizione di stato di riposo in stato di rilassamento durante gli occhi aperti e chiusi.

In conclusione, è importante sottolineare le due principali novità di questo lavoro che sono il framework per selezionare una finestra appropriata che consideri le caratteristiche stazionarie dei segnali in esame e un modo per evidenziare i nodi centrali nello spazio dei sensori secondo il grafico misure teoriche impiegate per caratterizzare la rete di connettività efficace. Da questo quadro è stato possibile ottenere un algoritmo che fornisce un modo per valutare le caratteristiche stazionarie dei segnali EEG considerando statistiche di ordine elevato. I risultati dell'applicazione del nostro framework a un set di dati originale consentono di calcolare la connettività effettiva utilizzando la lunghezza del segmento che fornisce caratteristiche più stazionarie per il segnale EEG che compone i set di dati. Qui, la finestra di 4 secondi selezionata dalla strategia di ricerca considerando l'algoritmo era quella che spiegava meglio le caratteristiche fisiologiche dell'attività neurale in analisi. Questo lavoro di tesi fornisce uno strumento che può essere utilizzato per eseguire analisi di connettività efficaci su un set di dati molto più ampio considerando anche diverse configurazioni e condizioni di esperimento.

1. Introduction

The analysis of signals for medical diagnosis and their processing either for supporting the labor of physicians and medical doctors or to research pathological/healthy conditions on patients is one important area in the biomedical field. Supervising, tracking, and storing the variation over time of the huge number of variables that provide information of the health state of a person is a challenging process, it involves a synergic link between hardware, sensors and any other elements that are able to transduce the measured variable onto a readable domain from which further processing can be made with information treatment techniques implemented using computers or dedicated processing devices.

The appropriate conditions to obtain meaningful information from physiological processes makes the signal acquisition even more difficult. There are needed specific equipment with particular configurations, hardware, and processing steps in order to acquire data that explain the physiological process accurately and correctly. Moreover, the diversity on the domains that can explain the physiological variables in terms of biochemical reactions, bioelectric potentials, pressure changes, light, and magnetic responses (to name a few) in the human body make this process even more challenging.

In this way proper instrumentation elements are needed to acquire the information, and there exist a lot of devices in charge of those specific tasks [1]. Depending on the physiological characteristics, how much information is needed to be acquired, if the acquirement is invasive/non-invasive and the costs of the tests there exist different devices that measure and quantify the physiological variables.

Moreover, the different systems that compose the human body provide different types of information, for instance, the cardiovascular system performs complex processes that can be monitored; the cardiac rhythm can be characterized and evaluated through the electrocardiographic signals (ECG) acquired non-invasively and its sound could also be registered to obtain the vibrations produced by the heart and the blood circulating in this system, the so-called phonocardiogram (PCG) [2].

Other examples comprise the characterization of the skeletal muscle states by means of observing the bioelectrical potentials in the muscles, known as electromyogram (EMG), or the registration of the vibration signal related to the contraction of the muscles (vibromyogram - VMG).

On the other hand, the analysis of the brain is undoubtedly one of the most challenging practices that can be achieved not only by physicians but also from the bioengineering point of view. The most common and non-expensive way to have a representation of the brain activity is done by considering the electroencephalogram (EEG), which represents the general bioelectrical variation of the potentials that are transferred to the scalp from the cortical areas in the brain. Similarly, the electroneurograms (ENG) that registers the nerve action potentials provide a way to characterize the conduction velocity when an action potential is produced at the level of a nerve. The event-related potentials (ERPs) comprise the bioelectric potential patterns produced after external stimulation by means of electrical, light or sound, and characterize the brain response in relation to a certain stimulus as the result of motor, cognitive or sensory events.

There exist many more examples of signals that convey meaningful information of the systems and the physiological processes that are carried out by them in the human body. As it was described earlier, the signals are the product of the physiological interactions and reflect the natural behavior of the systems. In the same way, the alteration of the healthy physiological processes that affects their performance can be analyzed too, and these pathological processes are characterized quantitatively to enhance the diagnosis in clinical applications and to improve the characterization in the research practice.

More than performing the classical analysis of signals and images from which it is possible to find meaningful information to understand the basic features that characterize the general state of the health of the brain, bioengineers devote their efforts to find sophisticated ways to analyze and provide more information from the raw signals that are being acquired by specialized equipment.

Moreover, the techniques developed by bioengineers have been accepted more in the clinical field during the recent years. Passing from the classical analysis and processing of signals which was primarily devoted to filtering, frequency analysis and modeling from the point of view of signal parametrization, the modern information analysis of physiological signals intends to characterize the complex biological systems, their interactions and the processes as a whole considering the signals as the primary source of information. This allows to study quantitatively the different pathologies, the healthy states, and the nature of the systems behind a specific process in consideration improving non-invasive diagnostics and providing tools for physicians and doctors in their diagnosis labors.

Is in this way that the biomedical signal analysis has a huge impact not only in the medical sciences but in the research practice. Specially the complex interactions in the brain have gotten great attention due to the recent development of technologies that comprise portable and relatively inexpensive devices [3]. Moreover, the great computing capabilities of modern computers allow to perform very complex processing schemes to multivariate long-lasting signals like EEG.

The neural activity represented by EEG signals is one of the starting points to characterize the brain processes, is in this way that this thesis is elaborated, to provide a way to perform connectivity analysis for resting-state conditions in healthy subjects, specifically, to observe the influence of the signal partitioning process of the signals in the connectivity results.

1.1. The brain

The brain is a very complex organ that has been extensively studied throughout history. It was no earlier than the XIX century that the brain activity registered through electric signals was first observed by registering the signal variations using electrodes placed on the scalp and connected to a galvanometer [4]. Since then, there have been revolutionary advancements in the understanding of the brain, its core importance in commanding the behavior of the systems interacting in the human body, and its regulatory role in most physiological processes carried out by the other organs.

A first look at the brain as an organ comprises the understanding of its anatomy and its organization. Neuroanatomic locations provide a way to understand the functional and spatial organization of the different regions identified in the brain structure [5]. Relative location identifiers classify the volumetric positioning of the regions, as such, we have the

anterior, posterior, superior, and inferior areas besides the rostral, caudal, ventral, and dorsal as shown in Figure 1.

From these locations, there are identified three main divisions: the forebrain, the midbrain, and the hindbrain. The forebrain is composed of the telencephalon/cerebral cortex, the diencephalon, and the basal ganglia in charge of the modulation of motor movements. The cerebrum, an area of complex functions processes the perception and control of the conscious motor movement. Finally, we have the left and right hemispheres devoted to sensory and motor information processing are interconnected by the so-called corpus callosum.

Moreover, there are identified 4 lobes that denote anatomical and functional processes at different areas. These regions process the perception of sensations, language, speech, movement, cognition, and some other high-level functions. Figure 2 shows the location of the lobes as the division of the cerebrum.

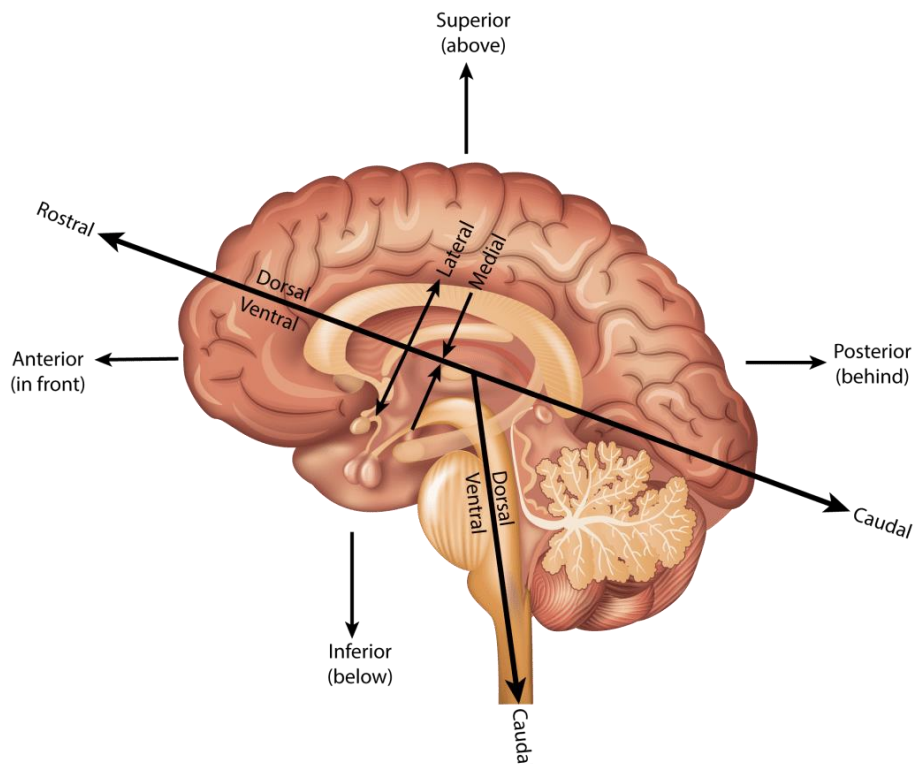


Figure 1. Relative position identifiers of the brain. Image taken from [6]
<https://www.thescienceofpsychotherapy.com/glossary/rostral/>

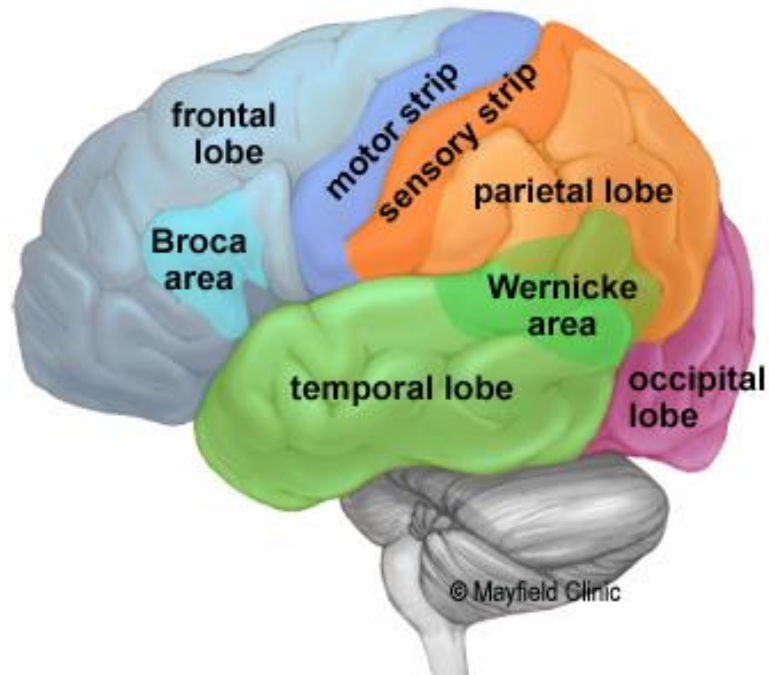


Figure 2. Division of the cerebrum into lobes. Image taken from [7] <https://mayfieldclinic.com/pe-anatbrain.htm>

There are identified different functions carried out by each lobe. The frontal lobe is involved principally in concentration, self-awareness, intelligence, behavior, personality, and emotion processing, besides engaging tasks like planning and problem-solving. Other important functions are related to speech processing both at speaking and writing.

The parietal lobe covers the somatosensory cortex, and it is located at the level of the center of the brain in the superior region in the caudal direction connecting to the anterior region. Its main function is devoted to the interpretation of language and the words, as well as the sensory signals coming from the motor, vision, hearing, and memory information. It is engaged in spatial and visual perception, being important to carry out location and navigation processes.

The temporal lobe located in the lateral region is found to be important in language understanding considering the well-known Wernicke's area, it is involved in the sequencing and organization of tasks as well as the hearing processing by the auditory cortex and the memory formation handling performed by the hippocampus.

The posterior region is characterized for covering the occipital lobe a region located at the back of the brain structure. Its main function is the processing and interpretation of visual information through the primary visual cortex.

As described above each lobe covers broad regions that perform very complex functions. Different areas delimited anatomically perform the processing of sensory and motor information, these cortices can be stimulated to produce muscular contraction or can be activated as a response to a sensory stimulus. In the same way, they can be mapped topographically by defining subregions, specialized areas in charge of very specific tasks. As an example, the Brodmann areas were defined as an atlas of the brain classifying and grouping the subregions devoted to specialized processes delimiting anatomically and functionally the cytoarchitectural organization of the neurons.

Other important structures are the hypothalamus, thalamus, pituitary gland, pineal gland, and basal ganglia, among others. They play important roles in the control of behaviors, hormone regulation, temperature and pressure modulation and control, sensory message conduction, metabolism control, and internal clock rhythm regulation, among other functionalities.

The hindbrain composed principally by the cerebellum, pons, and medulla oblongata is responsible for the regulation of fundamental functions for survival, wakefulness, sleep and it is also involved in the respiratory rhythm and motor activity coordination. The cerebellum is in charge of balance, movement, and coordination tasks. The pons is engaged in bladder control, hearing, posture, swallowing, sleep, and respiration tasks. The medulla oblongata controls diverse many autonomic functions like breathing, blood pressure, and some reflexes, it influences the HRV as well [8].

1.2. Neural activity

The neural activity is the result of the interaction among the different cells that compose the brain circuits. Considering the neuron as the building block of the brain network and the nervous system, among its basic functions it is in charge of interconnecting to other neurons, receiving sensory inputs and transmitting motor commands to the muscles that act as the end effectors of the body. They are composed by three main parts, the dendrites which are the “terminals” of this type of cells and whose function is to connect with other neurons, the soma (or cell body containing the nucleus) in charge of the cell metabolism, and the axon, a long structure depicted as a flexible tubular element through which the electrical impulses travel.

The neurons are in charge of transmitting information, they are like information channels that are highly interconnected among them, they react to stimuli and process the information locally and in a general way according to the complex structure provided by regional networks that compose the different areas in the brain. That information flux and the interactions produced there correspond to the neural activity which can be detected and quantified in different ways, for instance, by measuring the oxygen flow in the brain providing functional imaging of the brain performance (fMRI).

The way in which the neurons have a connection interface is known as the synapsis and it is defined as a biochemical/electrical process that permits the transmission of action potentials triggered at the cell body of the neuron and that are generated by the change of the membrane potentials due to the stimulation received from other neurons in the complex junction between axon <-> dendrites or dendrites <-> dendrites over two or more cells.

The Central Nervous System (CNS) works around the way in which the action potentials (AP) are transferred among the neurons, treating them as the information that flows in the form of synaptic currents. The APs are the natural reactions of the neurons at different kind of stimuli; the nerves at sensory levels react to touch, light, chemical changes, touch, and pressure, transducing the external information into electrical responses encoded in the APs. At the level of the CNS, the neurons are chemically stimulated at the synapse occurrence from the interaction of the neurons.

Depending on the type of synapsis, either excitatory or inhibitory then a repolarization or hyperpolarization response is produced in the following neuron, producing excitatory postsynaptic potentials (EPSP) or inhibitory postsynaptic potentials (IPSP) [9]. From these

low-level interactions between two neurons there are produced other processes that encode the frequency of the interaction (i.e., the firing rate of the neurons), the amplitude of the membrane potentials during the synapsis, and in more complex scenarios a population of neurons can respond to the angular movement of repetitive motor actions [10], or provide different cortical activations depending on the motor movements in precision or force tasks [11]. This escalates in complexity from the different neurons that are being interconnected, and the important ability of the nervous system to adapt known as neural plasticity can be produced as well [12].

1.3. Origin of electroencephalographic signals and brain rhythms

The interactions produced among the neurons generate currents that flow from the cell membranes in the intra-extracellular junctions. That continuous flow of ionic currents generates what is called field potentials, translated into bioelectrical potentials as a product of the neural excitation/inhibition of the population of cell neurons. These bioelectrical potentials that merge the neural activity from the high-level processes of the different population of neurons flowing from deep structures up to the cortices can be then measured as the variation of electric signals over the scalp, generating what is known as electroencephalographic signals.

Specifically, the field potentials are developed in the soma and the dendrites of the pyramidal cells located on the external layer of the brain at the cortex level. These are generated from the EPSP and IPSP during the synaptic interaction among a large group of neurons, the difference of the electrical potentials in the cortex as result of the sum of the postsynaptic potentials produce electrical dipoles evidenced as the cortical electrical activity on the brain surface.

The electric potentials are distributed over the cortex and many voltage gradients are produced as result. This electric activity passes through the skull, and other intermediate structures arriving to the scalp from which non-invasive electrodes connected to instrumentation devices acquire the signals to measure and record the attenuated version of the cortical potentials that are corrupted by internal/external noise sources as well as artifacts. Thanks to the attenuation of the bioelectric potentials, specialized equipment must be employed in the recording and despite their high sensitivity, accuracy, and time resolution they are not able to acquire all the slight changes in amplitude and the differences in voltage over very small regions due to the spatial resolution restrictions given the electrode placement. Details about EEG equipment as a brain activity recording tool will be given in the subsection: Functional imaging methods.

From the extensive study of the EEG electric potentials, there have been identified oscillatory characteristics associated to different brain state conditions of a person. Due to their periodicity, they are known as brain rhythms and are defined in the frequency domain and bounded as follows:

- Delta band (δ): 0.5 – 4 Hz
- Theta band (θ): 4 – 8 Hz
- Alpha band (α): 7 – 13 Hz
- Beta band (β): 13 – 30 Hz
- Gamma band (γ): >30 Hz

The frequency intervals that define these brain rhythms bound the oscillatory characteristics of these common waves and provide meaningful information of the health condition of the brain and the CNS. Figure 3 shows the typical shapes of the brain rhythms from above DC level up to the 30 Hz frequency.

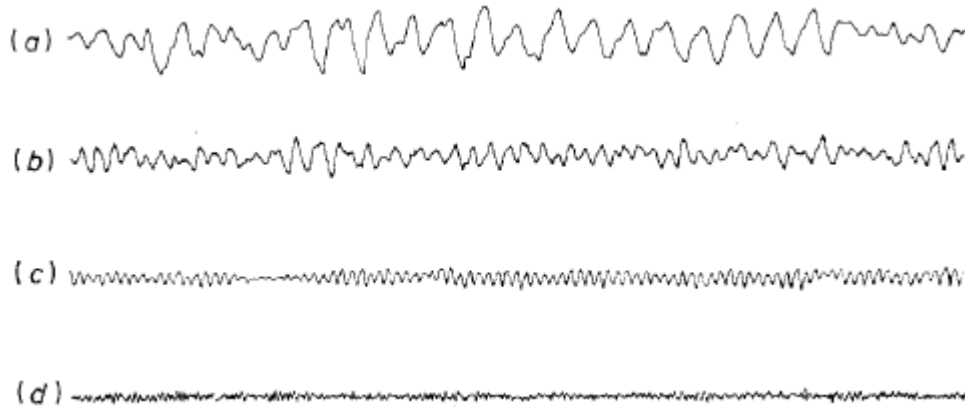


Figure 3. Shapes of the brain rhythms. a) delta frequency band, b) theta frequency band, c) alpha frequency band, d) beta frequency band. Taken from [13]

The alpha brain rhythms can be detected easily in the posterior part of the head in correspondence to the occipital lobe of the brain with bilateral synchrony, in this way, their amplitude is higher over this area. These signals are commonly found as sinusoidal shaped waves that in pathological conditions might be presented as sharp variations. The alpha waves are a distinctive feature that indicates relaxation during awareness state in tasks that do not involve concentration or attention, i.e., it is a rhythm associated to the resting state of the brain. These signals are more prominent at the closed-eyes state condition during awareness and have been thought to be scanning patterns waiting for active thinking processes, and are involved in clearing sensory information from distractors [14].

The incidence of the alpha waves is greatly reduced by opening the eyes, or after receiving any kind of visual stimulation, or during the change of the waiting state by engaging to attention tasks, for instance, anxiety, mental concentration in active thinking and hearing unfamiliar sounds [4].

As opposite to the alpha rhythm, the beta band reflects the active thinking process of a person, it is produced when active attention is being produced, and, as result, it is thought to be the waking rhythm of the brain. It is produced normally in adults when attention tasks are produced, for instance, when a problem is solved and in general in active thinking processes, high frequency components of the beta band, around 22 – 29 Hz, are related to behavioral performance, representing feature components of the behavior of a person. The beta band is related to the transmission and modulation of information among different cortical areas when attention tasks are being produced [14]. Anatomically, these waves are produced in the frontal and central regions, corresponding to the frontal lobe and part of the temporal and parietal lobes of the brain.

Higher frequency components of the brain waves, larger than 30 Hz are classified as gamma components. Their amplitudes are usually very low and they are thought to play a role in the language processing as explained in [15]. They convey information related to different sensory inputs and stimuli and memory processes in the short term. The gamma wave band

is used for event-related synchronization of the brain; however, EEG signals are not usually considered for this kind of assessment.

When the awareness state changes to drowsiness and sleep, the scanning function of the alpha rhythm is replaced by slower frequency components. The theta band frequencies appear during the first stages of sleep and the delta band takes over in deep-sleep states. In this way, the appearance of theta and delta components during attention and/or wakefulness states in adults can be considered as abnormal and can be sign of pathological conditions like tumors.

Brain rhythms characterize basic health conditions of the neural activity. This knowledge added to the different cognition experiments and the variety of ways to acquire brain activity provide useful elements to understand the behavior of the neural interaction during basal and pathological conditions. Some examples of the investigation of brain activity include monitoring coma, resting state conditions and brain death, investigating evoked potentials from external stimuli, analyzing the effects of anesthesia, understanding seizures produced by epileptic events, the test of drug effects, monitoring brain development, assessing mental disorders, investigating the sleep disorders, analyzing connectivity patterns and information transfer across different brain areas, and other brain computer interface applications that enable the link between computer devices and neural activity systems, among many more research topics and applications.

Due to the difficulty and the large set of applicable problems, it would be useful to understand how the technologies for brain activity acquisition work, this is done in the following chapter.

2. Brain imaging techniques

Imaging techniques are the processes of using technology to view the human body in the interest of diagnosing, monitoring, and treating medical problems in a non-invasive way.

In the process of diagnosis, the imaging techniques help the physicians to better understand the complications in the patient's body, optimize the wellbeing of the patients, support the decision-making process, and avoid unnecessary procedures. In many cases, such as in the diagnosis of breast cancer, or neuropathologies like Alzheimer (just to name a few applications) these tools can be lifesaving. Additionally, these technologies provide monitoring capabilities of the progress of diseases and assists in the determination of treatments.

2.1. Technologies for brain imaging: A brief description

In the following subsection the technologies for brain imaging are going to be reviewed. They are divided into *structural imaging methods*, which provide the structure of the body, the detection of large-scale diseases such as tumors and injuries; and *functional imaging methods*, that assist in the diagnosis of metabolic diseases and functions of the body.

2.1.1. Structural imaging methods:

A. *Computerized Tomography (CT)*

A computerized tomography (CT) scan integrates a series of X-ray images that are taken from different angles around the body and then by using computer processing creates the cross-sectional images, which are called slices of the bones, blood vessels and soft tissues inside the body. Within this process, the computer is able to remove the radiographic “shadows” that other parts of the body may cast on the organ of interest. In general, the CT scan provides better resolution than the conventional X-rays procedure and detects tumors and other lesions at earlier stages.

The scanner is shaped like a donut and the organ of interest (to be examined) is placed at the center of the donut’s hole. The patient is exposed to a small dose of radiation during the scan, the same as with the conventional X-ray procedure. The source of the x-ray emission rotates around the patient on one side, while the X-ray detector rotates directly opposite, such that it detects the X-rays that have been differentially absorbed as they passed through the tissues of the body part.

Depending on the patient’s symptoms, they might be injected with (or consume a drink of) a dye to increase the contrast between the normal and abnormal tissues.

B. *Magnetic Resonance imaging (MRI):*

Magnetic Resonance imaging uses magnetic fields that exploit the physical properties of matter at the sub-atomic level, especially of water, that account for about 75% of the mass of the human body.

Moreover, the scans not only provide higher-definition images than CT scans, but they are able to show the sagittal and coronal sections of the brain, not just the axial sections to which CT scans are limited.

Even though CT scans are the primary tool for imaging the chest and abdomen, they are also used as tools for the brain, hands, feet, and spinal column. The diseased or damaged tissues usually contain more water, thus easy to be detected with MRI.

In certain cases, the patient may be injected with a contrast agent, just as for CT scans. The agents generally used are compounds of the element gadolinium, same purpose as iodine, but with less risk of allergic reactions.

2.1.2. Functional imaging methods

A. *Electroencephalography (EEG)*

Electroencephalography (EEG) measures the brain's overall neuronal activity over a continuous period using electrodes attached to the scalp. Computers then analyze the brain activity which is sensed by electrodes positioned at different locations on the scalp.

The sensors detect the electrical currents that are generated mainly by the dendrite of the pyramidal neurons that are found in massive numbers in the cortex. Since these neurons are oriented parallel to one another, they amplify the signal from their common activity.

The oscillations in the EEG are then observed as the sum of the various oscillations which are produced by the various assemblies of neuron, with the "harmonics" being superimposed on one another to produce the total recorded trace. For analytical purposes, the trace has the equivalent two characteristics as a sound wave: its oscillation frequency and its amplitude.

Additionally, EEGs provide excellent temporal resolution and compared to fMRI and PETs are rather inexpensive, however the spatial resolution is quite poor. Nonetheless, EEGs can assist in diagnosing epileptic foci, brain tumors, lesions, clots, etc. They can also help to locate the sources of migraines, dizziness, sleepiness, and other conditions.

Another application of EEGs is for constructing brain maps, and procedures such as Evoked Potentials are often used. In this procedure, the subject is exposed to a certain stimulus (which can be an image, a word, or a tactile stimulus) and then the neuronal response is associated with this stimulus in the brain which is recorded on the EEG.

B. *Functional magnetic Resonance imaging (fMRI)*

Functional Magnetic Resonance Imaging (fMRI) is used to visualize the activity in the various regions of the brain, by using the same basic principle applied in MRI, just with the difference of the computers that analyze the signals.

The phenomenon was discovered in the late 19th century, when neurosurgeons discovered that the brain's cognitive functions make local changes in the blood flow. More specifically, when a group of neurons becomes more active, the capillaries around them dilate to bring more blood and thus more oxygen to them. Within the red blood cells, the oxygen is carried by the hemoglobin, which also contains iron atom. When a hemoglobin molecule releases its oxygen, it becomes deoxyhemoglobin and has a paramagnetic property. Therefore, it causes a slight disturbance in the magnetic field of its surroundings. This process is used in fMRI to detect the concentration of deoxyhemoglobin in the blood. The increase in blood flow to a more active area of the brain surpasses the area's increased oxygen demand, so the concentration of deoxyhemoglobin declines. In the procedure of fMRI this decline is interpreted as increased activity in that specific area of the brain.

The process involves one fMRI image that is recorded of the brain before the subject performs a task and a second one while the subject performs a task. Then the intensities of the images are subtracted from each other, such that the areas with the biggest differences will appear as “lit up”. Those areas represent the parts of the brain that are the most densely infused with blood, thus the areas with the highest neuronal activity.

C. Positron emission tomography (PET)

The physiological phenomenon of PET is the same as of fMRI, that locates the group of neurons in the brain that is active. It is used to show the functional activation of the brain and detects tumors and blood clots. The difference from fMRI is that the subject has to be injected with a solution that contains a radioactive substance. The substance is dissolved in water or may be the water itself and because of the dilation of the capillaries it will bring more of this solution to the more active areas of the brain, therefore giving off more radioactivity during the PET scan.

The principle of work in the PET, looks at the positron, which is an elementary particle that has the same mass as an electron, however with the opposite charge. The positrons that are emitted in this procedure come from the decay of the radioactive nuclei in the solutions that was injected in the subject’s bloodstream, when these positrons are emitted, they annihilate the electrons in the surrounding atoms, thus releasing energy in the form of two gamma rays that move in diametrically opposite directions. There are sets of detectors that are positioned around the subject’s head, which measure the gamma rays that are emitted. Then the computer uses these data to calculate the position in the brain from which the rays came. The computer can reconstitute a complete image of the brain and the most active areas.

A set of detectors placed around the person’s head measures the pairs of gamma rays emitted. The computer then uses the resulting data to calculate the position in the brain from which these rays came. Through massive calculations, the computer can thus reconstitute a complete image of the brain and its most active areas.

D. Magnetoencephalography (MEG)

Magnetoencephalography (MEG) is the newest non-invasive functional imaging technology that allows scientists and clinicians to view the brain in action, such that it measures the very weak magnetic fields generated by the brain’s electrical activity. The MEG signals are able to show the absolute neuronal activity and compared to the other techniques provides timing as well as spatial information about the brain activity. Most importantly, provides temporal characteristics about brain activation with sub-millisecond precision.

2.2. EEG as a brain imaging tool

EEG is the most often used clinical tool in diagnostics of different types of neurological disorders. Primarily, the EEG measures the electric potential field at the same approach as MEG measures the magnetic field. With adequate sampling and precise analysis of the electric field, the EEG can give reliable information about the neuronal activity in the brain and the temporal dynamics of this activity in the millisecond range [16].

The EEG is commonly analyzed in terms of the temporal waveforms at certain channels, also looking at the power of rhythms in the spontaneous EEG, as well at the amplitude and latency of the peaks and troughs in the Event-Related Potentials (ERPs) or at the specific elements in pathological or sleep stages. However, it has not been considered as an

imaging method that has the potential to infer active areas in the brain that generates these waveform features.

Taking into consideration the biophysical point of view, an active electrode on the scalp measures the electric field that is generated by the sum of the momentary post synaptic potentials in the brain. Because of the volume conduction, these electric fields distribute in the brain and reach in attenuated form the scalp surface. Then each electrode is able to measure a local part of this field. With adequate number of electrodes that are distributed over the scalp, the electric field can be measured and reconstructed as a so-called scalp potential map. A new map is formed at every instant in the millisecond range. Every time the map topography changes, the distribution and/or orientation of the active dipoles in the brain changes as well.

The rationale for basing the analyses on topographic information and in more general for treating the data from the entire system as a multivariate vector is the following:

1. The topographic measures are reference-independent, meaning that the shape of the electric field at the scalp will not change even if one chooses another reference, but only will shift the zero line without influencing any spatial characteristics of the field.
2. Topographic information has a direct neurophysiologic interpretability, meaning that topographic differences are indicative of the changes in the configuration of the active cerebral sources.
3. Multivariate analyses allow for better utilization of the added information provided by high-density electrode montages while also retaining statistical rigor.
4. EEG mapping is the precursor for EEG source imaging. Using sophisticated source and head models, the position of the generators that generate the scalp potential map can be estimated with high reliability and reasonable precision.

2.3. Relationship between EEG and Connectivity

The access of the dense array EEG mapping systems has provided the possibilities to detect the spatiotemporal distributions of brain electric activity over the scalp. Many investigations in cognitive neuroscience, clinical neurology, psychiatry, and neurosurgery have exposed the power of EEG source imaging in describing dynamic brain activity. A central theme in neuroscience has become the detection of a particular brain region with a specific function [17].

In contrast to source imaging that has the purpose to identify the functional segregation, connectivity offers a valuable tool for understanding the brain networks through which the brain functions under a highly interconnected organization. There are two types of connectivity, functional that measure the correlation between the neural masses and effective connectivity, which evaluates the causal relationships among neural masses.

3. Effective Connectivity background, limitations, and improvements.

3.1. Effective Connectivity

Effective connectivity refers specifically to the influence that one neural system exerts over another, which can be at a synaptic or population level as Aertsen and Preißl suggested in 1991 [18].

That “effective connectivity should be understood as the experiment and time-dependent, simplest possible circuit diagram that would replicate the observed timing relationships between the recorded neurons.” Two significant points can be derived that effective connectivity is dynamic (active dependent) and that it depends on a model of interactions or coupling [19].

In this way, the effective connectivity corresponds to the intuitive notion of coupling or directed causal influence, that rests specifically on a model of that influence. This is important since it means that the analysis can be reduced to model comparison.

In this regard, the analysis summarizes the scientific process, since each model matches to an alternate hypothesis about how the observed data resulted. Thus, the general implementation of effective connectivity is to test the hypotheses concerning coupling architecture that have been investigated experimentally. The fundamental aspect of this analysis is that it ultimately rests on model comparison or optimization.

3.2. Typical measures

In this section it is described the conceptual framework for estimating neural connectivity according to what is explained in [20], where the most important definitions and considerations with respect to the connectivity measures are given. Let us first introduce some definitions of what is considered as connectivity.

- *Neural entity* is a set of neurons that are under consideration. The activity of a neural mass is going to be denoted with the symbol ι_n and that of N neural masses to be analyzed by the vector $\iota_{N \times 1}$.
- *Anatomical connectivity* is the axonal, monosynaptic connection of one neural mass with another.
- *Neural connectivity* is the causal influence of one active neural mass upon another. The strength of the neural connectivity (or the causal effect) of the neural mass m upon the mass n is going to be denote by $K(m, n)$, with all connectivity strengths arranged into the matrix $\mathbf{K} = \{K(m, n)\}_{m,n=1\dots N}$.

Neural connectivity is intervened by the transmission of action potentials over anatomical connections, thus affecting the target with a connectivity delay $T(m, n)$. The set of all delays is denoted by the matrix $\mathbf{T} = \{T(m, n)\}_{m,n=1\dots N}$.

By using the state evolution equation formulated generally as a Nonlinear Autoregressive Moving Average Model with exogenous inputs u_t (NARMAX). The evolution of activity in a neural network is going to be described as:

$$\mathbf{u}_t = f\left(\mathbf{u}_{t-\Delta t}, \dots, \mathbf{u}_{t-p_u\Delta t}, \zeta_t, \zeta_{t-\Delta t}, \dots, \zeta_{t-p_\zeta\Delta t}, \mathbf{u}_t, \dots, \mathbf{u}_{t-p_u\Delta t}, \mathbf{K}, \mathbf{T}\right)$$

Where \mathbf{u}_t is the state vector describing neural activity, f a nonlinear function that governs the dynamics of the neural network, \mathbf{u}_t an external input (e.g., a stimulus), ζ_t a noise input, Δt is the discretization period, and p_u, p_ζ, p_u , are, respectively, the time lags of the states, noise, and input, required for the model to be Markovian.

When a simple model assumes f to be linear, without external input and without dependence on past values of noise input (meaning the MA component is going to be eliminated), is actually the linear p -order Multivariate Autoregressive Model:

$$\mathbf{u}_t = \sum_{k=1}^p \mathbf{K}_k \mathbf{u}_{t-k\Delta t} + \zeta_t \quad (1)$$

The state evolution equation must be supplemented with the EEG/MEG observation equation:

$$\mathbf{v}_t = \mathbf{L}\mathbf{u}_t + \xi_t \quad (2)$$

Equations (1) and (2) define the EEG/MEG state space model and indicate that estimation of neural connectivity can fall within the framework of state-space estimation. With respect to the MVAR definitions, the following measures of connectivity are being described.

3.2.1. Cross-Correlation and Coherence

Statistical dependencies between signals are detected by using correlation (for the time domain) and coherence (in the frequency domain). The correlation between signals arises when there is true connectivity between brain areas.

A linear relationship between signals is represented in a simple model, where one signal is delayed and the second one is a noisy version of the other:

$$y_t = ax_{t-\tau_0} + e_t \quad (3)$$

where τ_0 represents the time delay between signals x and y and e a noise term. When there is a positive delay, it means that the direction goes from x to y . Then the cross-correlation (*corr*) between x and y is expressed by the time domain expectation operation:

$$\text{corr}_{x,y}(\tau) = \langle x_t | y_{t+\tau} \rangle \quad (4)$$

which is maximal for $t = \tau_0$. The correlation coefficient can be calculated by normalizing the cross-correlation by the energy of each signal. While for the frequency domain, the linear relationship between signals can be estimated based on the coherency (complex coherence):

$$C_{x,y}(v) = \frac{x_v y_v^*}{|x_v| |y_v|} \quad (5)$$

where x_v and y_v are Fourier transforms of x_t and y_t , respectively. The squared module of C is the coherence, which ranks between 0 (no dependence) and 1 (maximal dependency). The slope of the phase can be used to estimate the time delay between the signals. In fact, if there is a delay τ_0 between x and y , then:

$$y_\nu = \langle y_t | e^{-i2\pi\nu t} \rangle = \langle x_{t-\tau_0} | e^{-i2\pi\nu t} \rangle = x_\nu e^{-i2\pi\nu\tau_0}$$

$$C_{x,y}(\nu) = e^{i2\pi\nu\tau_0} \quad (6)$$

3.2.2. Granger Causality (GS)

This method originates from the definition of causality in the statistical sense, which was given by Wiener [21] and according to which a time series has a causal effect on another if the capability to predict the second time series worsens when the information about the first one is removed from all the other available information. Granger then provided an implementation of this definition using linear autoregressive models of stochastic processes. The GS suggests directionality, since a variable causes another variable if the first one contains information that helps predict the future of the second one. The relationship can be bi-directional such that it enables the detection of directed and reciprocal influences. The most common implementation of the GS is founded on linear AR modelling of time series, under the assumption that the two variables are stochastic and wide-sense stationary.

Two time series $x(1)$ and $y(2)$ are modeled by a reduced AR (including just the past samples from the time series itself) and by a bivariate one BVAR (also including the past samples of the other time series), as follows:

- *Reduced Auto-regressive (AR)*

$$x_t = \sum_{k=1}^P A_k(1,1)x_{t-k\Delta t} + e_\ell$$

$$y_t = \sum_{k=1}^P A_k(2,2)y_{t-k\Delta t} + e_i \quad (7)$$

- *Bivariate (BVAR)*

$$x_t = \sum_{k=1}^P A_k(1,1)x_{t-k\Delta t} + \sum_{k=1}^P A_k(1,2)y_{t-k\Delta t} + e_t$$

$$y_t = \sum_{k=1}^P A_k(2,1)x_{t-k\Delta t} + \sum_{k=1}^P A_k(2,2)y_{t-k\Delta t} + e_t \quad (8)$$

where k is the time lag between samples and p is the model order, i.e., the maximum lag included in the model. In order to advance the prediction of each time series, which is due to the other one is assumed if the variability of the residual of the BVAR model (8) BVAR σ_e^2 is significantly reduced with respect to the variability of the residual of the reduced AR model (7) AR σ_e^2 , as expressed by the following indexes:

$$GC_{x \rightarrow y} = \ln \left(\frac{AR \hat{\sigma}_e^2(2)}{BVAR \hat{\sigma}_e^2(2)} \right) \quad (9)$$

$$GC_{y \rightarrow x} = \ln \left(\frac{AR \hat{\sigma}_e^2(1)}{BVAR \hat{\sigma}_e^2(1)} \right) \quad (10)$$

A reduction of the variance BVAR $\sigma_e^2(1)$, BVAR $\sigma_e^2(2)$ of the residuals of the bivariate model (8) with respect to the variance AR $\sigma_e^2(1)$, AR $\sigma_e^2(2)$ of the residuals of the univariate

model (7) results in a GC index greater than zero, such that it fulfills the Wiener-Granger definition.

The bi-directional causality is represented by different parameters of the model. This means the directionality of the method: $GC_{x \rightarrow y} = GC_{y \rightarrow x}$.

3.2.3. Multivariate Time Series

A. Directed Transfer Function (DTF)

Another approach was introduced specifically for the brain functional connectivity by Kaminski and Blinowska in 1991 [22]. Considering the spectral representation of the MVAR model as in (14), the Directed Transfer Function (DTF) directed from m to n was defined as follows:

$$B_{m \rightarrow n}^2(\nu) = |B(\nu; m, n)|^2 \quad (11)$$

A normalization of DTF is then performed by dividing each value of the estimator by the squared sums of all elements of the relevant row:

$$\Gamma_{m \rightarrow n}^2(\nu) = \frac{B_{m \rightarrow n}^2(\nu)}{\sum_{l=1}^N B_{m \rightarrow l}^2(\nu)} \quad (12)$$

The normalized DTF values belong to the interval $[0, 1]$, and satisfy the following condition:

$$\sum_{n=1}^N \Gamma_{m \rightarrow n}^2(\nu) = 1 \quad (13)$$

B. Partial Directed Coherence (PDC)

Partial Directed Coherence (PDC) was introduced as a factorization of Partial Coherence. Similarly to DTF, the structure is based on a MVAR modelling of the entire set of time series representing the brain activity at different sites. Nevertheless, PDC is based on the transfer matrix $A(\nu)$ of the predictive MVAR filter (instead of its inverse $B(\nu)$, like DTF):

$$\begin{aligned} \Pi(\nu; m, n) &= \frac{A(\nu; m, n)}{\sqrt{\sum_{l=1}^N A(\nu; l, n)A^*(\nu; l, n)}} \\ \Pi_{m \rightarrow n}^2(\nu) &= |\Pi(\nu; m, n)|^2 \end{aligned} \quad (14)$$

By comparing the two approaches it was detected that there is more accuracy and a better interpretation of the quantitative values for DTF, however a more accurate reconstruction of the network structure was provided by PDC.

C. Normalizations of DTF and PDC

The results on connectivity employing DTF and PDC have been greatly analyzed, and despite that these estimators reveal similar structural characteristics in the networks that they highlight [23], multiple normalization schemes have been proposed to provide more stability and accuracy in the estimations. In this way, a list of versions based on DTF and PDC are explained below.

The generalized PDC (gPFC) [24] shown in Eq. (15) accounts for the imbalances produced by the variance of the estimations, and provides a more robust estimation for small samples.

$$\begin{aligned}
\bar{\pi}_{ij}(f) &= \frac{\frac{1}{\Sigma_{ii}} A_{ij}(f)}{\sqrt{\sum_{k=1}^M \frac{1}{\Sigma_{ii}^2} |A_{kj}(f)|^2}} \\
0 &\leq |\bar{\pi}_{ij}(f)|^2 \leq 1 \\
\sum_{j=1}^M |\bar{\pi}_{ij}(f)|^2 &= 1
\end{aligned} \tag{15}$$

The renormalized PDC (rPDC) was introduced in [25] and eliminates the dependence of the statistical significance on the frequency by normalizing the PDC definition by the inverse covariance matrix to provide an estimator that does not depend on the unit of measurement. The rPDC is shown in Eq. (16).

$$\begin{aligned}
\lambda_{ij}(f) &= Q_{ij}(f)^* V_{ij}(f)^{-1} Q_{ij}(f) \\
\text{where,} \\
Q_{ij}(f) &= \begin{pmatrix} \text{Re}[A_{ij}(f)] \\ \text{Im}[A_{ij}(f)] \end{pmatrix} \text{ and} \\
V_{ij}(f) &= \sum_{k,l=1}^p R_j^{-1}(k,l) \Sigma_{ii} Z(2\pi f, k, l) \\
Z(\omega, k, l) &= \begin{pmatrix} \cos(\omega k) \cos(\omega l) & \cos(\omega k) \sin(\omega l) \\ \sin(\omega k) \cos(\omega l) & \sin(\omega k) \sin(\omega l) \end{pmatrix}
\end{aligned} \tag{16}$$

Normalizations on the DTF measure have been proposed too. On Eq. (17), the full frequency DTF (ffDTF) was proposed by Korzeniewska in 2003 [26], and eliminates the dependence of the denominator on the frequency information which provides a more clear interpretation of the information flow at different frequencies.

$$\eta_{ij}^2(f) = \frac{|H_{ij}(f)|^2}{\sum_f \sum_{k=1}^M |H_{ik}(f)|^2} \tag{17}$$

Moreover, the direct DTF (dDTF) Eq. (18), was also proposed in [26], and is considered as the product of the partial coherence and the ffDTF. It provides an interpretation of the frequency domain conditional Granger causality.

$$\delta_{ij}^2(f) = \eta_{ij}^2(f) \left(\frac{\hat{S}_{ij}(f)}{\sqrt{\hat{S}_{ii}(f) \hat{S}_j(f)}} \right)^2 \tag{18}$$

Where the partial coherence pCoh corresponds to the second term squared, and explains the remaining coherence (i.e., correlation in the frequency domain) that cannot be explained by a linear combination of the coherence from node i to j , and is related to the proportion of coherence measured with respect to all other measured variables in the coherence matrix.

3.2.4. Dynamic Causal Modeling

The basic principles rely on the individual neural populations and the connections between and within them, which are described by biophysically plausible models [27]. This simulated activity is mapped to the measured data through the forward model, which is adequate for the recorded data. After that the following calculations are made:

- Likelihood which is the probability of the data given the model and its parameters
- Prior which is the probability of the parameters given a model.
- Model Evidence which is the probability of the data given a model.

Then these parameters are combined through Bayes' theorem to estimate the posterior, which is the probability of the parameters given the data and the model. This Bayesian model inversion permits to answer the following questions:

- Which model architecture is most likely to generate the data?
- What parameter estimates have the highest probability given the data and the model?

In this way, it is possible to obtain a source reconstruction framework from which a state space model based on the physiological characteristics mapped through a mathematical formalization is being produced and explains the connectivity among regions on the neural activity under study.

3.3. Effective and functional connectivity

Brain connectivity provides a way to understand how the cortical regions communicate, in this sense, it allows to interpret the behavior and the interactions that occur between different sources exploring the information flow either locally among channels in EEG or the sources from dipoles, or more generally by considering broader cortical areas from lobes or regions of interest.

The mathematical formulations from which the flow of information is characterized relies on the definition of *causality* which states the relationship between two temporal series (e.g., time varying signals) if the past information from one of them, $x(n)$, improves the prediction of a second series, $y(n)$. This was well explained by Granger [28] and provided a way to evaluate the directionalities and the flow of information between the series when there existed a lack of reciprocity among them.

This causal relationship was first defined for econometric models but was later popularized in neuroscience analysis that considered EEG, MEG and fMRI data since there is an intrinsic correlation between the temporal series in econometrics and the time varying signals produced by the sources that are topographically related and simultaneously recorded using an EEG acquisition system for instance.

Causality differently from correlation establishes the effective connections that are produced between the sources. From this point of view, this kind of connectivity explains the causal relationship whose directionality can be obtained by applying the Granger principles. As it was explained in the previous section, there are different ways to calculate effective connectivity, and they are intended to quantify if the signal sources covary even if the structures from which these series are being measured do not have any anatomical connection (i.e., there is no physical connection among them).

This indicates that some hidden structures, that are not being measured, are participating actively, and are mediating between the two non-anatomical related areas, and thus, they are responsible of their communality. In this sense, the link among the different structures can be produced through intermediate networks/systems or directly by showing the actual connectivity between two sources. When more than two variables are under examination, it becomes a multivariate problem, which, according to the number of sensors that are being simultaneously employed to account for the biopotentials generated in the scalp, this is the case that applies for systems like EEG.

On the other hand, the functional connectivity provides a temporal relationship between spatially remote neurophysiological events, quantified from the correlation between these variables. It guarantees that some form of link exists between the correlated structures, however it cannot quantify in which way this is happening. This is why effective connectivity is more powerful than functional connectivity, it provides a broader point of view and explains how intermediate structures are linked in a neural process allowing the analysis of complex brain activity.

3.4. Applications of effective connectivity

Considering the definitions of effective connectivity and what it has represented in the advancement of neuroscience, numerous developments have been performed in order to explain what is happening in the brain when a certain task is performed. Reviews like the one provided by Sakkalis [17], permit to have a broader view of the actual methodologies in connectivity analysis, not only from the effective point of view, but also from a functional sense.

There are examples related to the theoretical analysis of the connectivity indexes in order to provide a significant assessment on the use of a certain connectivity measure in the evaluation of the neural activity. This category includes the comparison of connectivity estimators applied to high-resolution EEG recordings and synthetic signals to obtain the directionalities and the connectivity among different sources in the brain as explained in [23].

In the same way, works like the one developed by Johnson et al [29], and Ramihi et al [30], intended to analyze the cortical excitability following different tasks both for attention and consciousness tasks. Ramihi and colleagues provided a framework in which a series of images were shown to a group of participants and from the classes of images, they were able to characterize the connectivity information from the participants according to the psychophysical tasks. Johnson's team characterized the electrical activity and connectivity patterns of people who underwent short memory tasks.

More theoretical evaluations like the one presented in [31] intended to analyze the effective connectivity measures and their performance in detecting the causal effects and the statistical significance considering control data generated synthetically. They evaluated the information theoretic measures, MVAR model-based measures defined in time and frequency as well as phase-based metrics. The simulated data was produced considering the Henon maps, and it was possible to establish that the Partial Granger causality, MVAR Granger causality and conditional Granger causality are appropriate measures that account for the processes underlying.

Some other applications that evaluated the spurious connections that can arise from EEG signals and fMRI data considering Granger causality is evaluated in a graphical approach in [32], which provided a useful way to obtain interrelations in EEG and fMRI data able to characterize spurious causalities.

Other works related to the analysis of pathologies have been published as well. An example of this is the one presented by Varotto and colleagues [33] in which it is explained an approach to evaluate the effective connectivity characteristics on vegetative state patients. They were able to compare the connectivity results with control groups and they found that alpha and theta bands were significantly different in comparison to healthy subjects. This serves as a basis to characterize what is happening to the neural activity in patients that are unconscious due to a pathological condition.

De Tommaso and colleagues in 2012 [34], provided a statistical analysis on patients that suffered from migraine in order to characterize their brain activity after intermittent flash stimulation. They were able to find a statistically significant increase on the phase synchronization for the alpha band on patients that did not have aura. Moreover, the Granger causality increased in these patients in comparison with the control groups and the patients without aura. This evidenced the causal relationships and the differences according to the pathology type and characterizes the variables under consideration.

Recent works with patients that suffer from treatment-resistant schizophrenia [35] evaluated the connectivity produced in specific points anatomical locations in the brain. By performing the source localization on EEG recordings of schizophrenic patients, Wada and colleagues were able to analyze the aberrant connectivity that is produced between the anterior cingulate cortex and the default mode network which is considered characteristic of this kind of pathology. By evaluating the isolated effective coherence (iCoh) they were able to find significant correlation of the neurophysiological basis between these areas regarding the characterization of the TRS.

Epilepsy has been analyzed in terms of connectivity as well. On [36] the interictal EEG activity was analyzed for patients with childhood absence seizures. By analyzing the partial directed coherence (PDC) they found out that there exists a correlation between the highly significant increase of outgoing connectivity in frontal and central cortical areas for the patients in comparison with the control subjects.

In the same line, the characterization of the EEG activity in relation to the connectivity patterns in children with autism has been of interest by the researchers. In [37] a group of children with autism and healthy children were evaluated to characterize the connectivity changes according to the main frequency bands that characterize the brain rhythms. As a main result, they found that it is possible to discriminate between the brain activities considering the metrics derived from the connectivity measures.

Other works like the one presented in [38] characterized the connectivity patterns and the areas of more connectivity on heroin abstinent and non-addicted subjects. They found that there were alterations in the effective network by comparing the two subject groups, being evident for weaker causal pathways in the parietal region and stronger for the occipital area.

Advances in biometric identification (BI) as shown in [39] are intended to provide non-conventional ways of electrophysiological characterization of the brain activity. The

evidence from the authors shows that even though EEG data is contaminated with volume conduction, it provided comparable results to BI applications using MRI. The connectivity measures based on Granger causality, phase synchronization and coherence were tested considering KNN approaches, SVM and LDA.

Combination of techniques that measure the brain activity has been reported in [40], where it is demonstrated that EEG and MEG data can be combined to provide improvements in the effective, functional and spectral power analysis. The analysis was performed in healthy subjects under conscious resting state conditions.

Non-conventional applications of effective connectivity analysis are explained in [41], [42] and [43]. In [41] the researchers provided an analysis of the effective connectivity and its variations in response to emotional music. They evaluated the theta, alpha, beta and gamma frequency bands in order to characterize the connectivity from emotional music. In [42] Dynamic Causal Modeling was employed to characterize the resting state conditions for motor imagery. In [43] there were extracted a set of features from effective connectivity values needed to perform the classification of objects that were presented to the subjects as visual information.

3.5. What do these works have in common?

The research works presented in the previous section provide an evaluation of the effective connectivity considering different applications that comprise the theoretical analysis of connectivity, the analysis of pathologies, classification of brain activity and resting state conditions analysis.

Independently on the application, all these works share the same processing structure. This framework is presented in Figure 4 and comprises 6 principal steps from which the effective connectivity analysis is performed. The first stage corresponds to the signal acquisition and pre-processing, from which the data is acquired according to the brain imaging technique that is available. There are principally three main technologies to perform the acquisition of the data of interest.

1. Electroencephalographic data
2. Magnetoencephalographic data
3. Electrocardiographic data

From this list, the most common one as explained in the state of the art is the EEG data since it is the most affordable option in terms of portability, ease of use and data availability [44].

The second stage corresponds to the effective connectivity measure estimation and corresponds to the implementation of algorithms to calculate the connectivity measures in order to have a 'raw' representation of the effective connectivity. As explained previously, different measures can be obtained and can be used jointly to provide a representation covering different points of view. The working domain definition goes next and corresponds to the definition of the source domain that is intended to be employed in order to estimate the connectivity relationships across the areas or sources. In this case, the sources can be defined in the channel space where the electrodes from the EEG equipment are used as the sources. The definition of regions of interest (ROIs) can be done as well, as it comprises different channels in order to evaluate the average connectivity across groups of electrodes or dipoles representing the sources topographically distributed in the brain.

After the calculation of the measures either directly in the sensor space to evaluate the connectivity characteristics in the channel space or the average connectivity measures by considering the ROIs, the fourth stage which comprises the generation of surrogate data from the original time series is performed as the starting point to evaluate the connectivity matrices through statistical analysis. Such statistical analysis can be performed using the analysis of variance or t-test depending on the application, in this way the statistically significant connections are obtained and only the meaningful information according to the connectivity measures and the statistical analysis are maintained. Finally, post-hoc tests are performed to guarantee the significance on the results under repeated measures. At the end of these steps, the statistically significant connections are obtained, and it is possible to perform the analysis of the connectivity patterns derived from the signals.

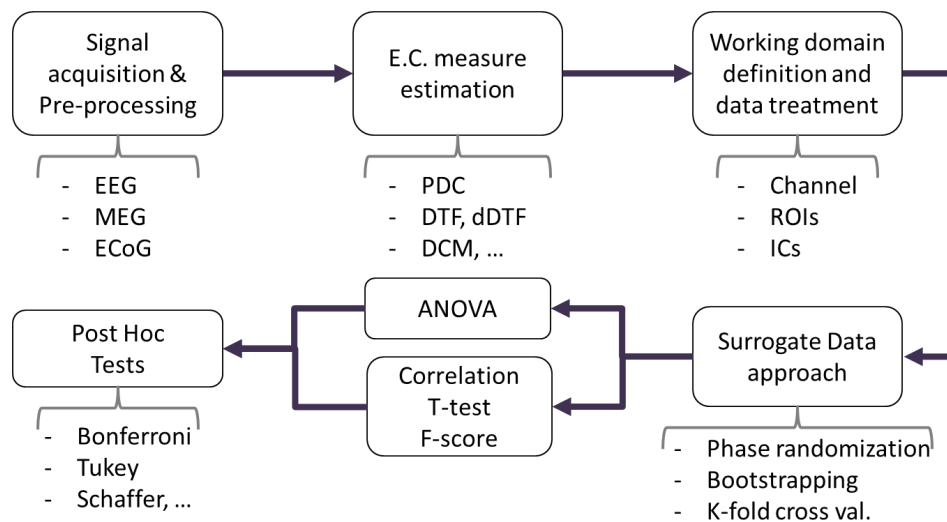


Figure 4. Effective connectivity processing scheme.

3.5.1. Connectivity examples for resting state conditions

In order to start exploring the effective connectivity analysis in resting state conditions and have hands-on application from the framework shown in Figure 4, let us consider a couple of examples which provided a thorough analysis of the resting states during eyes open, and eyes closed.

A. Comparison of connectivity analyses for resting state EEG data

In this work, Olejarczyk and colleagues [45] worked on a method to analyze resting-state EEG data from 19 healthy subjects. For the opened-eyes condition, the subjects were asked to look at a display, fixating the gaze to a cross, and for the closed eyes condition, they were asked to maintain a relaxed state while being seated on an armchair. The recordings lasted 10 minutes and were acquired at a sampling rate of 1000 Hz. The EEG dataset was composed by 128 signals acquired by a high-density array of electrodes. They provided the usual pre-processing stages comprising band-pass filtering (1 – 45 Hz), artifact rejection based on ICA, common average re-reference, and an electrode selection stage from which they rejected about 25% of the total of electrodes (32 channels).

In order to provide an analysis of the connectivity, they isolated the physiological frequencies (alpha, beta, gamma, and delta), and estimated different connectivity measures: Direct Transfer Function (DTF), Transfer Entropy (TE) and Phase Locking Value (PLV).

To perform the evaluation of the connectivity they estimated the significant connections according to adjacency matrices at each frequency band besides the whole spectrum (1 - 45 Hz). The weighted adjacency matrices were analyzed by using indexes based on graph theory like density, degree, strength, path length, global efficiency, clustering coefficient, local efficiency and betweenness centrality, which were appropriate parameters to characterize the high-density array of sources defined in the channel domain from which connectivity measures could be estimated.

They performed three different types of ANOVA analysis to compare the graph theory parameters at each frequency band and condition. In this way, they conducted a three-factor ANOVA evaluating the conditions (opened-eyes/closed-eyes), the frequency band (alpha, beta, gamma, delta, theta, and whole spectrum) and the 96 EEG signals. Then a two-factor ANOVA considering the condition and EEG channels, and finally, a two-way factor considering the condition and the frequency band. They performed the evaluation for each graph-theory parameter.

A.1. What did they find?

- In accordance with the state of the art they found that the closed-eyes state in the alpha and the whole frequency bands exhibited more unique characteristics when the adjacency matrices were compared among the different connectivity measures.
- The multivariate TE showed less significant values compared to its bivariate formulation which according to the authors suggests spurious connections. As an important characteristic, they noted that nonlinear measures like the PLV were able to capture local connections on contiguous electrodes which was not possible to obtain for the linear measures like the DTF.
- Connectivity results suggested that the information flux travels to the frontal region of the brain from the posterior area when the alpha rhythm in eyes closed condition was evaluated. Similar results were found for the analysis of the whole spectrum.
- Differences between the resting state conditions are mainly observed for the alpha band.
- The long-range connectivity goes from the posterior part of the brain to the frontal area. The frontal region corresponds to an area of higher synchronization in the alpha band for closed eyes.
- The main areas involved in the characterization of the brain areas are the ones located in the anterior and posterior lobes.

By comparing the strength at each frequency band, there were noticed small differences for the DTF value w.r.t the other measures in consideration. Only three from the total of electrodes exhibited significant differences between the opened and closed eyes conditions in the alpha band. However, when the same measure was compared considering the ROI, the ANOVA analysis provided statistically significant differences in the posterior, right temporal and frontal regions, which provides similar results to the ones obtained for the PLV and TE measures in the channel domain. It hypothesizes that considering the regions of interest provides more sensitivity to the changes in connectivity and the results could be comparable to the ones obtained in the other domains. It suggests an increase of the strength during the closed-eyes condition.

B. The difference of brain functional connectivity between eyes-closed and eyes-open using graph theoretical analysis.

As a second example of the methodology implementation, let us now consider the work done by Tan and colleagues [46]. This research work intended to differentiate the functional connectivity among the resting state conditions of eyes open and eyes closed by considering different graph theory measures like the degree, strength, path length, global and local efficiencies, and the clustering coefficient. In order to do this, the study was performed with 21 healthy subjects with an EEG system of 128 channels. The sampling rate was 500 Hz, and the total acquisition time was set at 3 minutes per resting state condition. An epoch of 10 seconds was employed to quantify the connectivity in the network by considering the synchronization likelihood measure. The alpha, beta and theta frequency bands were considered for the analysis.

The main results from [46] considering the alpha band show that:

- After opening the eyes, the connections in the posterior region were decreased in bilateral way for the alpha band.
- There was an increment of the global efficiency and a reduction of the clustering coefficient, mean shortest path length and local efficiency for the alpha band.

3.6. Limitations and possible improvements

On Table 1 there are defined the substages part of the outline of the processing scheme shown in Figure 4. The data summarized in this table is intended to show the general characteristics of different connectivity works. Excepting for the case where Dynamic Causal Modeling is employed (last column - Friston 2019 [47]), there are several works that employ the same steps in order to perform the connectivity estimation, changing specific substages depending on their objective, for instance, considering different frequency bands, or employing different source definitions.

Table 1. Substages in the processing outline considered in Figure 4.

STEPS	Varotto - 2014	Olejarczyk - 2017	Baccalá - 2007	Johnson - 2012	Tommaso - 2013	Friston - 2019	
WINDOW LENGTH	2 s	20 s	~20 s	~5 s	~60 s	1 s	
PREPROCESSING							
1	Filtering	✓	✓	✓	✓	✓	
2	Normalization	✓	✓	✓	✓	✓	
3	Artifact rejection	✓	✓	✓	✓	✓	
4	Phys. Rhythms (e.g. Alpha, Beta, etc.)	✓	✓	X	✓	✓	
WORKING DOMAIN DEF.							
A.	Channel space	X	✓	X	X	X	
B.	ROIs	✓	X	✓	✓	✓	
C.	Dipoles	X	X	✓	X	X	
E.C. MEASURES							
1	E.C. selection	✓ (PDC)	✓ (DTF, TE, PLV)	✓ (DTF, dDTF, PDC)	✓ (TMS-ER)	✓ (GC, PS)	N.A.
2	E.C. Calculation	✓	✓	✓	✓	✓	N.A.
a.	Frequency band	✓	✓	X	X	✓	N.A.
b.	Whole spectrum	✓	✓	X	X	✓	N.A.
c.	Time domain	X	X	✓	✓	X	N.A.
3	Graph measures	✓	✓	X	X	X	N.A.
POST-PROCESSING E.C.							
1	Corrections	✓	✓	✓	✓	✓	N.A.
STATISTICAL ANALYSIS							
1	ANOVA	✓	✓	✓	✓	✓	N.A.
a.	Variable definitions	✓	✓	✓	✓	✓	N.A.
b.	Tests	✓	✓	✓	✓	✓	N.A.
c.	Statistical Connectivity analysis	✓	✓	✓	✓	✓	N.A.
RESULTS							
		✓	✓	✓	✓	✓	✓

By looking at the Table 1, one can notice that another big difference is related to the window length employed for the MVAR fitting process to perform the calculation of the connectivity measures. Moreover, these works do not provide any explanation on why they performed the analysis considering that window duration and no other. The rationale is the use of a time window so that it is long enough so the frequency information that characterizes the brain activity under analysis will be covered, and the connectivity measures will be able to provide information about the neural activity.

This is an issue that is not usually addressed and the segment length selection is not evaluated, which is critical since the window size has a substantial effect in the estimation of effective connectivity information [47]. Some authors have presented some observations about this topic:

- *Sameshima and Baccalá* [48]

“Without too much justification, Marple Jr. (1987) suggests that the total number of observed samples should be at least three times the number of parameters for a minimally adequate fit.”

- *Rotondi et al., 2016* [36]

For epoched recordings: “In case of MVAR it has been recommended that, as a rule of thumb, the ratio $(N * m)/(M * p)$ should be of 10 or larger. (Schlögl and Supp, 2006)”

- *Sakkalis, 2011* [17]

“Stationarity is still required within each time interval for which coherence is calculated, meaning that in practice one should carefully decide on the optimal section length (window) over which each coherence estimate is measured.”

As it can be seen, there exist some rules of thumb and very general considerations regarding this issue, however these are only suggestions that are not always considered and the effective connectivity analysis is usually performed without any analysis of the effect of the window size in the results.

This means that the influence of the window size in the MVAR fitting process is totally overlooked. Moreover, as it can be observed on Table 2 from a short list of works that have performed effective connectivity analysis, it can be seen that the window duration employed is not common, even when similar neural activity was evaluated.

Table 2. List of window durations on different works that perform connectivity analysis.

Research work	Window duration	
Varotto et al., 2014	2 s	Resting-state condition
Olejarczyk et al., 2017	20 s	
Astolfi et al., 2007	20 s	
Van de Steen et al., 2019	1 s	
Johnson et al., 2012	5 s	
De Tommaso et al., 2013	60 s	
Hu et al., 2017	10 s	
Maharathi et al., 2016	10 s	Other applications
Valizadeh et al., 2019	2 s	
Ghahari et al., 2020	100 s	
Muthuraman et al., 2015	1 s	
Rotondi et al., 2016	3 s	
Shahabi & Moghimi, 2016	2 s	
Rahimi et al., 2019	1 s	
Lee et al., 2020	3.5 s	
Bakhshayesh et al., 2019	0.3 s	

This heterogeneity on the window length definition is what defines the objective of this thesis work. The aim is to find a way to select a window size such that the stationary characteristics of the signals is maintained in overall along the EEG signals, which is a necessary condition in order to perform the MVAR fitting process and provide an appropriate estimation of the effective connectivity.

Is at this point where a window size selection approach based on the stationary characteristics of the EEG signals could be implemented and evaluated to observe its influence in the connectivity results as a factor of the statistical analysis. In this way, it is proposed the following processing approach in which a window selection stage is included in the effective connectivity network. The modified approach is shown in Figure 5.

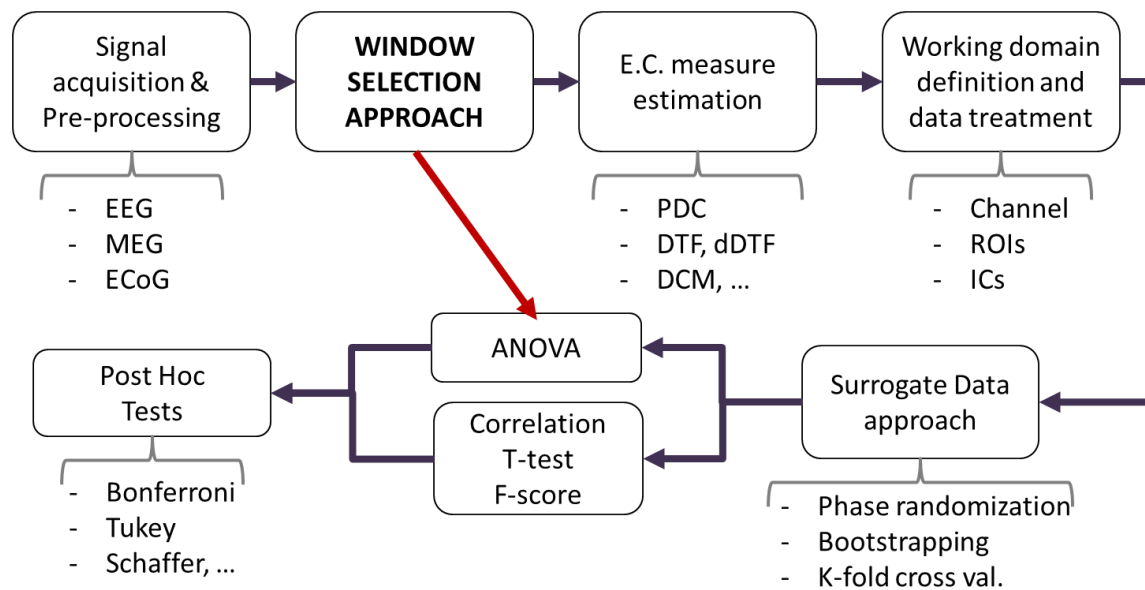


Figure 5. Modification on the E.C. statistical analysis to account for the window length.

According to Figure 5 there is included a window selection stage which is intended to provide a tool that based on the stationary characteristics of the EEG signals under evaluation it is possible to obtain a segment length that maintains these features along the signal. The following chapter describes the data available for this process and the considerations that were used to provide this window selection approach.

3.6.1. Characteristics of EEG signals

In this section there are summarized the characteristics of EEG signals and the considerations taken to perform the window selection approach by analyzing the stationary characteristics of the EEG data and using the kurtosis as a feature to account for stationarity.

A. EEG as a stochastic process

Electroencephalographic signals are electric biopotentials that can be measured, acquired, and recorded by placing electrodes over the scalp. These signals are the result of the propagation of cortical potentials generated in the intricate neural network and lead to the cortex spreading through the skull passing to the scalp where can be finally recorded using the electrodes, specifically, surface electrodes.

Considering the complex processes carried out in the brain, the EEG signals are a mixture of different time-varying components, in this way, brain activity registered as EEG potentials can be categorized as a product of non-linear, time-varying, and stochastic processes.

The non-linearity characteristic of EEG signals demands the use of appropriate methods that go beyond the classic processing techniques based on the frequency and/or temporal analysis to provide a description of the process underlying and analyze the signals. Consequently, the use of high order statistics as a way to describe such kind of non-linear random process might fit that goal to account for the statistical characterization of the signals. Regarding the time-varying behavior of the EEG signals, if they are analyzed in short segments, those can be assumed to be stationary, which is one of the main assumptions given an effective connectivity framework like the one described in this work.

Nondeterministic signals like the EEG potentials cannot be characterized mathematically in a closed form, their stochastic nature makes them more useful to be analyzed statistically, for instance, by accounting for their high order statistical moments.

One of the main purposes of this thesis work is to provide a way to select an appropriate segmentation duration in order maintain the stationarity in between the segments to then evaluate and provide further processing in Effective Connectivity, therefore, first, there are discussed the statistical characteristics of stochastic processes from which the framework for segment selection is derived.

B. Order moments of an EEG signal

EEG signals when recorded simultaneously from different sources (i.e. locations over the scalp) are considered to follow a multivariate Gaussian distribution [49]. As the result of a stochastic process they can be characterized according to their *probability density functions (PDF)*, specifically, the order moments of the PDF provide a way to understand the random process behind the data generated, which is appropriate for processing EEG signals.

For a random variable, the *expectation* is the value that such a variable is expected to take. It is denoted as $E[x]$, and it is the mean of the random process x , and corresponds to the first-order moment of the PDF. It is defined as shown below:

$$\mu_x = E[x] = \int_{-\infty}^{\infty} x \cdot p_x(x) dx \qquad \mu_n = \frac{1}{N} \sum_{n=0}^{N-1} x(n) \qquad (19)$$

Where $p_x(x)$ is the PDF of x , μ_x is the expected value of the random process in the continuous domain and μ_n is its discrete definition for a discrete vector $x(n)$ containing N components, $n = 0, 1, 2, \dots, N - 1$. For a random noise process, the expected value is assumed to be zero.

Similarly, the second-order moment of the PDF $p_x(x)$ corresponds to the mean-squared (MS), and it is defined as

$$E[x^2] = \int_{-\infty}^{\infty} x^2 \cdot p_x(x) dx \qquad MS = \frac{1}{N} \sum_{n=0}^{N-1} (x(n))^2 \qquad (20)$$

The corresponding central definition of the mean-squared accounts for the spread of the probability distribution. This second central moment assesses the dispersion concerning the expected value of the PDF and it is known as the *variance* (see Eq. (21)); one of the important

statistical characteristics used for the approach of segment selection explained in this thesis work.

$$\sigma_x^2 = E[(x - \mu_x)^2] = \int_{-\infty}^{\infty} (x - \mu_x)^2 p_x(x) dx \quad \sigma_x^2 = \sqrt{\frac{1}{N} \sum_{n=0}^{N-1} (x(n) - \mu_x)^2} \quad (21)$$

Usually, a better representation of the spread is calculated according to the *standard deviation* (SD), defined as the squared root of the variance ($SD = \sigma_x$). For a random process with a zero mean, the mean-squared and the variance are the same.

As a way to characterize the variability of the process, it can be used the *coefficient variation* (CV), defined by the ratio between the standard deviation and the mean (σ/μ). This statistical attribute can be useful to perform comparisons and characterize the variability that exists between different processes that exhibit different means.

Other higher-order moments like *skewness* and *kurtosis* are used to characterize the probability density functions derived from a random process. The normalized version of the third-order moment (Skewness) can be defined as follows:

$$S_x = \frac{1}{\sigma_x^3} \int_{-\infty}^{\infty} (x - \mu_x)^3 p_x(x) dx \quad S_x = \frac{E[(x - \mu_x)^3]}{\sigma_x^3} \quad (22)$$

Skewness as its name suggests shows how much a distribution lacks symmetry, in other words, how a distribution is skewed to the left or the right with respect to the maximum likelihood of the distribution. As can be inferred, a normal distribution such as the Gaussian has a skew value of zero.

The normalized version of the fourth-order moment known as kurtosis characterizes if a PDF has a large peak around its mean value. It represents how much the distribution is different from a Gaussian PDF, thus, a high kurtosis value is proportional to the relative difference with a normal distribution of similar characteristics, while low kurtosis indicates a smooth transition of the PDF values near the mean value at the top of the distribution. For the purpose of this work, the kurtosis value is estimated to account for how different the distribution is from a normal distribution, for which it necessary to normalize its value by subtracting a constant value of 3, which is the kurtosis of any normal distribution. In this way, kurtosis is defined as:

$$K_x = \frac{1}{\sigma_x^4} \int_{-\infty}^{\infty} (x - \mu_x)^4 p_x(x) dx \quad K'_x = \frac{E[(x - \mu_x)^4]}{\sigma_x^4} - 3 \quad (23)$$

The quantity K'_x corresponds to the excess of kurtosis w.r.t the normal distribution's 4th order moment estimation, accordingly, a high positive K'_x indicates a strong peak with a heavy tail from the distribution, and a negative K'_x corresponds to a virtually flat PDF. For the purpose of this work, the K'_x values are required to be close to zero so that the samples from a segment with that estimated kurtosis follow a normal distribution, a characteristic needed to guarantee the stationarity of a signal segment.

Sudden changes of EEG signals over time as the ones produced by seizures can be characterized using the high order statistics of the distributions derived from the measurement of the signals. Even more complicated processes can be performed, like

automatic signal segmentation implemented to detect preictal, ictal, and postictal periods during the seizures [50].

The order moments corresponding to the first (mean), second (mean squared and variance), third (skewness), and fourth (kurtosis) as explained earlier characterize the random process defined by its Probability Density Function – PDF.

As the objective is to find a segment length duration common for all or the majority of the channels of an EEG recording, the 4th central moment, the kurtosis explained by the excess considering a normal distribution (K'_x) is the principal statistical measure used in this approach as a scale to quantify the non-stationarity of the EEG signals. The main reasons that support its use are the following:

1. Kurtosis accounts for how peaky or flat is a distribution compared to a normal PDF (e.g. Gaussian), hence, a low Kurtosis value means that data is normally distributed, which is a characteristic of stationary signals.
2. In this way, Kurtosis estimation of different segment durations of a signal can assess how much a segment is stationary, needed for E.C.

4. Materials: EEG datasets and preprocessing

There are several approaches used to record brain activity (as explained in the section *Technologies for brain imaging: A brief description*) some examples are Functional Magnetic Resonance Imaging (fMRI), Positron Emission Tomography (PET), Single Photon Emission Computerized Tomography (SPECT), Functional Near Infrared (fNIR), Magnetoencephalography (MEG), and Electroencephalography (EEG), among others [3], [51], [52].

Each of these brain imaging techniques offers different advantages respecting temporal and/or spatial resolution besides the sensitivity in recording the brain activity. Moreover, the fundamental working principle differs among them comprising different physical properties to be measured. In particular, the EEG technique comprises high temporal resolution for signal acquisition, low cost (relative to the application considered), and great wearable/portability capacities, which make this technique an affordable way (both in economical and procedural terms) to record brain activity, at the expense of lower spatial resolution and more difficult preparation for the acquisition [3].

As a result of the acquisition of EEG signals, there are obtained a set of waveforms which correspond to the digital conversion of the variation over time of the biopotentials recorded across the scalp of a person whilst is performing a specific cognitive/non-cognitive task. Different electrodes that cover the scalp area register the voltage variations at different locations of the scalp giving as result a recording comprising as low as 1 and up to 256 signals [53].

Functional and effective connectivity analysis can be done from the imaging techniques mentioned previously, however, the possibility of analyzing the directionality on the flow of information offered by Effective Connectivity allows to understand how different areas of the brain interact when brain activity is produced. In this sense, the first step in a comprehensive effective connectivity analysis is the acquisition of brain activity data recorded using imaging techniques. For the effective connectivity approach, electroencephalographic signals are often used for processing.

4.1. EEG Dataset

The EEG dataset considered for this thesis was provided by the Istituto di Bioimmagini e Fisiologia Molecolare (IBFM) of the Consiglio Nazionale delle Ricerche (CNR). Such dataset comprises brain activity of ten healthy and ten chronic stroke patients with monolateral upper-limb deficits, and it was used to obtain quantitative electroencephalographic markers from the cerebral activity of the subjects. The recordings and the corresponding metrics were employed to evaluate the motor improvement success rate of the stroke patients who went through a robot-assisted rehabilitation program [54]. The brain activity was recorded in resting-state conditions and during motor tasks as a way to characterize and evaluate the evolution of the patients during rehabilitation [55].

As the purpose of this work is the analysis to provide a basis in the processing stage of the effective connectivity only the signals of the healthy subjects were considered. In this way, a total of 20 recordings corresponding to two different resting-state conditions of the 10 healthy subjects were used for the assessment and selection of an appropriate segmentation duration to obtain the multivariate autoregressive model needed for effective connectivity.

The resting-state EEG signals considered were acquired from each of the subjects while they were in a supine position. They were asked to be aware of their surroundings during two different states; while keeping their eyes opened (resting-state condition 1 - R1) and closed

(resting-state condition 2 - R2). The acquisition was performed for 5 minutes overall for all the patients.

The signals were acquired using the EEG signal acquisition equipment Synamps 2/RT from Neuroscan [56]. This is an amplifier of EEG, event-related potentials (ERP), and evoked potentials (EP), and has a sampling rate up to 20 kHz (Bandwidth: DC to 3500 Hz) comprising analog-to-digital converters of 24-bits. The system includes a total of 70 channels; 64 monopolar, 4 bipolar, and 2 high-level, which are sufficient to have a high-density EEG recording [57].

The placement of the electrodes over the scalp was performed using the 10-20 standard. Figure 6 shows the topological location of 62 of the 70 channels. The sampling frequency for the resting-state recordings for all of the participants was set at 1000 Hz. Regarding the acquisition characteristics considering the electronics set up of the equipment, there was applied an active filtering scheme for the power line frequency at 50 Hz, omitting any other acquisition feature. Further processing of the signals was performed digitally with the help of a computer.

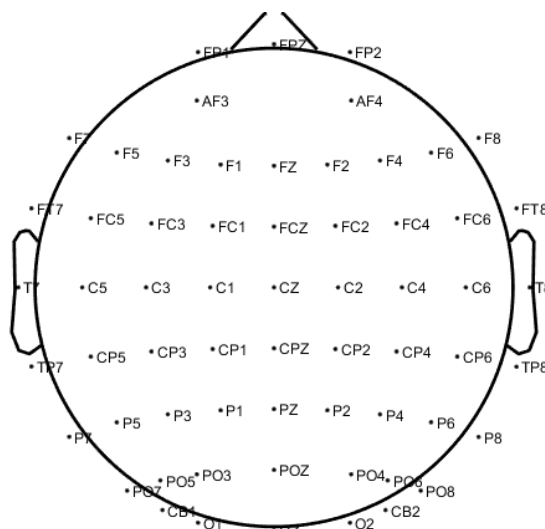


Figure 6. Channel locations over the scalp using the EEG system Synamps 2/RT from Neuroscan. Only 62 out of 70 channels are shown since apart from the two high-level electrodes, the channels M1, M2, LDA, LBIC, RDA, RBIC were not used for recording. (Plot generated using EEGLAB [58])

4.2. Noise and artifacts in EEG signals

Before starting the description of the main steps considered for the selection of appropriate segment durations within the Effective Connectivity framework, let us have a closer look at the signals that were analyzed to define a pre-processing stage that minimizes the noise and possible artifacts that affect the recordings.

As an example, Figure 7 depicts a short segment of the signal recorded by the channel F8 located at the frontal right position on the scalp (see Figure 6). As described previously, the sampling frequency was set at 1000 Hz, from which it can be inferred that the total number of points of this segment is 2000 samples, corresponding to a signal length of 2 seconds occurred in the time interval 100 to 102 from the total duration of 328 seconds (~ 5.5 minutes). Moreover, it can be observed that the amplitude is normalized with respect to the mean and the overall standard deviation of the signal (known as z-score).

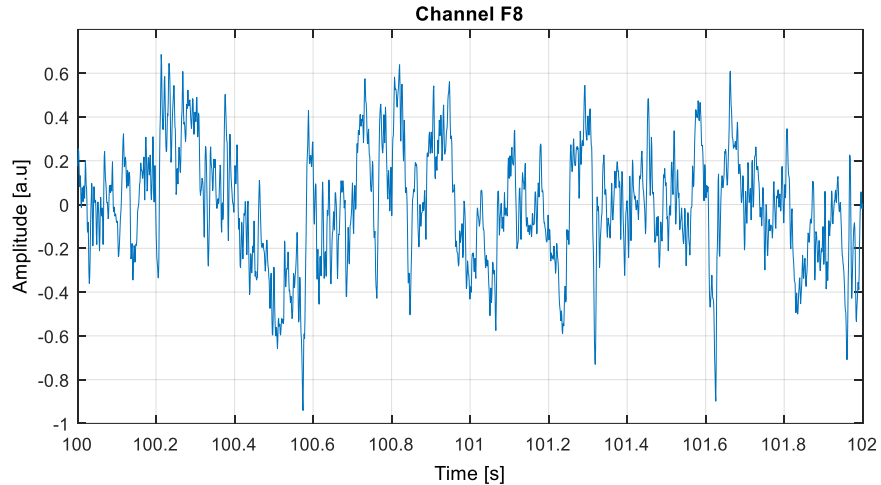
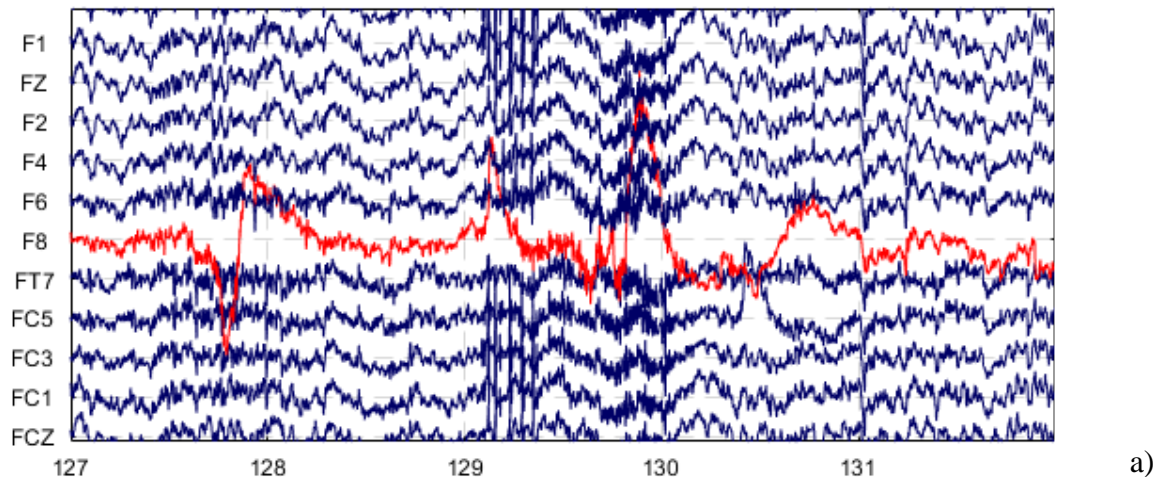


Figure 7. A segment of an EEG signal recorded by the channel F8. Taken from the EEG dataset of subject 10 (S10) during the closed eyes resting-state (R2).

In total, the dataset for each resting-state condition is composed of 68 signals which are processed to improve the information that can be obtained from them. Considering the noisy environments and the uncertainty in the measurement process, different factors might produce errors in signal acquisition. Such kind of interferences (i.e. artifacts) that affect the signal digitization include, but are not limited to sudden movements of the patient during the acquisition, fluctuations of the thermal charge generated in the electronics components that are part of the amplification stage and/or variations of the same nature at the junction of the electrode and skin, moreover, spontaneous biopotentials can arise and affect the signals as well [59]. These can be categorized as internal if they are produced by physiological processes that contribute either to unnatural oscillatory components in the signal or sudden amplitude changes, and external if the artifact sources are identified from the environment setting of acquisition, the equipment, or procedural misplacement of the electrodes [60].

Figure 8.a shows a set of signals acquired by eleven electrodes during the time interval 127 to 132. This figure is aimed to show how the recordings are stored, comprising the time-series variation of the biopotentials in a parallel way (i.e. matrix wise). The signal registered by the electrode F8 during this time interval is plotted in red to highlight some artifacts that were probably produced by sudden movements from the subject. It is worth to notice that those artifacts are very common and interfere with the signal during its overall registration.



a)

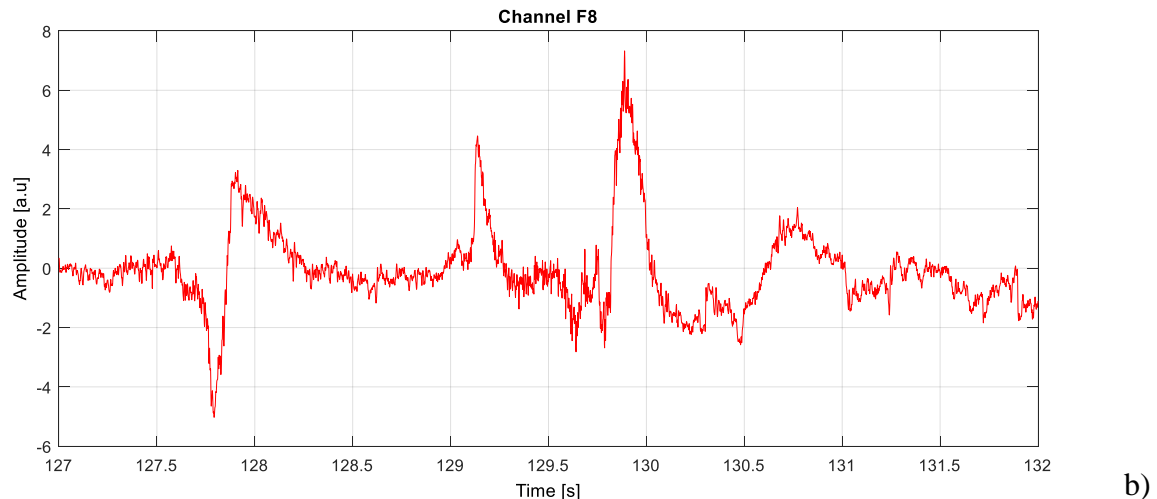


Figure 8.a. Subset of signals registered by 11 out of a total of 68 channels. Figure 8.b. Same segment of the signal from the channel F8 containing artifacts.

Figure 8.b depicts the isolated segment of the signal registered from the channel F8. Can be observed the great difference in magnitude concerning the same signal at a different time interval (second 100 to 102) as shown in Figure 7. Here, after normalization, the amplitude reaches a maximum of about 6 a.u. and a minimum of -4 which are about one order of magnitude higher than the values presented at previous instants. Such kind of abrupt changes in the amplitude suggest the presence of artifacts as explained above, and it is needed to minimize their effects or eliminate them to have clean signals to work with.

Is for this reason that a preprocessing stage is defined to obtain clean versions of the signals which is the initial step to provide a processing framework for the segment length selection and further effective connectivity analysis.

4.3. Preprocessing stage

For the purpose of preprocessing and Effective Connectivity testing, the EEGLAB toolbox was employed during the development of this thesis work. EEGLAB [58] is a toolbox designed for the high-level computational language MATLAB® to provide a set of tools for processing and analyze electroencephalographic signals. It has a graphic user interface from which it is possible to import and read different file formats (e.g. CNT/EEG files from NeuroScan™ acquisition equipment or the EDF standard file format for medical devices, among others), and also, it incorporates a large set of functions specifically designed for the EEG signal processing which vary from classical signal processing ones like the application of filtering strategies, frequency representation through the Fourier transform, calculation of power spectral densities, and time-frequency methods combining Wavelet transform for multiresolution analysis and signal visualization, to more complex uses as the Independent Component Analysis (ICA) [61], epoching, labeling and visualization of Event-Related Potentials (ERP), Evoked Potentials (EP), statistical analysis of the signals, and artifact rejection, among other functions.

Figure 9, shows a block diagram describing graphically the main steps considered for the Effective Connectivity framework for this thesis work. As can be noted, the first step corresponds to the signal acquisition, which has been done by the IBFM lab, grouping all the signals of interest, and providing them for processing. The second step is the

preprocessing stage in which filtering, ICA, artifact rejection, and channel selection are performed as data cleaning processes. The third stage corresponds to the application of high order statistics as metrics to establish a non-parametric framework to select an appropriate segment length that captures the smooth variations over time of the varying system underlying the EEG signals. The fourth stage corresponds to the validation of the results found in the segment length selection, and finally, the window found is applied to test the effective connectivity for the resting state conditions and each of the subjects.

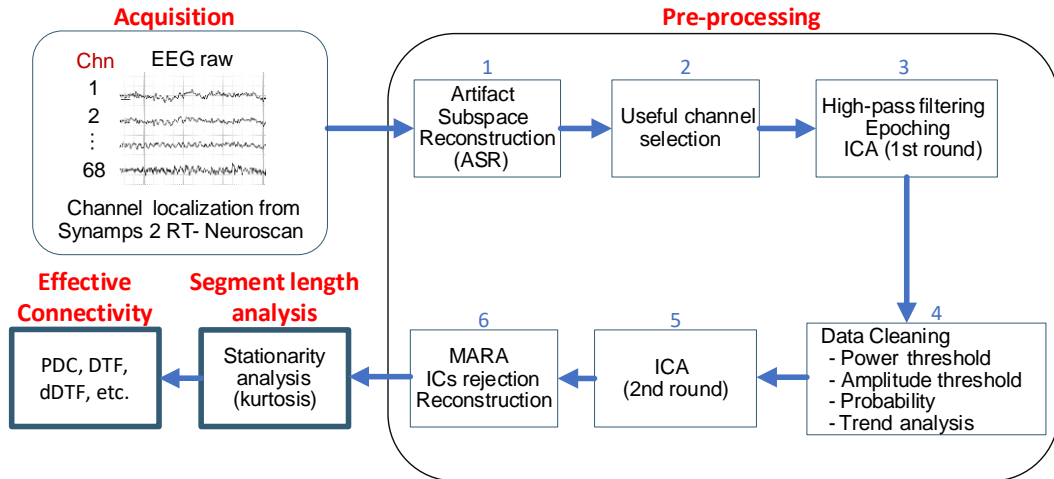


Figure 9. Pre-processing block diagram for the data cleaning process.

Figure 9, also shows in detail the preprocessing stages followed to clean the EEG signals from noise and artifacts during recording. The first step corresponds to the Artifact Subspace Reconstruction (ASR) [62], a method that considers signal segmentation and variance estimation as a metric to establish exceeding values from a threshold that are evaluated by a Principal Component Analysis decomposition, then the artifact segments are rejected and signal reconstruction is performed to obtain a cleaner version of the signal [63]. The next step is the selection of useful channels from which some of the channels are discarded considering that they do not convey any useful brain activity information since they were not actively part of the set of electrodes connected to register the signals.

The preprocessing stages 3 to 5, are considered as artifact rejection strategies based on classical approaches, inspecting abnormal trends, improbable data, atypical spectral characteristics, and channel statistics. These are performed in between ICA decomposition steps, employed for source separation, component selection, and elimination using complementary tools as the Multiple Artifact Rejection Algorithm (MARA) [64], [65], a supervised machine learning algorithm that considers frequency, temporal and spatial features to reject component sources derived from ICA.

A. Artifact Subspace Reconstruction (ASR):

As explained by Chang et al. in [66], in a general way, Artifact Subspace Reconstruction (ASR) can be understood as a method based on Principal Component Analysis (PCA) to find the underlying components that exhibit large variances with respect to clean segments of the same signals. These are automatically identified by the algorithm and are used to find the variance thresholds as the features to reject the components with large deviations, recognized as artifacts. After the rejection, the signals are transformed back into the time domain from the remaining components and a cleaner version of the original dataset is obtained.

A segment from a signal X_t is decomposed into its principal components C_t by considering a mixing matrix A_r given as $X_t = A_r C_t$. The rejection of the large variance components is then performed in the principal component space $Y_t = V_t^T A_r C_t$, and a clean version of the original dataset (X_t) is can be reconstructed using the selected PCs from $C_t \rightarrow C'_t$ (i.e. C'_t is the clean version of C_t). The reconstruction is carried out using the pseudoinverse of the truncated matrix $V_t^T A_r \rightarrow C'_t = (V_t^T A_r)_{trunc}^+ Y_t = (V_t^T A_r)_{trunc}^+ V_t^T X_t$, hence, the time domain projection in the channel space is:

$$X'_t = A_r (V_t^T A_r)_{trunc}^+ V_t^T X_t \quad (24)$$

Where X'_t is the clean version of the signals after the rejection of large deviated components performed in the PC space. Let us consider the ASR framework as follow:

A.1. Reference Data extraction:

The extraction of reference data is performed after segmentation into windows of 1 second windows for each of the signals of the recording, followed by the root-mean-squared calculation across them. Then, normalization is done considering the z-score and artifact windows are identified if their scores are outside the range of -3.5 and 5.5. The windows that exhibit values inside the RMS range are concatenated and build the reference data vector X_r . Tolerance values can be applied in order to allow small percentage of windows with high variance to be part of the reference so the vector X_r , has sufficient data to continue with the calibration process.

A.2. Threshold identification:

The reference vector X_r is filtered using a IIR filter to eliminate frequencies associated to brain oscillations, giving as result the vector \widetilde{X}_t . Afterwards, the mixing matrix $A_r = Cov(\widetilde{X}_t)$ is calculated and so the eigenvalues and eigenvectors of A_r are obtained in the matrices V_r and D_r respectively. The principal components obtained by $\widetilde{Y}_t = V_r^T \widetilde{X}_t$ are used to estimate the mean μ_i and the variance σ_i^2 of the RMS of 0.5 second windows from \widetilde{Y}_t of the i-th component. Finally, the threshold for artifact classification is set as $Th_i = \mu_i + k\sigma_i$, where k is a cutoff hyperparameter that defines how stringent the artifact selection will behave.

A.3. Artifact components rejection and signal reconstruction:

Eigenvalue decomposition is applied to the $Cov(\widetilde{X}_t) = V_t D_t V_t^T$ considering a sliding window of 0.5 seconds length and a shift size of 0.25 seconds. At each iteration, a IIR filter like the one described in step 2 is applied to each segment in the channel space. By considering the thresholds Th , the ASR strategy identifies the j-th principal components $(V_t)_j$ with variance $(D_t)_j$ is larger than Th_j . If $(D_t)_j > \Sigma_i (Th_i (V_r)_i^T (V_t)_j^2)$ then the i-th PC values are replaced with zero vectors, and Eq.(24) is used to reconstruct the clean version of the segment.

B. Channel selection

The EEG signal acquisition equipment Synamps 2/RT registers brain activity coming from 70 channels that are located over the scalp following the 10-20 system. The cap containing the 70 channels has 64 monopolar, 4 bipolar and 2 high-level electrodes which for the registration performed by the IBFM lab only the monopolar ones were considered. This leaves the channels LDA, LBIC, RDA, RBIC, HL1, HL2 (4 bipolar + 2 high-level)

connected but not actively registering the EEG data. In addition, two more monopolar channels, M1 and M2, are left aside too since they are not actively used for registration. Hence, from a total of 70 channels, only 62 were used for active registration of brain activity. Regarding the processing, the 62 signals are considered as an initial step, however, after the following artifact rejection steps, the preprocessing framework could discard some other signals that are not useful to consider, as explained in the following subsections.

C. Pipeline for artifact rejection

Besides the ASR tool, EEGLAB [58] offers other approaches for rejecting artifacts in continuous and epoched data. This is based on the estimation of statistical metric thresholds useful to track epochs or larger segments from the dataset to discard if necessary.

The two approaches mentioned above offer different advantages, however, artifact rejection following epoched data can be applied to non-labeled signals, which does not require expert knowledge about EEG data to characterize the noise and the artifacts. In this way, despite that for resting state conditions usually epoching is not applied, such process was implemented in order to provide a more rigorous approach for data cleaning.

First, a passband filter with cutoff frequencies of 0.5 and 100 Hz was applied to consider useful frequency information of brain rhythms. Then an epoching scheme was performed recalling that resting signals convey frequency information comprising delta (0.5 – 4 Hz), theta (4 – 8 Hz), alpha (8 – 13 Hz) and beta bands (>13 Hz). This suggests that slow variation components (due to the delta band) have periods of about 2 seconds, which to be noticeable in the frequency domain would need at least ~10 times that duration. Similarly, for the theta rhythm, considering the lower bound of the interval of 4 Hz, oscillatory components have periods of 0.25 seconds which would require at least a segment of 2.5 seconds to generate an appropriate frequency representation of the signal.

Considering the upper bound given the delta rhythm, the epoching of the signal would be set at 20 seconds, but, this kind of oscillatory components is produced in deep sleep primarily [49], in a like matter, theta waves appear as consciousness slips towards drowsiness, which are not part of the resting state conditions considered in this project, which is related to wakefulness state in closed eyes and opened eyes conditions. As only beta and alpha rhythms are noticeable during these conditions, a 1-second epoch is considered with no overlapping, so the signals are divided into non-overlapping segments of 1 second duration each, enough to have 8 cycles of the slower components from the alpha rhythms. Thus, each epoch contains 1000 points.

After epoching a first step of Independent Component Analysis decomposition is performed using the binary Infomax ICA¹ algorithm (BINICA) that can be found as an extension of the EEGLAB interface. BINICA is a C compiled binary version of the ICA algorithm based in the Infomax approach and it optimized to run in less time than other implementations.

Data cleaning according to this pipeline is then started by rejecting extreme values that can be present at a certain trial (i.e. epoch), if the amplitudes (defined in microvolts) are outside

¹ Binary Infomax ICA by Sigurd Enghoff based on the Matlab version of Scott Makeig and collaborators. Makeig S, Anthony J. Bell, Tzyy-Ping Jung and Terrence J. Sejnowski, Independent component analysis of electroencephalographic data in: D. Touretzky, M. Mozer and M. Hasselmo (Eds). Advances in Neural Information Processing Systems 8:145-151 (1996).

the range $-75 \leq \text{ampl} \leq 75$ within a specific epoch, then that segment is marked to be rejected. Another consideration for artifact rejection is based on abnormal trends, this approach calculates the slope of a linear model fit from the data of each segment. The fit between the signal and the line is evaluated using the R-square measure which at a limit set at 0.05 determines the correlation that exists between the EEG data and the model. For this case, the maximum slope was defined at $10 \mu\text{V}/\text{epoch}$, if the slope exceeds such value in the trial, then it is marked for rejection.

Improbable data can be also tested to reject epochs from the recordings. This can be done by estimating the probability the distribution of the amplitudes that are present at the different epochs, from which, the probability of a datapoint can be obtained. This holds by assuming that artifacts are improbable events from which a probability of occurrence can be defined for the trials. Thresholds are set considering the first and second order moments of the distribution and in this case, were set at 4 times the standard deviation of the distribution. Larger values are considered as artifactual components and are marked for rejection.

Kurtosis is also employed to determine in this case abrupt changes in the signals, such changes are related to artifacts. When high kurtosis values are found it means that in a segment exists high differences in between the amplitudes of a trial, in the opposite case it means that all values have similar values. The thresholds set for this rejection consideration is set at 5 times the standard deviation from the mean kurtosis value.

Finally, the last consideration for epoch rejection is based on spectral estimates of the segments. The amplitude changes of the spectral quantities are expressed in decibels and are fixed in a range from $-50 \leq \text{dB} \leq 50$ for the 0 to 2 Hz frequency components. A multi-taper frequency decomposition approach is used by the tool to obtain accurate spectral values and after comparison with the frequency information in the epoch it marks the trial for rejection if exceeds those limits.

All the marked epochs are then rejected automatically, some of them are marked more than once considering the different metrics.

After the epoch marking according to the thresholds, statistics and frequency features estimated from each of the segments of the signals, a second round of ICA decomposition is recommended to improve the quality of the components. It can reveal more independent components that are associated to neural activity. REFERENCES. Then epoch inspection and rejection are performed to obtain the final clean version of the signals.

D. MARA algorithm

ICA decomposition provides a set of components that are either driven by artifacts or by neural activity, in this way, different algorithms for artifact rejection have been designed under that assumption of independence between the artifactual components and the neural sources.

The Multiple Artifact Rejection Algorithm (MARA) [65] has as objective the identification of independent components coming from artifacts to then perform the reconstruction of the signals in the channel space domain. At this point all of the preprocessing steps performed thus far are part of the useful and necessary procedures needed in the MARA framework to estimate the artifactual ICs.

The MARA algorithm was designed to use 6 features as the most representative ones after considering a feature selection scheme based on a Linear Programming Machine (LPM), which in the validation stage originally grouped a total collection of 38 parameters. The 6 parameters are estimated from the dataset in order to perform the linear classification scheme for this purpose [67]. These representative data are estimated from spectral, scalp map and temporal information of the signals.

The first feature corresponds to the current density norm (1), derived from the ICA scalp maps and used to estimate the location of the sources of the signals. To do this, the $l^2 - norm$ between the considered ICA scalp map component and a predefined topological set of locations is calculated, and so, the one with the minimum norm is selected as the source. Large $l^2 - norm$ values are characteristic of the artifact components; hence, this value can be used as a discriminant feature of abnormal trends in the signals.

The range within pattern(2) is obtained as the logarithm of the difference between the maximum and minimum values in the scalp map component. This feature provides a high value when movement artifacts are present or there is a poor junction between the electrodes and the scalp. Another factor that can be obtained is the third order central moment (3), which is considered to check how much the distribution of the magnitudes is skewed, thus, it is useful to detect possible outliers from the IC vectors.

Some parameters associated to the components' spectral information are also used as characteristic terms taking into account a prototype of the curve given by $1/f$ (4) and its shape (5). The parameters $k_1, \lambda, k_2 > 0$ define such curve $f \rightarrow \frac{k_1}{f^\lambda} - k_2$, and are estimated following the log-power at 2 Hz, 3 Hz, and the local minimum values in the frequency bands 5 - 13 Hz and 33 - 39 Hz respectively. The logarithm of λ and the mean squared error of f given k_1, λ, k_2 in the range of 8-15 Hz are used as the features. Artifacts are recognized as such when there exist high values in the 20-50 Hz range when the value of λ is high and k_1 low.

The last spectral feature accounts for the average log-power of the alpha rhythm in the range of 8-13 Hz (6). Abnormal values are considered as artifact derived components.

All of these features are fed into a linear classifier pre-trained with data coming from a reaction time (RT) study which was hand labeled by experts to obtain a parametric model for classification. The model parameters after training were tested for generalization and according to the results it shows efficiency in the automatic detection of artifactual independent components considering different sources of artifacts including but not limited to muscular, eye and external artifacts [65].

In this way, all the preprocessing steps give as result a refined version of the original dataset both in temporal and component spaces. This scheme is repeated 20 times, one for each of the 10 subjects and considering the two resting state conditions R1 and R2; opened eyes and closed eyes, respectively. Then, the processing scheme is started and the objective is to find the appropriate segment length to perform the effective connectivity analysis of the brain activity.

E. Results of preprocessing

Considering the example of the EEG signal registered by the channel F8 for the subject 10 in resting-state condition R2 - closed eyes, (see Figure 8), Figure 10 shows the result after the preprocessing steps performed for the time segment 127 to 132 seconds.

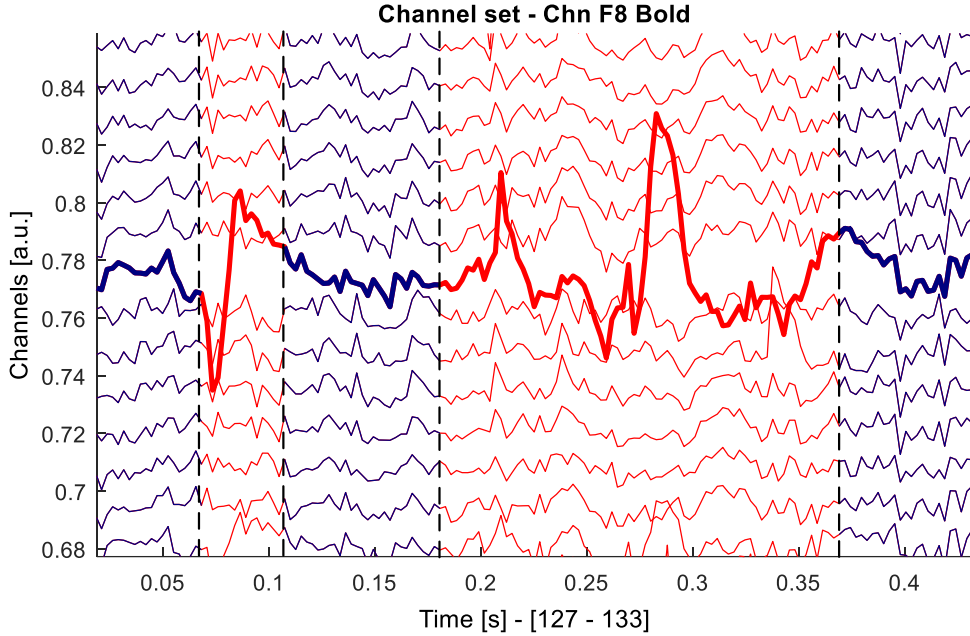


Figure 10. EEG signals after preprocessing. The bold signal corresponds to the F8 recording during the time interval 127 to 133.

As can be observed in Figure 10, the result of the preprocessing stage produces an automatic segmentation and channel rejection after the ASR application. It produces the labeling of segments that are cataloged as artifacts in each of the signals, and that produces the rejection of the whole segment in all the channels i.e. the segments plotted in red. After that, the remaining segments, the ones plotted in blue are concatenated and the clean version of the data samples is generated.

It is necessary to clarify that for the case depicted in the previous figure, the algorithm detected such large variations and according to the thresholds it was better to reject the segment than to perform the reconstruction of the signal. In summary, as it has been described through these sections as a didactic example, the artifact localized at the interval 127 – 132 s of the F8 signal was needed to be rejected and not minimized, which as consequence produced the loss of EEG data during the duration of the artifact.

As a consequence of the filtering and data cleaning stage of the algorithm, the recordings are shortened and data is lost in the process, but the resulted signals are clean from artifacts and undesired noise, so it is possible to perform further processing.

F. Dataset revisited.

As explained in the section *EEG Dataset*, the analysis and processing of the EEG data are based on recordings acquired from 10 healthy subjects considering two resting-state conditions (opened eyes – R1, and closed eyes – R2). Each recording lasted about 5 minutes and contains samples coming from 68 electrodes located over the scalp acquired at a sampling frequency of 1000 Hz.

Then, a data cleaning process to reduce and reject the effect of artifacts and noise from the signals was performed using the implementation summarized in Figure 9, as result, the EEG datasets were shortened considering the stringent rejection procedure for the heavily affected portions of the signals by the noise. Table 3, shows the original size of the raw dataset and the reduced size after the data cleaning process.

Table 3. Recordings' characteristics before and after the cleaning process

Subject record	R1 - Opened eyes			R2 - Closed eyes		
	Raw signals duration [s]	Cleaned signals duration [s]	Selected channels	Raw signals duration [s]	Cleaned signals duration [s]	Selected channels
S1	305	46	51	311	172	53
S2	308	235	59	314	256	60
S3	284	46	59	204	43	58
S4	192	101	54	278	123	53
S5	308	205	57	306	155	59
S6	308	230	57	311	226	60
S7	353	135	54	313	212	55
S8	315	197	61	319	231	62
S9	189	145	55	184	116	58
S10	303	172	60	328	240	61
Mean	286	151.2	57	287	177.4	58

Starting from the data cleaning process, there is selected a subset of channels that contain a group of clean EEG signal sources from which it is possible to perform the segmentation analysis. From the original set of signals composed of 68 data series for the 10 subjects in both conditions, the number of channels is reduced on average to a proportion of ~84% its original value, corresponding to 57/58 signals as shown in Table 3. Such a number represents the overall amount of channels that is maintained after the pre-processing stage.

Moreover, the duration of each of the recordings after the artifact rejection process is reduced to ~53% of the original length on average. This suggests that the data was heavily affected by noise and artifacts; from an average duration of about 4.8 minutes, only 143 seconds were useful for processing.

From these pre-processing results, it can be observed that some of the recordings were more affected by noise components than others. For instance, the dataset S1 - R1 had an original duration of 305 s and was reduced to 43 s, similarly, the same happened for S3 - R1 and S3 - R2. If each of these results is analyzed one can infer that there were more data rejected in the opened-eyes resting-state condition compared to the closed-eyes condition, which can be since in opened-eyes condition more artifacts can be generated (e.g. blinking eyes artifacts are present over the recordings).

According to these results, the pre-processing stage shows to be useful in rejecting noisy data, and the parameters selected according to the guidelines explained in Preprocessing offer a rigorous data cleaning process which due to the nature of the brain activity investigated in this work can take place. Considering that resting-state conditions are used to analyze the normal rhythmic components of the EEG signals, no engaging tasks are involved and continuous noise-free signals are needed.

5. Methods on Segmentation and Effective Connectivity

5.1. EEG segmentation

5.1.1. Segment length analysis on EEG data

A. Segmentation and kurtosis estimation

Following the EEG signal processing strategy depicted in Figure 11, after the pre-processing stage from which the datasets are filtered and cleaned out from artifacts and undesired components, a signal resampling step is done to provide a new sampling frequency of 250 Hz, this step is performed to meet the requirements according to the literature; which states that such sampling rate is sufficient to accomplish Effective Connectivity analysis [48].

After that, a pass-band filter is employed to limit the frequency components outside the usual brain activity range ($f = 0.5 \text{ Hz} - 50 \text{ Hz}$). Finally, the segmentation is performed as a way to estimate the statistical characteristics over the signals at specific time intervals. It is worth to mention that the subprocesses of the block diagram are performed individually to each of the signals composing the artifact-free datasets.

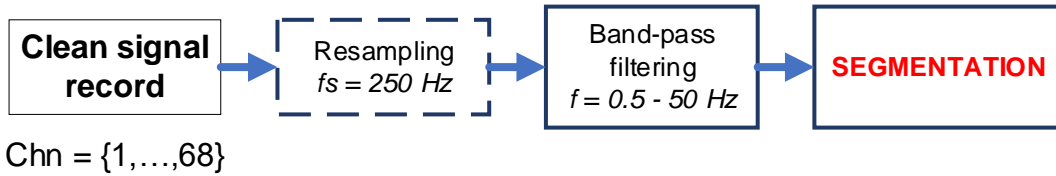


Figure 11. Processing pipeline after data cleaning.

Segment length analysis in this approach is based on an iterative piecewise subdivision of the datasets into blocks called segments/windows, from which it is possible to obtain estimations of the dynamical properties of the EEG signals and the nonlinear processes behind them.

To explain the segmentation procedure, let \mathbf{W}_L be the *basis window length* defined as the elemental duration of the segments in milliseconds/seconds, and N_w be the *total number of windows* (i.e. the number of segmentation operations) considered to perform the iterative segmentation. According to these parameters of the processing scheme, it is defined the following simple mathematical relation:

$$h = N_w \cdot W_L \quad (25)$$

Where h corresponds to the longest segment duration for a specific segmentation procedure. From Eq.(25) it can be checked that the inequality $0 < W_L \leq h$ holds and states the possibility to have a basis-window length equal to the longest segment duration in the case $N_w = 1$.

By considering the *total duration of the recording* (t), as well as the dummy variable w_l , used to keep the value of the segment duration for a specific *segmenting step* ($i = 1, \dots, N_w$), at each iteration, it is produced a matrix of size t/w_l by $w_l \cdot f_s$ samples that contains the segmented signal with non-overlapping segments. The indexed version of the dummy variable (w_{li}) refers to the segment duration according to the segmenting step iteration, so that:

$$w_{li} = i \cdot W_L, \quad \forall i = \{1, \dots, N_w\} \quad (26)$$

In summary, the iterative process for the segmentation of a signal is explained from its sequential splitting according to the window length (w_{li}) that is increased at each iteration by a factor defined as a multiple of the basis window (W_L) according to Eq.(26). In this way, the signal of duration t is divided into non-overlapping pieces, each one of length w_{li} . The resulted segments are then stored in matrix form and are organized in chronological order. The procedure is repeated N_w times producing a total of N_w matrices of segments for each of the signals that compose the dataset. Figure 12 shows the relationship that exists between W_L , w_{li} and N_w in the segmentation procedure of an EEG signal.

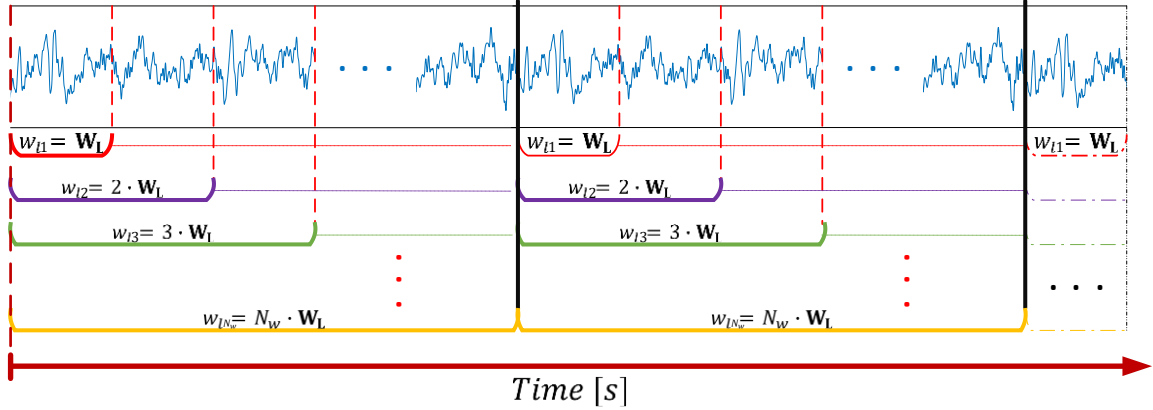
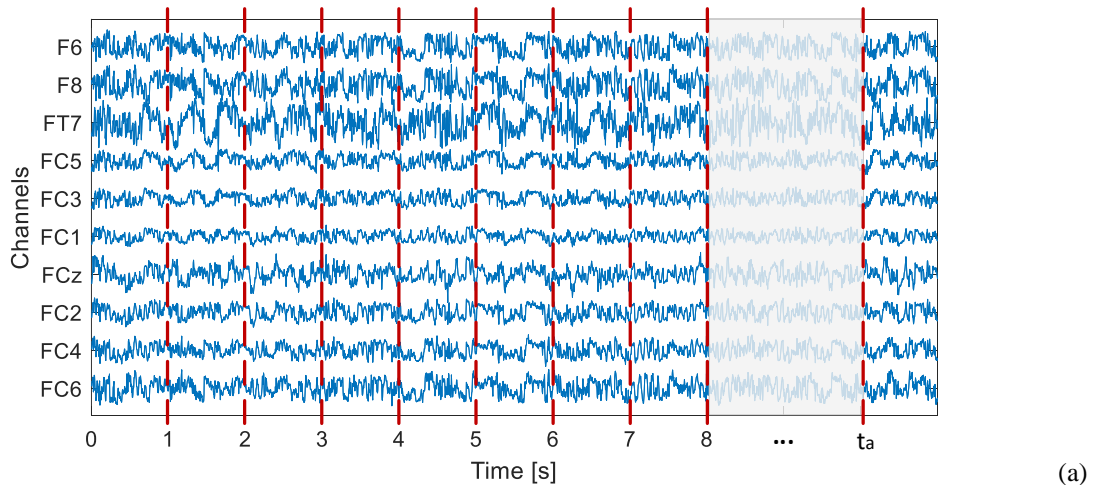


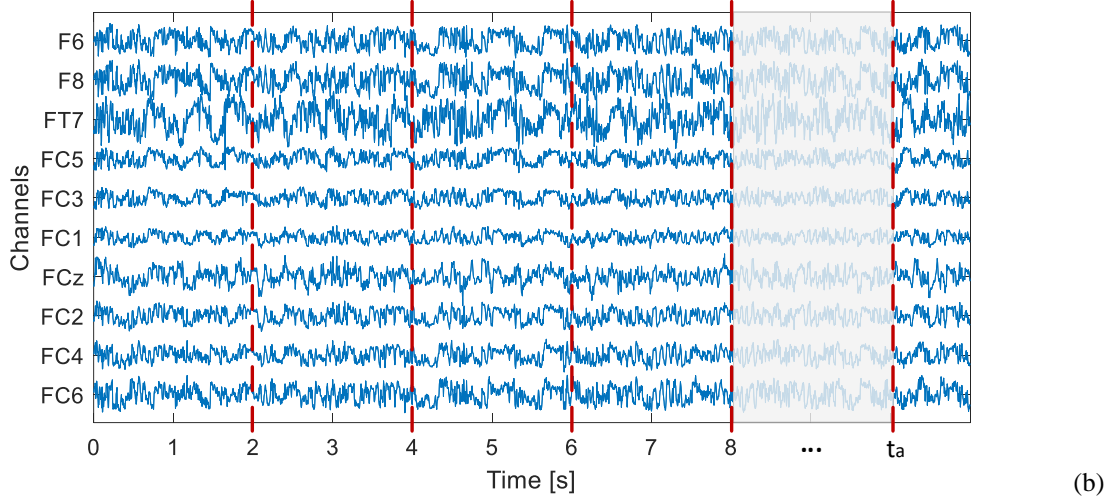
Figure 12. The general approach for segmentation performed on an EEG signal.

Figure 12 depicts the process of segmentation for a signal of generic duration. As can be observed, the process is performed sequentially, at a first iteration a window duration $w_{l1} = W_L$ is used to break the signal into non-overlapping pieces, then, the segmented signal is stored in a matrix. In the second iteration, the process starts by considering a new window duration $w_{l2} = 2 \cdot W_L$, followed by the same partition method. The segmentation is stopped after reaching the largest window for the process when $w_{li} = N_w \cdot W_L = h, i = N_w$.

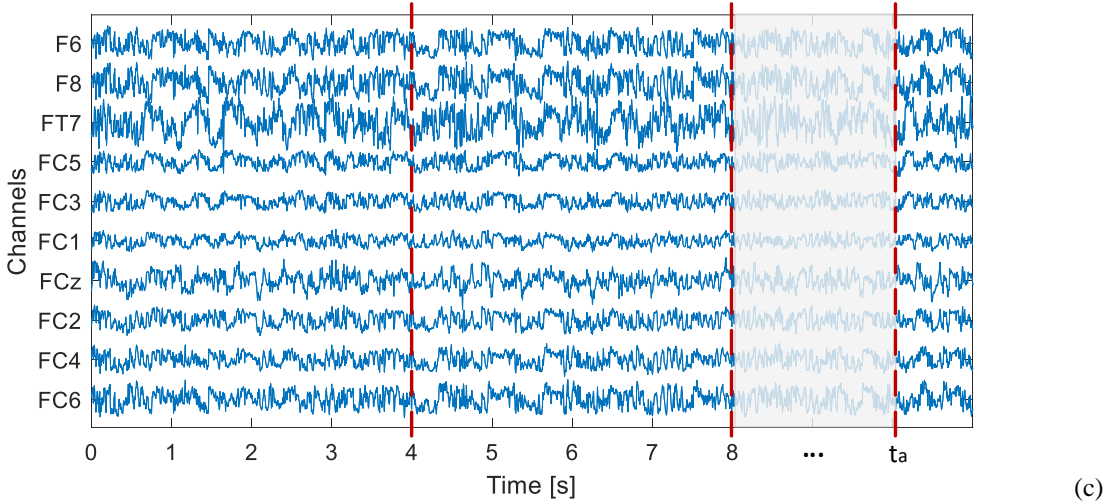
Figure 13 instead shows the non-overlapping segments of a subset of channels from an EEG recording. There are shown the bounds of the segments considering a basis window length $W_L = 1$ second and the sequential partitioning considering $w_{l2} = 2s$ and $w_{lN_w} = 4s$.



$$w_{l1,j} = (x_j, x_{j+1}, x_{j+2}, \dots, x_{j+W_L-1}, x_{j+W_L})$$



$$w_{l2,j} = (x_j, x_{j+1}, x_{j+2}, \dots, x_{j+2 \cdot W_L - 1}, x_{j+2 \cdot W_L})$$



$$w_{lN_w,j} = (x_j, x_{j+1}, x_{j+2}, \dots, x_{j+N_w \cdot W_L - 1}, x_{j+N_w \cdot W_L})$$

Figure 13. Segmentation bounds over time for a subset of channels considering a segment duration of (a) 1 second, (b) 2 seconds, (c) 4 seconds ($i = N_w$).

By considering any basis window length, it is easily confirmed that any of the segments of the iteration $i = 1$ (*i.e.* $w_{l1} = W_L$), it is composed of a sequence of samples defined by $w_{l1,j} = (x_j, x_{j+1}, x_{j+2}, \dots, x_{j+W_L - 1}, x_{j+W_L})$, where j corresponds to the starting index where the starting of the segment is located with respect to its occurrence in time. Thus, $w_{li,j}$ defines the data vector resulted from a specific segment, a data block formed by a number equal to $i \cdot W_L$ samples that initiates at the time instant corresponding to the index j . Figure 13 shows the generic segment definition for $w_{l1,j}$, $w_{l2,j}$, and $w_{lN_w,j}$ (Figure 13. (a)-(c)) and their graphical description considering a real case scenario when $W_L = 1s$. The arbitrary time instant t_a defines a time point in which the segmentation is restarted at a future instant, displaying the continuous segmentation over the signals.

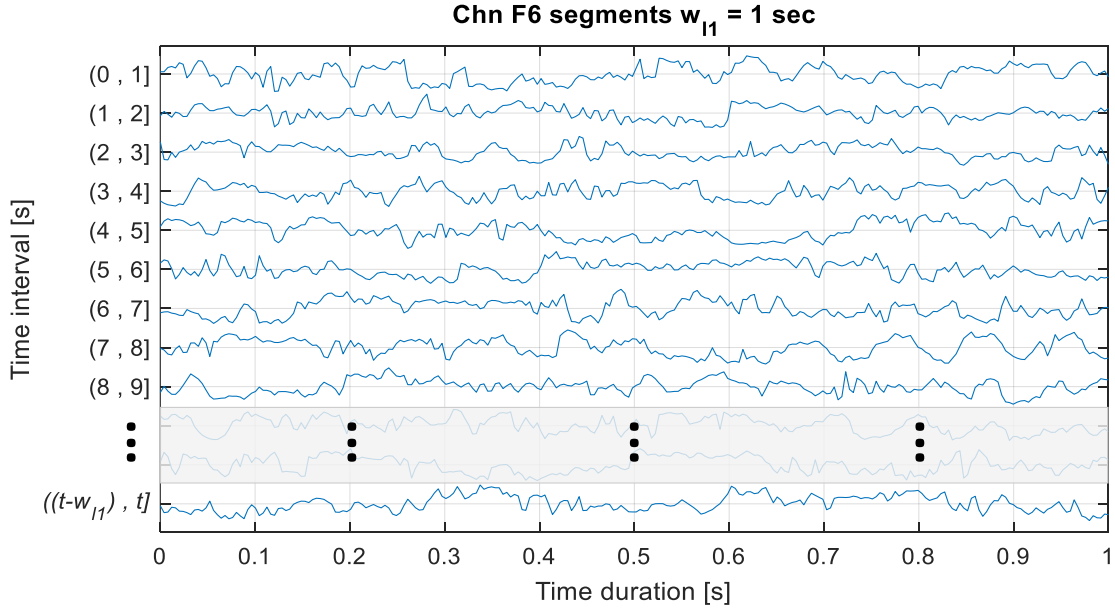


Figure 14. Graphical representation of the result of segmentation for $w_{l1} = 1$ s of an EEG signal coming from the channel F6.

Figure 14 shows the way how the matrix comprising the windows is built for a signal acquired from the channel F6 by considering the first segmentation iteration $w_{l1} = W_L = 1$ s. The time intervals are stored sequentially considering the occurrence in time of the segment up to the last segment defined by the half-open interval $((t - w_{l1}), t]$. In general, a segmentation matrix of generic size in number of samples, t/w_{li} rows by $w_{li} \cdot f_s$ columns is built ($t \times 250$ for this specific case). Similar procedure is followed for the remaining segmenting steps ($i = 2, \dots, N_w$).

The basis window length defines the different segment durations at different iterations and from them, it is possible to obtain the time intervals that comprise the samples stored in a segment. Figure 15 shows exactly that relationship which is useful to understand the further process based on kurtosis.

Considering that the segmentation procedure is the same for all the signals of a dataset, Figure 15 depicts how are the segments being extracted from a generic basis window W_L , which besides to define the limits of the segments, also plays a significant role to track down the windows over time making possible to perform the estimation of statistical features that characterize that specific time interval, and so, it can be analyzed the variation of the statistical characteristics of the EEG process with respect to time, not only for a single signal but for the complete set, among resting states and subjects.

From Figure 15, it is possible to see that there are obtained different subdivisions from the same sources; the brain activity represented by the EEG signals is being segmented in different ways considering two fixed parameters, W_L and N_w . From the sequential segmentation, as shown in Figure 14, there are obtained a series of matrices of the same size for all the channels considering the relative duration given by w_{li} at an iteration $i = (1, \dots, N_w)$. By considering the same segment durations across channels it is possible to compare their statistical quantities and by analyzing the spread of those statistics it is possible to define an approach to find the most common segment duration across channels exhibiting high relative stationarity, for the two resting-state conditions and for all the subjects of the experiment.

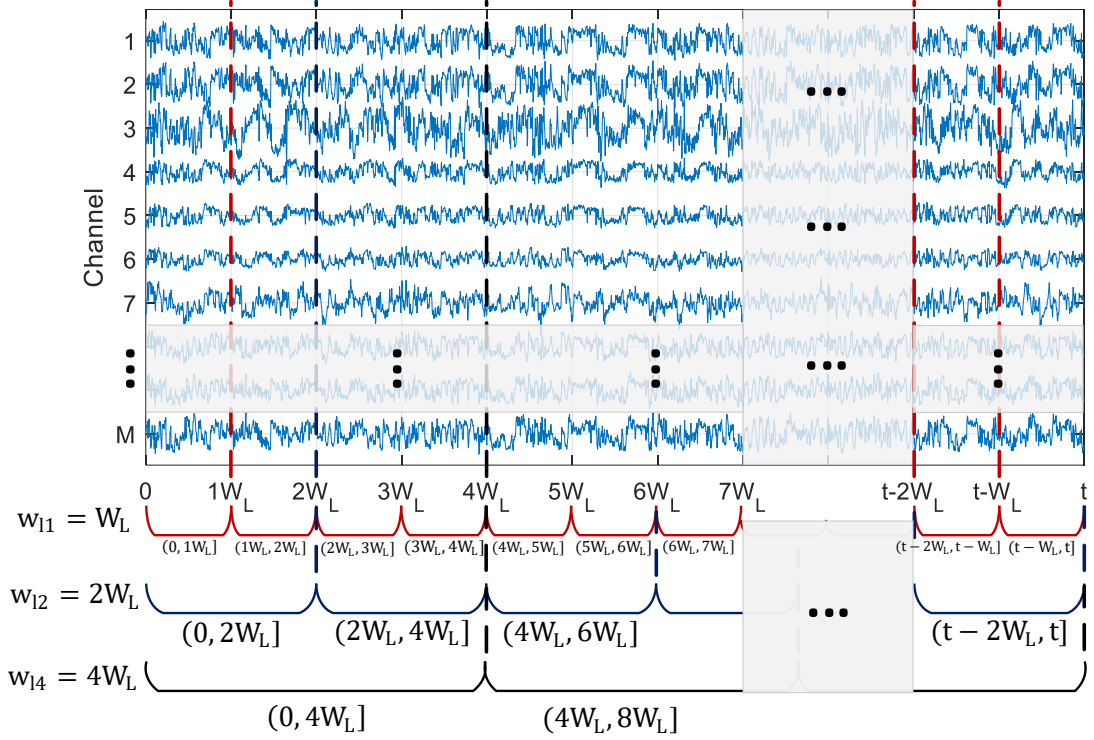


Figure 15. Signal segmentation considering the basis window length to locate in time the window.

As explained earlier, the size of each segmentation matrix is $t/w_{li} \times w_{li} \cdot f_s$ samples, then, the statistical measures like the ones explained in equations (19) - (23) can be applied to each of the rows of the matrix, giving as result a new representation of the data, a vector which depending on w_{li} comprises the statistical moments' estimations exhibited by a signal at the time interval defined by the boundaries of the range referred to as the row index of the matrix (see Figure 14). Hence, it can be defined that:

$$W_{matrix} \in R^{t/w_{li} \times w_{li} \cdot f_s} \rightarrow s.c \in R^{t/w_{li}}, \forall chn = \{1, \dots, M\} \quad (27)$$

Where W_{matrix} is an array containing the segments of a signal and $s.c$ stands for statistical characteristic whose values are being mapped into. From Eq.(27), it is noted that the statistical characteristic space has a dimension of only t/w_{li} components (i.e. a vector), each of them indicating the statistical attribute exhibited by the segment at a specific time interval. In this way, it is possible to account for the variation over time of these statistical characteristics considering different window ranges.

The expression from Eq.(27) is provided as a generalization on the estimation of statistical characteristics from a matrix of segments. From this, one could estimate all the statistics (or a subset of them) to provide a better explanation of the stochastic processes defined by all the PDFs derived from the different segments.

However, some of the order moments are not useful, or in other words, they cannot be estimated to account for their variations that exist from segment to segment. Let consider the first-order moment (Eq.(19)). From the pre-processing steps that involve the mean subtraction and the filtering subprocess, this statistical quantity is reduced towards zero, making it not useful for characterization. Moreover, as a consequence, the second-order moment (mean-squared) and the second-order central moment (variance) are approximately the same being the variance centered around a small mean value ($\mu_x \rightarrow 0$).

The coefficient variation under these circumstances is not useful to represent the variations

over different processes since the ratio (σ_x/μ_x) goes to infinity as long as the mean is reduced to zero. Thereby, only higher-order moments like the skewness and kurtosis contribute to the process characterization, and as it will be demonstrated from the dataset, the skewness is very small since the PDFs from the segment means to follow a normal distribution.

In this way, the 4th order central moment (Eq.(23)) and its definition accounting for the existing excess from a normal distribution is the statistical quantity used to determine the non-stationarity behavior exhibited by a segment of fixed duration extracted from the segmentation process explained before. As result, a much more detailed form of the expression summarized in Eq.(27) is found below:

$$Wmx_{i,chn} \in R^{t/w_{li} \times w_{li} \times fs} \rightarrow \mathbf{K}_{i,chn} \in R^{t/w_{li}}, \forall chn = \{1, \dots, M\} \quad (28)$$

Where K_i is a vector that contains the kurtosis excess estimated at each segment from the $Wmx_{i,chn} = W_{matrix}$ at iteration i and channel chn (i.e. a vector of kurtosis values calculated from each row of the windowed matrix). Then, each component of the vector $K_{i,chn}$ explains the degree of non-stationarity of a segment at a specific time interval bounded by the duration w_{li} on each channel.

From the segmentation process and the formation of the N_w segmenting matrices it can be inferred that the sizes differ from each other, producing kurtosis vectors that have more components for the first segmenting steps (i.e. when i is close to 1), specifically, the largest $K_{i,chn}$ vector-length is produced when $i = 1$, and as long as i increases, the number of components of the kurtosis vector decreases. In this way, to provide a framework to compare the statistics resulted from the segmentation in a signal coming from a channel (and later on from different channels), a 1-D interpolation step is performed to obtain the same number of kurtosis samples across the different $Wmx_{i,chn}$ considering different widow durations w_{li} .

In this way, the number of kurtosis samples is bounded to the number of rows obtained by the expression t/w_{l1} given that $w_{l1} = W_L$, thus, the basis window length is the main parameter from which the $K_{i,chn}$ vector-length is defined.

Figure 16 shows the representation of the kurtosis values considering different window lengths. For K_1 (second row of the table figure), each block representing the kurtosis value exhibited by a basis segment is grouped in a vector. Thus, the number of components for this first case is the maximum since the number of segments is the highest, that is why for subsequent segments, the interpolation allows completing the number of components considering larger windows. The cells containing the interpolation values (I) are shown to represent how this procedure is performed to complete the samples for further processing. It is necessary to explain that the first cell comprising the fixed duration of a segment should be located at half of the period of the segment, however, for the sake of illustration, it is placed at the beginning of the vector to visualize better how the interpolation values are completing the vector lengths.

The array formed by all the kurtosis values characterizes the stationarity of the segments that each block represents and so, from it, it can be possible to perform estimations, not in the discrete-time domain but the kurtosis domain. Let consider an example in which the analysis case is focused on the EEG signal coming from the channel F1 (see Figure 17) for the resting state condition R2 (Closed eyes) acquired from subject 10. In this case, the segmentation was performed by considering a $W_L = 1$ second and $N_w = 10$, which corresponds to a sequential segmentation considering windows of durations that go from 1 to 10 seconds.

As a result of the segmentation and kurtosis estimation, a matrix similar to the one shown in Figure 16 is generated, from it, there can be obtained the distributions of the 4th order moments according to the window lengths from the same signal, thus, the expected value of the kurtosis under those different parameters are estimated and their variances can also be analyzed.

	$(0, W_L]$	$(W_L, 2W_L]$	$(2W_L, 3W_L]$	$(3W_L, 4W_L]$	$(4W_L, 5W_L]$	$(5W_L, 6W_L]$	$(t - W_L, t]$...
K_1	W_L	W_L	W_L	W_L	W_L	W_L	...	W_L	W_L	W_L	W_L	...
K_2	$2W_L$	I	$2W_L$	I	$2W_L$	I	...	$2W_L$	I	$2W_L$	I	...
K_3	$3W_L$	I	I	$3W_L$	I	I	...	$3W_L$	I	I	$3W_L$...
K_4	$4W_L$	I	I	I	$4W_L$	I	...	$4W_L$	I	I	I	...
...
K_{N_w}	$N_w \cdot W_L$	I	I	I	I	I	...	$N_w \cdot W_L$	I	I	I	...

Figure 16. Kurtosis estimation from segment to segment and disposition of interpolation values for a generic signal.

Figure 17 shows the distributions of the kurtosis values for the F1 channel under the conditions described above. The expectance value from each of the distributions calculated from the fitted PDF is also presented individually for each case. As can be noted, all of the graphs are in the same kurtosis range to observe the differences between them. Gaussian distributions are fit to check the correspondence between the kurtosis values and the densities that arise from the data, and as depicted, it is possible to state that the kurtosis values follow normal distributions and that considering the expectation it is possible to compare them.

Similarly, Figure 18 comprises the PDFs found for a different segmentation setting, $W_L = 50$ ms and $N_w = 20$. In this case, the distributions estimated every 100 ms are shown, and as the number of kurtosis values from those vectors is larger than in the Figure 17 example, the distributions are more accurate but the kurtosis values are less significant since they are derived from less number of samples (i.e. shorter windows comprise fewer data points).

From Figure 18, it can be distinguished that as the segment length increases (e.g. $w_{li} \geq 400$ ms), the kurtosis distributions start to follow a more gaussian shape and the skewness from this 4th order statistic quantity decreases. Likewise, the example of Figure 17, the mean values and the spreads from the densities are similar (i.e. their values are close to each other) and a comparison strategy can be defined.

The data characteristics noticed from these two examples on a single signal under different segmentation parameters are generalized for the remaining signals from the EEG recording, moreover, the same is found for different EEG datasets of the other subjects.

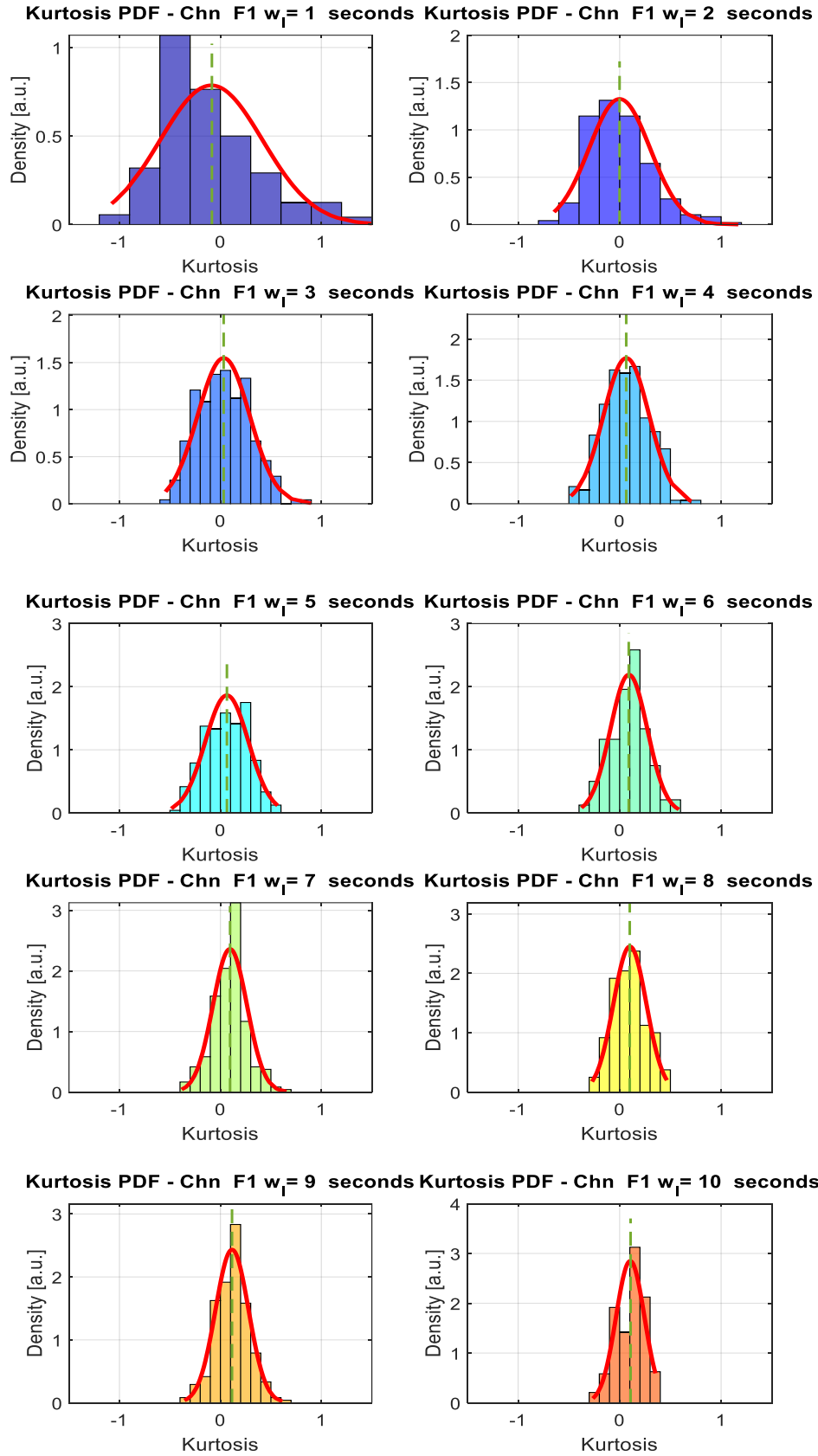


Figure 17. Kurtosis distributions of the channel F1 of subject 10 (S10) in R2, estimated from different segment lengths considering $W_L = 1s$ and $N_w = 10$.

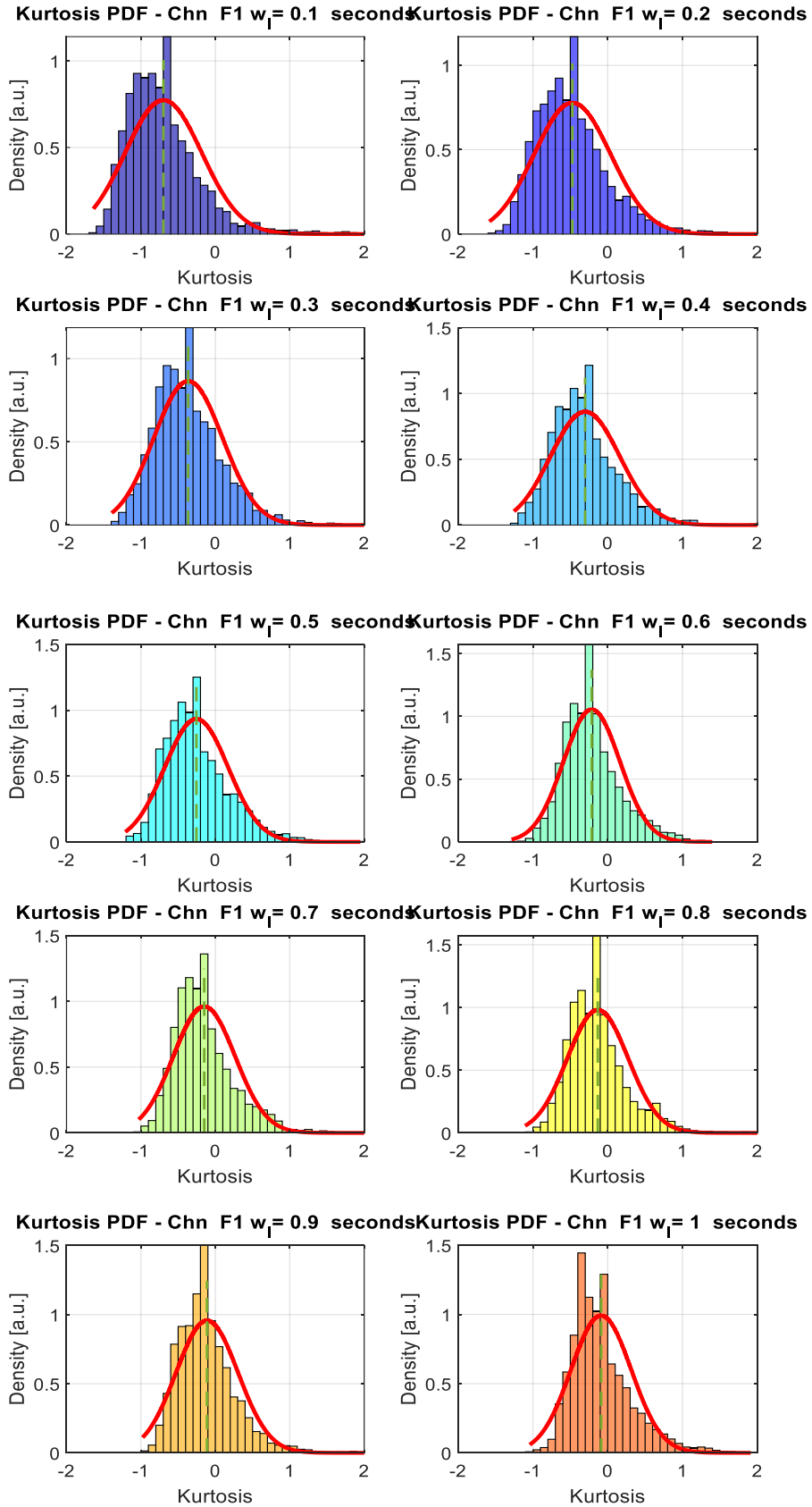


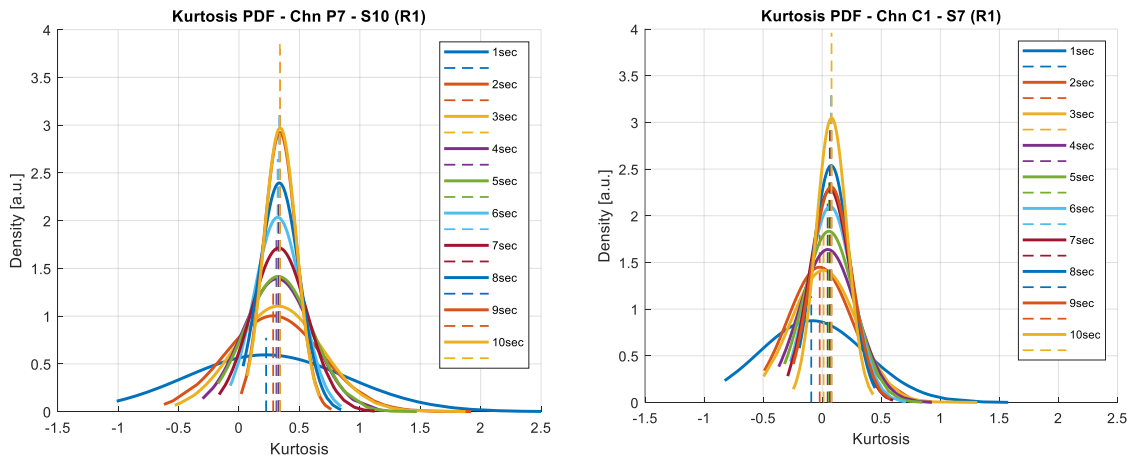
Figure 18. Kurtosis distributions of the channel F1 of subject 10 (S10) in R2, estimated from different segment lengths considering $W_L = 50\text{ms}$ and $N_w = 20$. Shown PDFs of tenths of a second.

B. Kurtosis as a feature

As described before in the section *Characteristics of EEG signals*, the statistical quantities explain certain characteristics of the data under analysis. In this case, kurtosis is employed to examine the non-stationarity variation from segment to segment at different window configurations. This means that kurtosis is a feature estimated from the data, or putting it in a better way, it is a feature derived from shorter portions of the data and explains the dynamic change of the underlying process referred to the segments. In this sense, different conditions of segmentation can provide more or less information about the non-stationarity, and, as a way to select which duration would be appropriate to explain most of the stationarity (not only for a single signal, but for a dataset), it is necessary to compare the features, first for a single channel then for a complete dataset, and finally, among conditions and subjects.

To perform this, let consider the kurtosis densities estimated from a segmentation configuration when $W_L = 1$ s and $N_w = 10$. As can be observed in Figure 19 there are considered the kurtosis densities from the channels P7, C1, of subjects 10 and 7 in opened-eyes resting condition (R1), and channels CP3, AF4 from subjects 4 and 5 in closed-eyes condition (R2). These channels and subjects were selected randomly for demonstration purposes.

From the superimposition of the kurtosis densities under analysis, it is noted that from different segment lengths, the expectances (means) are close to each other and tend to increase as the number of samples in the window grows. Such behavior is common for the majority of the channels, even for the ones with larger dispersion among densities like the S10 (R2) - AF4 channel in the bottom right figure. It is also important to evidence that usually mean-kurtosis values from shorter segments are close to the distribution expectance of the longer ones. This also holds across the channels that form a recording (the set of EEG signals of a subject).



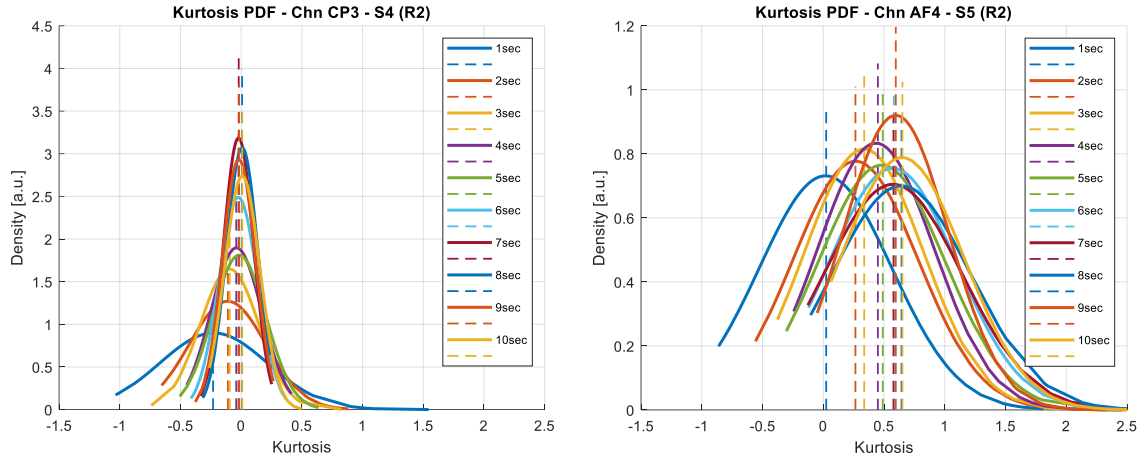


Figure 19. Kurtosis densities estimated from signals of different recordings.

Then, following the comparison strategy, but now applied to the case of analyzing different channels at the same time, it is built a single distribution comprising the kurtosis components defined by all the $K_{i,chn}$ vectors ($i = 1, \dots, N_w$), in that way a single PDF is fit to the data, and a similar process of superimposition but now across channels is performed to analyze the kurtosis data.

Figure 21 shows the histograms and the fitted kurtosis distributions of 4 signals acquired from the same subject (S10 – R2), so all of them are a representation of the EEG activity measured at the same times from different locations on the scalp. Specifically, the data comes from 2 frontal electrodes (F1, F4, first row on top of the graph) and the other 2 located at the posterior area of the scalp in the occipital area (PO4, PO5, second row at the bottom of the graph). These electrodes were selected because of the large distance relative to the frontal and posterior areas of the skull (for the specific locations see Figure 6.), so it could be possible to observe the non-stationary characteristics of the EEG potentials represented by the kurtosis values generated at different locations but referred to the same brain activity, besides to analyze the correlation that exists between neighboring channels (PO4, PO5, and F1, F4 pairs).

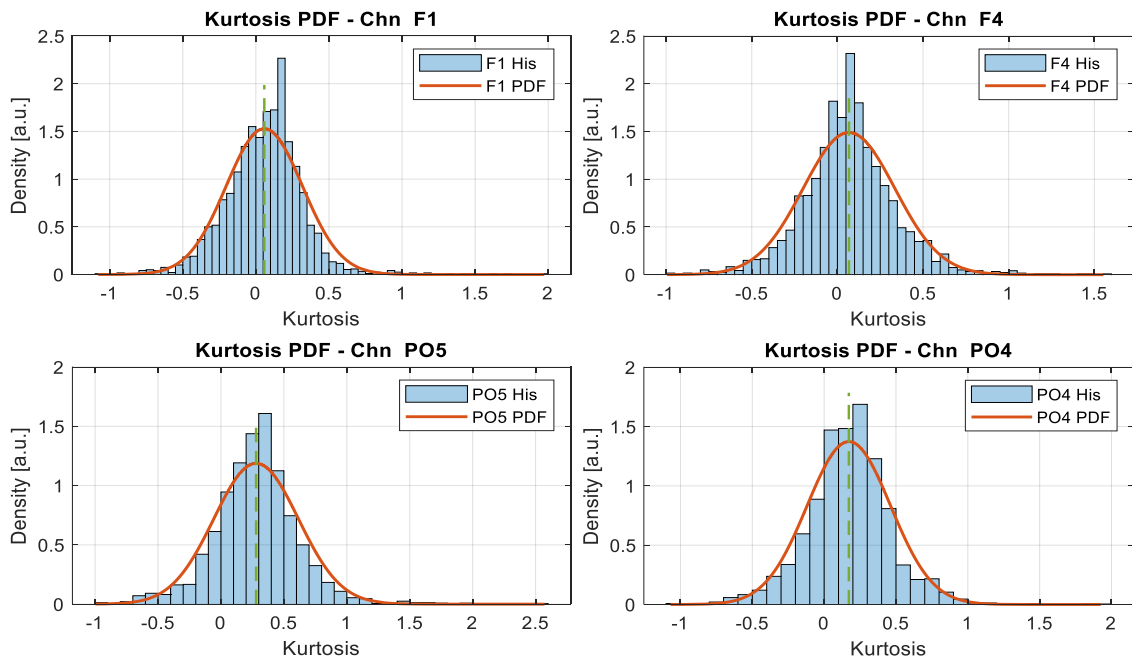


Figure 20. Kurtosis distributions considering all the segment estimations.
Subject 10, resting-state: closed-eyes condition

The distributions exposed in Figure 20 show the kurtosis values of all the segment configurations for $1 \leq i \leq 10$ for a basis window length $W_L = 1$ s. As result, all the vector components from the windowing process as well as the interpolated values were combined forming a single vector from which the distributions were produced. By doing this, the values from different segment durations are shuffled and then organized according to their magnitude, in this way similar kurtosis values exhibited by different segment lengths are organized close to each other and so it would be possible to obtain the expected kurtosis value derived from different window configurations.

As can be noted from the densities, they have similar shapes, and their distributions consider comparable domain limits (i.e. the kurtosis values are bounded within the same approximate limits $-1.5 \leq K \leq 2$). This is an interesting observation because it can be used to compare the same EEG process considering kurtosis distributions derived from different source channels. In this way, Figure 21 depicts the superimposition of the kurtosis densities of the 4 channels investigated.

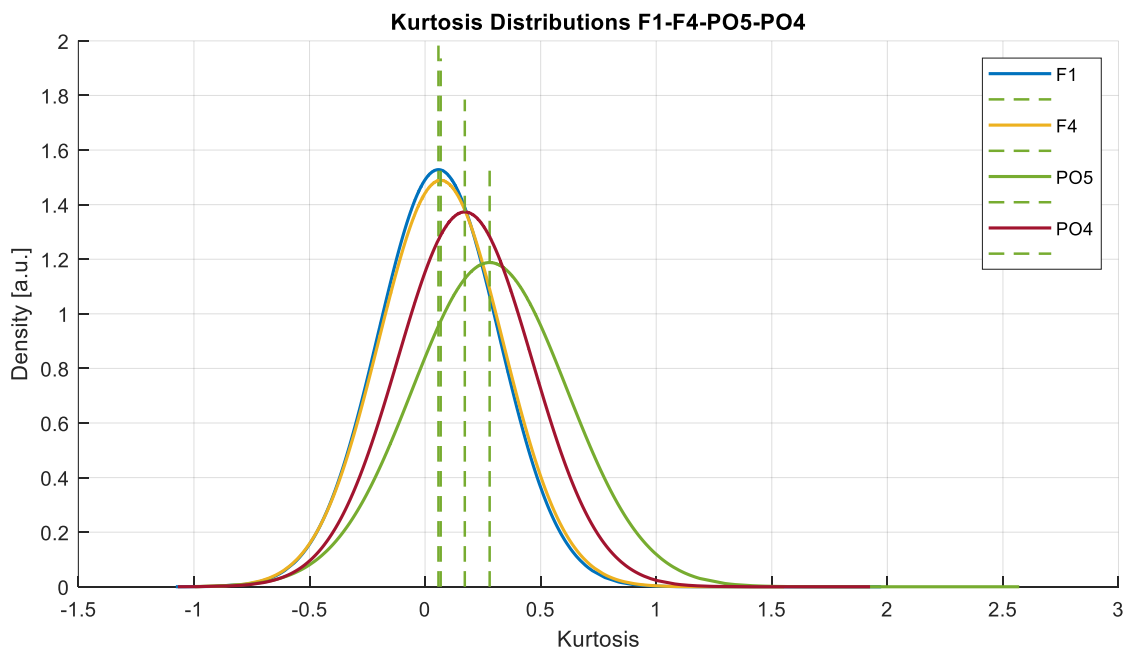


Figure 21. Kurtosis distributions considering all the segment estimations.

The relationship that exists between the frontal channels F1 and F4 is evident, their kurtosis values are distributed approximately in the same way in almost the same domain, it is an expected behavior since the locations of these channels are very close and by considering the closed-eyes resting-state condition (see also Figure 22), the brain rhythms in the anterior area of the scalp are not so prominent, instead, the alpha rhythm that goes from 7 Hz to 14 Hz registers a higher power spectra magnitude around these limits, and is more noticeable in the occipital area covered by the channels PO5 and PO4. This could be the reason why the kurtosis distributions are not as related to each other explaining the characteristic dynamics of the brain activity process considering the frequency components that arise at the alpha frequency range.

Even though there exist small differences between the distributions, their expected means (dashed green lines) are values that are present in all the distributions; the mean of the F1 kurtosis distribution is a value found within the F4, PO5, and PO4 densities, and the same occurs for the remaining permutations of the expectancies. This can be generalized, and if more channels are compared, there will be subsets of distributions that are closer than others.

Thus, it sets a starting point to look at how different the kurtosis distributions are considering their most probable value and if they are present or not in the estimated densities from the remaining signals of an EEG recording.

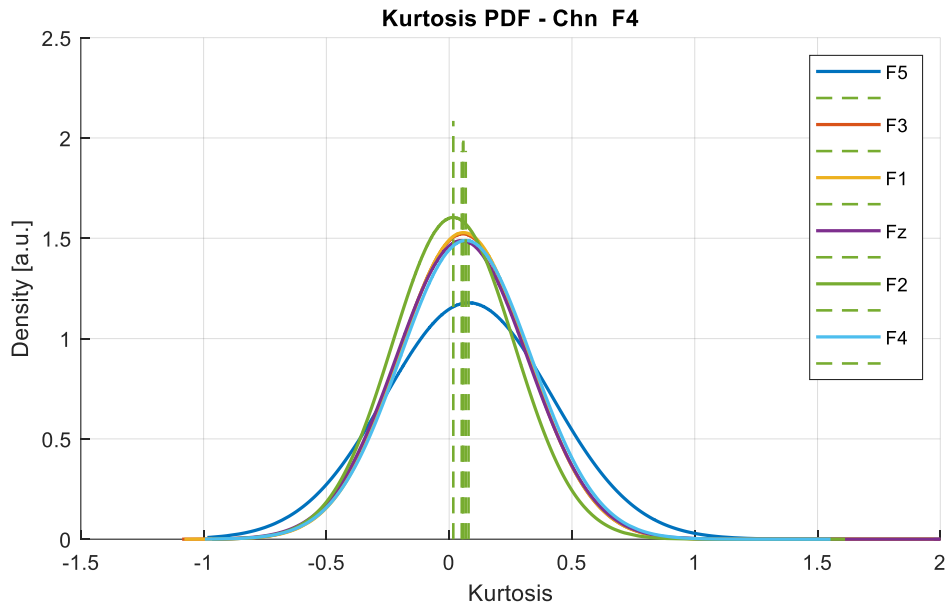


Figure 22. Kurtosis distributions from frontal channels F1, F2, F3, F4, F5, and Fz (S10 - R2). Observe that the densities are very close to each other suggesting similar EEG processes from different locations in the same region. Complementary graph w.r.t Figure 21.

B.1. Kurtosis variance

By examining the kurtosis expectancies and the distributions it is introduced the basis of an action course to compare the segment durations in a block (all at once) among the channels' signals of a dataset. Seeing the distributions plotted in Figure 23 that are estimated from all the channels composing the EEG recording taken from subject 10 in closed-eyes resting-state condition, it can be observed that the generalization presented previously holds. It was said that the expectance value of an arbitrary distribution is part of any of the remaining kurtosis PDFs, however, it is having a lower or higher likelihood of being observed following the point of view of the process obtained from a channel.

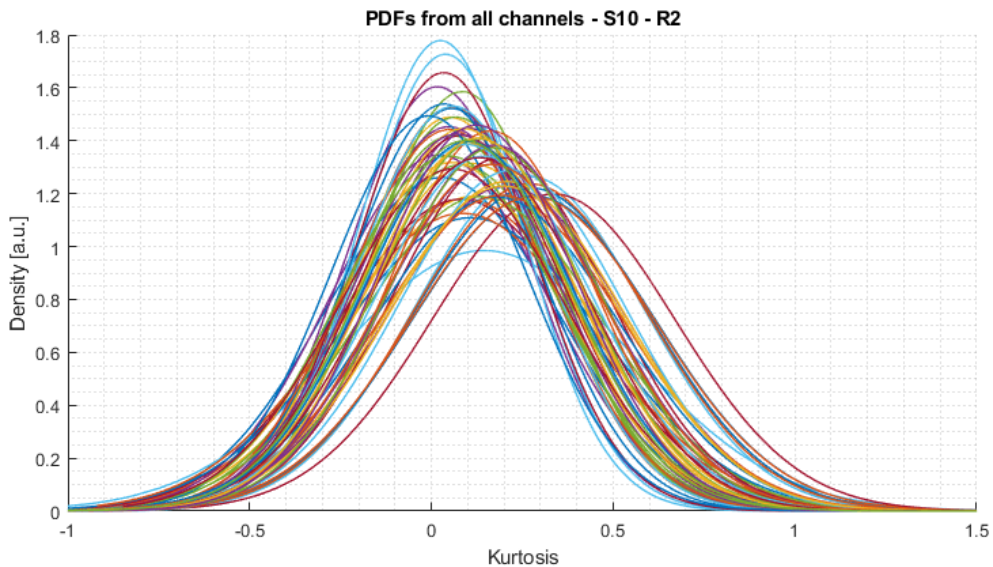


Figure 23. Kurtosis distributions from all the signals acquired from S10 in R2.

In this way, a better representation of the data would be expressed in terms of the spread of the kurtosis data obtained from the different segment durations among the different channels that compose the EEG recording. Since it was demonstrated that the combination of the kurtosis samples considering different segment durations provides a gaussian PDF for any channel (see Figure 20 and Figure 23) and that such representation is the overall distribution of the $K_{i,chn}$ vectors combined, then, it is possible to come back to the single $K_{i,chn}$ densities and estimate the dispersion that exists on each of these vectors.

In order to show the kurtosis dispersion obtained from the distributions $K_{i,chn}$, the heat plot depicted in Figure 24 shows the estimation of the variance of the kurtosis vectors considering a segmentation procedure with a $W_L = 1s$ and $N_w = 10$. Each row is referred to a channel that composes the dataset and the columns are the estimated variances of the kurtosis according to the segment duration under analysis ($1s \leq w_l \leq 10s$). The lower the variance the brighter the color, from yellow to dark blue. The color code is relative to the maximum and minimum values among the variances.

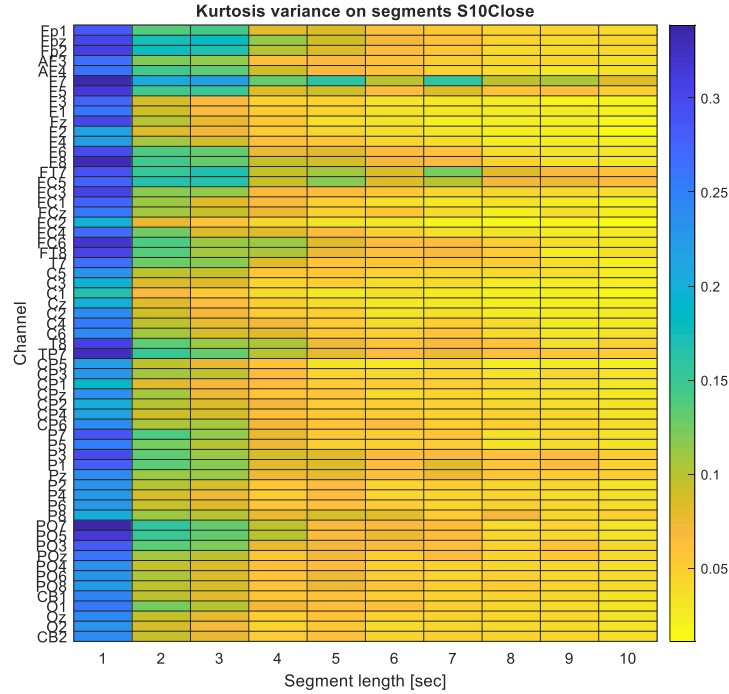


Figure 24. Kurtosis variance presented as a heat plot. From signals of the dataset of S10 in R2.

By considering the variance of the Kurtosis to account for the spread of the values at different windows' durations, the outcome is twofold:

1. The kurtosis vector (K_i) generated for each channel is then re-expressed as a single value representing the deviation from the mean considering a specific segment length. In further processing, this is computationally less expensive than a vector of t/w_{li} components. The data re-expression can be explained as follows:

$$K_{i,chn} \in R^{t/w_l} \rightarrow K_{\sigma_{i,chn}^2} \in R^1, \forall Chn = \{1, \dots, M\} \quad (29)$$

2. Similar means and variance values from different length sizes permit us to compare the dispersion that exists on a dataset containing different signals, as it was introduced earlier and exemplified in Figure 21-Figure 22.

Hence, since the kurtosis distributions and their spreads are similar across channels (Figure 22), it is possible to design a searching approach to find a variance range as short and small

as possible and common for most of the channels, so that the kurtosis value is close to its expected mean according to each signal's kurtosis density. And to do it, the kurtosis variances ($K_{\sigma_{i,chn}^2}$) compiled in matrix form (the array employed to generate the heat plot of Figure 24) are used to estimate the probability density function that groups the data of the kurtosis variances for all the channels in a recording.

As an example, Figure 25 shows the PDF derived from the kurtosis variances obtained at each segmentation setting considering windows going from 1 to 10 seconds, these data come from the same dataset that has been discussed in the last sections (S10 – R2). The distribution follows a Chi-square shape.

From the variance distribution, it is now necessary to define a searching strategy to find a variance range as short and small as possible and common for the majority of the channels from the dataset, such that the kurtosis expectances be close to each other in that range so that similar stationary characteristics are expected to be shared among such channels.

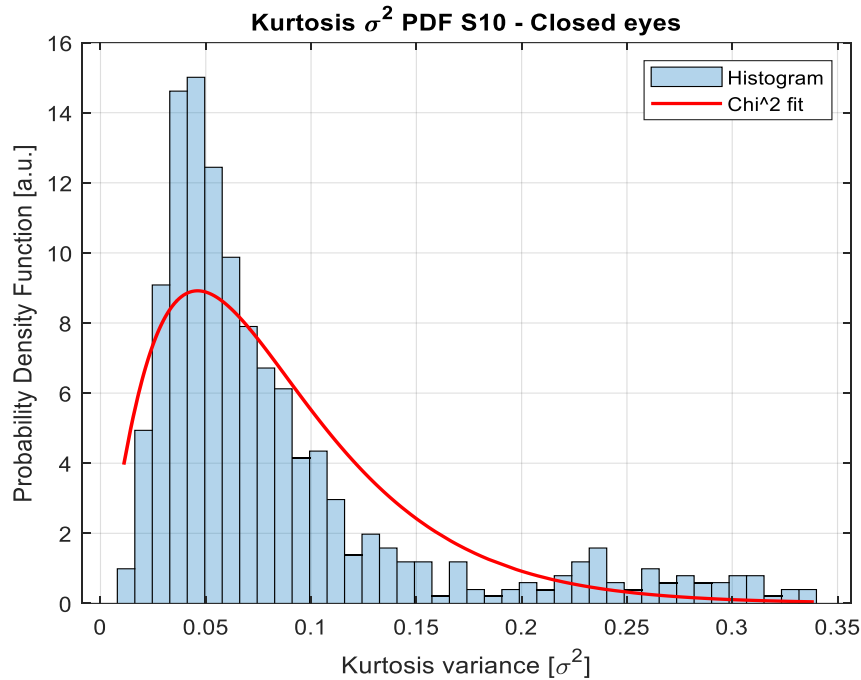


Figure 25. Kurtosis variance density (K_{σ^2} PDF), estimated by considering the array of kurtosis values from the 60 channels that compose the S10 – R2 dataset.

In summary, by finding an appropriate variance range then it is hypothesized that the number of channels sharing the kurtosis variance in that interval is maximized, and common segment durations exhibiting the same variance across the EEG signals are found in the process. As a consideration, the segmentation, the statistical feature calculation, and the searching strategy can be performed by considering different window configurations for short segments ($w_{li} < 1s$) and long segments ($w_{li} > 1s$).

Up to this point, the segment duration has not been discussed. There were described some examples considering long segments, but in the following sections, it is expected to analyze in more detail the differences between short and long windows according to the searching strategy and the outcomes that are produced from them.

However, it would be useful to contemplate that after this point if the segmentation is performed by using longer windows, then, the kurtosis estimation would be more reliable, but the segment duration would be increased, which can bring some advantages and disadvantages, for instance:

- It supposes a tradeoff between the reliability of the expected value of kurtosis and an appropriate segment length that includes the dynamics behind the EEG process.
- The longer the window the longer is the EEG recording needed to perform effective connectivity analysis, which also requires the use of higher model orders to do the fit of the MVAR model.
- Depending on the kind of brain process we are investigating, shorter windows would be needed to capture the highly dynamical behavior of the process in consideration, for instance, cognitive processes have frequencies higher than 15 Hz, such rapid changes need shorter segments to capture appropriately the process in consideration.
- In the opposite case, if the objective is to observe and study brain activity in deep sleep and drowsiness, the frequency range is 0.5 to 7 Hz which requires windows of durations larger than 2 seconds.

By analyzing the results and evaluating the performance of the segment selected according to the approach described in this work, the idea is to address these inquiries and answer them according to the objective of providing a pre-step for data segmentation in the effective connectivity framework.

5.1.2. Stationary segments: The searching strategy

In order to explain the searching procedure, let us start by looking at the kurtosis variance distribution estimated from the EEG recording of the subject 2 (S2) during opened eyes resting-state condition (R1). Figure 26 shows the K_{σ^2} density and the fitted Chi-square (χ^2) distribution (red dashed line). The density was derived from the matrix of values represented by the heat plot shown in Figure AN 1.

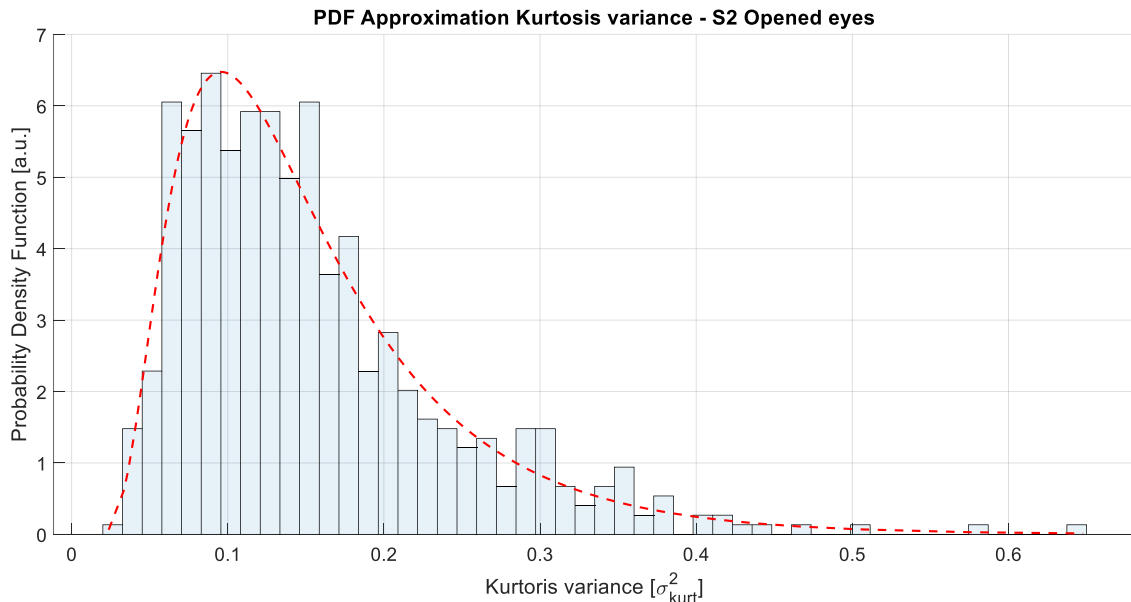


Figure 26. Kurtosis variance PDF. (S2 – R1).

Then, the K_{σ^2} matrix of the S2 – R1 dataset organizes the kurtosis variances with respect to the basis segment length $W_L = 1s$ (w_{li} , for $i = \{1, \dots, 10\}$) for each channel of the EEG recording. In this way, the searching algorithm is defined as follows:

Input: K_{σ^2} matrix

Variables: low_thr – Lower threshold variable
 $high_thr$ – Higher threshold variable
 max_pk – Max peak of the distribution
 $min_var[1, M]$ – Vector with the lowest K_{σ^2} of each channel
 $max_var[1, M]$ – Vector with the highest K_{σ^2} of each channel
 $metrics$ – Vector with the metrics of the searching process

User defined variables:

$threshold_1$ – No. of channels that have at least one segment within the range
 $threshold_2$ – Highest relative variance mean w.r.t $max_var[1, M]$ vector
 $threshold_3$ – Max. Number of iterations performed by the searching method

1-> PDF estimation

- a. MLE for a Gamma distribution $\equiv \chi^2$ distribution
- b. Gamma fit

2-> Find $max_pk = \max(\text{Gamma}(\alpha, \beta))$

3-> $low_thr = high_thr = K_{\sigma^2}(max_pk)$

4-> $min_var[1, M] = \min K_{\sigma^2}, \forall \text{chn} = \{1, \dots, M\}$

$max_var[1, M] = \min K_{\sigma^2}, \forall \text{chn} = \{1, \dots, M\}$

5-> Loop

$low_thr = low_thr - 0.001$

$high_thr = high_thr + 0.001$

6-> Find σ^2 values from K_{σ^2} s. t. $\rightarrow low_thr \leq K_{\sigma^2} \leq high_thr$

$temp_K_{\sigma^2} = low_thr \leq K_{\sigma^2} \leq high_thr$

7-> Sort matrix $temp_K_{\sigma^2}$ w. r. t channels

8-> Select the segment with the lowest duration per channel

$temp_sel[1, M] = \text{selected segments}$

9-> Relative variance calculation

$rel_var[1, M] = temp_sel[1, M] ./ max_var[1, M]$

$sum_chn[1, N_w] = \text{sum of channels per } w_{li} \text{ within variance range}$

10-> If: $\text{count}(temp_sel[1, M]) \geq threshold_1$

$m_var = \text{average}(rel_var[1, M])$

11-> If: $m_var \leq threshold_2$

$$metrics = \begin{bmatrix} m_var \\ low_thr \\ high_thr \\ sum_chn \end{bmatrix}$$

-> Until k iterations $> threshold_3$

The variance range searching strategy shown above receives as input the kurtosis variance matrix K_{σ^2} of size $M \times N_w$ (channels \times number of segments), each of its components corresponds to the kurtosis variance of one of the EEG signals after segmentation at a specific window length.

The user-defined variables are used as processing parameters, and as described in the algorithm, they are used in specific cases:

1. $threshold_1$ – Number of channels that have at least one segment (expressed by the kurtosis variance at a window duration - $K_{\sigma^2, w_{li}}$) within the range defined by the searching interval: $low_thr \leq K_{\sigma^2} \leq high_thr$. If the number of channels is lower than the threshold, then, the algorithm restarts the searching by setting a new range, wider than the previous one. Since the idea is to find a variance interval which is common for a large set of channels, this threshold sets a boundary to skip computations in the case searching conditions are not met.
2. $threshold_2$ – Highest relative kurtosis variance average. After averaging the rel_var vector, the result expresses the mean of the kurtosis variance relative to the maximum variance found on each signal. If this threshold is exceeded it means that the variance range which is common for the channels (on average) is very similar to the expectance of maximum kurtosis variances, which could represent that the searching space covers most of the K_{σ^2} density.
3. $threshold_3$ – Maximum number of iterations performed by the algorithm. If this bound is not set, the algorithm runs forever. So, this corresponds to a stop threshold.

A practical example of the actual use of the searching algorithm is presented in Figure 27. It is depicted the iterative increase of the searching range defined by the lower and higher bounds of the kurtosis interval generalized as follows.

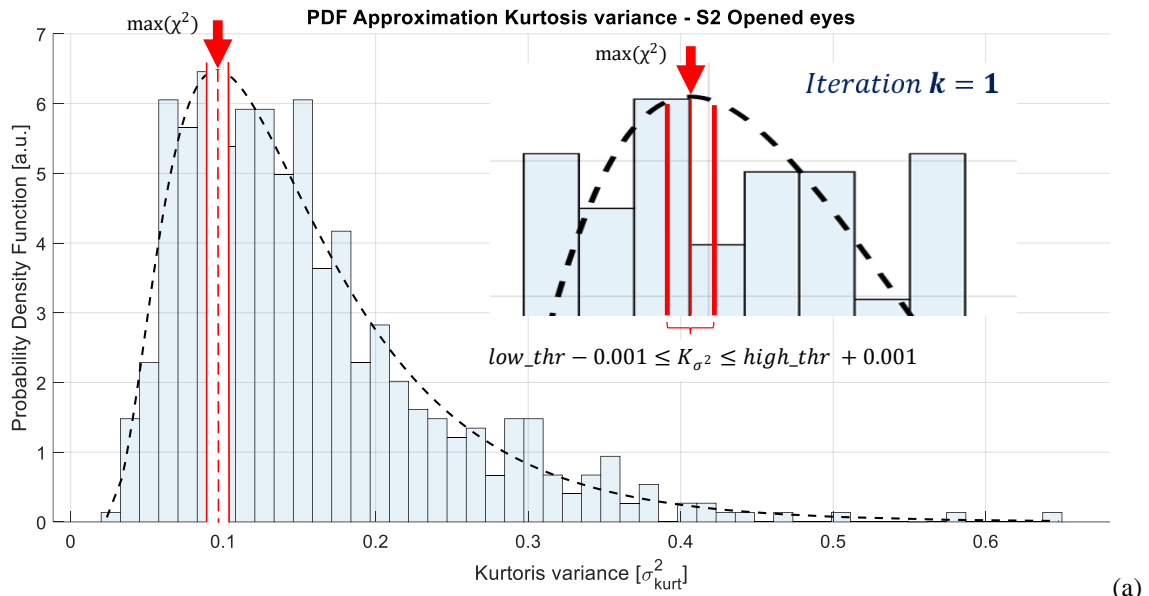
$$low_thr - (k \cdot 0.001) \leq K_{\sigma^2} \leq high_thr + (k \cdot 0.001) \quad (30)$$

Where low_thr and $high_thr$ are the bounds of the searching interval initialized as the K_{σ^2} value associated with the max point of the distribution fitted from the data (i.e. $\max(\chi^2)$). The index k refers to the iteration step inside the loop. Hence, the expression in (30) provides the updating rule of the variance range to search for at the step k .

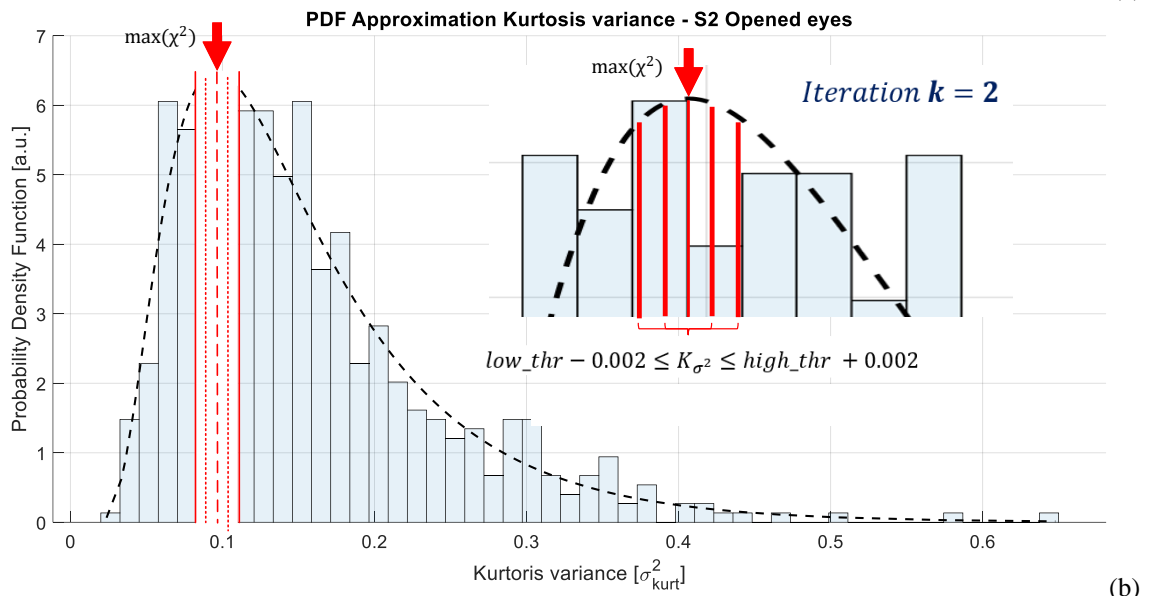
By observing Figure 27.a, the searching range corresponds to $low_thr - 0.001 \leq K_{\sigma^2} \leq high_thr + 0.001$. As this is a real example, the kurtosis variance interval is $0.099 \leq K_{\sigma^2} \leq 0.101$, for the $\max(\chi^2) = 0.1$. The searching algorithm then starts to look for the segments identified as the ones which exhibit a variance magnitude inside the interval. As there can be more than one window per channel whose dispersion is found within the range, the result of the searching is organized in vector form from lower to higher w.r.t each of the channels of the dataset.

Such an arrangement permits to find which are the lower segment durations for the set of channels that exhibit a K_{σ^2} within the searching-interval limits (if there is any), and so, the lowest segment durations on each channel under those searching conditions are grouped to form the vector $temp_sel$ (line 8 of the algorithm) which is employed to compute the relative kurtosis variance considering the highest values of the K_{σ^2} on each channel. The calculation results in the rel_var vector (line 9) whose components are the proportions of the kurtosis variances computed as the amount of the selected variance from the channel over the highest magnitude of the variance.

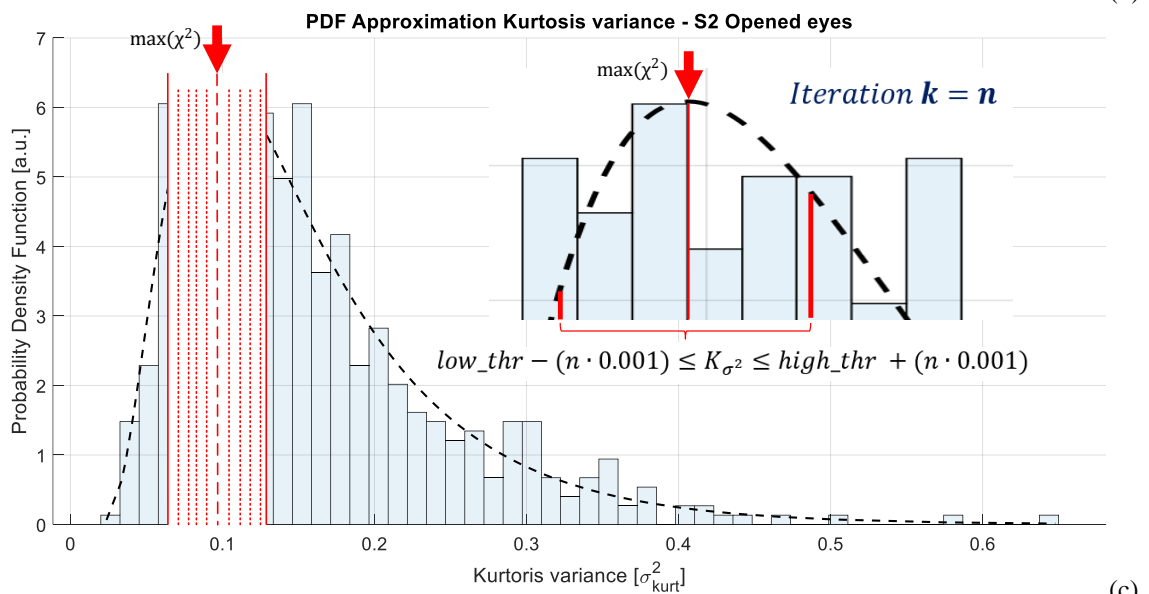
As explained earlier, it can happen that only a small subset (or none) of the channels contains at least one segment configuration whose kurtosis variance is found within the range. In such a case, it is necessary to account for the number of signals that have a positive result from the searching, since the idea is to maximize the number of channels that exhibit a small variance range. The vector sum_chn vector (line 9) sums the channels with a positive searching result and organizes them with respect to the window length of the kurtosis variance matrix.



(a)



(b)



(c)

Figure 27. Searching algorithm at different iterations.
a) iteration $k = 1$, b) iteration $k = 2$, c) iteration $k = 3$.

Furthermore, if the number of channels which do not have any segment with a K_{σ^2} within the searching-limits is higher than the $threshold_1$ then, the loop is reestablished, and the interval is updated to initiate the searching again. If, on the contrary, the number of channels is lower than the threshold, the process continues with the computation of the average of the relative kurtosis variance from the rel_var vector (line 10). Finally, if the average is small, it means that the selected segments have a kurtosis variance which is lower than the $threshold_2$, and by that, it is guaranteed that both the K variance range is small (i.e. the kurtosis dispersions are close to each other as well as the kurtosis values w.r.t their expectancies) and the number of channels exhibiting similar kurtosis is maximized considering the shortest window duration as possible.

In this way, after the evaluation of those conditions, some metrics related to the vectors that were generated during the process are combined and as result, it is generated an array comprising the values in consideration and then it is updated as long as the searching process keeps going.

From this algorithm, it is clear that it can be generalized with subtle changes to other recordings to provide a framework that considers all the kurtosis variance matrices so all the datasets can be processed and the results for all of them are obtained.

Figure 27 b-c, shows schematically how the searching range is extended as long as the iteration steps are increased. Since the loop is done indefinitely, a stop flag is set to finish the searching after a $threshold_3 = 1000$ iterations, which would be enough to cover the whole K_{σ^2} domain from the distribution, considering the $\Delta\sigma^2 = 0.001$.

A. Stop criteria.

The stop criteria in the searching approach can be formalized as follows considering the thresholds.

- The $[\arg \min(K_{\sigma^2})]$ subject to a channel chn , and the variances selected from the channels $[\arg \text{sel}(K_{\sigma^2})]$ combined in the vector $temp_sel$, can be expressed as relative magnitudes from the maximum variances $[\arg \max(K_{\sigma^2})]$ on each channel. Hence:

$$K\sigma_{selected}^2 \leq \frac{1}{N_{chn}} * \sum_{i=1}^{N_{chn}} thr_i \quad (31)$$

$$thr_i = G * \left(\arg \max_{chn \ i} \sigma^2 \right), \forall G \in \{0,1\} \quad (32)$$

- For instance, if $G = 0.3$, it means that only 30% of the selected kurtosis w.r.t the maximum kurtosis in the channels is allowed to continue the processing.

$$K\sigma_{selected}^2 \leq 0.3 * \left(\arg \max_{chn \ 1:M} \sigma^2 \right)$$

B. Searching domain

By considering the vectors $min_var[1, M]$ and $max_var[1, M]$ which contain the lowest and highest kurtosis variance values channel-wise respectively, it is possible to construct a searching domain limited by these bounds.

Figure 28 shows the searching domain as a function of the kurtosis variances expressed by the channels that compose the dataset. The $\min \sigma^2$ and $\max \sigma^2$ values that result in the red and black plots, set the limits of the possible values that segments (w_{li}) can exhibit regarding its stationarity measured in terms of kurtosis. In this way, intermediate values can be obtained from non-boundary segments, and by using the searching approach, close kurtosis variances across

the channels can be found.

For the case in consideration (subject 2 EEG recording in opened-eyes resting-state condition), after setting the relative kurtosis variance mean of the selected channels every 10% and increasing it from 20% to 70% of the maximum kurtosis variances, the algorithm can select the segment lengths whose K_{σ^2} average is not larger than the relative proportion expressed by each percentage threshold. As result, Figure 28 shows the kurtosis variances after the selection according to the percentage limits. These correspond to the K_{σ^2} values found to be expressed by the shorter possible segment on each channel considering a specific percentage bound. In accordance, the K_{σ^2} magnitude meeting the conditions is color-coded according to the percentage limits, so each color indicates the variance of a segment within the searching limits such that the relative kurtosis variance mean is close to the percentage threshold.

As can be observed, the lower the percentage threshold the closer the selected K_{σ^2} values are from the min σ^2 bound, however, as can be noted also the lesser number of channels that meet the requirements are found, i.e. approaching the limit most channels do not have any value plotted on the graph according to the percent bound. Consequently, by increasing the searching limits (Eq. (30)) the results are translated in the increment of channels with similar characteristics considering higher kurtosis values, and so, if the graph is observed for the 30% threshold, it can be seen a considerable number of channels compared to the 20% limit and maintaining K_{σ^2} values close to the lower bound. The same happens for 40% and 50% limits, however, the dispersion among the channels also starts to be evident.

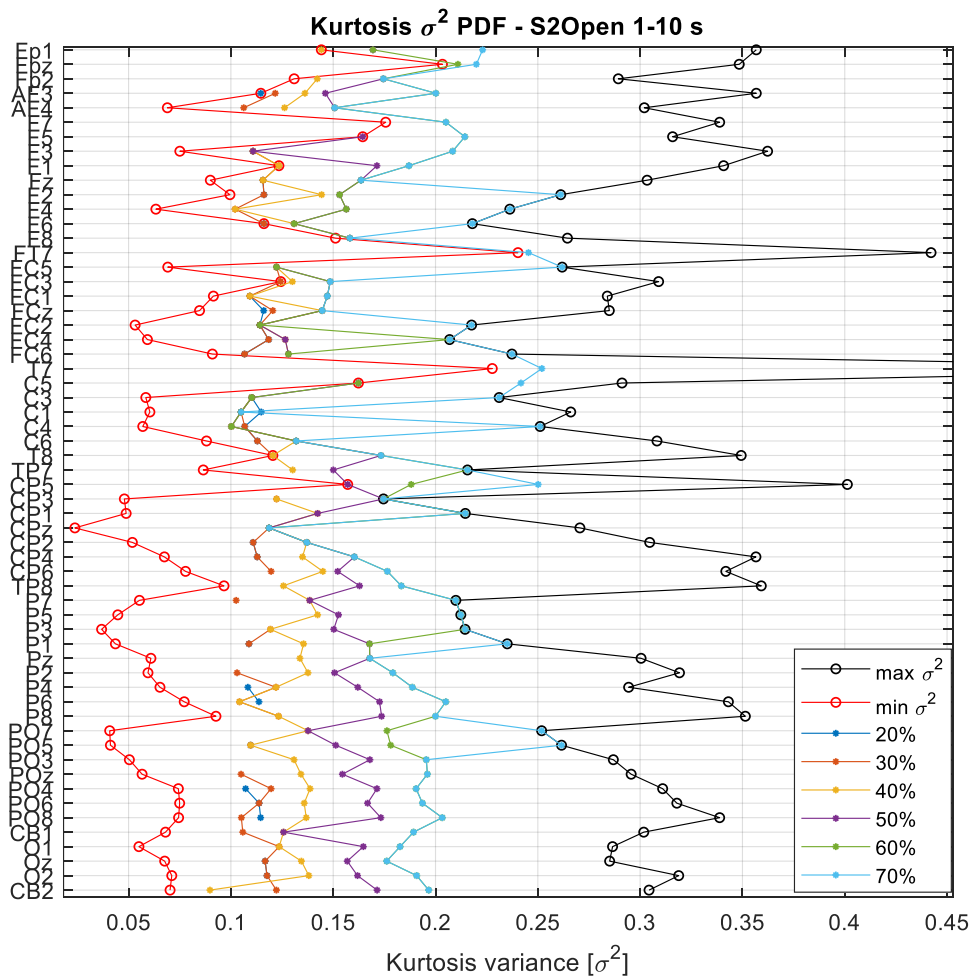


Figure 28. Kurtosis variance searching space bounds and relative variances. (S2 – R1)

For higher percentage limits, as for 60% and 70%, the dispersion of the kurtosis variance values is very large, however, in those cases a larger number of channels share the variance interval in consideration and are approaching the higher bound ($\max \sigma^2$) which suggests that the searching interval is very wide and that it is considering almost all the values from the distribution.

Figure 28 shows graphically the definition of the searching space as well as the kurtosis variance values considering different thresholds with respect to the maximum relative K_{σ^2} found at each channel for a particular segmentation strategy, in this specific case, considering a $W_L = 1s$ and $N_w = 10$. The color-coded plots show which is the kurtosis variance within the searching interval that a channel exhibits if it exists. Such representation permits us to have a sense of how close the kurtosis variances across the channels are and also depicts how many channels meet the conditions at that interval. However, it would be also useful to check the interval limits from which such results are found. In this way, Figure 29 comprises the searching intervals at the different percentage thresholds from which the channels expose the values within the searching domain.

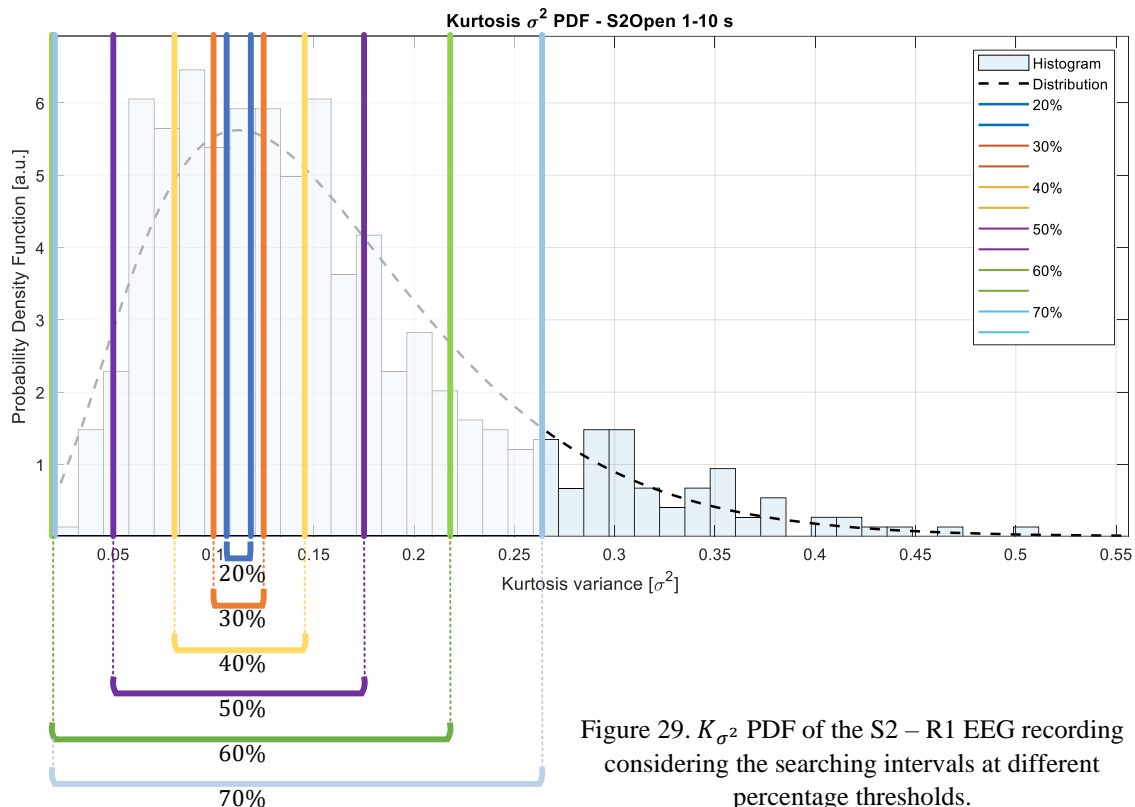


Figure 29. K_{σ^2} PDF of the S2 – R1 EEG recording considering the searching intervals at different percentage thresholds.

As can be observed from the searching strategy, by defining sequentially higher percentage thresholds the searching interval is increased and covers a wider area from the density. By covering a larger area, a greater number of segments on each channel meet the conditions for selection, which at the end after the ordering procedure would result in the selection of the minimum variance segment of each channel ($\min \sigma^2$). That is why a sequential increase of the searching interval is performed by the algorithm, and restricting the relative quantity of kurtosis variance allows to analyze which area from the density is being covered, how many channels are being identified in those limits, and which are the segments that are contained in the searching range.

The searching domain and the corresponding limits related to the relative proportions of the maximum kurtosis variances bring an analysis tool from which it is possible to provide an informed decision on how to select the minimum segment duration shared for most of the

channels, which guarantees similar stationary characteristics among the signals. By considering different percentage thresholds, it is possible to check graphically the areas covered by the searching interval, and depending on the type of segmentation, either for short ($W_L < 1s$) or long ($W_L \geq 1s$) windows, the selection of the segment duration is derived from the statistical characteristics coming from the dataset, so overall it can be considered as a non-parametric method for that purpose.

The information coming from this procedure is summarized in matrix form and corresponds to the last step of the algorithm: the definition of the *metrics* array (line 11). Table 4 comprises the searching interval associated with the relative kurtosis variance expressed in percentage and the corresponding number of channels that meet those searching conditions with respect to the segment durations from 1 to 10 seconds. These data are derived from the searching space and the kurtosis density described in Figure 28 - Figure 29 respectively.

Table 4. Segment durations and number of channels sharing kurtosis variances according to relative percentages.

	10%	20%	30%	40%	50%	60%	70%	80%	90%	100%
Lower limit	0.1096	0.1066	0.1006	0.0796	0.0496	0.0076	0	0	0	0
Upper limit	0.1156	0.1186	0.1246	0.1456	0.1756	0.2176	0.2636	0.3016	0.3416	1.1136
1 sec	0	0	0	0	1	7	22	35	49	59
2 sec	2	2	6	15	31	55	59	59	59	59
3 sec	1	2	3	16	36	48	53	55	57	59
4 sec	3	6	9	25	38	48	54	55	57	59
5 sec	3	6	13	30	47	51	54	55	57	59
6 sec	1	5	10	34	50	53	54	56	56	59
7 sec	1	5	10	31	50	52	55	57	57	59
8 sec	4	5	11	25	50	55	57	58	58	59
9 sec	1	2	5	19	46	53	55	56	57	59
10 sec	2	6	13	27	47	57	57	58	58	59

By having a close look at the data from Table 4, it is possible to check what was explained before. As long as the searching interval is increased, the number of channels exhibiting a kurtosis variance in that range also increments. As the purpose of the algorithm is to maximize the number of channels by defining a short and small variance range common for them, from the table, it is possible to perform an informed decision for the segment selection.

As can be observed, the number of channels in the searching ranges lower than 30% is very low compared to wider searching intervals. By considering the limits on the kurtosis density from Figure 29, 40% and 50% ranges cover the most probable kurtosis variances of the whole dataset. At 40% considering a window length of 4 seconds, only 25 channels share the kurtosis variance from that range, however, if the 50% is then considered the number of channels increases to 38 which is ~63% of the total of channels from the dataset. Moreover, by considering a segment window of 5 seconds, 30 and 47 channels are found in the variance ranges of 40% and 50% respectively. In this way, by looking at the K_{σ^2} PDF using a segment of 5 seconds allows selecting 47 channels (~78% of total channels) sharing a kurtosis variance in the range of $0.0496 \leq K_{\sigma^2} \leq 0.1756$, which comprises a probable proportion of the density.

After performing the searching in the kurtosis variance domain, it is then possible to return to the kurtosis space after the selection of the window duration. For the example that has been

explained along the last sections, considering Table 4, there was selected a segment length of 5 seconds, at a kurtosis variance range of 50% of the maximum variances explained by the segments. From this, there were found 47 channels meeting this criterion. Figure 30.b. shows the kurtosis distributions of each of the channels within the 50% searching interval ($0.0496 \leq K_{\sigma^2} \leq 0.1756$), the blue distributions correspond to the ones inside the range while the red plots are the densities from the channels with higher variances.

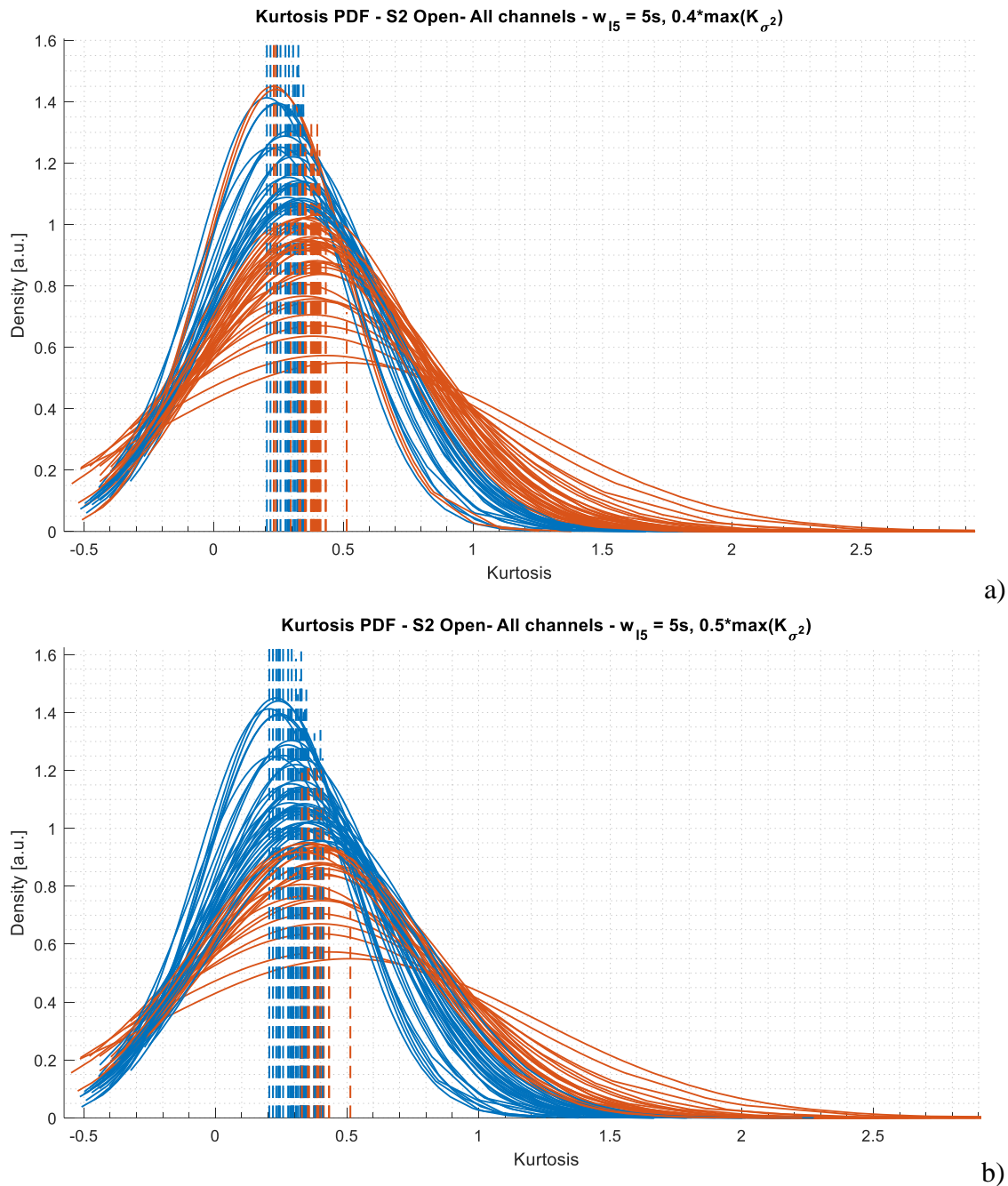


Figure 30. Kurtosis distributions of all the channels composing the S2 – R1 EEG recording for a segment duration $w_l = 5$ s. In blue, K PDFs inside the interval defined by a) 40% the relative max (K_{σ^2}), b) 50% the relative max (K_{σ^2}). In red K PDFs outside those limits.

The 40% corresponding to the interval $0.07957 \leq K_{\sigma^2} \leq 0.14557$ allows to perform the discrimination of the kurtosis PDFs shown in Figure 30.a. As the searching space is reduced,

the dispersion displayed by the expectances across channels also decreases (dispersion on the location of the expectance values of the blue distribution), however, the number of channels is not as high as in the previous case.

The reduction of the kurtosis dispersion observed in Figure 30.a among the channels is derived from the searching interval restricted to the relative variance expressed in percentage from the K_{σ^2} domain, and provides a way to maximize the number of channels sharing similar kurtosis values guaranteeing similar dynamical behavior across the signals within a fixed segment duration which can be employed in the calculation of Effective Connectivity.

5.2. The effective connectivity framework

In order to perform the effective connectivity analysis, let us recall the processing scheme that was introduced in the section *What do these works have in common?*. As shown below (recalling Figure 4), this process considers 6 principal steps; the usual signal acquisition and pre-processing treatment (implemented in the same way as explained in the section *Preprocessing*), applied to the EEG signals; the Effective Connectivity measure estimation, from which different connectivity indices can be estimated; the working domain definition either at the channel domain, regions of interest (ROIs) domain or independent components domain considering the estimation of dipoles; then, the generation of surrogate data using phase randomization, bootstrapping or cross validation approaches to sample the original data to estimate the significance of the connectivity measures and calculate the adjacency matrices as the pre-step of the statistical analysis employing ANOVA and the post-hoc tests using Bonferroni correction.

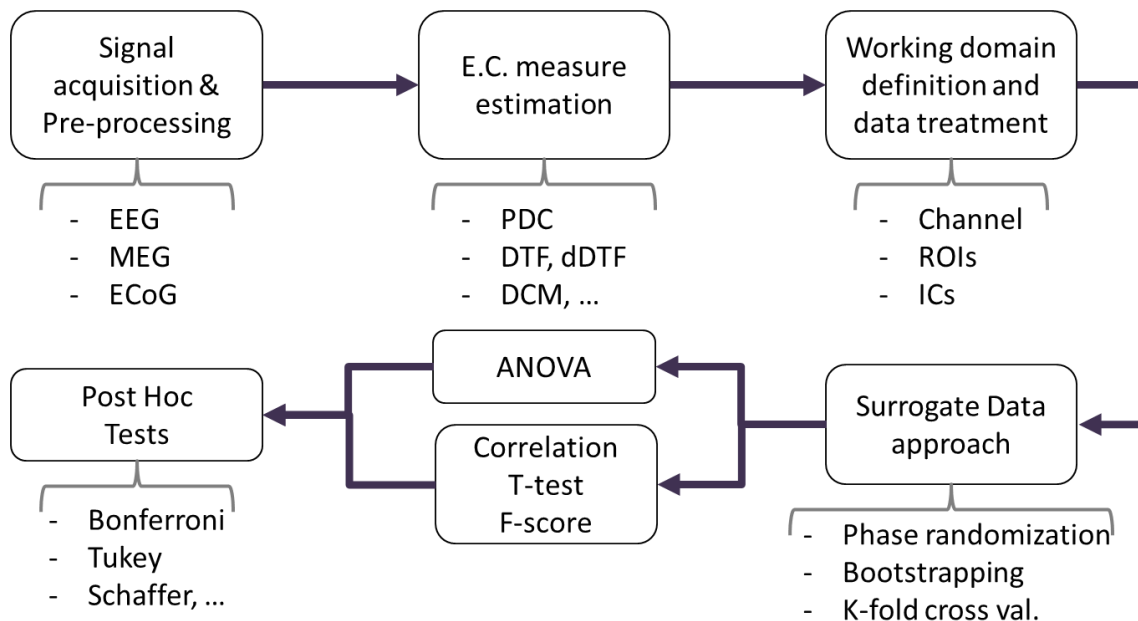


Figure 4. (Recall) Effective connectivity processing scheme.

As final results of this approach there are obtained the statistically significant connections among the nodes that compose the working domain (e.g., ROIs, channels, or dipoles), their amplitudes, and other kind of customizable parameters that can characterize the existent connectivity across the different regions associated to the nodes.

As it was described earlier, this approach is affected by the stationarity characteristics of the window chosen in regard to the fitting process of the MVAR model, from which the connectivity measures are then estimated. As it was shown previously, the window selection depends on the characteristics of the question under investigation for the research work (see

Table 2), however, even though some works investigate similar brain regions, pathologies, and brain conditions during rest, attention, wakefulness/drowsiness, or sleep, the windows employed on such works have durations that are very different from each other.

In this way, by considering the window selection approach based on the stationary characteristics given high-order statistical moments as the one described in this thesis work, it could be possible to obtain the window length that exhibits similar stationarity across the signals composing the EEG recordings of different subjects following the same experiment conditions under analysis. Then, a modification of the processing scheme from Figure 4 is proposed as shown in Figure 5 to account for the window length characteristics and then observe the effective connectivity results for the resting state condition analysis of healthy subjects under eyes-opened (R1) and eyes-closed (R2) conditions.

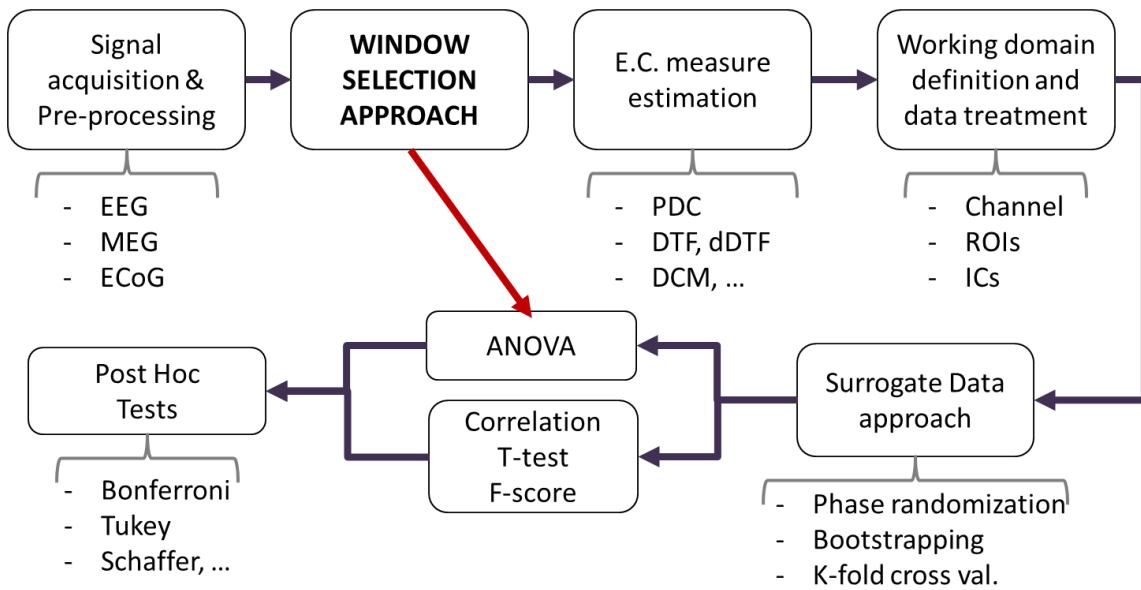


Figure 5. (Recall) Modification on the E.C. statistical analysis to account for the window length.

According to Figure 5, the window selection approach would be an intermediate step that considers the stationary characteristics of the EEG signals. In order to test the influence of the window length in the connectivity process, it is then used as a factor in the statistical analysis, either by performing ANOVA or t-tests, where the interactions of the window length are evaluated to obtain the effects on connectivity.

In accordance with the results obtained from the window selection algorithm as described in the section (see *Selected window durations*); for the short window class, the segment duration for the MVAR fitting process was selected at 400 ms, being the window size that exhibits similar stationary characteristics in the short term. On the other side, durations larger than 1 second were also analyzed and as result, a window length of 4 seconds was obtained as the most common for the EEG recordings from the different subjects in consideration. In this way, to check the influence of the window size in the effective connectivity analysis, besides the windows of 400ms and 4s, there were selected the windows of 2s and 20 s according to the works of Varotto [33] and Olejarczyk [45], who studied resting state conditions in similar settings to the ones explained in this thesis work.

5.2.1. Effective Connectivity estimation

The resting state condition datasets comprised EEG recordings from 10 healthy subjects as explained earlier in the section *EEG Dataset*. In order to perform the window selection approach, there were discarded 4 datasets (from subjects S1, S3, S4 and S7) because there was

a significant reduction on their total durations after performing the stringent data cleaning process.

In this section it is described the effective connectivity estimation, which comprises the statistical significance analysis and uses the same recordings employed for the window selection approach. However, due to the small cohort size translated into a reduced number of samples to perform the statistical analysis, the number of subjects for effective connectivity was increased from 6 to 8, including the recordings from subjects S1, S4 and S7, and discarding S9 since its connectivity amplitudes were out of the normal range for effective connectivity (i.e., they were significantly larger than 1). Hence, the datasets employed for the effective connectivity analysis were (S1, S2, S4, S5, S6, S7, S8 and S10) and they comprised signals that exhibited very similar stationary characteristics as summarized in Table 9.

A. EEG data characteristics:

Each of the selected EEG recordings (S1, S2, S4, S5, S6, S7, S8 and S10) were individually segmented into non-overlapping windows according to the four window lengths defined previously (i.e., 400ms, 2s, 4s and 20s). In this way, there were obtained 4 new segmented data series for each subject at each resting state condition, producing a total of 8 different segmented matrices per subject obtained from the original cleaned EEG recording.

The segmentation procedure was carried out following the total duration of each of the clean recordings and segmenting them into a chain of segments of 400ms, 2s, 4s and 20s. In this way, for instance, considering the S10 recording in opened-eyes condition which has a total duration of 172 seconds (see Table 4), there were produced 430, 86, 43 and 8 segments for each window duration (i.e., 400ms, 2s, 4s and 20s), respectively.

After this, epochs of 25 times the duration of each window length were employed to characterize the connectivity during those periods (except for the 20 seconds segment for which all the segments were employed since the number of signal slices was less than 25). This is done to guarantee the proper fitting of the MVAR model since it produced singular matrices when the total number of windows were employed for this purpose. This establishes a boundary in the epoch duration to perform the fitting process and from it, a characterization of the connectivity in the long-term given the epoch definition is performed.

From this process, there were obtained epochs of 10s (25 windows*400 ms), 50s (25 windows*2s) and 100s (25 windows*4s), respectively. For the window of 20 seconds the epoch duration was different for each subject recording since it was defined according to the original duration of the cleaned version of the recording, so, if on average the duration of all the recordings was 167 seconds, then, the epoch was on average 160s, corresponding to the duration of 8 non-overlapping 20s windows.

In this way, it is possible to characterize the connectivity given the epoch durations, its dynamics given the segment durations and their frequency components contained on the epochs. This process is performed at each resting state condition for the group of subjects considered.

B. Connectivity measures

The connectivity measure in this case, was the DTF, calculated as following the theoretical definitions explained in the section *Typical measures*. This connectivity index was estimated using the SIFT plugin for EEGLAB [68], [69]. The toolbox received as input the data coming from each of the 4 segmented recordings to calculate the connectivity across the channels at

each window length configuration from each subject's recording. As result of the connectivity measure estimation, a 4-D matrix as the one depicted in Figure 31 was obtained, generating an array of size $NChn \times NChn \times NFrequency \times NWindow$.

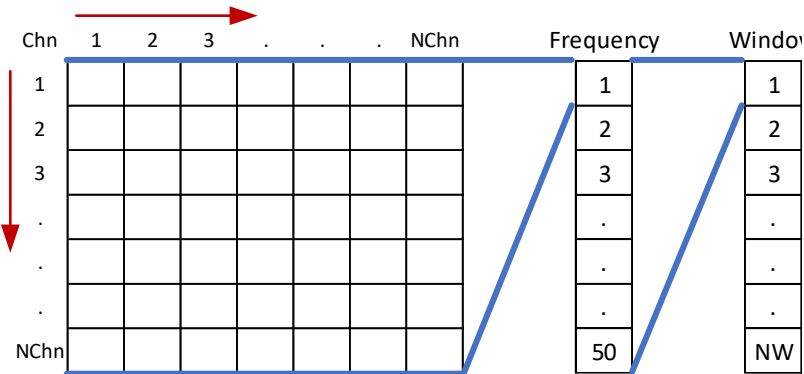


Figure 31. Matrix organization for the connectivity measures of size $NChn \times NChn \times Frequency \times Window$.

$NChn$ corresponds to the number of channels composing the EEG recording, having a maximum number of 62, hence the influence from channel i (at each row) to the channel j (at each column) is contained in the 2D matrix of size $NChn \times NChn$. Since the DTF is a directed measure, the values contained in the lower triangular portion of the $NChn \times NChn$ matrix correspond to the inflows in connectivity from the pair of channels i, j . Likewise, the outflow is masked in the upper triangular part of the matrix.

The $NFrequency$ is the number of frequencies considered for the connectivity estimation, for this case the frequency range considered was 1 - 45 Hz, given the band-pass filtering stage performed during the pre-processing, so each entry of the frequency page of the 4D matrix gathers the connectivity measures across all the channels (i, j) at the specified frequency (each index at the corresponding page representing the connectivity at a frequency f , increasing in steps of 1; e.g., index 12 corresponds to the connectivity at the frequency of 12 Hz). Finally, each window index (i.e., the temporal reference along the epoch) going from 1 to NW comprises the connectivity information of the frequency bandwidth (i.e., 1 to 45 Hz), defining the dynamical variation over time of the connectivity values on the epoch.

The 4D matrix of size $NChn \times NChn \times Frequency \times Window$ comprises the connectivity values obtained for a subject at a specific resting state condition. Since the window length was previously defined as well, then the $62 \times 62 \times 50 \times NW$ array of DTF values provide the connectivity information at each frequency obtained at every segment composing the epoch that has a size of NW (10s, 50s, 100s and ~160s for each window length respectively). Since the idea is to characterize the alpha and beta frequency bands, then, the average of the components on those ranges (i.e., the average on the third dimension of the 4D DTF matrix over the pages [7 – 13] Hz, and [14 – 25] Hz, respectively) is performed, and results in two different arrays of size $62 \times 62 \times NW$ each, characterizing the connectivity for the alpha and beta frequency bands respectively. By doing this, the connectivity characteristics are now sorted by those frequency ranges at each window length partition (i.e., 400ms, 2s, 4s and 20s) thus allowing to group them considering the results obtained for each subject. Then, the resulting matrices from each recording are concatenated forming a new matrix of size $62 \times 62 \times [8 * NW]$ (8 subjects * number of windows).

Then, a second average step in the 3rd dimension of the matrix is performed, and a single 2D array is obtained, it characterizes the overall effective connectivity over a specific window length. This process is performed for each of the selected window segments producing the final 2D matrices employed to perform a statistical analysis (e.g., ANOVA or t-test) to establish the significant effective connections of the alpha and beta frequency bands, giving as result the so-called adjacency matrices.

C. Surrogate data

The significance of the connections is established by generating surrogates of the original data considering the phase randomization of the data series as explained by the Theiler algorithm [70]. This procedure consists of employing the clean EEG recordings and generating from them a set of sampled copies of the frequency data that contain randomly shuffled sample points from the original series, then they are transformed back in the time domain. By doing this process, it breaks any phase relationship existent in the new copies while maintaining the amplitudes of the original source. This process generates a number of shuffled series (usually 100) and then they are used to estimate the connectivity patterns from which surrogate connectivity matrices at each window duration are estimated. After this, a t-test is performed by comparing the connectivity matrix coming from the original series and the surrogate ones, establishing the significance of the connections, and providing the adjacency matrices for statistically significant values.

D. Adjacency matrices

The adjacency matrix is an array that encodes the directed or undirected relationships of a group of nodes that compose a network. For instance, given the high dense array of electrodes of the EEG cap containing 62 channels in our case, its adjacency matrix is a 62×62 array that contains the one-to-one connectivity relationship among the electrodes. By construction, the DTF matrices obtained in the previous stages provide the adjacency matrices at each frequency of every window that composes an epoch. Then by performing the t-test across the time dimension at a specific frequency range like the alpha (i.e., testing the connections that remain significant over the whole epoch in the band of 7 – 13 Hz) and setting up a threshold of significance, e.g., $\alpha = 0.05$, the effective connections of the adjacency matrix that are not statistically significant ($p > 0.05$) are set to 0, providing the directed relationships that are considered as meaningful statistically.

From this 2D representation of the significant values of the adjacency matrix, a network is built by mapping the indices of the array as the nodes that compose the network of 62×62 channels, from the statistical test, the significant connections that remain are the ones that define the connectivity diagram from the channels. In Figure 32, there are depicted the adjacency matrices resulted from this process for all the windows considered at each resting state condition for the alpha band.

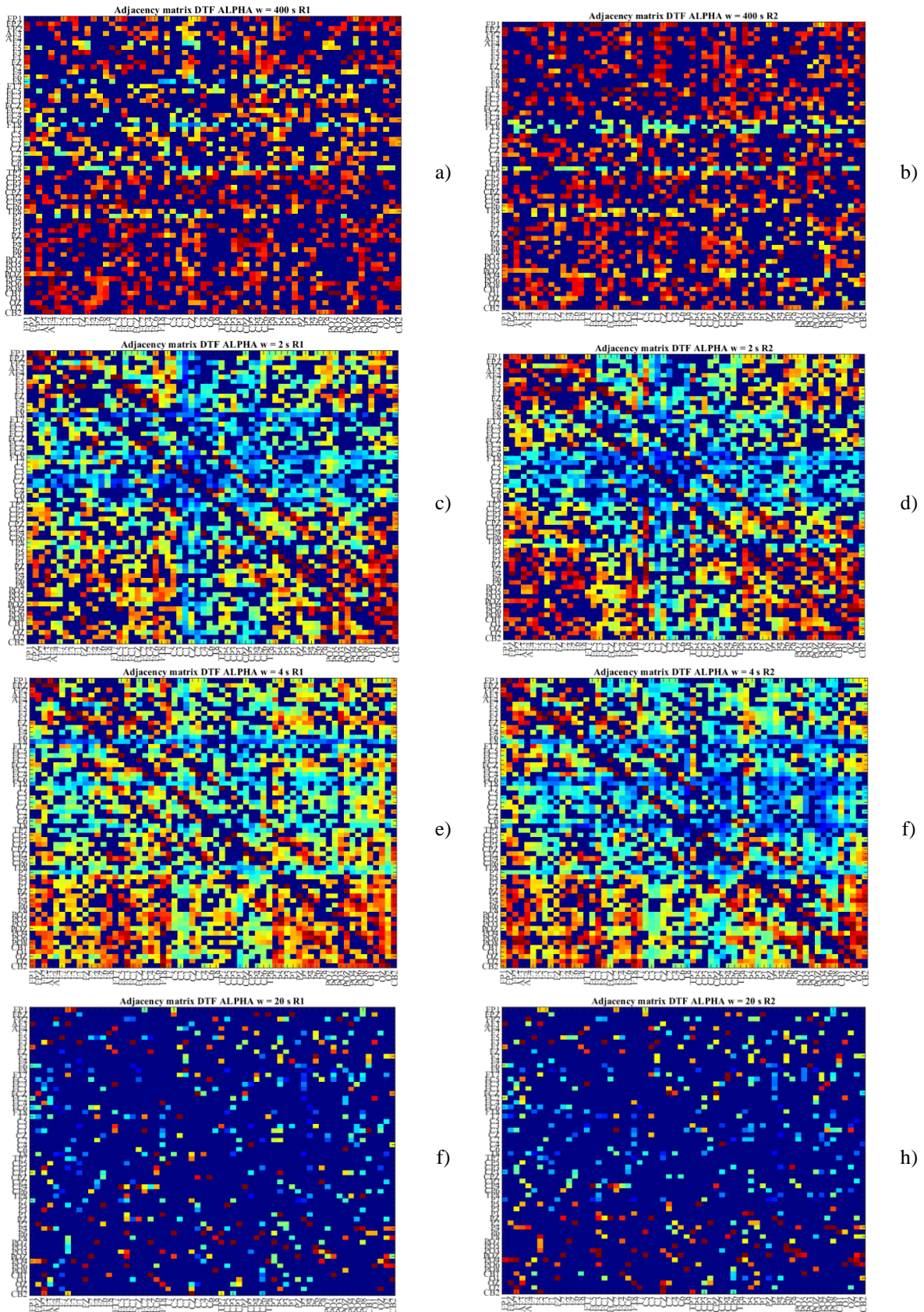


Figure 32. DTF adjacency matrices for each window duration (400ms, 2 s, 4 s, 20 s) during eyes open (a, c, e, g) and eyes closed (b, d, f, h).

The amplitude of the connections is represented by color, going from dark blue (minimum) to dark red (maximum). In this way, the connections that have higher amplitudes can be recognized visually from the adjacency matrices.

The first elements of the adjacency matrices (from top to bottom or left to right) correspond to the nodes located in the frontal part of the EEG cap according to the topographic distribution of the electrodes. In this way, the elements in the central part of the array are related to the electrodes in the central region and the last electrodes to the posterior area. In this way, from the adjacency matrices it is possible to observe some clusters of electrodes that exhibit connections with high amplitudes incoming and outgoing mostly between the frontal and posterior regions for the windows of 2 s and 4 s. The distribution of electrodes presents statistically significant high values over these areas according to the color-coded scheme employed; however, the adjacency matrices are not easy to analyze, and other strategies can be employed to obtain the relationships among the nodes according to the DTF values.

6. Results and Analysis

Considering the approach discussed as part of the processing methodology of the EEG signals, it is important now to discuss the results derived from that methodology for the different recordings available. The first part of this section is devoted to the results obtained for the selection of the segment length for each of the recordings available. The second part accounts for the effective connectivity analysis considering the segment duration selection and common segmentation procedures found in the literature as a way to compare and analyze the outcomes in connectivity.

6.1. Results on window length selection

6.1.1. Selection of EEG recordings for processing

Let us recall that there was a total of 20 EEG recordings, coming from 10 different subjects in two resting-state conditions. As summarized in Table 3, the EEG signals were shortened in time as a consequence of the preprocessing stage, in addition, there was performed a channel selection procedure among the signal sources concerning the possible instabilities and noise that affected them.

Table 3. (RECALL) Recordings' characteristics before and after the cleaning process

Subject	R1 - Opened eyes					R2 - Closed eyes				
	Raw signals duration [s]	Cleaned signals duration [s]	Clean signals percentage	Selected channels	Channel Selection percentage	Raw signals duration [s]	Cleaned signals duration [s]	Clean signals percentage	Selected channels	Channel Selection percentage
S1	305	46	15%	51	82%	311	172	55%	53	85%
S2	308	235	76%	59	95%	314	256	82%	60	97%
S3	284	46	16%	59	95%	204	43	21%	58	94%
S4	192	101	53%	54	87%	278	123	44%	53	85%
S5	308	205	67%	57	92%	306	155	51%	59	95%
S6	308	230	75%	57	92%	311	226	73%	60	97%
S7	353	135	38%	54	87%	313	212	68%	55	89%
S8	315	197	63%	61	98%	319	231	72%	62	100%
S9	189	145	77%	55	89%	184	116	63%	58	94%
S10	303	172	57%	60	97%	328	240	73%	61	98%
Mean	286	151.2		57		287	177.4		58	

As a following step of the preprocessing stage, it is then possible to perform a recording selection. The criterium used to do it is based on the relative reduction of the dataset length. If a threshold is set at 50% of the original duration of each recording, then, the datasets which were reduced to less than that threshold are marked as not useful (i.e. meaning that more than half of the samples from the EEG signals were eliminated).

As the process is considered for both resting-state conditions, therefore, if one dataset has more than half of its samples after the pre-processing in one state but contains less than the threshold for the other condition, then both recordings are discarded. As an example, consider the recordings from subjects S1, S4, and S7 which after pre-processing had at least half of their original duration for the states R2, R1, and R2 respectively, and did not meet the requirement for their counterpart resting-state cases.

The S1 recording in R1 had an original duration of 305 seconds and was reduced to 46 seconds, corresponding to only 15% of the initial time. Such reduction suggests that the signals were

heavily affected by noise and artifacts, and consequently only a few seconds were able to be maintained. In the same fashion, the recordings from subjects S4 and S7 had an important reduction that went to 44% and 38% in the R2 and R1 conditions, respectively. Also, subject 3 recordings were reduced drastically in both conditions, suffering a reduction of 84% and 79% of their times.

As it will be explained in the section *Subjects S5, S6, S8, S9, and S10*., subjects S6 and S9 in both resting-state conditions present certain particularities from their statistical features which could lead to their discarding from the analysis, however, they are kept observing the characteristics and to compare them with the remaining datasets.

After these considerations, only 6 pairs of EEG datasets are counted for analysis (S2, S5, S6, S8, S9, and S10).

6.1.2. Window selection approach

A. Single EEG dataset analysis

As discussed in the methodology description, the segmentation approach can be performed by considering short segment lengths whose durations are below 1 second ($w_{li} < 1s$), and long segments that are considered when $w_{li} \geq 1s$. For this data analysis, both segment duration categories are employed considering the indications summarized in Table 5.

Table 5. Segmentation characteristics for long and short segments.

a. $W_L = 0.05 \text{ s}, N_w = 20 \rightarrow w_{li} = \{0.05, 0.1, 0.15, \dots, 1\}$	Short segments
b. $W_L = 1 \text{ s}, N_w = 10 \rightarrow w_{li} = \{1, 2, 3, \dots, 10\}$	Long segments

The segmentation procedures based on these characteristics have the particularity of being complementary. They were chosen in this way to allow the characterization of the EEG signals when the segments are short below 1 second to account for higher frequency components present on the EEG signals. On the other hand, slow modulations in time can be captured if longer segments are considered for analysis. In this case, segments as short as 50 ms were considered as the basis window length from which the segmentation procedure is employed. Hence, multiple segmentations were performed considering an upper limit of 1 second.

Similarly, a basis segment duration $W_L = 1 \text{ s}$ was chosen for long segment length analysis, in this case, the largest segment is of 10 seconds, sufficient to account for low-frequency components that can be present in the signals.

From these considerations, the Algorithm 1) was employed in both conditions, and the following results show the kurtosis variance searching approach applied to the selected recordings.

A.1. Subject 2 (S2):

Table 4 shows that the raw EEG signals acquired from the subject 2 (S2) had a duration of 308 and 314 seconds for opened-eyes and closed-eyes resting-state conditions, respectively. After pre-processing, the datasets were shortened to about 80% of their initial durations, giving as result signal lengths of 235 and 256 seconds. Then, segmentation was applied considering long duration windows. As results, the heat plots of Figure 33 show the kurtosis variances (K_{σ^2}) as function of the segment length intervals that go from 1 second up to 10 seconds. The color code reflects the K_{σ^2} magnitudes contemplating bright yellow colors for lower K_{σ^2} values and dark blue ones for higher kurtosis variance magnitudes.

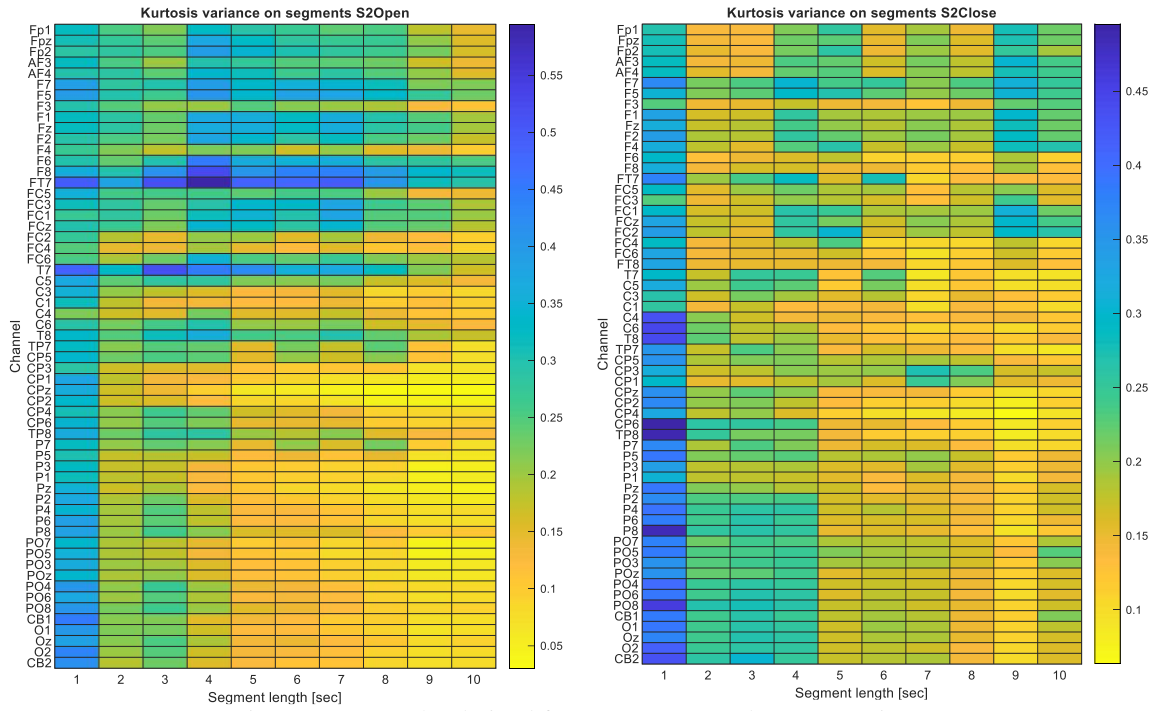


Figure 33. Heat plot derived from 1 to 10 seconds segmentation considering the K_{σ^2} values. Left: S2 - R1 K_{σ^2} . Right: S2 - R2 K_{σ^2}

From the plots, it can be observed that longer segments have lower variances which in principle would be appropriate to account for most of the stationarity of the segmented signals. However, longer segments do not provide a good representation of high-frequency components that are of interest according to the brain activity in consideration.

According to the temporal frequency characteristics of the brain rhythms, the lower limit needed to provide a close-fitting representation of the frequency components of the alpha rhythm has to be set at a minimum of $w_{low} = 0.143$ s. By looking at the segments like the ones of the segmentation in Figure 33, their durations are very long, even for the lower kurtosis variances which could represent properly the slow dynamics of the oscillatory components that can be registered in EEG signals, however, for the case of the analysis presented in this work, according to the characteristics of the brain activity, such slow oscillatory components would never be present in awake resting-state conditions, so it would be useful to search for shorter segments, and the considerations defined by the methodology in this thesis approach were defined to account such characteristics to then apply them in the effective connectivity analysis.

These observations hold for all the kurtosis variance representations derived from all the EEG recordings; however, each variance matrix has unique characteristics regarding the K_{σ^2} as a function of the segment duration, hence it is necessary to perform the analysis of the particular characteristics of each dataset to provide results that can be generalized across the recordings and resting-state conditions.

From the K_{σ^2} matrices represented as heat plots in Figure 33 for S2 - R1 (left) and S2 - R2 (right) there are obtained the searching domains constrained by the lower and upper bounds presented in Figure 34.

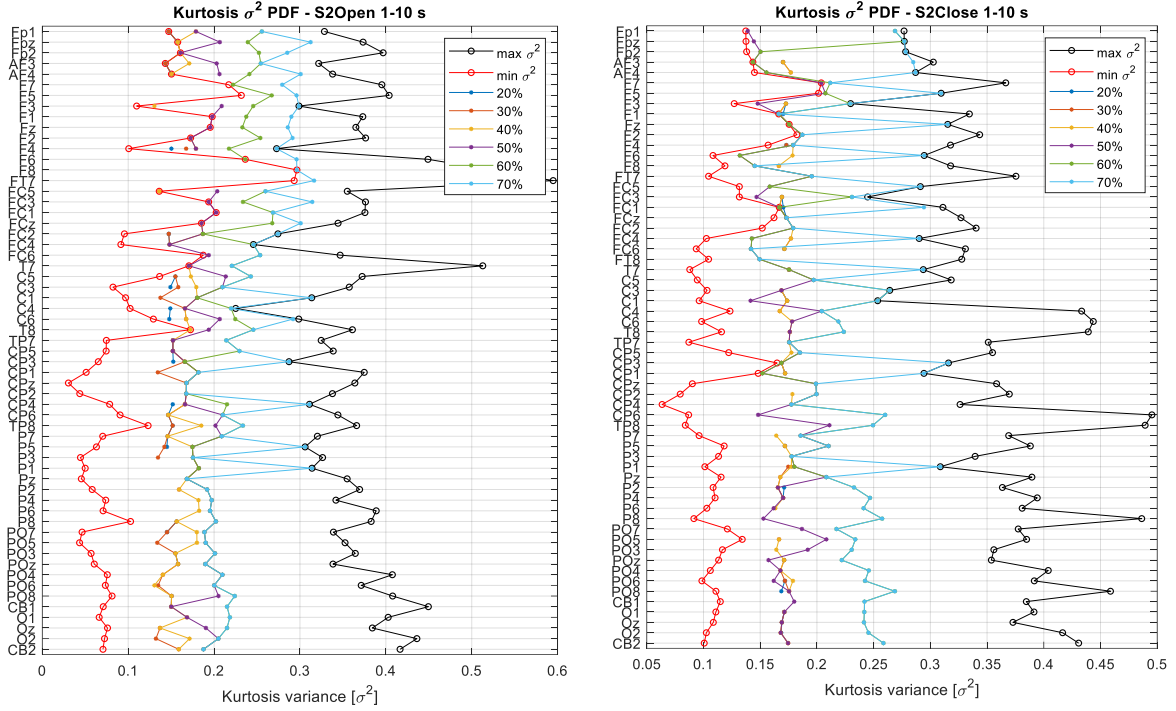


Figure 34. Kurtosis variance (K_{σ^2}) searching domain for S2 – R1 (left) and S2 – R2 (right). Considering segmentation characteristics from Table 5.a.

Considering a segmentation that goes from 1 second to 10 seconds, lower and upper bounds ($\min \sigma^2$ – red plot and $\max \sigma^2$ – black plot) on each resting-state condition are defined as the relative minimum and maximum values of kurtosis variance magnitudes exhibited by each of the channels composing the EEG dataset. In between the limits, the searching strategy (Algorithm 1) works to find segment durations exhibiting low kurtosis variances so that the spread back in the kurtosis domain is small across the channels' K -distributions, which guarantees common kurtosis magnitudes, and hence stationarity if their values are restricted to be small and common for all the channels while maintaining similar stationarity characteristics as well.

Figure 34 shows the K_{σ^2} (kurtosis variance) variations from segment to segment when different relative variance proportions are set as thresholds to maintain common values in all the channels. Those thresholds are relative to the maximum variance on the channels ($\max \sigma^2$). For visualization purposes, these thresholds were increased from 20% to 70% of the largest variance, so each point represents the variance found on one of the segments of a channel whose value belongs to that proportion w.r.t the largest variances. Those percentages proportions can be represented as variance intervals and are depicted in Figure 35.

The searching domain and the selected variances according to the thresholds produce the plots in between the lower and upper bounds in Figure 34, as can be observed, the lower the threshold the closer to the lower bound plot. In some cases, the variances near a specific threshold do not represent a significant change with respect to the next one. This is the case of all the percentage threshold variances in the left panel (S2 – R1) of Figure 34 for the channels located at the posterior part of the scalp (lower part of the figure), whose kurtosis variances are almost the same, and in some conditions, they are recognized exactly equal e.g. some K_{σ^2} points of the 50%, 60% and 70% thresholds are the same according to the algorithm.

Similar behavior is observed for the S2 – R2 case (right panel on Figure 34), in this case, variances belonging to the 30%, 40%, and 50% are shared, however, the 50% seems to be more

common for more channels.

As a complementary graph, Figure 35 shows the associated searching intervals to each of the percentage thresholds in Figure 34. As can be observed, the lower the threshold the shorter is the interval which is set to look for common segment lengths among the channels. The intervals determine the minimum and maximum limits to look for the segments that exhibit a variance within the accepted range according to the likelihood of occurrence derived from the kurtosis variance density.

In detail, for both resting-state conditions, Figure 35 a-b, the 50% searching interval (delimited by the purple vertical lines) cover a probable part of the distribution which is translated in the increase of segments of all channels composing the dataset with similar kurtosis variance characteristics, guaranteeing similar stationarity behavior among the channels because of the kurtosis spread being restricted to those limits. It is clear that as long as the searching interval is increased, the whole variance density is considered, and in the limit, because of the segment selection characteristics of the algorithm, the lower bound variances would be chosen, which are not optimal as discussed in previous sections.

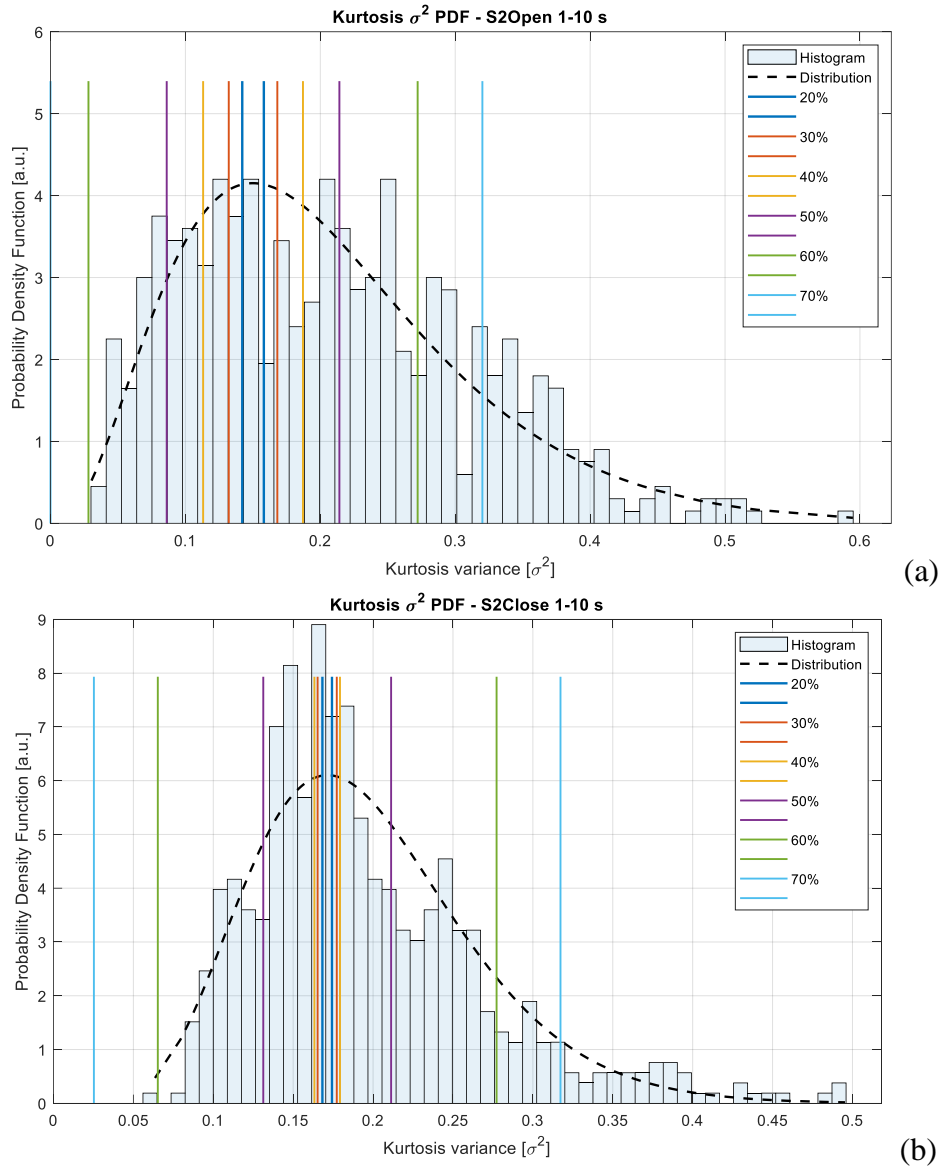


Figure 35. K_{σ^2} searching intervals with respect to $\max \sigma^2$ proportion thresholds. a. S2 – R1 K_{σ^2} distribution and b. S2 – R2 K_{σ^2} distribution.

The representations of the searching domain, the searching intervals, and the kurtosis variance distributions can be used to construct a heat plot that depicts the number of channels that can be found in an interval considering a specific kurtosis variance interval used in the searching stage by the algorithm. Accordingly, Figure 36 depicts the number of channels (color-coded) as a function of the searching interval defined as the kurtosis variance range where a subset of channels exhibit close kurtosis values among them w.r.t the window length defined for the segmentation.

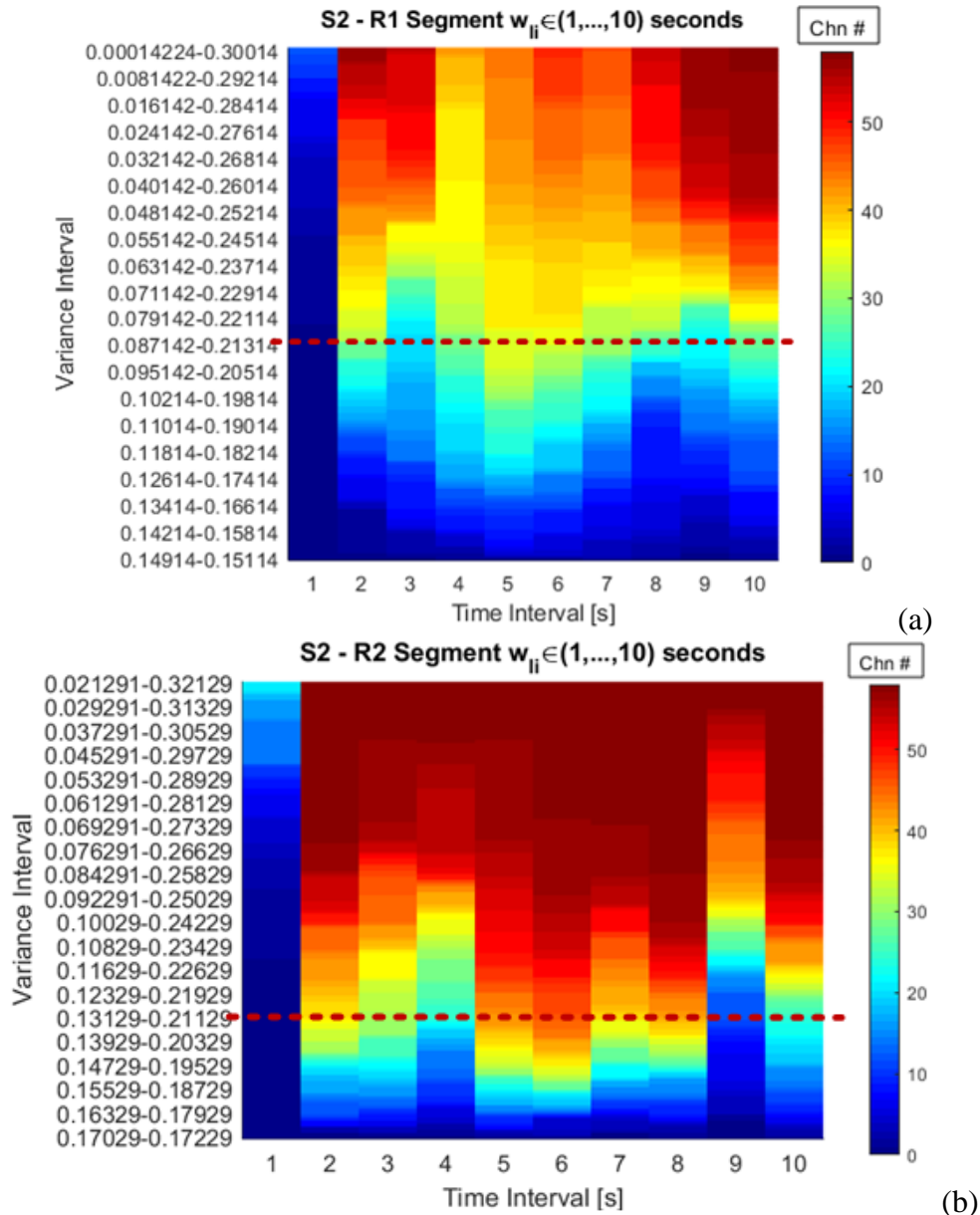


Figure 36. The number of channels as a function of the segment length and the searching interval in terms of the kurtosis variance. a. S2 – R1 b. S2 – R2.

The variance range found for 50% of the largest K_{σ^2} delimited in the kurtosis variance PDFs in Figure 35 a and b, is shown in Figure 36 as the dashed line. By considering that threshold defined by the 50% range, it is possible to observe that in the case of the resting state in opened-eyes condition (Figure 36.a) the highest number of channels sharing similar gaussian characteristics is found at $w_1 = 5s$ when the range is defined as $0.086 \leq K_{\sigma^2} \leq 0.214$. To be exact there are 34 channels exhibiting similar stationarity features in that range, and by looking at the interval considering the K_{σ^2} PDF, it can be said that the algorithm is covering the most

probable values for kurtosis variance which by being located near the apex of the density, then, the kurtosis values are close to each other assuring the common stationary observation across channels.

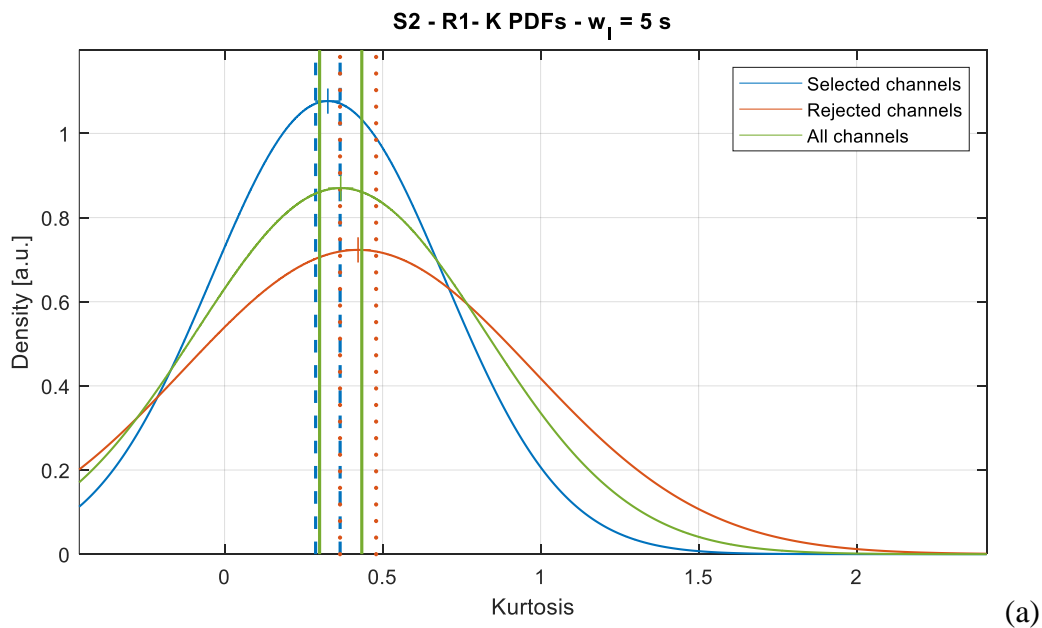
Similarly, Figure 36.b shows the kurtosis variance 50% threshold defined for the interval $0.13129 \leq K_{\sigma^2} \leq 0.21129$. In this case, there are different options to select the appropriate segment length. Segment $w_l = 6s$ is the one from which more channels are found, 48 in total, however, shorter segments like $w_l = 5s$ provides 44 channels sharing the same features. Finally, a $w_l = 2s$ can be considered as well, where can be found 39 channels.

According to these outcomes, for S2 – R1 the selected window is $w_l = 5s$ and for S2 – R2 the segment length is defined at $w_l = 6s$. The tables summarizing the number of channels with respect to the percentage thresholds, variance ranges, and segment durations are found in the annex as Table AN 1 and Table AN 2 for the resting state conditions R1 and R2 respectively.

The variance interval defined for the 50% threshold can be used to return to the kurtosis domain and perform the selection of the channels that are below the threshold that was set considering the K_{σ^2} values. In that way, it is possible to estimate the probability density functions from the kurtosis values, considering:

1. The whole set of EEG signals that were segmented by using the selected window length.
2. The subset of channels that are below the threshold defined by the kurtosis variance interval.
3. The subset of channels that are considered as discarded since their variances are exceeding the limits of the variance boundaries.

In this way, the derived PDFs bring a way to evaluate the spread of the kurtosis values among the channels selected, and for the discarded ones, having as reference the kurtosis PDF of the whole set of signals. Figure 37 depicts the distribution fitting performed for the selected channels for S2 in both resting-state conditions.



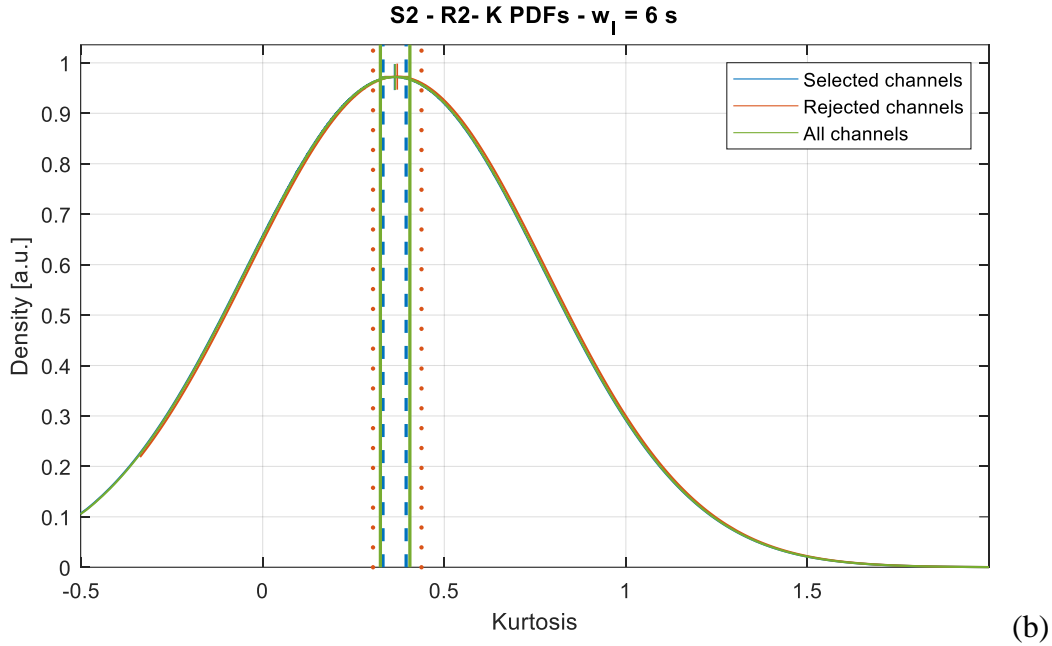


Figure 37. Kurtosis distributions considering the selected channels from the percentage threshold.
a. S2 - R1 $w_l = 5s$ b. S2 - R2 $w_l = 6s$

Figure 37 in both conditions (a, b), depicts the kurtosis distributions of three sub-datasets derived from the segmentation procedure. In Figure 37.a, it is depicted in green the kurtosis distribution of all the segments from all the signals of the S2 – R1 recording. Moreover, it is shown the standard deviation with the parallel lines with the same color. In blue is plotted the distribution of the kurtosis magnitudes considering the 5-second segment length from the selected channels, the standard deviation is shown considering the dashed parallel lines. Finally, the fitted PDF for the discarded signals is plotted in red, as can be observed from the graph, there exists a significant deviation from the discarded kurtosis values w.r.t the density defined from the whole dataset. On the other hand, the PDF from the selected channels is more similar to the distribution of all the channels.

In Figure 37.b the fitted distributions are almost the same for the three cases. Considering the variance range $0.13129 \leq K_{\sigma^2} \leq 0.21129$ the segmentation procedure using a $w_l = 6s$ does not discriminate a large proportion of channels with very different stationary attributes considering the kurtosis domain. From this figure it could be said that all the signals from the EEG channels that are considered at that segmentation window have mean values very similar among them which reflects in the small differences among the spreads, that is why the PDFs are so similar and their standard deviations are almost equal.

To perform a comparison between the short and long windows, let us now consider the segmentation approach for short windows, below 1 second. The basis window length was defined as $W_L = 50$ ms and $N_w = 20$. From such segmentation, the kurtosis variance matrix represented as a heat plot is shown in Figure 38. The figures were derived from the S2 – R1 and S2 – R2 datasets.

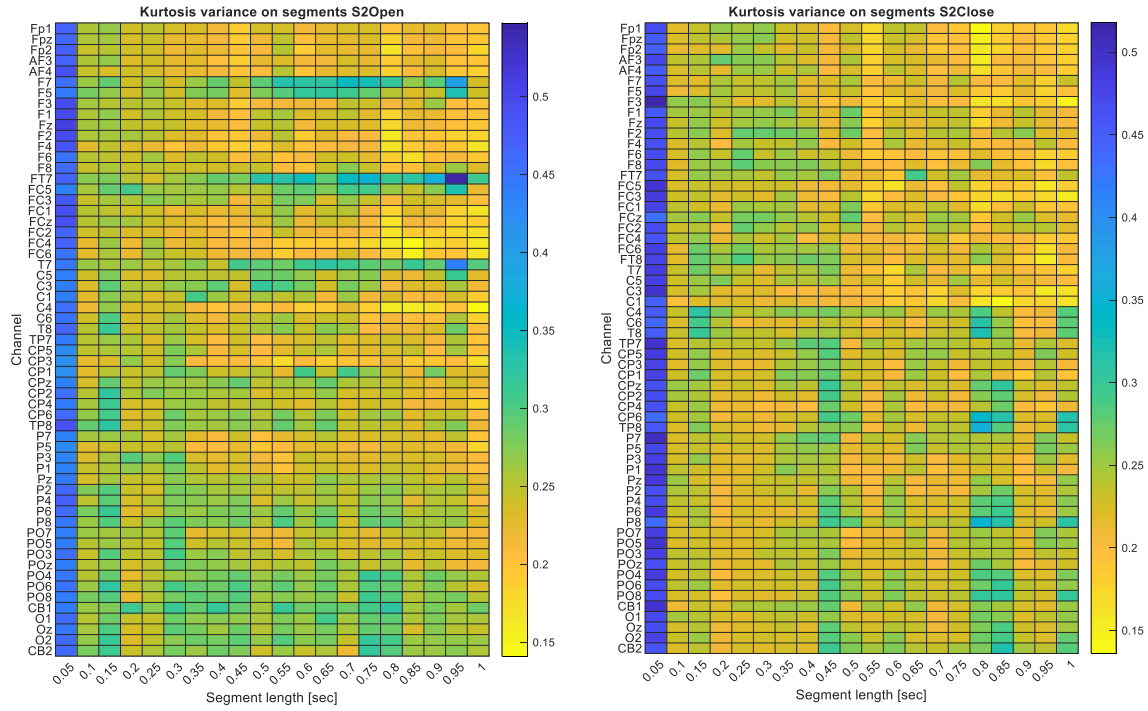


Figure 38. Heat plot derived from 50 ms to 1-second segmentation considering the K_{σ^2} values. Left: S2 - R1 K_{σ^2} . Right: S2 - R2 K_{σ^2}

Following these kurtosis variance values, the searching space defined in Figure 39 for S2 – R1 (left) and S2 – R2 (right), provide a hint on the percentage threshold selection for the segment length selection across channels. Considering the S2 - R1 resting-state condition, the first threshold that groups most of the channels corresponds to 50% of the maximum variance exhibited by each of the channels, such threshold is translated into a variance range of $0.2409 \leq K_{\sigma^2} \leq 0.2529$ for the opened eyes condition (Figure 39 left). On the other hand, for the S2 – R2 condition, the percentage threshold is defined at 40%. As can be observed in Figure 39 right some channels are grouped from that consideration. The variance range for that threshold (40%) corresponds to $0.2281 \leq K_{\sigma^2} \leq 0.2321$ (Figure 39 right).

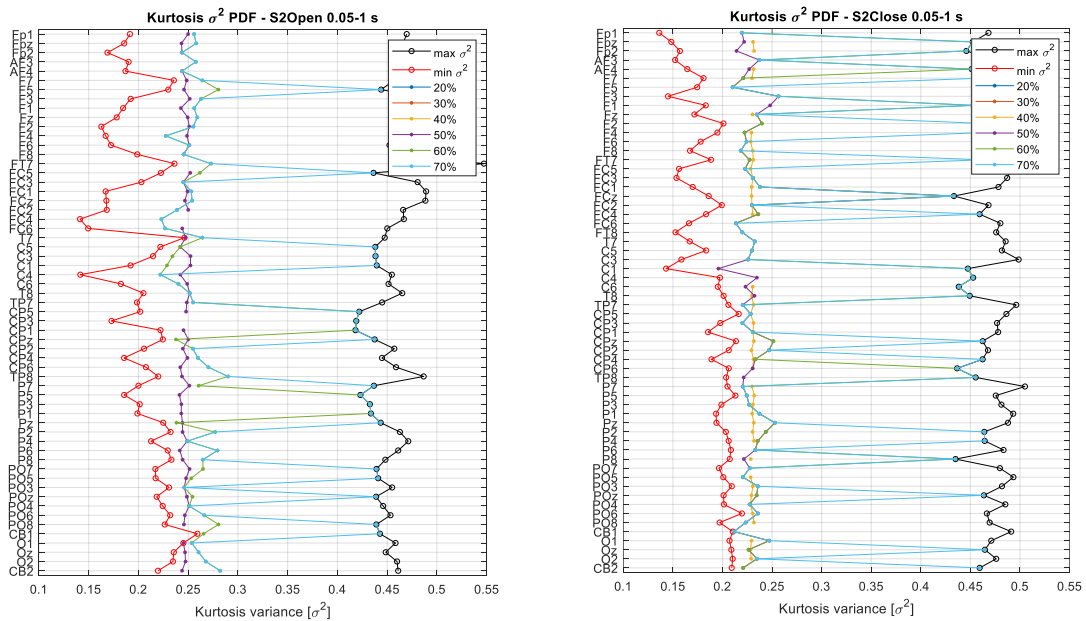


Figure 39. Kurtosis variance (K_{σ^2}) searching domain for S2 – R1 (left) and S2 – R2 (right). Considering segmentation characteristics from Table 5.b.

However, from Figure 39 it can be noted the superimposition of some of the variance values at higher percentage thresholds (e.g. 60%, 70% in R1 and 50%, 60% in R2 condition), which suggests that in broader searching intervals the variances are similar and thus, a lower threshold would be more appropriate to be selected. In this way, the searching intervals at 50% in the case of the opened-eyes condition are maintained as well as the 40% threshold in the closed-eyes in accordance to the limits defined in the kurtosis variance distributions as can be observed in Figure 40.

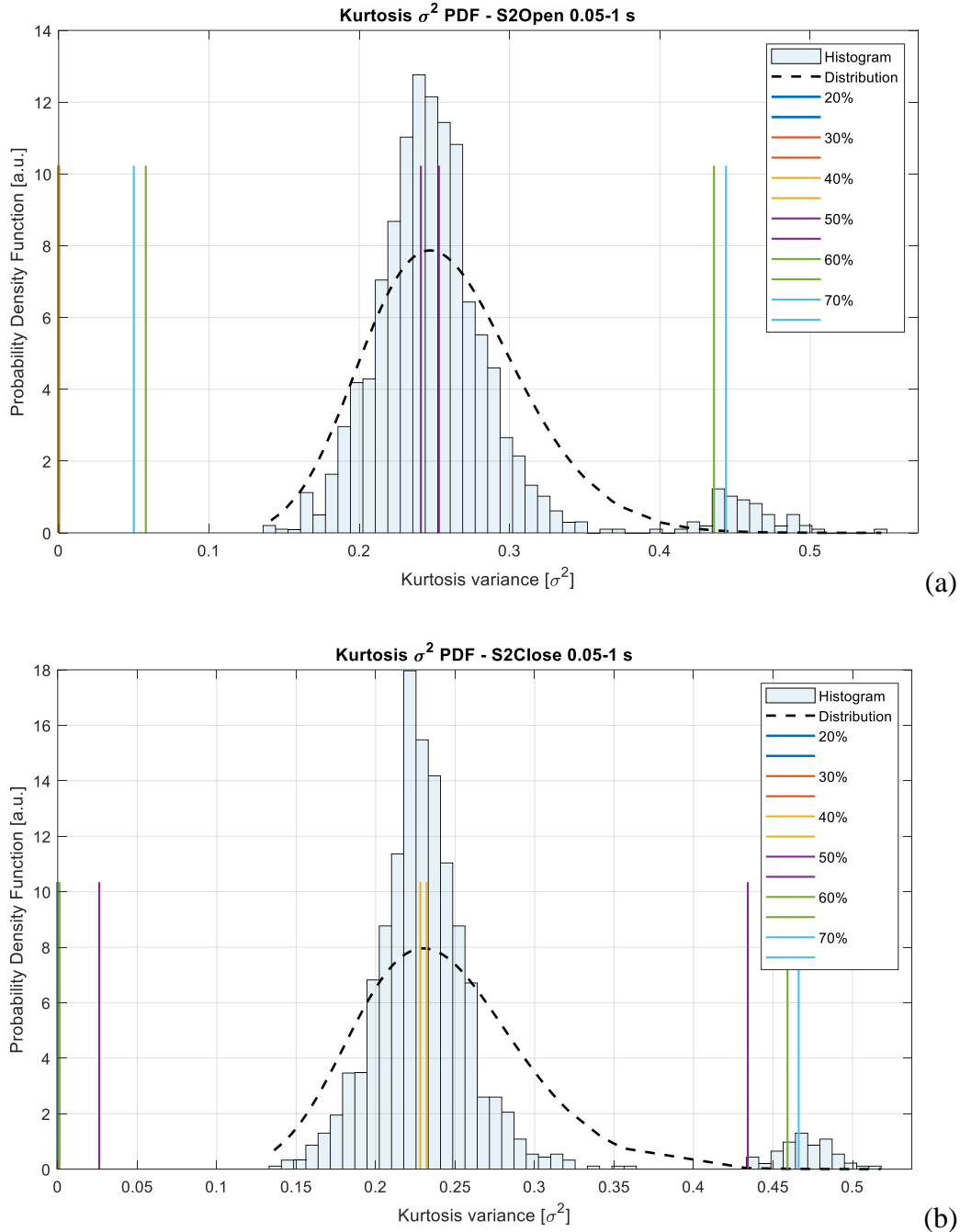


Figure 40. K_{σ^2} searching intervals with respect to $\max \sigma^2$ proportion thresholds. a. S2 – R1 K_{σ^2} distribution and b. S2 – R2 K_{σ^2} distribution. From 50 ms to 1 s

The boundaries of the searching interval according to the percentage thresholds that are suggested by the algorithm show a concentration of the most probable kurtosis variance magnitudes at 50% for S2 – R1 and 40% for S2 – R2, however, when examining the number of

channels found at each of the kurtosis variance intervals associated to the percentage thresholds summarized in the arrays Table AN 3 and

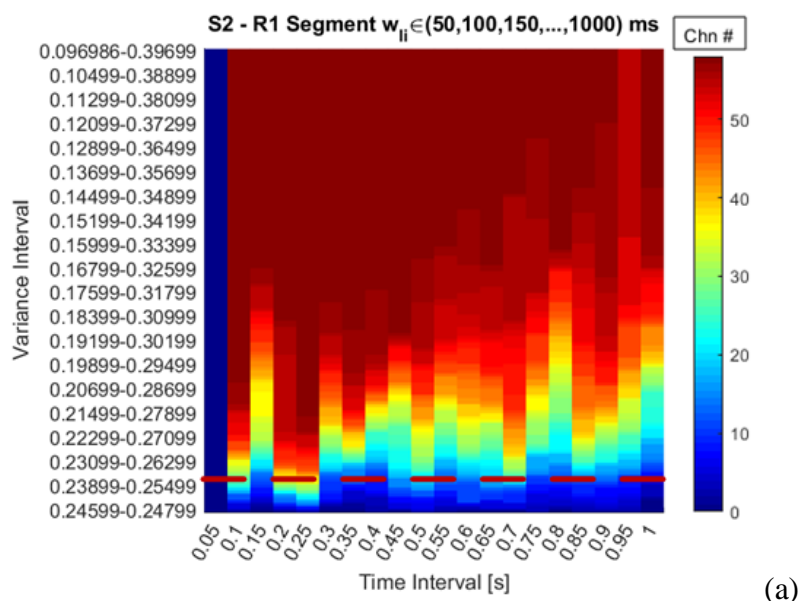
Table AN 4 for S2 – R1 and S2 – R2 respectively, one can notice that common channels exhibit similar characteristics when considering a $w_l = 250$ ms for the S2 – R1 condition, which is the highest number of common channels (23) at 50% of the $\max \sigma^2$ per channel considering the limits in Figure 40.a.

Similarly, the kurtosis variance limits for the S2 – R2 at 40% of the largest kurtosis variance consider a maximization in the number of channels when the $w_l = 300$ ms. There are only 8 signals with similar stationary characteristics considering the narrow interval associated with the 40% threshold (Figure 40.b). In such a case it would be useful to consider a larger variance range, which if selected, the total number of signals would be considered for a 50% threshold at a $w_l = 100$ ms.

Considering that the maximum number of signals within the 40% limits is only 8, it would be better to consider the higher range corresponding to 50% ($0.0261 \leq K_{\sigma^2} \leq 0.4341$). From this increase, Figure 41 depicts the number of channels as a function of the 20 windows and the variance searching intervals.

The 50% range (S2 – R1) depicted in Figure 41.a with the dashed line might be very restrictive in order to find a better segment length. As can be observed there might be better segment lengths considering broader variance ranges, in this case, an interval defined at $0.2309 \leq K_{\sigma^2} \leq 0.2699$ might present a larger number of channels with similar characteristics, however, the percentage ranges might be very small in between. This means that the computational time for this kind of segmentation is very large to account for such small changes, and this is why it was not possible to consider the exact number of channels and the associated percentages.

A similar situation occurs for the S2 – R2, Figure 41.b, a better range is depicted with the black dashed line and suggests that within the kurtosis variance limits $0.1981 \leq K_{\sigma^2} \leq 0.2621$ and using a $w_l = 300$ ms most of the channels are covered, and similar stationary characteristics are found. The yellow dashed line considers the broader variance range at 50% which goes out of the range of the heat plot, which means that the whole density is considered.



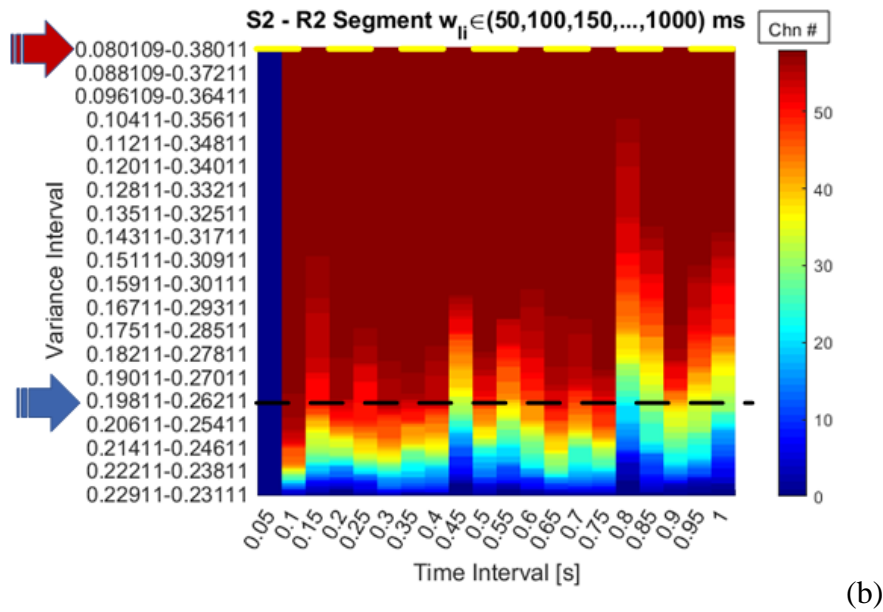


Figure 41. The number of channels as a function of the segment length and the searching interval in terms of the kurtosis variance – Short window segmentation. a. S2 – R1 b. S2 – R2.

Figure 42 shows the kurtosis PDFs for the selected channels, the discarded ones, and the whole set of signals considering a segmentation of 250 ms and 100 ms according to the 50% threshold in both resting-state conditions. As can be observed, all the fitted distributions are almost the same, producing the same shape and magnitudes. This suggests that the rejected channels in the S2 – R1 does not deviate from the original set of kurtosis values. In the same way, it happens for the kurtosis distributions of the analyzed channels in the S2 -R2 conditions.

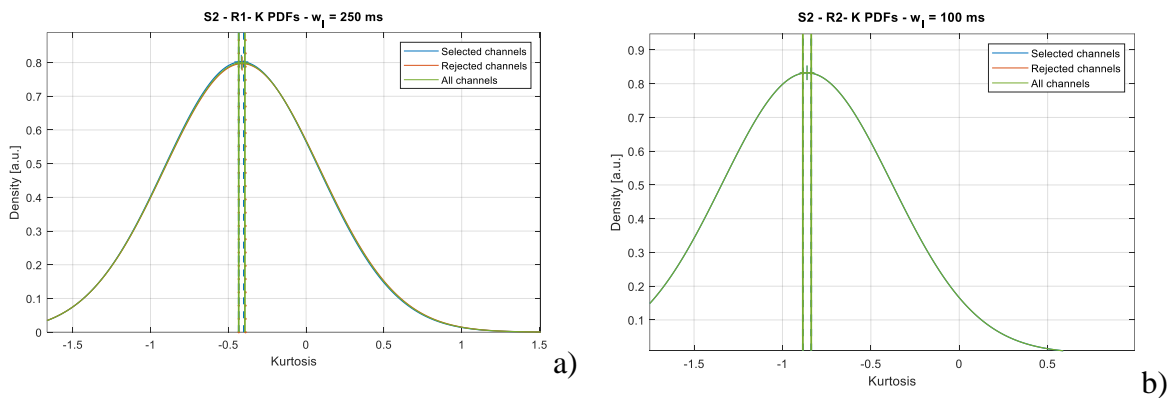


Figure 42. Kurtosis distributions considering the selected channels from the percentage threshold. a. S2 - R1 $w_l = 250ms$ b. S2 – R2 $w_l = 100ms$

Considering shorter segments for kurtosis analysis requires the analysis of smaller intermediate steps of the percentage thresholds, in this way, the heat plots like the ones presented in Figure 36 and Figure 41 are needed to perform the selection of the window.

A.2. Subjects S5, S6, S8, S9, and S10:

The analysis performed for subject 2 (S2) considered the main ideas behind the representation of the statistics derived from the EEG dataset. These ideas can be generalized concerning what does the kurtosis value represents and how its spread is depicted in a tractable way considering its probability density function. Based on this concept, in this passage there are deemed all the

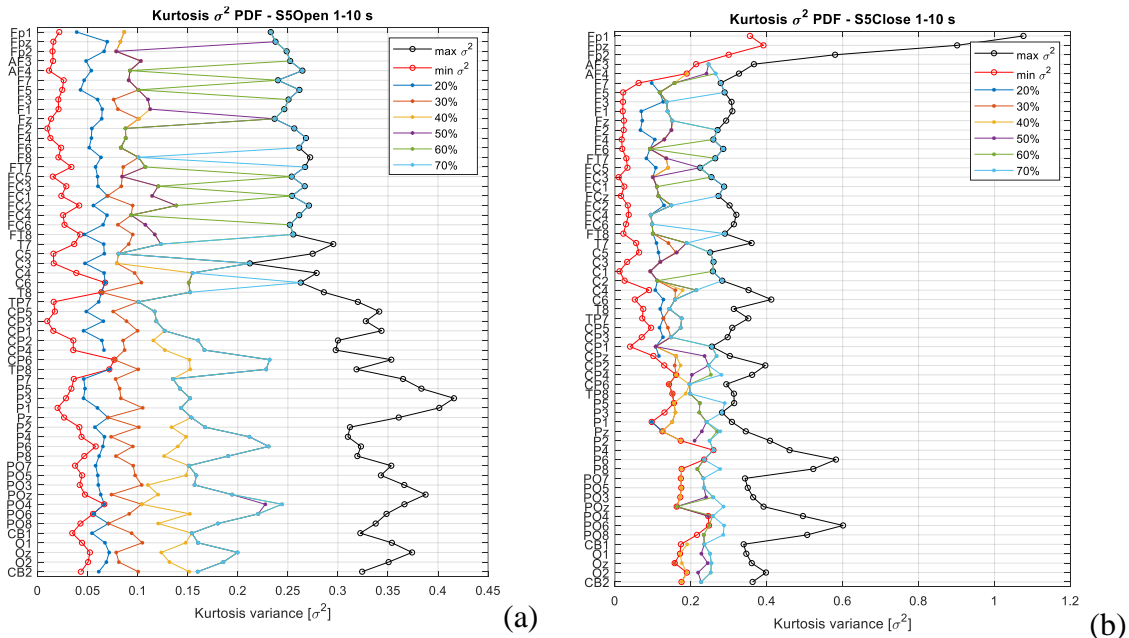
resulting distributions, searching domains, and kurtosis-variance/segment-length plots of the remaining selected datasets (S5, S6, S8, S9, and S10). Thereby it is expected to provide a concise explanation and description of the results to then perform a further analysis that attempts to generalize the data for all the EEG recordings as the previous step for effective connectivity analysis.

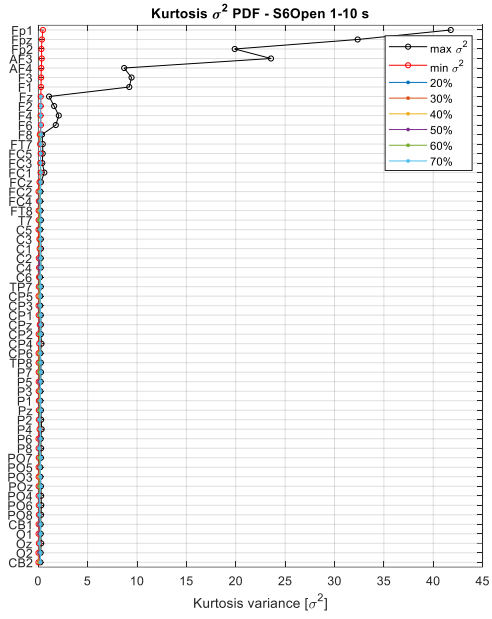
As explained earlier, the kurtosis variance values that are obtained for each of the segment lengths can be represented as heat plots (e.g. Figure 33 and Figure 38 for S2), such kind of figure embodies the matrix of K_{σ^2} derived from each EEG dataset, however, in those examples they were shown for explanation/representation purposes and do not provide a useful way to analyze the statistical quantities more than to check where the lower and higher variances are more concentrated according to the segment length.

In this way, since it is more useful to analyze the searching domain graphs, the densities, and the number of channels-variance interval-segment length plots, the K_{σ^2} heat plots from EEG recordings S5, S6, S8, S9, and S10, are found in the annex section in Figure AN 2, for the long and short window segmentation approaches respectively.

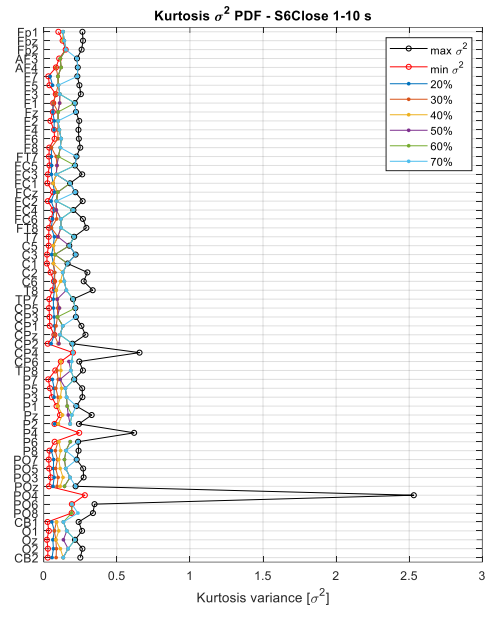
Long window duration analysis

For this first part of the analysis, it is being considered the long window segmentation approach from a $W_L = 1s$, $N_w = 10$ and $w_{li} \in (1, \dots, 10)$. As result, the K_{σ^2} heat plots (Figure AN 2) define the searching domain for each dataset in both resting-state conditions R1 and R2. The following graphs (Figure 43) show the searching domain and the variances found at different extents (percentage thresholds) considering the largest K_{σ^2} on each channel. There are shown the resulted graphs for all the subjects under analysis in both resting-state conditions.

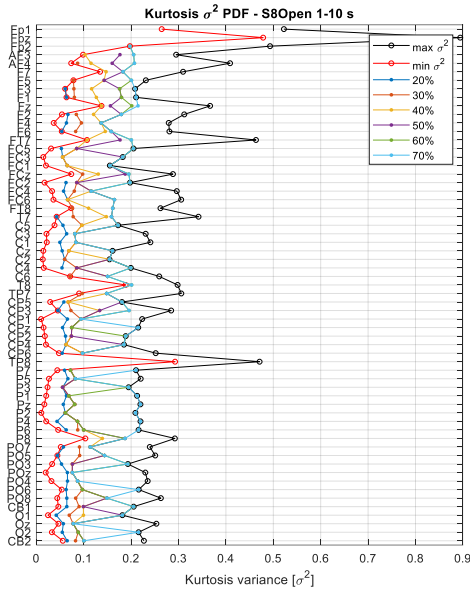




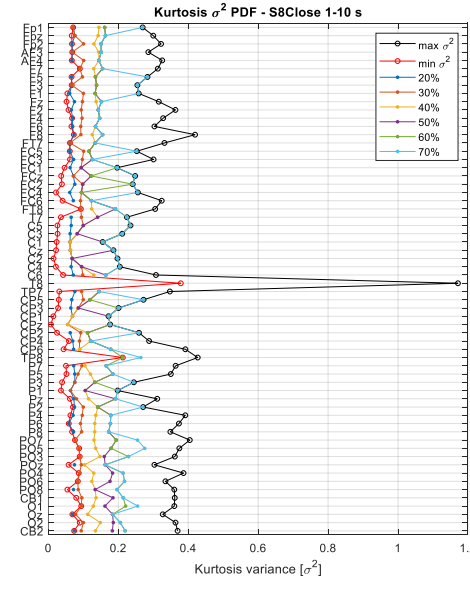
(c)



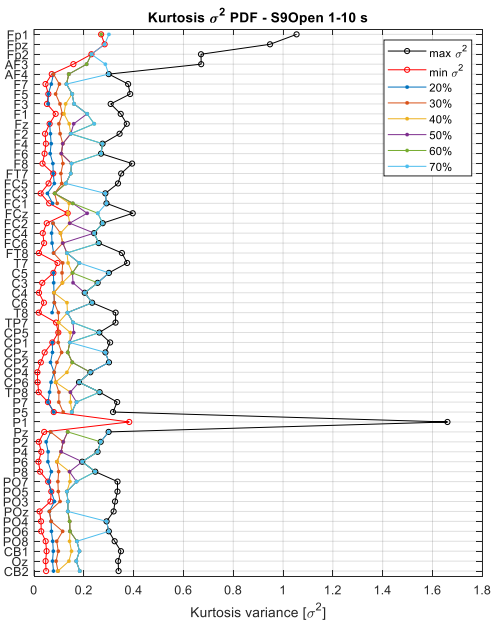
(d)



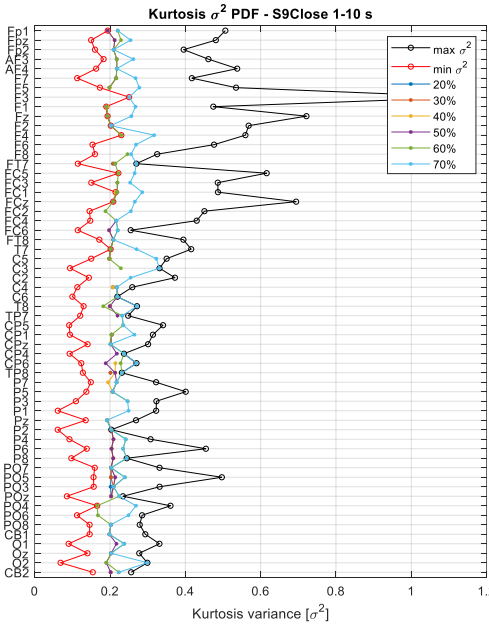
(e)



(f)



(g)



(h)

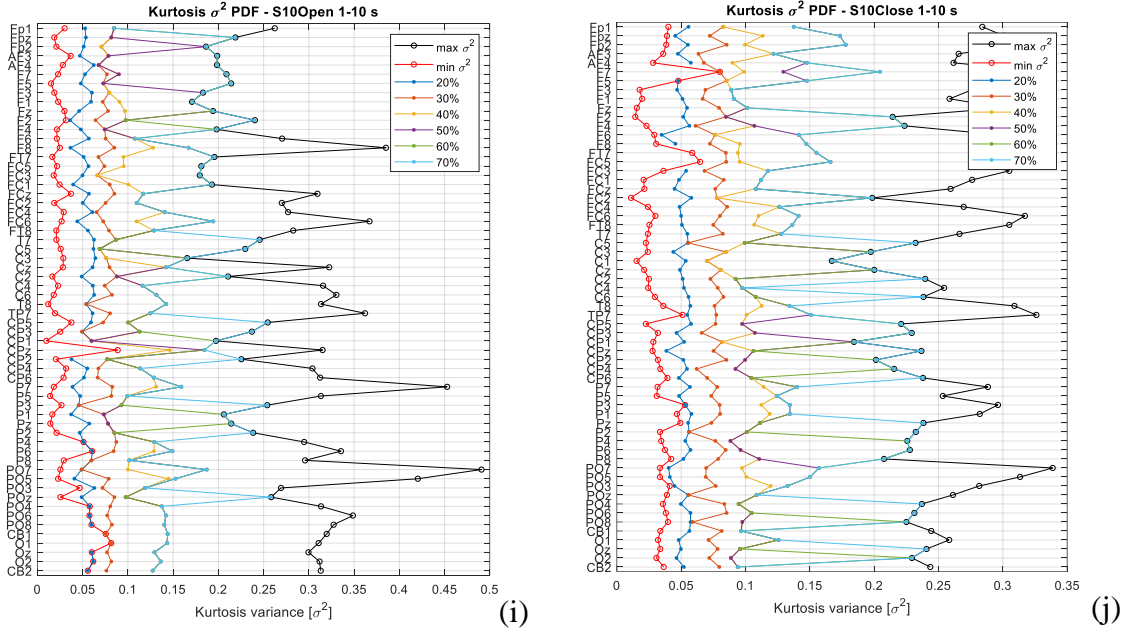


Figure 43. Kurtosis variance (K_{σ^2}) searching domains for segmentations from 1 to 10 seconds. Resting-state conditions depicted in pairs: a, b) S5 – R1, R2. c, d) S6 – R1, R2. e, f) S8 – R1, R2. g, h) S9 – R1, R2. i, j) S10 – R1, R2

As explained previously, the searching domain is limited by the lowest kurtosis variances that are represented by the red plot in all of the graphs ($\min \sigma^2$), on the other hand, the upper bound is graphically defined by the black plot marked as $\max \sigma^2$. These bounds define the searching domain from which the segments are selected under the considerations defined in the methodology. The lowest kurtosis values cannot be selected since they probably correspond to the longest segments. Intermediate values with respect to the maximum variance are then found and are represented by the plots associated with the proportions of the largest variance values.

By considering the searching domain bounds in all of the graphs under the segmentation characteristics of 1 to 10 seconds, there are identified three main searching domain configurations. First, a very narrow domain in which it is difficult or not even possible to identify the lower and upper boundaries as shown in Figure 43.d, corresponding to the EEG dataset of S6 in R1.

Secondly, a mid-range domain in which the different kurtosis values according to the thresholds are found in between the boundaries, and from which most of the recordings belong to; Figure 43. b, d, e, f, g, h, for S5 – R1, S6 – R2, S8 – R1, R2, and S9 – R1, R2.

Finally, the third category is defined for the searching domains which are broad enough to identify and classify the variance ranges belonging to a certain threshold without much overlapping for the lower variabilities (small percentage thresholds). This is the case in Figure 43. a, i, j, on datasets S5 – R1 and S10 – R1, R2.

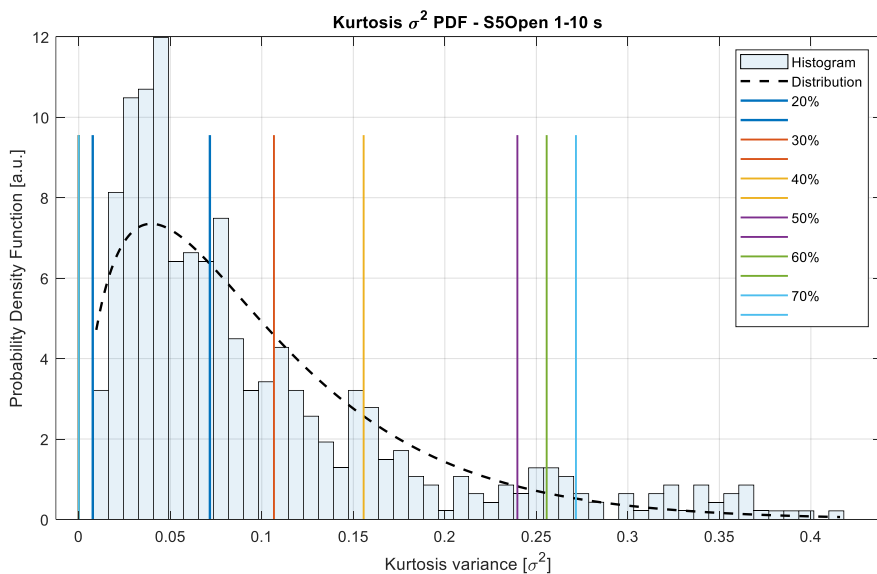
From the first category (Figure 43.d), the algorithm is not able to identify the segments and their corresponding variances that meet the threshold requirements, it means that the searching boundaries are so close to each other that it would require a smaller value for the $\Delta\sigma^2$ step in the searching algorithm (i.e. $\Delta\sigma^2 < 0.001$) to find the variances under each threshold. It is computationally complex, and it would take so much time to do complete this task for one single dataset. Moreover, by considering the characteristics of the other EEG recordings which

do not require special considerations for performing the searching, it suggests that the S6 – R1 recording had some issues during its recording and the data itself can be corrupted.

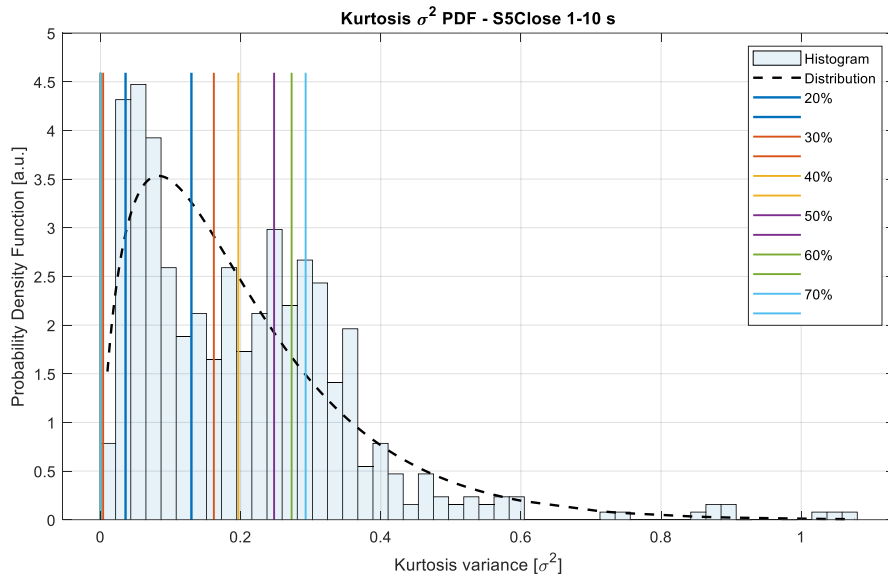
For the second category from which most of the recordings exhibit the same characteristics, it can be observed that the algorithm was able to find the variances belonging to the thresholds, in most cases, lower percentage thresholds (lower than 50% - blue, red, and yellow plots) are close to the lower bound of the kurtosis variances, in some cases, there exists superimposition of some values across thresholds from which it is not possible to discern among the kurtosis values that are within a certain range. On the other hand, for values larger than 50% the variabilities among the values are significant, as can be observed for the “jumps” in the K_{σ^2} magnitudes from channel to channel. This suggests that the kurtosis values meeting the lowest of the percentage threshold requirement are sparse considering the heat plots and are not concentrated in a portion of the kurtosis variance PDF.

For the last category, the broad searching space allows to find the kurtosis magnitudes for each threshold very easily, even for the lower percentage ones, the algorithm is able to find them for the majority of channels and it is possible to choose from them the proper segment length for effective connectivity since the K_{σ^2} magnitudes are uniformly found for all of the channels. For the larger variances case, starting from the 50% threshold, the same behavior as in the mid-range category holds, the variability among the segment variances is very large and it might not be possible to select a segment length meeting the threshold characteristics since it would consider a larger portion of the kurtosis variance density.

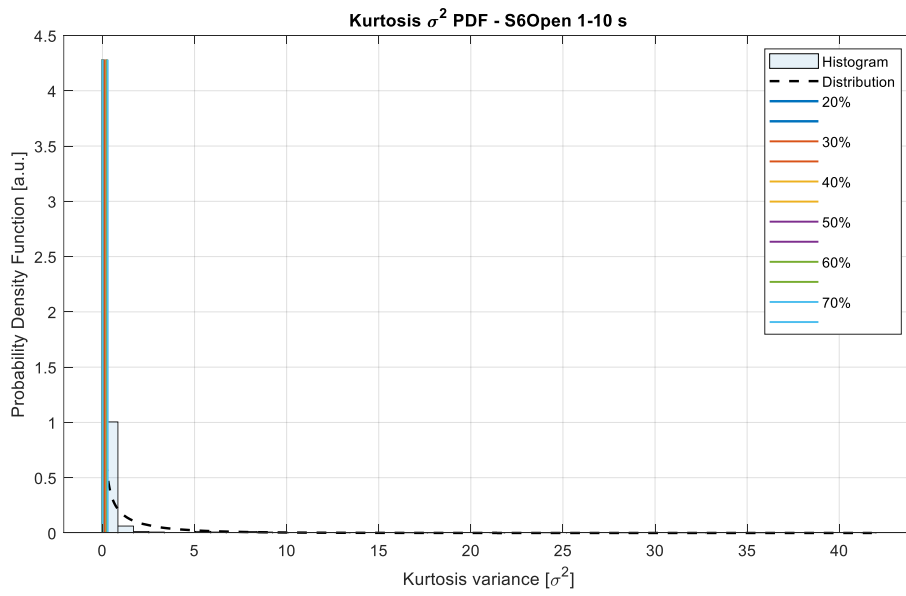
These observations provide an overview of the kurtosis variance searching domain and can be complemented using the probability density functions where the searching ranges w.r.t the percentage thresholds are graphically defined. Thereby, Figure 44 comprises the kurtosis variance densities of the subjects S5, S6, S8, S9, and S10 in both resting-state conditions, and the variance ranges are depicted as well to observe to what extent each of the threshold ranges covers each PDF area and what would be the probability of occurrence for the variance values considered in between the bounds.



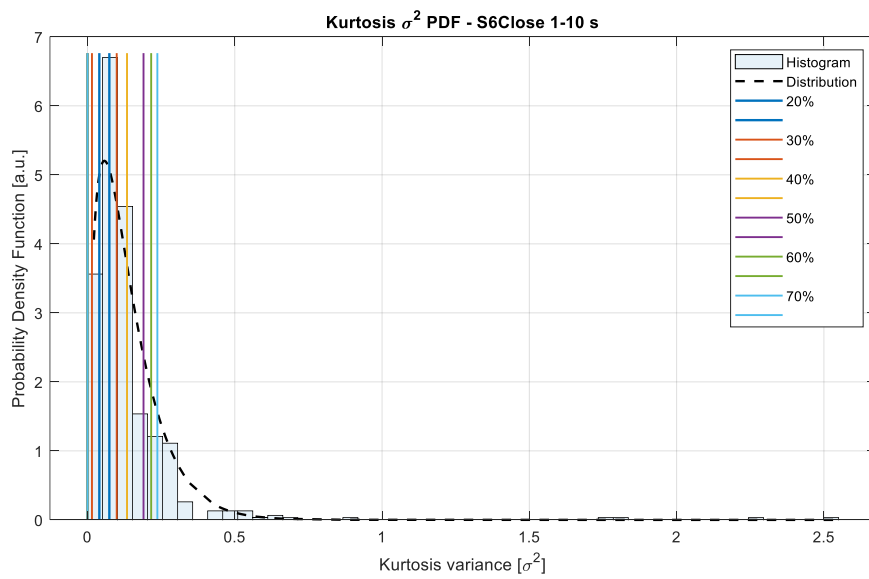
(a)



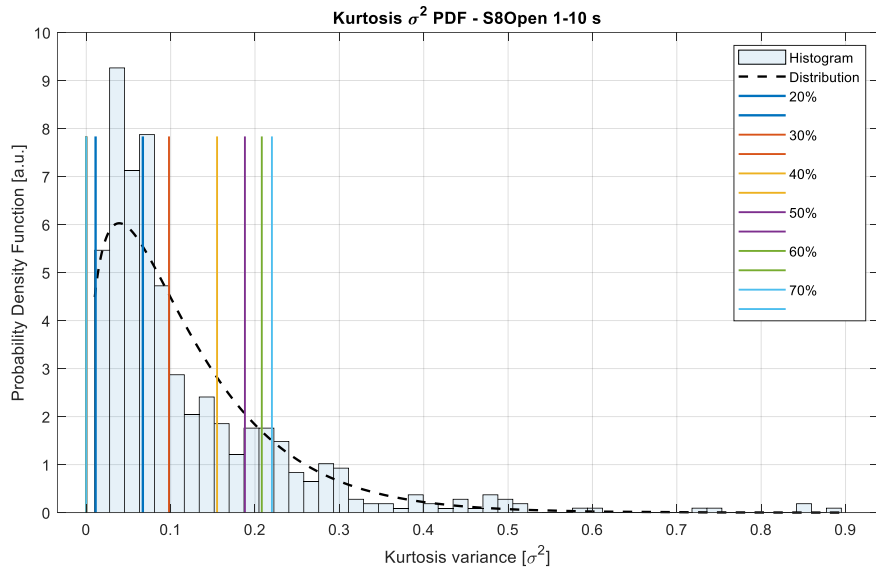
(b)



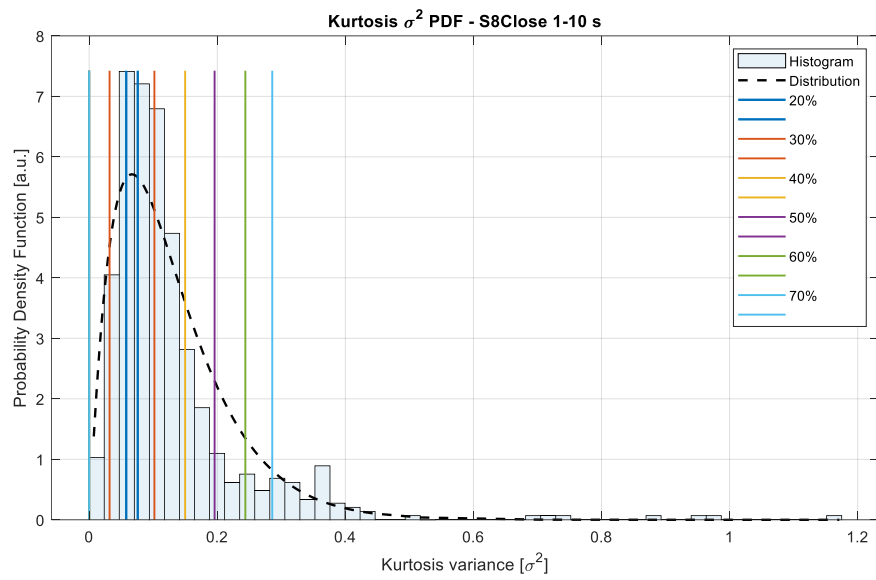
(c)



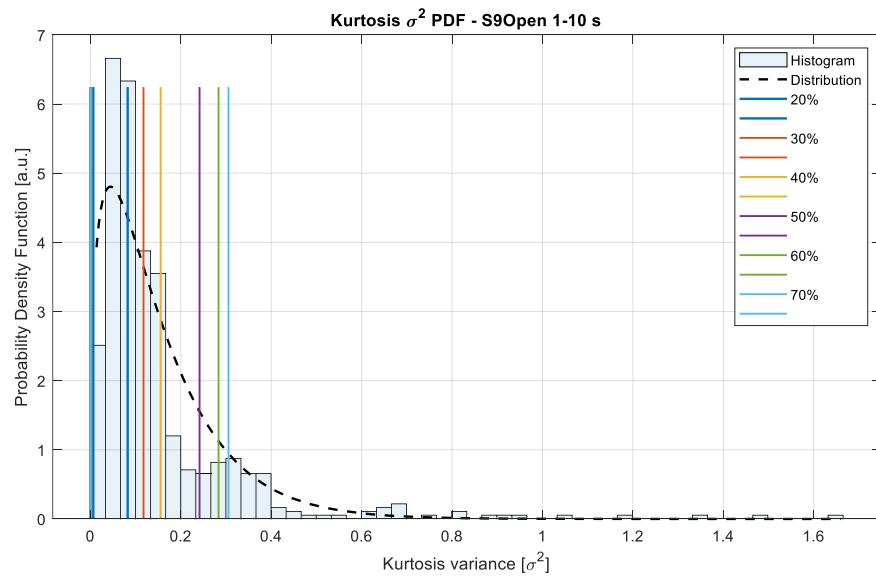
(d)



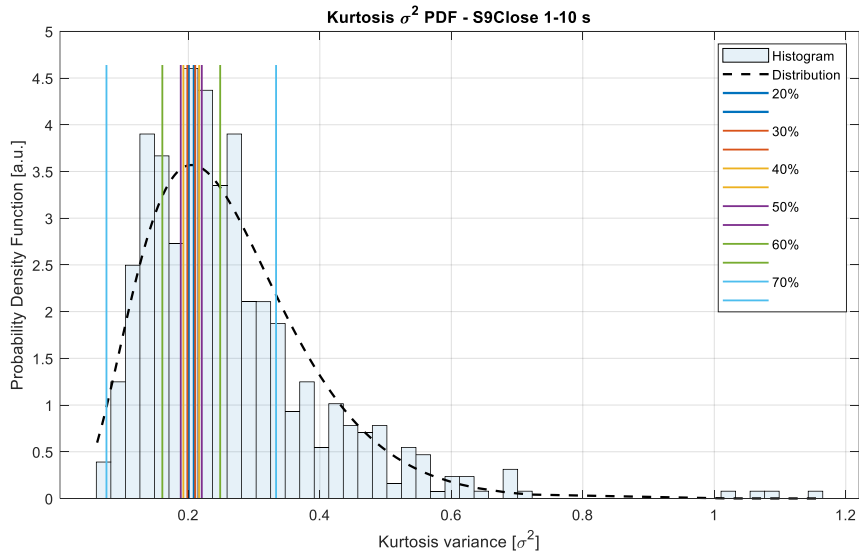
(e)



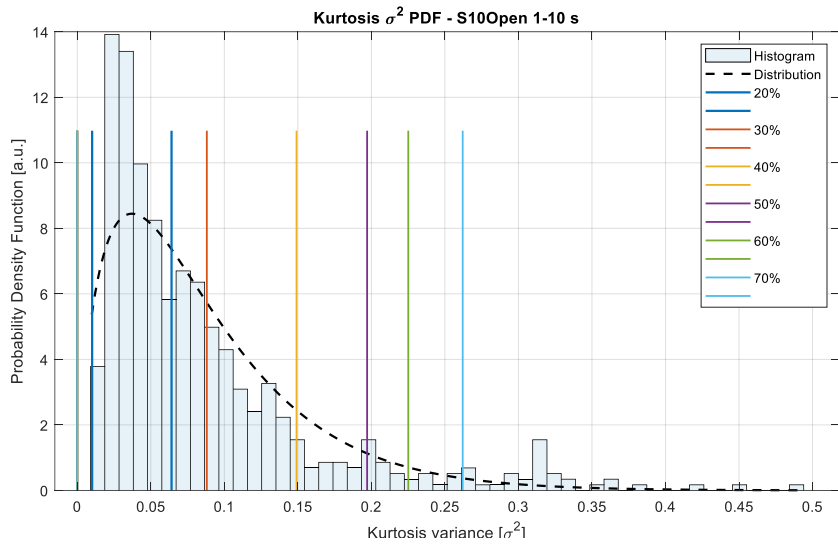
(f)



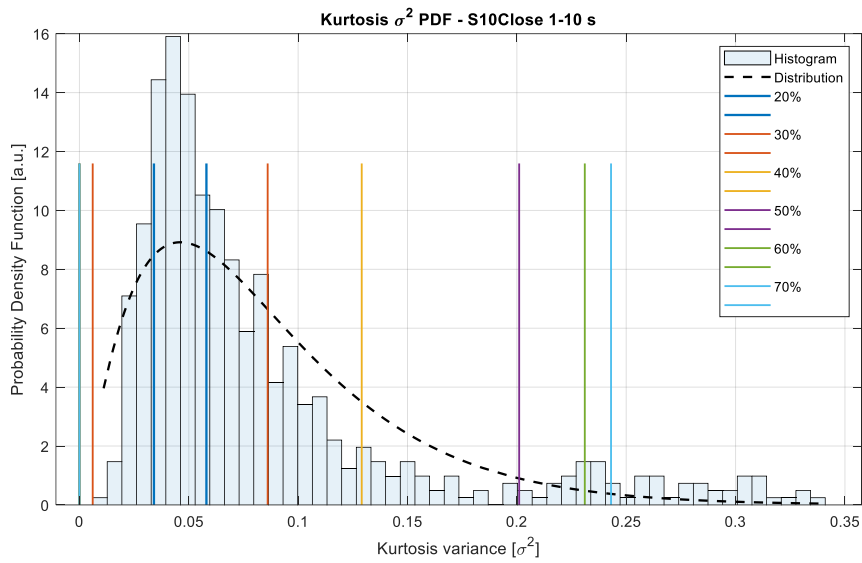
(g)



(h)



(i)



(j)

Figure 44. K_{σ^2} PDFs and the corresponding searching intervals with respect to max σ^2 proportion thresholds. Resting state conditions depicted in pairs: a, b) S5 – R1, R2. c, d) S6 – R1, R2. e, f) S8 – R1, R2. g, h) S9 – R1, R2. i, j) S10 – R1, R2

The distributions that are built from the kurtosis variance values coming from the statistical feature matrices represented in Figure AN 2 are depicted in Figure 44. As can be noted, the distributions follow a chi-square (χ^2) approximation since they correspond to the variance density of a normally distributed quantity (i.e. the kurtosis, as demonstrated previously). From the distributions and the corresponding percentage thresholds, the searching strategy finds the K_{σ^2} intervals in within the segments exhibit a variance in such limits.

The corresponding interval bounds for each percentage threshold on each dataset are plot as the parallel lines that limit a portion of the PDF. The broader the threshold limits, the larger is the area from the PDF being covered, and according to the considerations of this work, the purpose is to maintain that interval as short as possible and at the same time maximizing the number of channels sharing the same characteristics. As the datasets are independent of each other (even for the same subject), each resulting density has its own characteristics, which considering the relative values that are found it is needed then to obtain a representation of common channels sharing the same stationary attributes derived from the kurtosis quantity.

To do so, first, let's have a look at Table 6 and Table 7 which consider the variance interval at different percentage thresholds for all of the EEG recordings in both resting-state conditions respectively.

Table 6. Kurtosis variance range of different percentage thresholds, $w_i = 1,2, \dots, 10$ seconds. Subjects S5, S6, S8, S9, and S10 in opened-eyes resting-state condition R1

R1	Bound	10%	20%	30%	40%	50%	60%	70%	80%	90%	100%
S5	Lower	0.0346	0.0076	0	0	0	0	0	0	0	0
	Higher	0.0446	0.0716	0.1066	0.1556	0.2396	0.2556	0.2716	0.3216	0.3526	0.4156
S6	Lower	0	0	0	0	0	0	0	0	0	0
	Higher	0.0537	0.0877	0.1377	0.2007	0.2307	0.2487	0.2817	1.0197	0	0
S8	Lower	0.034	0.011	0	0	0	0	0	0	0	0
	Higher	0.044	0.067	0.098	0.155	0.188	0.208	0.22	0.251	0.296	1.04
S9	Lower	0.0334	0.0064	0	0	0	0	0	0	0	0
	Higher	0.0554	0.0824	0.1174	0.1554	0.2414	0.2834	0.3054	0.3344	0.3774	0
S10	Lower	0.0311	0.0101	0	0	0	0	0	0	0	0
	Higher	0.0431	0.0641	0.0881	0.1491	0.1971	0.2251	0.2621	0.3101	0.3221	0.4901

Table 7. Kurtosis variance range of different percentage thresholds, $w_i = 1,2, \dots, 10$ seconds. Subjects S5, S6, S8, S9, and S10 in closed-eyes resting-state condition R2

R2	Bound	10%	20%	30%	40%	50%	60%	70%	80%	90%	100%
S5	Lower	0.0747	0.0357	0.0037	0	0	0	0	0	0	0
	Higher	0.0907	0.1297	0.1617	0.1967	0.2477	0.2727	0.2927	0.3127	0.4117	0
S6	Lower	0.0542	0.0402	0.0152	0	0	0	0	0	0	0
	Higher	0.0602	0.0742	0.0992	0.1342	0.1902	0.2162	0.2372	0.2582	0.2732	1.0582
S8	Lower	0.0648	0.0578	0.0318	0	0	0	0	0	0	0
	Higher	0.0688	0.0758	0.1018	0.1498	0.1958	0.2438	0.2858	0.3238	0.3628	1.0678
S9	Lower	0	0.2004	0.1984	0.1924	0.1884	0.1604	0.0754	0	0	0
	Higher	0	0.2084	0.2104	0.2164	0.2204	0.2484	0.3334	0	0	0
S10	Lower	0.0441	0.0341	0.0061	0	0	0	0	0	0	0
	Higher	0.0481	0.0581	0.0861	0.1291	0.2011	0.2311	0.2431	0.2691	0.3011	0.3381

Table 6 and Table 7 summarize the upper and lower bounds of the kurtosis variance ranges associated with the percentage thresholds that go from 10% to 100% of the maximum variance accounted for on the EEG signals of each recording. As can be observed, a great part of the

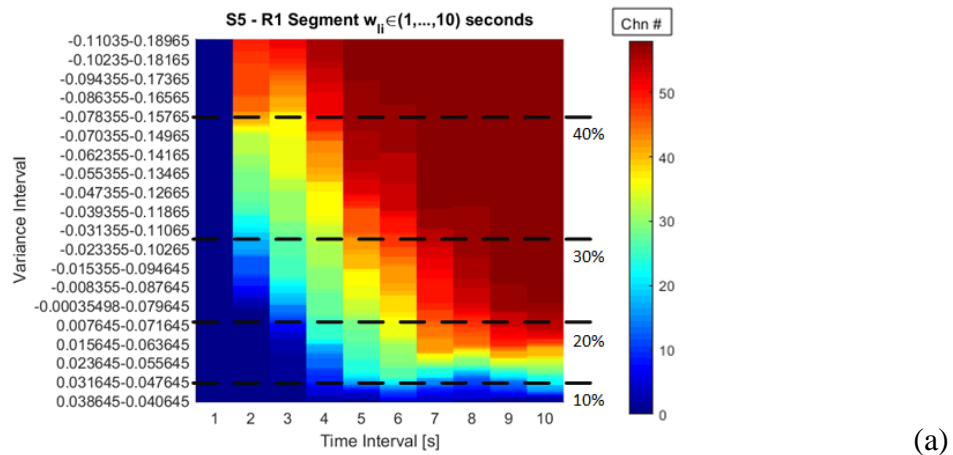
lower bounds of higher percentage thresholds (starting from the 30% in the R1 case excluding S6, and 40% in the R2 case, except S9) are assigned to a zero value. This means that the algorithm at that lower bound was out of range going towards the negative values of the PDF, which is not possible since the lower value of a quantity like a variance is always greater than zero, so any negative lower bound is redefined as zero, which is useful for representation and analysis.

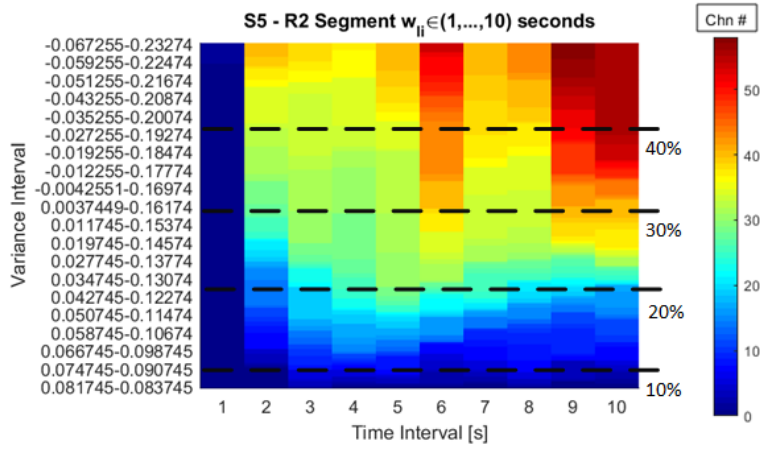
All of the interval limits comprised in the last two tables are graphically depicted in Figure 44, and as can be inferred from the graphs and the data, these bounds cannot be modeled or generalized among the EEG datasets but only explained through the densities. The compound of intervals and thresholds are data-dependent and correspond to the unique characteristics of the distributions.

Considering the particularities of the bounds, it can be noted that the lower limits are prone to go towards negative values as the searching interval and the percentage thresholds increase, this is due to the skewed shape of the χ^2 distribution and the searching approach which follows a linear increase of the searching intervals considering only the point of the largest probability of the density as the principal parameter to perform the searching.

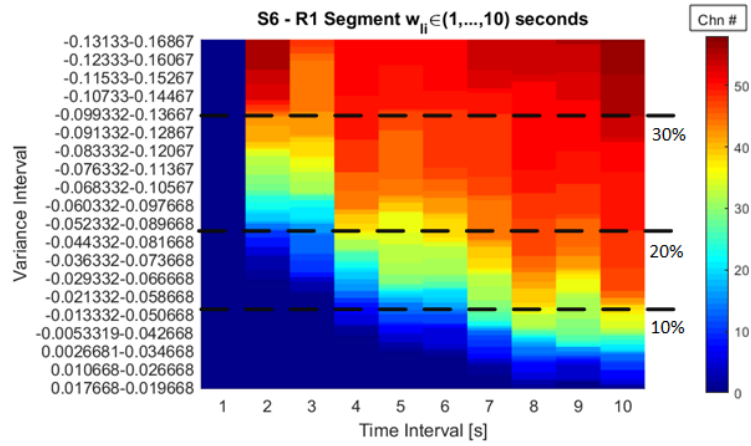
Considering the distribution S6 – R1 (Figure 44.c), it can be seen that it follows a very narrow and uniform tendency, despite preserving 75% of its original length after data cleaning (see Table 3), the kurtosis variance distribution is not in compliance to the characteristics of the other datasets. This observation suggests that the dataset presents odd features w.r.t the expected statistical behavior, thus it can be considered to be discarded, however, for comparison purposes, it is used to provide further analysis.

From the searching intervals, it is then possible to count how many channels exhibit similar stationarity as a function of the segment length. Thereby, Figure 45 shows the number of channels that a certain percentage threshold covers w.r.t the segment length. Each heat plot is the result of the processing of a subject’s recording and it was performed for resting-state conditions R1 and R2.

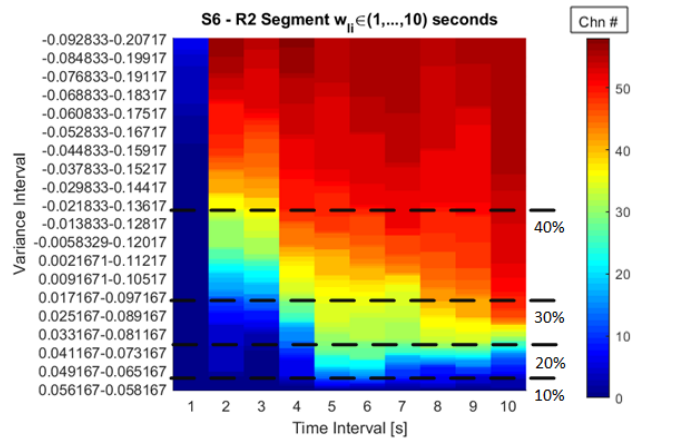




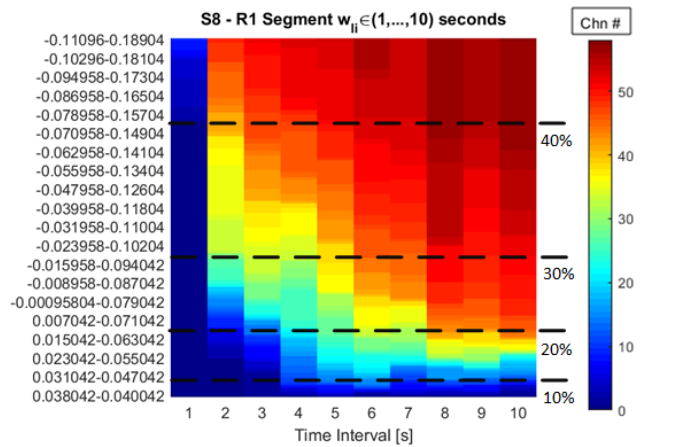
(b)



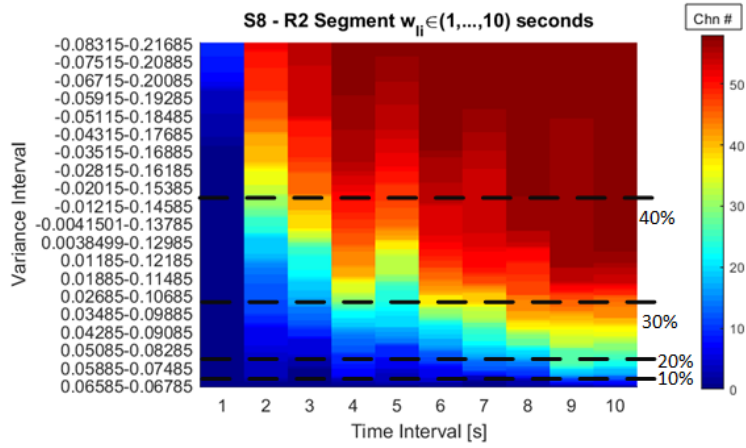
(c)



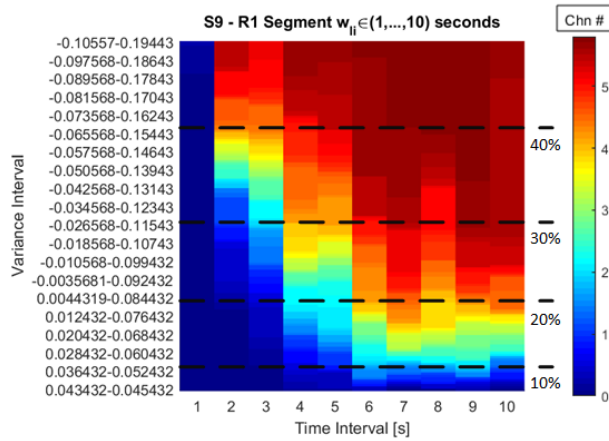
(d)



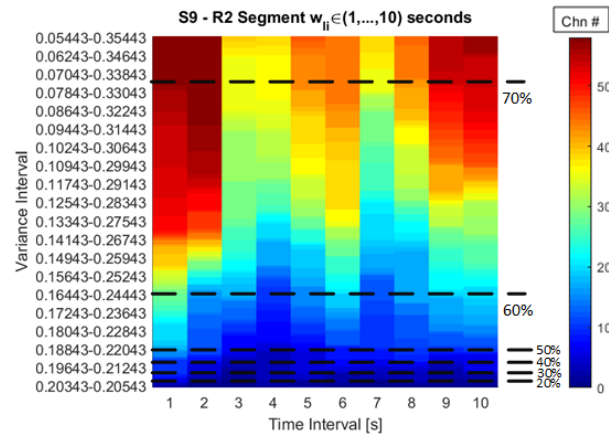
(e)



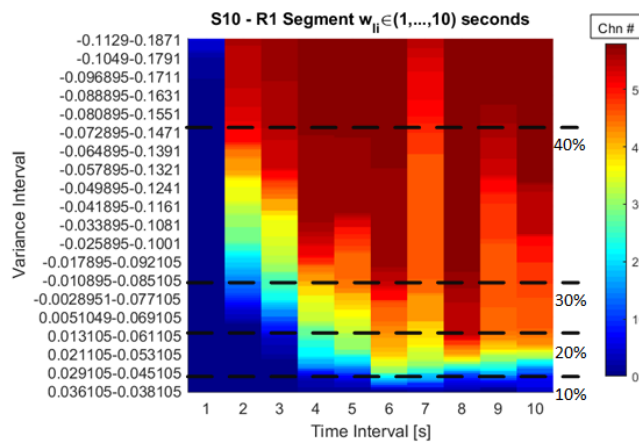
(f)



(g)



(h)



(i)

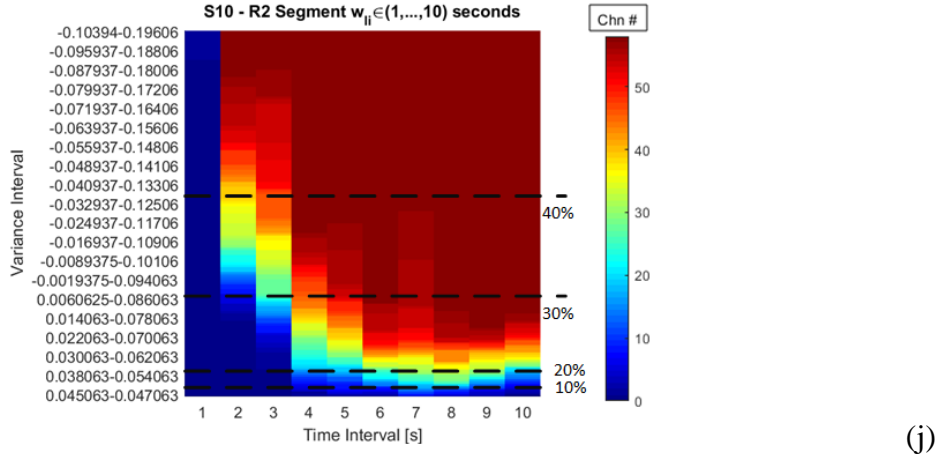


Figure 45. The number of channels as a function of the segment length and the searching interval in terms of the kurtosis variance – Long window segmentation.
a, b). S5 – R1, R2. c, d). S6 – R1, R2. e, f) S8 – R1, R2. g, h) S9 – R1, R2. i, j) S10 – R1, R2

Considering the intervals that are summarized in Table 6 and Table 7 (which are graphically depicted as the boundaries of the searching intervals on each PDF of Figure 44), there are derived the heat plots of Figure 45. On each of these plots, the percentage thresholds considering the values of the tables are represented as the dashed lines with their corresponding labels. The y-axis is referred to the kurtosis variance interval at which a certain number of signals share a value of variance within those limits. In accordance, it is possible to look for the intervals associated with the percentage thresholds as can be observed.

By setting the thresholds in the variance range that cover a certain number of channels helps to decide which of the segment lengths should be used to maximize the number of channels sharing similar magnitudes of the variance. Besides, by taking into account the corresponding K_{σ^2} distributions of each heat plot, it can be performed an informed decision of the portion of the density that is being considered and delimited by the variance interval, so it is determined the largest portion of the density that is going to be used to select the segment duration.

In most of the heat plots that were produced, the largest number of signals is found when the segmentation is done considering larger windows, it also increases as the variance interval is larger, however, the increment in the number of channels is not sensitive to shorter window durations, so it is necessary to consider larger thresholds to obtain a greater number of signals for short segments. As can be noted from the graphs, this behavior is common for all the plots except for Figure 45.h, corresponding to S9 – R1.

The dataset S9 – R1 is a particular example of the EEG characteristics that have been discussed so far. The kurtosis variance interval needed to account for the majority of channels is very broad (in respect to the min and max values of the K_{σ^2} of the dataset) which suggests that to obtain a large number of channels it is needed to consider the whole searching domain (Figure 43.h). By these observations, the S9 – R1 dataset could be discarded as well as the S6 – R1, as explained earlier.

In this way, according to the long window segmentation approach ($W_L = 1s, N_w = 10$), this analysis derived from the datasets that do not have any particularity can be treated as a common pattern for the kurtosis variance distributions.

Segment length selection strategy

Then, a process of window selection is performed by considering the shortest window within a kurtosis variance interval defined at the portion of the PDF with the broadest area and the lowest percentage range as possible. For the current state of this development, this is performed by

visual inspection considering the searching domains, the kurtosis variance probability distributions and the K_{σ^2} /segment-length plots like the ones on Figure 43 Figure 45.

Considering this selection strategy for the EEG datasets from subjects S5, S6, S8, S9, and S10 in R1-R2, Table 8 is built and summarizes the segment lengths that were considered for selection with their characteristics, including the variance intervals, their percentage thresholds, and the number of channels found within the interval.

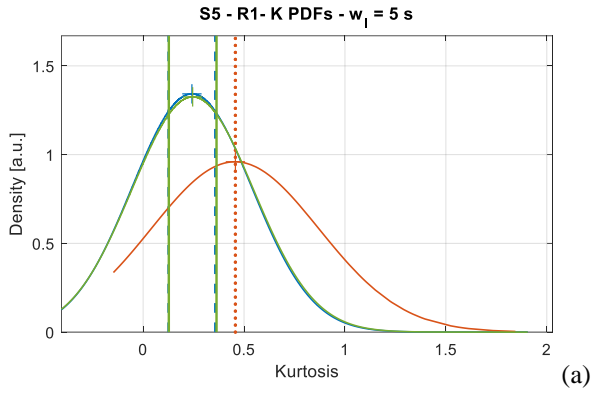
Table 8. Selected segment lengths (in green) for each subject and resting-state condition.

Subject	Condition	Lower	Upper	%	Win length	# Channels	Channel %
S5	R1	0.00764502	0.07164502	20%	7 s	44	--
		0	0.10664502	40%	4 s	48	--
		0	0.15564502	30%	5 s	41	72%
	R2	0	0.19674487	40%	4 s	29	49%
S6	R1	0	0.13766813	30%	4 s	35	61%
	R2	0	0.13416711	40%	4 s	48	80%
S8	R1	0	0.09804196	30%	4 s	33	54%
					5 s	38	--
	R2	0.03184988	0.10184988	30%	4 s	27	44%
S9	R1	0	0.24143193	50%	3s	50	91%
					4 s	50	--
	R2	0.13543015	0.27343015	67%	2 s	48	83%
S10	R1	0	0.08810486	30%	4 s	45	75%
	R2	0.00606251	0.08606251	30%	4 s	47	77%
5 s					54	--	
						Mean	69%

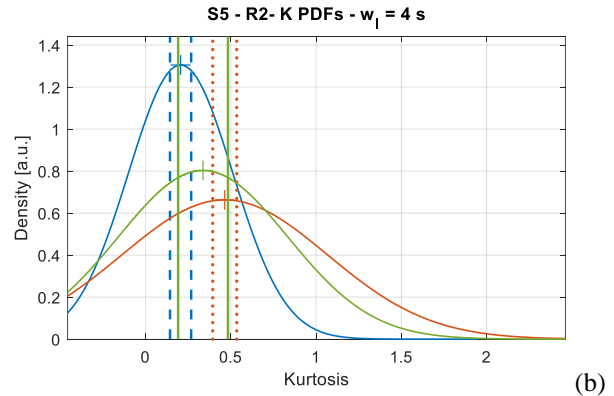
By considering the kurtosis variance distributions in Figure 44, some of the lower and upper boundaries on each dataset are considered for the selection of the window length in Table 8. As can be noted from the percentage thresholds, the proportions considered are from 30 to 40% of the largest variance of the segmentations. The heat plots in Figure 45 define which would be the segment length according to the segment length selection strategy discussed above. As result, for most of the subjects in both resting-state conditions, the most common window length was found at 4 seconds (for 7 out of 10 datasets).

As result, the selected window lengths (w_l) on each resting-state condition cover the most significant part of the PDF distribution in which more channels exhibit similar variances. As can be noted in the last column of the table, the number of channels being selected represent a large proportion of the original channel size after preprocessing, in all of the cases they represent more than two-thirds of the signals sharing similar stationary characteristics on average.

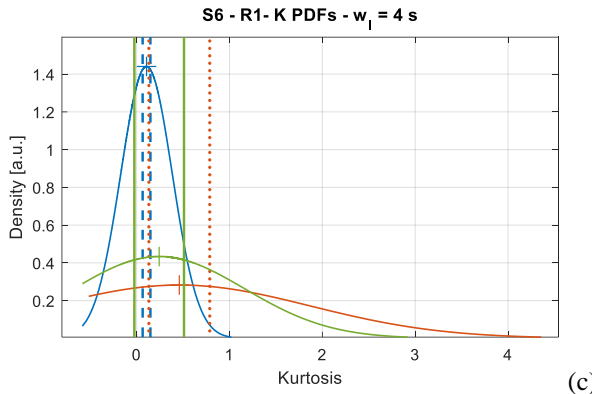
From these results, it can be said that the objective of maximizing the number of channels is being accomplished by analyzing the datasets in a relative way, i.e., according to the characteristics of each dataset. Now, it is necessary to show which are the deviations that exist in the kurtosis domain. Since the idea of considering the kurtosis variance as a feature is to select it in a way that is as small as possible and common for the signals composing an EEG dataset so that is reflected in the kurtosis distributions. To do this, Figure 46 shows the corresponding kurtosis distributions of all the signals from each dataset segmented at the selected window (from Table 8), in addition, the kurtosis densities fitted from the selected channels and the PDFs of the discarded signals are also shown.



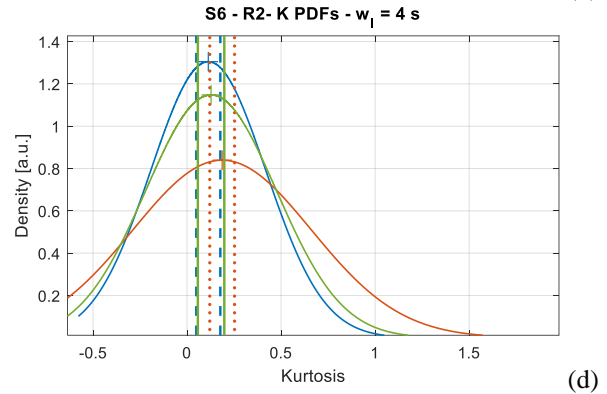
(a)



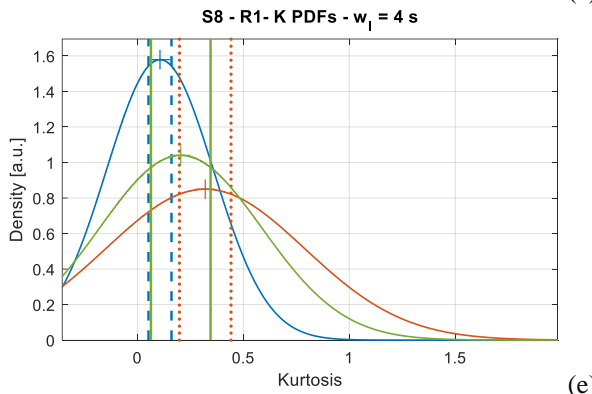
(b)



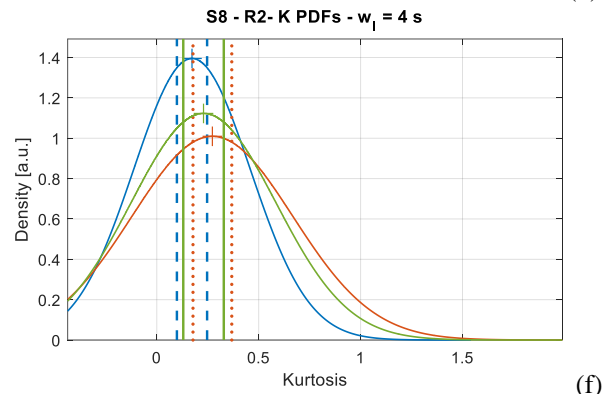
(c)



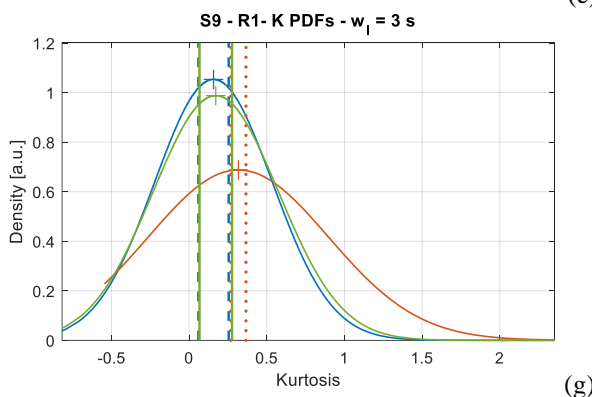
(d)



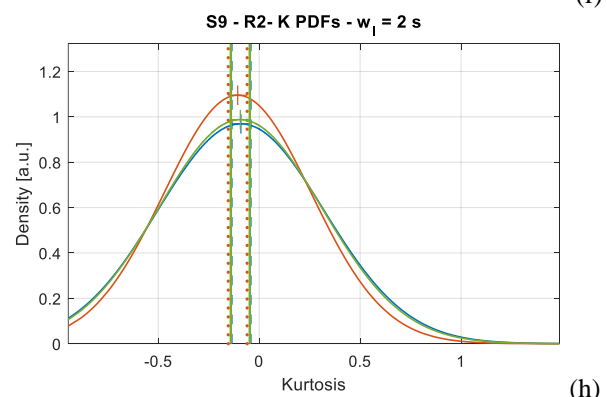
(e)



(f)



(g)



(h)

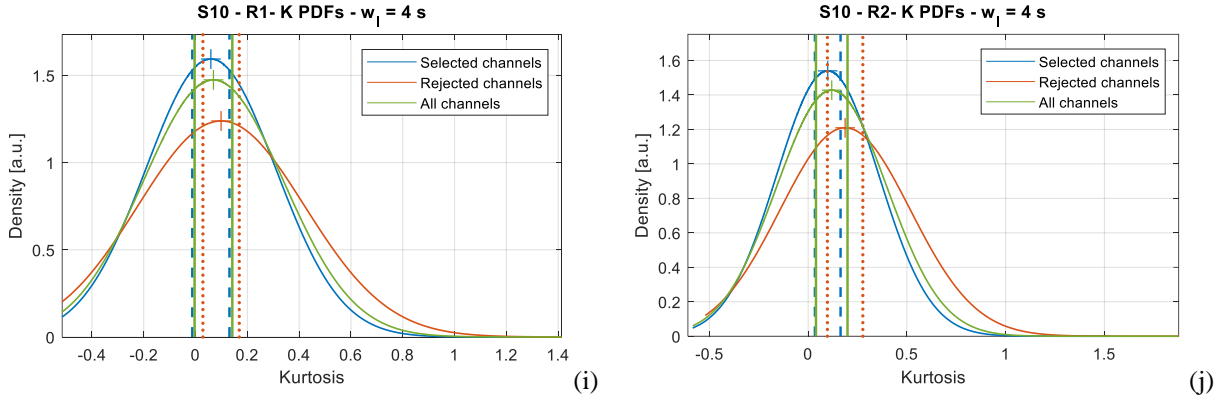


Figure 46. Kurtosis distributions considering the selected channels from the percentage thresholds. – Long window segmentation. Resting state conditions depicted in pairs: a, b) S5 – R1, R2. c, d) S6 – R1, R2. e, f) S8 – R1, R2. g, h) S9 – R1, R2. i, j) S10 – R1, R2

From the hypothesis of selecting the EEG signals that exhibit similar stationary characteristics using the segment durations that were chosen considering the kurtosis variance distributions and the searching intervals derived from the searching algorithm, it is possible then to consider the magnitudes of the kurtosis from each channel which comply with the variance range selected on each dataset.

Figure 46 shows the fitted distributions in three different cases:

1. By considering the kurtosis values of the whole set of signals composing a recording being subject of segmentation at the selected w_l (green plot on each figure).
2. Taking into account the channels that have kurtosis variances within the limits of the selected window length characteristics.
3. Using the channels that exhibit kurtosis variances outside the window length picked.

From this description it can be analyzed that kurtosis distributions coming from the selected channels should be different from the densities estimated from the signals considered for rejection since the stationary characteristics should be different and the spread, in this case, represented by the standard deviation, should be different from the one of the selected channels.

The parallel lines of the graphs in Figure 46 correspond to the standard deviation limits from the distributions, as can be observed, in almost all the graphs (Figure 46 a-g, j) the spreads from the blue (selected channels distribution) and the red (rejected channels distribution) are different from each other, and in some cases, they do not overlap at all (Figure 46 a, b, e, g). Since the expected kurtosis values are restricted by a narrow-spread interval defined by the variance range, it is supposed that the kurtosis estimations within that interval are close to each other and so they share similar stationary characteristics. Any signal not meeting these conditions has a larger variance and hence is discarded, which as consequence the compound of all of these signals provides a kurtosis distribution that should differ from the selected channels' density.

From the graphs in Figure 46, some cases have an overlapping in the expected value, however, the variance of those distributions is larger than the one defined by the condition of the percentage threshold. From it, the characteristics of the selected window durations in most of the cases (except for S9 – R2, Figure 46.h) correspond to these observations, which guarantee similar stationary characteristics among most of the channels composing the EEG recording.

Short-window duration analysis

The short window duration analysis of the EEG recordings of the subjects S5, S6, S8, S9 and S10 is included in the Appendix A.

6.1.3. Selected window durations

The results from the window selection for all the EEG recordings considered are summarized in Table 9.

Table 9. Segment selection for the considered EEG recordings

Subject	Condition	$w_l \in 1, \dots, 10 \text{ s}$	$w_s \in 50, \dots, 1000 \text{ ms}$
S2	R1	5 s	250 ms
	R2	2 s	300 ms
S5	R1	5 s	400 ms
	R2	4 s	200 ms
S6	R1	4 s	500 ms
	R2	4 s	450 ms
S8	R1	4 s	400 ms
	R2	4 s	400 ms
S9	R1	3 s	250 ms
	R2	2 s	400 ms
S10	R1	4 s	400 ms
	R2	4 s	450 ms

Table 9 shows the results of the window durations that were selected according to the segment length analysis that was proposed in this work. From the design of the algorithm, passing through the characterization and analysis of the kurtosis values derived from this approach, until the segment duration selection, this table shows the result of that process.

As it was commented before, the most common segment duration for the long window segmentation was the segment corresponding to 4 seconds being common in 7 out of 12 datasets in both resting-state conditions (6 subjects * 2 resting states). On the other hand, for the short window segmentation, the most common duration is 400 ms, which is common for 5 out of 12 recordings.

Regarding the channel selection that is derived from this framework, the set of channels that are common concerning each condition and segment length analysis type (short or long window segmentation), are shown in Table 10. In addition, the common elements across subjects, resting-state conditions, and type of segmentation are presented as a Venn diagram in Figure 47, and Table 11 shows the corresponding common channels in the intersection.

Table 10. Common channels of all the considered subjects according to resting-state condition on each segmentation approach

COMMON to 50 ms to 1 s	R1	PO4	FC1	CB1	FC2	Pz	Oz	P6	C3	CB2	17
		FC3	POz	CP1	PO8	PO3	P2	F3	C5		
	R2	CB1	PO6	Pz	O2	Oz	F5	P1	FC4	PO3	16
		P2	Fp1	F3	Fp2	AF4	CB2	O1			
COMMON to 1 s to 10 s	R1	P7	Pz	POz	CP1	CP6	C4	PO3	CP5	P2	13
		CP4	C5	CP2	P5						
	R2	FC1	FC2	FC4	C3	Fz	F1	FC3	C2	FCz	11
		C5	F2								

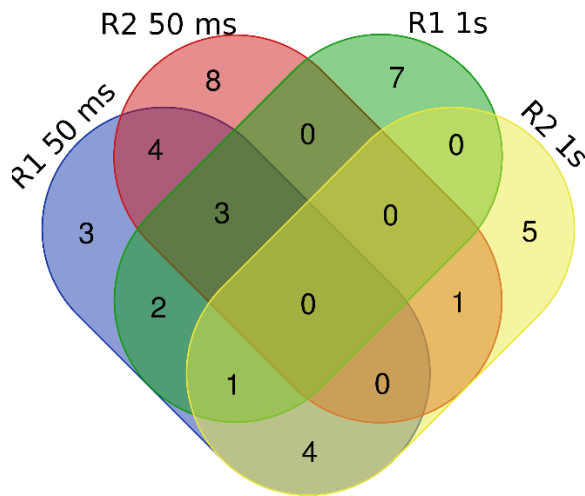


Figure 47. Venn diagram of the common channels across subjects and types of segments, derived from Table 10.
(Diagram generated using the web tool at <http://bioinformatics.psb.ugent.be/webtools/Venn/>)

Table 11. Common channels across subjects and segment types.

Data type	Common	Channels
R1-1s	3	P2
R1- 50 ms		PO3
R2-50 ms		Pz
R1-1s R1- 50 ms R2-1s	1	C5
R1 -50 ms R2- 50 ms	4	Oz
		F3
		CB1
		CB2
R1-1s R1- 50 ms	2	CP1
		POz
R1 -50 ms R2-1s	4	FC1
		FC2
		FC3
		C3
R2-1s R2-50 ms	1	FC4

From Table 10 it can be noted that there are 17, 16, 13, and 11 channels that are common across subjects for short segmentation in R1, R2, and long segmentation in R1, R2 respectively. These channels could be used as a further reference to compare not only the stationary characteristics on each dataset and the effective connectivity that exists among them but also to identify the EEG signals associated with them and analyze the common characteristics across the EEG recordings categorized by resting-state conditions and segmentation type.

Regarding Table 11 and Figure 47 there is no intersection of channels from Table 10 at any condition and subject. Some channels are shared in both resting-state conditions (e.g., 4 channels are shared between the R1 and R2 considering the short window segmentation), however, the number is not significant considering the total number of channels on a dataset which is 62.

6.2. Results on Effective connectivity

6.2.1. Results from state-of-the-art methods

Let us first apply the methods summarized in [45] and [46] that were explained in the section *Connectivity examples for resting state conditions*.

A. Comparison of connectivity analysis for resting state EEG data

As explained earlier in section *Comparison of connectivity analyses for resting state EEG data*, this work evaluated basic, integration, segregation and centrality measures explained in Table 15 for the delta, theta, alpha, beta, gamma frequency components as well as in the whole spectrum (1 – 50 Hz) by considering the DTF connectivity index to establish the causal relationships among the channels from the EEG equipment. In this way, the data available for this thesis (see EEG Dataset) were employed to recreate the same approach in order to establish similarities and differences on the connectivity results. A first comparable outcome of this process is evidenced in Figure 48 where the connectivity diagrams show the statistically significant relationships on their data and our data.

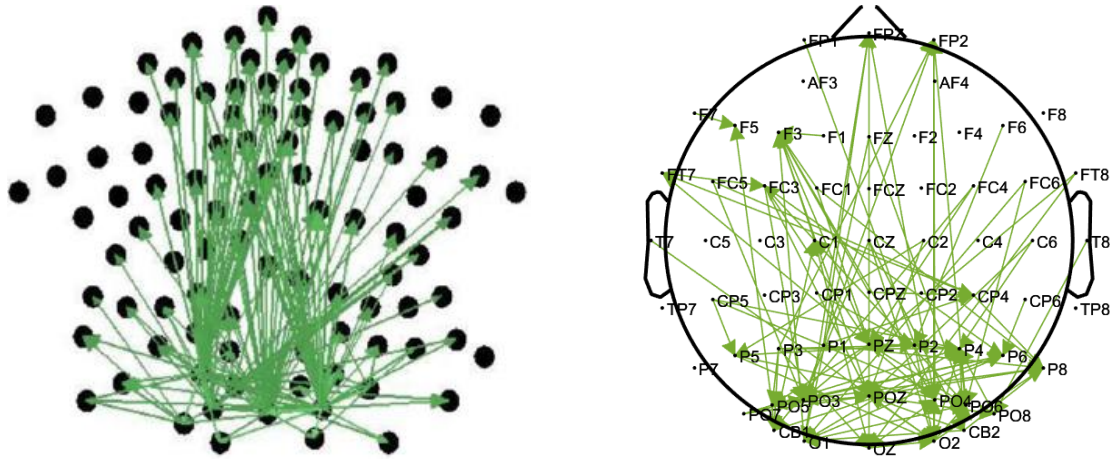


Figure 48. Connectivity diagrams of the window of 20 seconds using the DTF as connectivity measure - Connectivity during eyes closed (R2) condition. (left) results by [45] (right) results obtained with our data.

Considering the results from the work performed by Olejarczyk (Figure 48 - left), it can be observed a significant influence originated in the posterior region of the brain from which most of the connections are generated. The channels located in this area present local connections and provide an evident influence from the occipital-posterior region towards the channels located in the frontal area of the scalp. Similarly, the significant connections obtained from the data available for this thesis (Figure 48 - right) show similar connections that are kept in the posterior part of the scalp, being directed towards the frontal area as well.

The connections portrayed in these diagrams are a topographic representation of the scheme that was produced for the adjacency matrices (see Figure 32) as explained on the section of *Results on the graph theory indexes*.

Olejarczyk and colleagues provided an interaction analysis using the ANOVA statistical test and compared the eyes closed condition against the eyes open state for the alpha and beta frequency bands. On Table 12 there can be observed the ANOVA results and the p-values estimated from the interaction analysis for some of the graph-based parameters. The table includes some significant results for other connectivity measures employed in Olejarczyk's approach, including the multivariate transfer entropy (MV-TE) and the phase locking value (PLV) which are included in the table for comparison purposes.

Table 12. Interaction analysis between Condition*Band (Eyes open/Eyes closed * Frequency band – Alpha and Beta)

Graph based parameter	OLEJARCZYK et.al.						IBFM Dataset	
	MV-TE		PLV		DTF		DTF	
	ALPHA	BETA	ALPHA	BETA	ALPHA	BETA	ALPHA	BETA
Density	↑ Alpha (p < 0.0001)	- (p > 0.05)	↑ Alpha (p < 0.0001)	- (p > 0.05)	- (p > 0.05)	- (p > 0.05)	- (p > 0.05)	- (p > 0.05)
Strength	↑ Alpha (p < 0.0001)	- (p > 0.05)	↑ Alpha (p < 0.0001)	↑ Beta (p < 0.0001)	- (p > 0.05)	- (p > 0.05)	↑ Alpha (p < 0.0001)	- (p > 0.05)
Degree	↑ Alpha (p < 0.0001)	- (p > 0.05)	↑ Alpha (p < 0.0001)	↑ Beta (p < 0.0001)	- (p > 0.05)	- (p > 0.05)	- (p > 0.05)	- (p > 0.05)

Considering the interaction analysis summarized on Table 12, it can be observed that our results are consistent with the approach from Olejarczyk and colleagues. By evaluating the resting state conditions and the frequency bands using the data available for this thesis (IBFM dataset), the only statistically significant increment was evidenced for the alpha band on the strength

parameter which according to the ANOVA analysis its significance was evidenced for the channels located in the frontal, central and right lateral regions of the EEG setting. This is one main difference relative to the work made by Olejarczyk’s team since they did not find any significant increment for these three basic graph features using their data when the DTF measure was employed.

The degree and density were not statistically significant as it was evidenced in this thesis work as well. On the other hand, other measures like the multivariate transfer entropy and the phase locking value gave evidence of the significance on the alpha band. According to the authors, these measures account for the nonlinear characteristics exhibited by the EEG signals and those cannot be measured by linear models like the multivariate autoregressive employed for the DTF estimation.

Other result compared with the Olejarczyk’s approach corresponds to the difference of the connectivity measures between closed eyes and open eyes in the alpha band. The difference between the conditions is observed in Figure 49, and establishes the statistically significant differences ($p < 0.05$) observed between closed and open eyes.

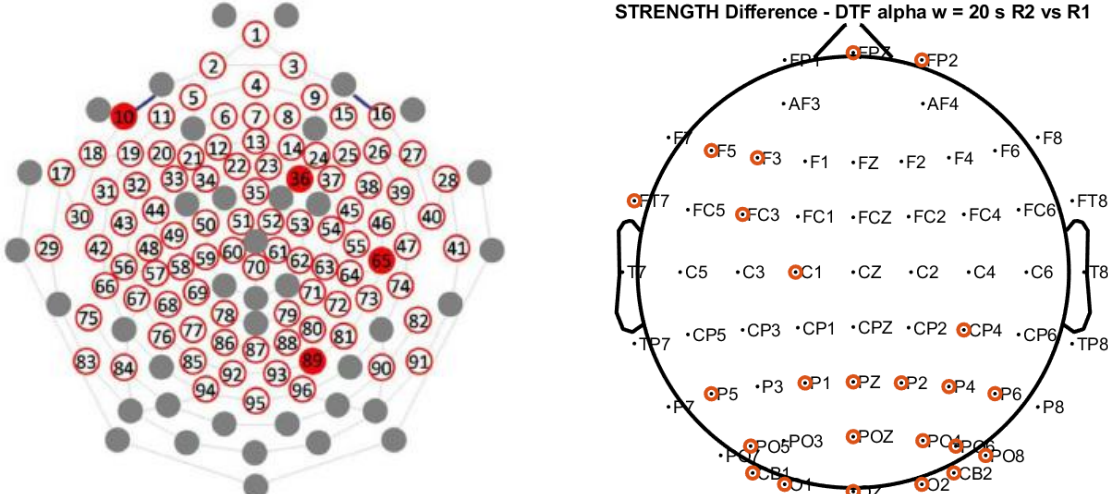


Figure 49. Strength difference between eyes closed and eyes open. (left) results by [45] (right) results obtained with our data.

Figure 49 shows the differences on the strength parameter between the closed and open eyes conditions. As can be observed from the results, the significant differences from Olejarczyk’s work (Figure 49 - left) show only 4 out of 96 electrodes (red filled circles) exhibiting significantly higher values on the strength when the closed eyes condition was produced. On Figure 49 right, for our data it is shown a distribution of channels that evidence a significant difference among those conditions when the alpha band was evaluated. In this case, there is an increment on the DTF amplitudes produced on the posterior area when the closed eyes condition was performed. Moreover, some central-frontal electrodes and prefrontal electrodes have larger amplitudes and provide a very similar distribution of central channels found in Figure 58. Specifically, channels from the pre-frontal, the left central-frontal joint and the parietooccipital region in a bilateral way exhibited higher values during the closed eyes condition in comparison to the open eyes state.

B. The difference of brain functional connectivity between eyes closed and eyes open using graph theoretical analysis

By applying the methods from [46] to our data, considering the characteristics explained in the section *The difference of brain functional connectivity between eyes-closed and eyes-open using graph theoretical analysis.*, there were found the connectivity indexes that characterized the resting state conditions as a function of the partial connections present in the connectivity diagram. Figure 50 shows the result of the mean cluster coefficient, local and global efficiencies that were obtained in relation to the cost of the network in the range of proportions of effective connections between 8% to 20% for the alpha frequency band.

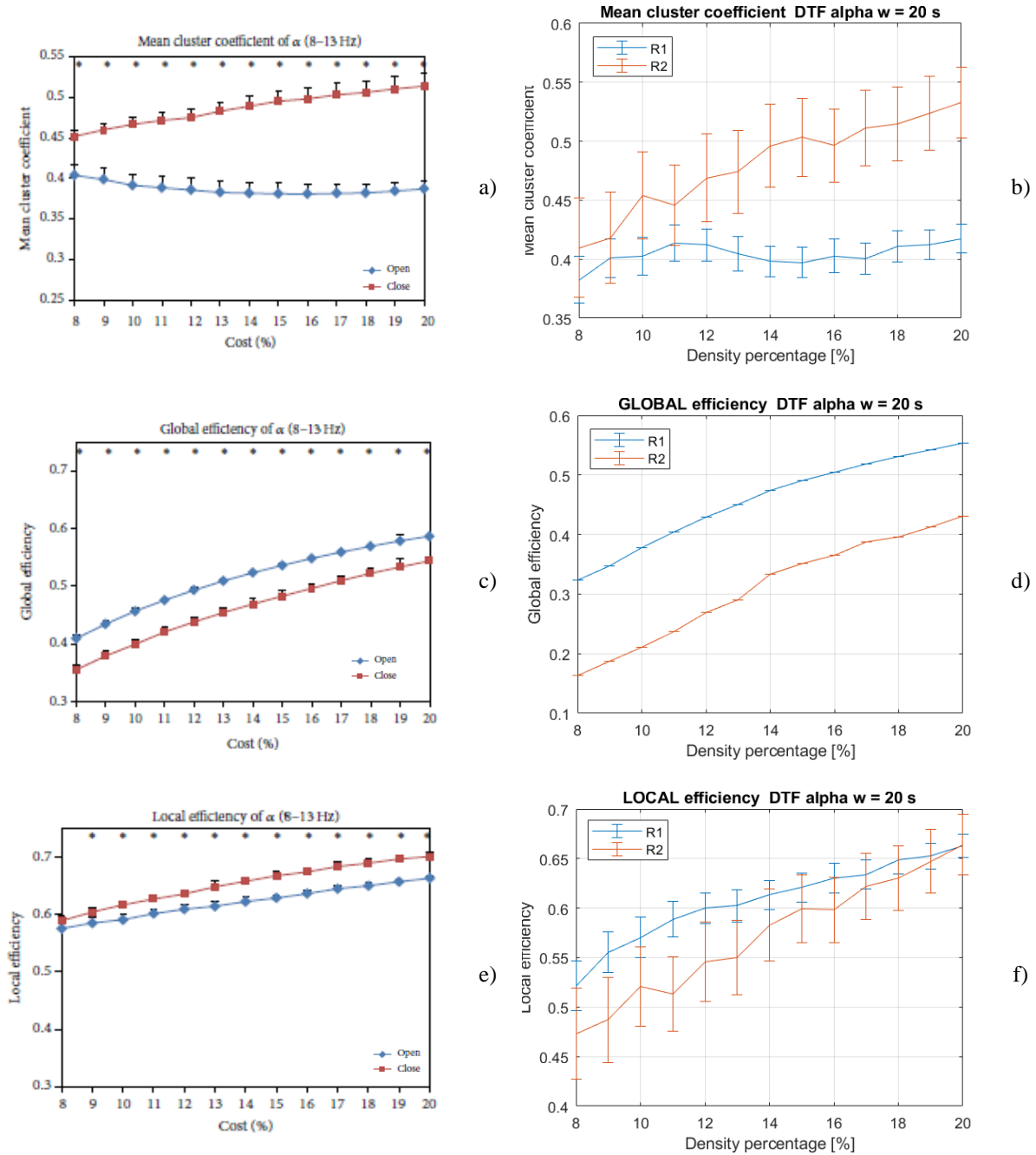


Figure 50. Graphs of mean cluster coefficient, global efficiency, and local efficiency as a function of the cost in the range of 8% - 20% at each resting state condition for the alpha band. Figures on the left are the results obtained by [46], and the ones on the right correspond to the results with the IBFM data.

On Figure 50 a, c, e, there are depicted the results of some graph parameters that summarize the variation over the cost in the network found from the data of Tan and colleagues. As can be observed, there is an increment of the local efficiency and the mean cluster coefficient over the range of costs for the closed eyes condition (red squared markers), while the global efficiency experimented a decrease for the same condition. On the other hand, the reduction of the local efficiency during the eyes open state is contrasted by the opposite trend applied to the IBFM data (Figure 50 f). This is a main difference for the alpha band characterization with respect to Tan's work. However, as it can be noted from the remaining graph-based parameters, the trends follow similar behaviors, even for the amplitudes of the measures that have been calculated. Figure 51 summarizes the results of the same graph parameters on the beta frequency band.

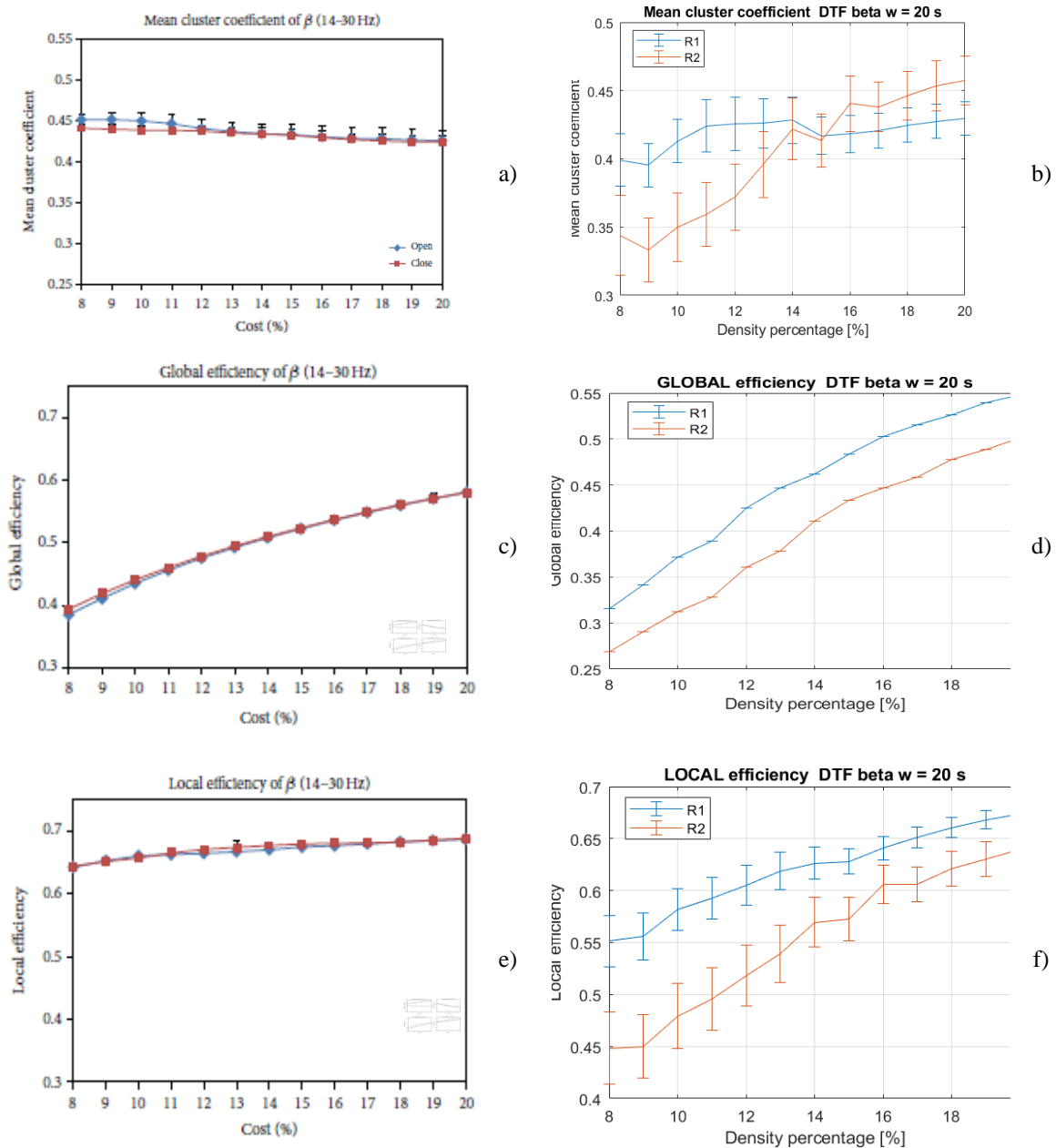


Figure 51. Graphs of mean cluster coefficient, global efficiency, and local efficiency as a function of the cost in the range of 8% - 20% at each resting state condition for the beta band. Figures on the left are the results obtained by [46], and the ones on the right correspond to the results with the IBFM data.

The results summarized in Figure 51 considering the data available for this thesis regarding the processing on the beta band range show more explicit differences in comparison with the alpha band case. Here there are significant variations that can be used to characterize these resting state conditions. The results by Tan and colleagues (Figure 51 a, c, e) show no significant differences in their data, the graph based indexes are not useful according to their approach to characterize the resting state conditions as opposed to the results obtained with the IBFM data (Figure 51 b, d, f). Specifically, the efficiency calculated globally and locally provide a significant difference by accounting the 95% in the confidence interval at each step of the cost variation.

Similarly to the alpha band case, the efficiencies incremented for the eyes open condition providing a way to characterize the resting states at each frequency band.

From the application of the connectivity approaches summarized in [45], [46] to our data, there were found the following observations:

- The local connections are reduced in the bilateral posterior area for the alpha band in the open eyes condition as could be evidenced in the connectivity diagrams from Figure 57.
- There is a bilateral distribution of the alpha rhythm over the posterior areas for the eyes closed state.
- During the state of eyes closed, there were exhibited more long-range connections coming from the posterior area in comparison to the eyes open condition.
- Eyes closed state had a stronger local activity in bilateral posterior areas in comparison with eyes open.
- After opening the eyes, the connections in the frontal area significantly decreased in the alpha band.
- The topological features of nodes and connections were significantly reduced in the posterior area when the state was eyes closed compared to the eyes open condition.
- It is hypothesized the involvement of channels belonging to the Default Mode Network (DMN) which are important part of the so-called resting state network.
- The main difference concerning the graph measure results considering our data are:
 1. The local efficiency for the alpha band (α) increased for the eyes open condition rather than the eyes closed one.
 2. There is a significant difference evidenced for the efficiencies in global and local terms between R1 and R2 for the beta band. This can be used to characterize the resting state conditions.

These observations can help to characterize the resting state conditions under analysis. The common observations regarding the group of channels that exhibit interconnections and the relationships to other areas are very similar to Olejarczyk results, however, the significance of the strength parameter was different in our data, which could be explained by the data available; in our case there were considered a smaller number of subjects and the adjacency matrices exhibited different distributions of electrodes participating on the connectivity.

On the other hand, by comparing Tan’s work, the graph-based parameters applied to our data showed different results for the beta band, suggesting that these could be used for characterizing the resting state conditions considering higher frequency rhythms, something that Tan and colleagues did not observe in their results.

6.2.2. Connectivity analysis from the ROIs point of view

The adjacency matrices obtained from the previous processing stage provide the significant connections that can be used to perform the connectivity analysis by considering the channels as sources. This analysis at the level of the channel domain gives a detailed view of what is happening with the connections and how they provide information on the influence among the sources as it was described in the examples explained in the section *Connectivity examples for resting state conditions*.

This detailed point of view can be difficult to analyze considering the large number of nodes that are present in the network, in this way, first, it is considered the definition of regions of interest (ROIs) that could lead to a more general point of view that characterizes the connectivity among broader areas in the scalp. Thus, the ROIs defined from the topographic map of electrodes was defined as shown in Figure 52.

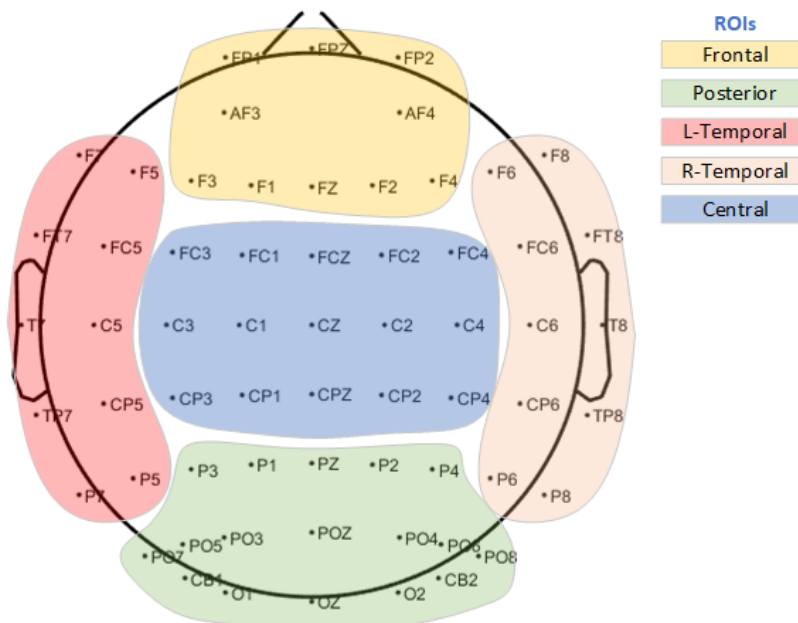


Figure 52. Regions of interest definition comprising the frontal, posterior, left-temporal, right-temporal and central regions.

The ROIs shown in Figure 52 are defined considering the works described in [23], [29], [33], [47]. These ROIs comprise the 62 channels of the EEG montage, however, by recalling the pre-processing stage in which some of the channels are discarded due to artifacts and filtering, the channels that are marked as not useful are not being considered part of the ROIs and they are ignored in the following calculations.

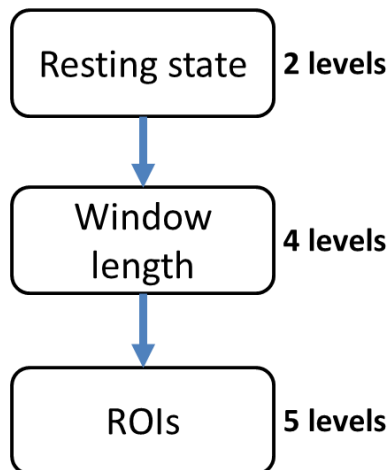
Considering the ROIs and the adjacency matrices found previously (see section Adjacency matrices), the DTF arrays that account for the connectivity in the network defined in the sensor space were employed to analyze the average strength from the ROIs as well as the relative density estimated from the group of channels that belong to each region. As a way to evaluate this, the ANOVA statistical tool was employed for this purpose.

A. The ANOVA analysis

The analysis of variance is a way to measure and establish the possible interactions that can be obtained from measuring different variables of interest under repeated measuring or particular settings. In this case, according to the examples and the state of the art described in the section *Applications of effective connectivity*, the factors considered for analysis can be defined from the condition under analysis (e.g., resting state, attention task, pathological/control, etc.), the source definition (e.g., the channels comprising the EEG acquisition system as shown in the previous section, the ROIs, or dipoles), the frequency band (e.g., alpha, beta, gamma, delta, theta, or non-conventional frequency bands), the SNR and path length from known networks (e.g., based on the analysis of synthetic signals [23]), or graph theory parameters (e.g., density, degree, strength, etc. [71], [72]).

In this way, there can be established the connectivity relationships of the physiological rhythms, their directionalities and the influence of a source that exerts onto another one. And as result, there can be characterized the high-level neural processes carried out by the subjects at specific experiment set-ups. In this case, it is done for the resting-state conditions during eyes open and eyes closed events. The ANOVA set-up is defined as depicted in Figure 53.

Three factors



INTERACTIONS

- a. Resting-State * Window-length
- b. Resting-State * ROI
- c. Window-length * ROI
- d. Resting-state * Window-length * ROI

ANALYSIS OF INTERACTIONS

1. Three-way interaction
2. Simple two-way interactions
3. Simple main effects
4. Simple comparisons

Figure 53. Three-factor ANOVA analysis and the possible interactions.

The three-factor ANOVA considers 2 levels for the resting state condition (i.e., eyes open (R1) and eyes closed (R2)), 4 levels for the window length (i.e., window sizes: 400ms, 2s, 4s and 20s), and 5 levels for the regions of interest (i.e., frontal, right-temporal, left-temporal, central and posterior). As result, two-way and three-way interactions as well as their main effects corresponding to each of the levels are obtained, and the statistically significant results show the connectivity patterns across the regions of interest.

The ANOVA analysis was defined for the ROIs since it was more convenient due to the number of repeated measures and the limited number of variables for the third factor (ROI factor). Here, there are defined two graph-based measures corresponding to the average strength and the average density of each region in contrast to the sensor space which also considers centrality, segregation and integration measures which can be only addressed in the nodal point of view according to what the theoretical definitions of the graph-theory states (see *Connectivity in the sensor space: Graph Theory indexes*).

In this way, considering that only two measures by region are being used (i.e., the relative density and relative strength), the definition of only five broad sources (i.e., the regions of interest), the 4 windows employed and the two frequency bands under analysis, then, it is possible to perform an ANOVA analysis. Hence, it would represent a less complex scenario for the processing rather than considering 62 sources and 8 graph-based measures to obtain the statistically significant measures and the connectivity between those regions.

B. Connectivity results

The connectivity measures are evaluated by considering the strength (amplitude) and the number of connections that are directed from or towards a node (e.g., an electrode) as explained previously. The definition of regions of interest (ROIs) permits the evaluation of the extent of connectivity in long and short distances [33], as well as to reduce the complexity in the evaluation of results in accordance to the high number of signals coming from the EEG cap (62 electrode sources at most in this setting).

In this way, the frontal, left-temporal, right-temporal, central and posterior regions as shown in Figure 52 were defined, and then, the degree measure was transformed into a normalized density by using the average degree value on each region and dividing it by the number of possible connections given the electrode array and the first line of electrodes interacting in-between regions. From this process, the average strength and the normalized density at each region were used to evaluate the connectivity from the defined ROIs.

*C. Three-factor interaction (Resting State * Window length * ROI)*

The first stage of analysis corresponds to the three-factor interaction that exists among resting state conditions, window length and regions of interest. The three-way interaction analysis determines if there exists an interaction effect between the conditions (R1/R2), the window lengths (400ms, 2s, 4s and 20s) and the ROIs (frontal, left-temporal, right-temporal, central and posterior) on a dependent variable, in this case, either the normalized density or the strength at the alpha or beta frequency bands. It means that there were defined four different 3-way ANOVA; for the normalized density in alpha band, average strength in alpha band, normalized density in beta band and average strength in beta band.

After performing the Mauchly's test of sphericity and performing the Greenhouse-Geisser correction on the normalized density and the relative strength for alpha and beta bands, the following tables comprise the p-values that summarize the significance of the interactions from the factors that are being evaluated. Specifically, From Table 13 and Table 14 it can be observed that according to the ANOVA results there are no statistically significant interactions between the three factors (Row: Res_State*Windows*ROI) for each connectivity relationship evaluated for the alpha band. This suggests that the segment durations provide similar results regarding the areas that have connections, however, it does not mean that the connectivity patterns suggest different networks over the ROIs.

Table 13 and Table 14, show the significance of the three-way interaction between the factors: resting state, window length and ROI for the normalized density and the average strength, respectively. The columns are organized as follows: 1. Factor under analysis, 2. SumSq: Sum of squares of the samples, 3. DF: Degrees of freedom, 4. MeanSq: Mean squared, 5. F: F-

statistic, 6. pValue, 7. pValueGG: Greenhouse-Geisser correction on p-value, 8. PValueHF, pValueLF: High and low boundaries for p-value.

From Table 13 and Table 14 it can be observed that according to the ANOVA results there are no statistically significant interactions between the three factors (Row: Res_State*Windows*ROI) for each connectivity relationship evaluated for the alpha band. This suggests that the segment durations provide similar results regarding the areas that have connections, however, it does not mean that the connectivity patterns suggest different networks over the ROIs.

Table 13. Significance of interactions for the normalized density of the alpha band.

Row	SumSq	D	MeanSq	F	pValue	pValueGG	pValueHF	pValueLB
	63.80058196	1	63.80058196	6643.316585	8.32995E-36	8.32995E-36	8.32995E-36	8.32995E-36
Error	0.278508009	29	0.009603724	1	0.5	0.5	0.5	0.5
Res_State	0.011136615	1	0.011136615	2.448230878	0.128505573	0.128505573	0.128505573	0.128505573
Error(Res_State)	0.131916413	29	0.004548842	1	0.5	0.5	0.5	0.5
Window	1.245129723	3	0.415043241	150.2128002	2.69639E-34	2.37141E-25	2.92265E-27	5.4148E-13
Error(Window)	0.240384055	87	0.002763035	1	0.5	0.5	0.5	0.5
ROI	2.946897686	4	0.736724421	153.2253827	2.51614E-45	3.96981E-31	2.55186E-34	4.24585E-13
Error(ROI)	0.557740704	116	0.00480811	1	0.5	0.5	0.5	0.5
Res_State*Window	0.019914728	3	0.006638243	3.138128684	0.029428081	0.032036434	0.029428081	0.086991234
Error(Res_State Window)	0.184035514	87	0.002115351	1	0.5	0.5	0.5	0.5
Res_State*ROI	0.124573992	4	0.031143498	14.43341442	1.35592E-09	1.03634E-07	1.95115E-08	0.000688274
Error(Res_State ROI)	0.250297376	116	0.002157736	1	0.5	0.5	0.5	0.5
Window*ROI	0.177278867	12	0.014773239	12.86692986	7.56505E-22	2.77284E-11	1.04838E-13	0.001211695
Error(Window ROI)	0.399558184	348	0.001148156	1	0.5	0.5	0.5	0.5
Res_State*Window ROI	0.019323016	12	0.001610251	1.578020827	0.095981242	0.160419654	0.141028062	0.219071946
Error(Res_State Window ROI)	0.355107783	348	0.001020425	1	0.5	0.5	0.5	0.5

Table 14. Significance of interactions for the average strength of the alpha band.

Row	SumSq	DF	MeanSq	F	pValue	pValueGG	pValueHF	pValueLB
(Intercept)	7410.987793	1	7410.987793	1291.119751	1.34086E-25	1.34086E-25	1.34086E-25	1.34086E-25
Error	166.4591064	29	5.739969254	1	0.5	0.5	0.5	0.5
(Intercept):Res_State	237.4324951	1	237.4324951	118.8771896	8.95872E-12	8.95872E-12	8.95872E-12	8.95872E-12
Error(Res_State)	57.92147446	29	1.99729228	1	0.5	0.5	0.5	0.5
(Intercept):Window	3446.862061	3	1148.953979	582.8811035	0	2.62312E-26	5.71455E-27	9.43944E-21
Error(Window)	171.4912262	87	1.971163511	1	0.5	0.5	0.5	0.5
(Intercept):ROI	5.719110966	4	1.429777741	5.790431023	0.000276632	0.001555756	0.000960039	0.022710638
Error(ROI)	28.64281082	116	0.246920779	1	0.5	0.5	0.5	0.5
(Intercept):Res_State:Window	11.9960413	3	3.998680353	5.282623768	0.002150689	0.018047277	0.017039303	0.028940171
Error(Res_State:Window)	65.85462189	87	0.756949663	1	0.5	0.5	0.5	0.5
(Intercept):Res_State:ROI	6.031976223	4	1.507994056	9.311461449	1.46184E-06	9.62093E-06	2.73771E-06	0.004834409
Error(Res_State:ROI)	18.78623581	116	0.161950305	1	0.5	0.5	0.5	0.5
(Intercept):Window:ROI	6.640697479	12	0.553391457	3.877868176	1.36056E-05	0.000417862	5.40068E-05	0.058547251
Error(Window:ROI)	49.66136169	348	0.142705068	1	0.5	0.5	0.5	0.5
(Intercept):Res_State:Window:ROI	1.985429049	12	0.165452421	1.217987895	0.268647462	0.293358386	0.2799052	0.278829753
Error(Res_State:Window:ROI)	47.27259064	348	0.135840774	1	0.5	0.5	0.5	0.5

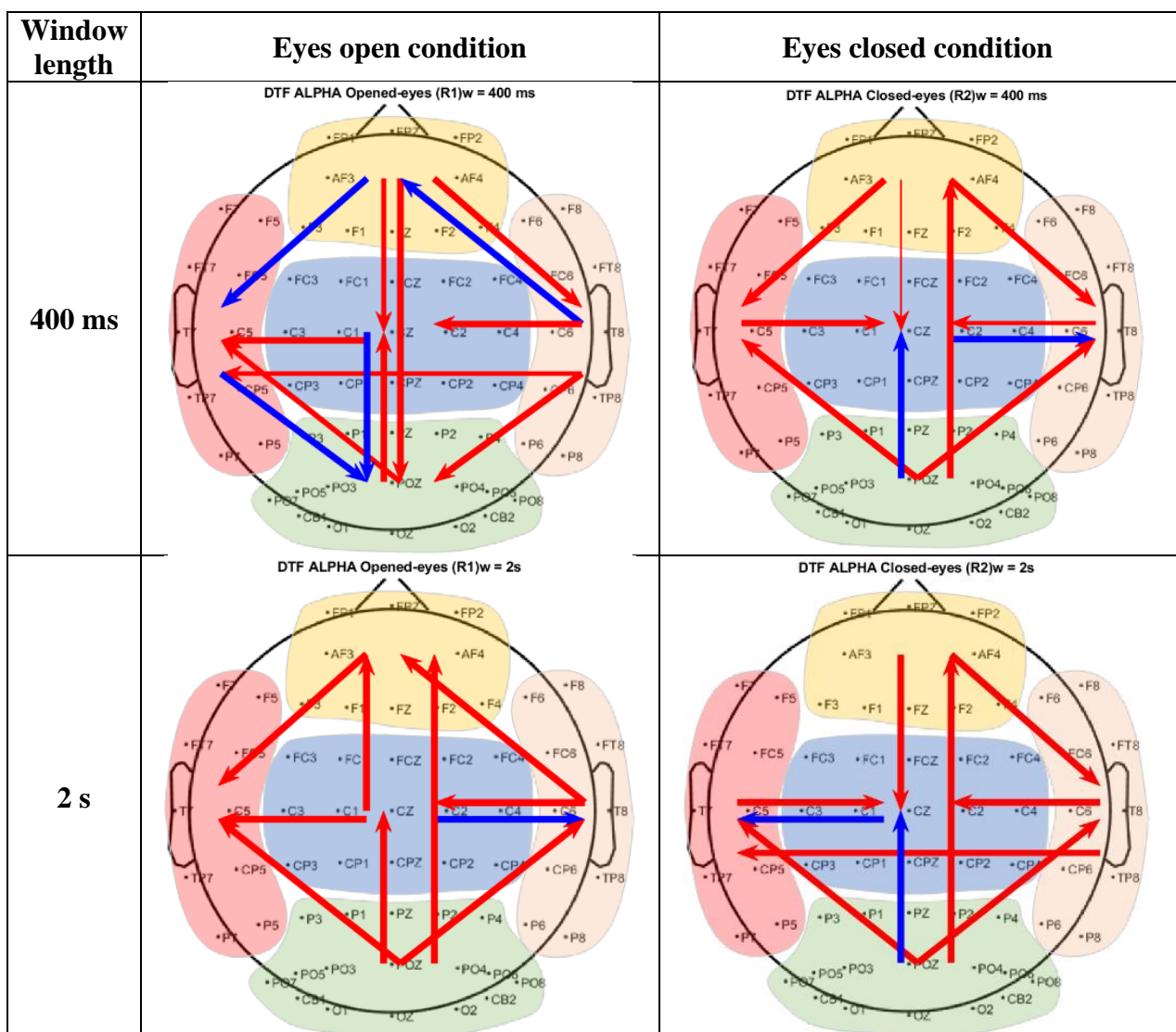
The same occurred for the interactions in the beta band which are shown in the annex section on

Table AN 15 and Table AN 16.

In order to obtain the connectivity from each of the regions of interest, the significance of the connections given the normalized density at each ROI was used to account for the connections and their directionalities. Moreover, for the case of the strength, it was used the normalized amplitudes on the ROIs so the causal relationships on the generalized network are tested and established. This was tested using the ANOVA setting and as result, the Table AN 17 found in the annex section shows the p-values evaluated for each of the windows at each frequency band for eyes open and eyes closed. Since these tables comprise a lot of information that is not

readable in a straightforward way, the connectivity diagrams displayed on Figure 54 summarize the statistically significant connections for the regions of interest. The arrows on the connectivity diagrams indicate the directionalities (i.e., the normalized density), the width indicates the average strength of the causal relationship, and the color indicates if the amplitude of the connection increased (red) or decreased (blue) from one ROI to the other.

As it can be observed from the connectivity diagrams, there are a lot of connections that according to the ANOVA analysis are significant. In some cases, like the one for the eyes closed condition for the alpha band, it can be observed that the connectivity structure from the windows of 400ms, 2s, 4s and 20s is very similar among the windows. Specifically, it can be noted that there are 4 main connections across the ROIs that are common for all the windows. These are: 1. The posterior – frontal link, 2. The posterior – right temporal, 3. The posterior – left temporal, and, 4. The frontal – central connection.



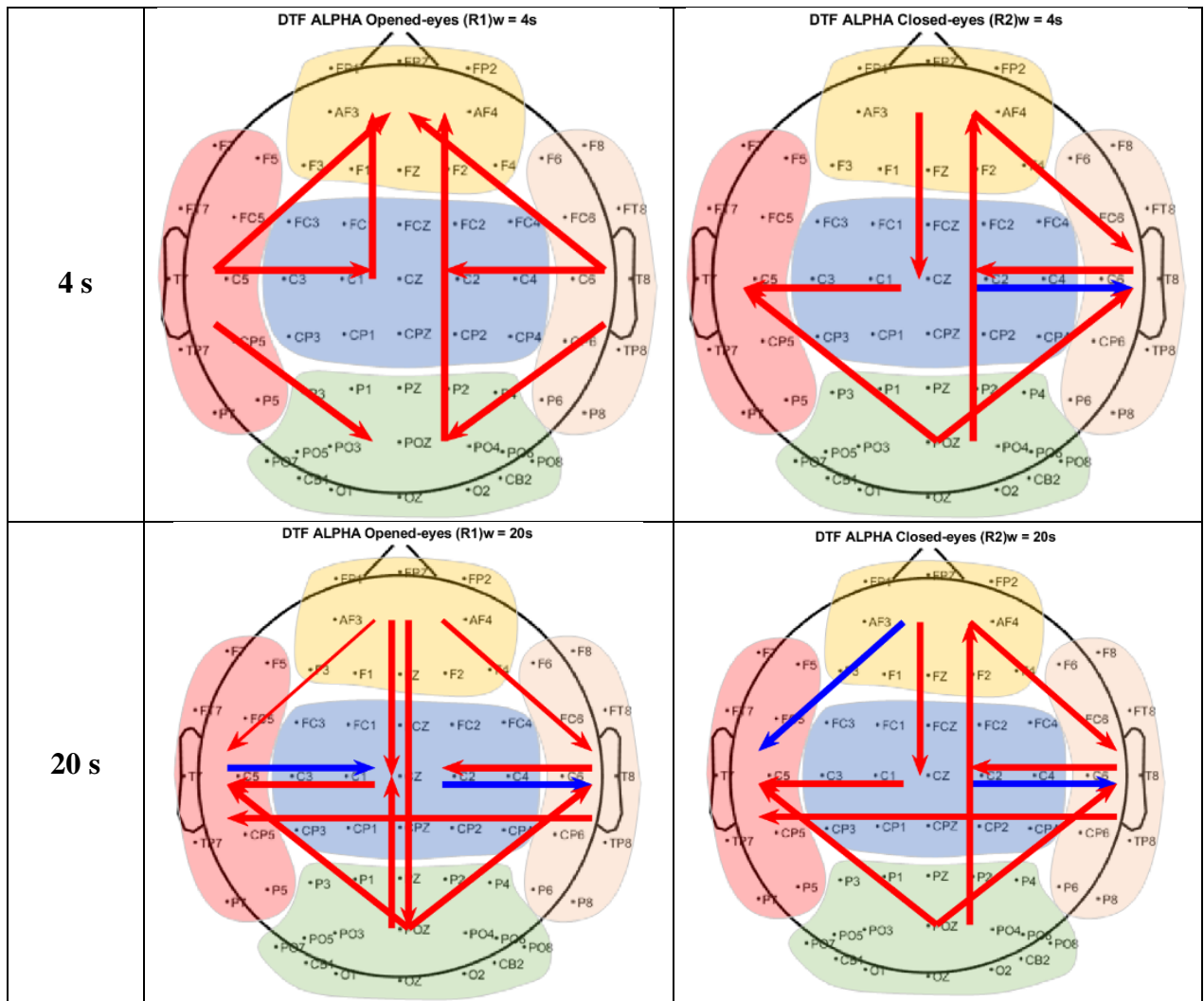


Figure 54. ROI connectivity diagrams obtained for the eyes open and eyes closed conditions for the alpha frequency band

This states that there are significant connections that start in the posterior ROI and are directed to the right and left temporal areas, as well as the causal relation that is being directed to the frontal area. There are other connections like the one occurring in the frontal area that is being directed to the right temporal region, and the interactions that occur towards the central region which is being influenced from the frontal and right temporal areas.

Unfortunately, as it can be noted, the connectivity diagrams are very general, all of the regions receive and generate connections that might not be correct since they consider very broad regions, a lot of channels participate in the region and the normalized density might detect slight changes occurring between regions. Moreover, when comparing the connectivity in the channel space there are no similarities, excepting for the influence of the posterior region directed to the frontal one. However, due to the very general point of view it is not possible to characterize physiologically the connectivity across the windows.

In the same way, these observations hold also for the beta frequency band as shown in the annex on Figure AN 4.

For all these reasons, in order to improve these results, it would be useful to consider narrower regions or less channels coming from the regions in order to get a better representation of the

connectivity among these areas. That is why the connectivity analysis in the channel space are now considered and analyzed in the following section.

6.2.3. Connectivity in the sensor space: Graph Theory indexes

The use of the adjacency matrices to encode the significant connections as result of the DTF estimation across the channels, provides the raw structure that shows the effective connections on the channels. This can be difficult to interpret due to the high density of connections considered as significant from the adjacency matrix. In this way, it is useful to consider graph theory measures to perform a characterization of the connectivity in the network that is able to show hidden structures, and central nodes that participate more in the transmission of information and clusters that could characterize the brain activity that is being investigated, i.e., the resting state conditions during eyes open (R1) and eyes closed (R2).

As explained in [73], there can be distinguished 4 broad classes of graph measures; the basic measures that reflect the importance of a node (channel) in the network by considering the number of connections it has with other nodes (i.e., the degree), the graph density which measures the actual number of connections in the network and that can be expressed as the percentage of links present in the network being 0% when no connections are considered in the graph and 100% when all the significant links are shown, and finally the strength, which accounts for the amplitude of the connection between two nodes, e.g., the DTF magnitude registered for the pair channel i, j in the matrix.

The second class of measures are the so-called measures of integration which account for how effortless the communication between the channels is performed. In this category, there are different measures that help to estimate this. The shortest path length between two channels as its name indicates, calculates the line with minimum length that connects two nodes on a surface, in this case given the topographic characteristics and the placement of the electrodes over the scalp of a person. Its value is defined for every pair of nodes and given the high density of nodes that form a network of electrodes, the *average shortest path length* is used to characterize the typical separation between the nodes.

Conversely, the *global efficiency* accounts for the inverse of the average shortest path length and indicates the capacity of a network to support the information flow, and in the case where networks are not fully connected it provides a better representation of the integrative communication characteristics among the nodes since unlike the average shortest path length, the global efficiency does not diverge to infinity when a connection is not present in the network. This provides a useful way to account for how easy the communication among the present nodes is since the adjacency matrices in our case are not fully connected considering that they only contain the statistically significant connections.

The third category of graph parameters are the so-called measures of segregation that characterize the independence of local structures found within the network given the formation of groups that are interconnected, i.e., clusters of nodes. The *clustering coefficient* accounts for the channels connected to a node which are interconnected to each other. Another measure of segregation is the *local efficiency* which is defined as the efficiency among the neighbors of a node.

Lastly, the importance of a node in the network is estimated by considering the *betweenness centrality*, a parameter that quantifies how central is a node in the information flow considering

the integration and effective connections produced within the structure. This measure calculates the number of the local short paths connected to a node and that represent the importance of a channel in the network. Table 15 provides the equations of the graph theory parameters.

The density parameter is a basic measure that quantifies the fraction of actual connections that are present on a network. When an adjacency matrix is calculated, it summarizes the effective directed connections among the channels that are significant in statistical terms as explained above, then, it is most probable that its density is less than the maximum number of possible connections on the network, defined as $N(N - 1)$, being N the total number of channels (i.e., 62). Thus, the density of a non-fully connected network given the statistically significant relationships condensed in the adjacency matrix will never be equal to $N(N - 1)$.

In these terms, the density is constrained by the number of significant connections of the adjacency matrix whose elements' magnitudes can be sorted from lowest to highest in order to generate the 'cost' variable, used as the independent variable from which the remaining graph-based parameters are calculated, and by these considerations they are defined as a function of the number of actual connections in the network. By sorting out the magnitudes, the cost represented as the proportion of connections encodes a linear scale from the highest to the lowest magnitudes.

Table 15. Graph theory measures applied to the adjacency matrices of significant connections.

Basic	Degree	$k_i = \sum_{j \in \mathcal{N}} a_{ij}$ <p>Where a_{ij} denotes the existence of the connection between i and j.</p>
	Density	$d = \frac{1}{N} \sum_{i \in \mathcal{N}} k_i$ <p>It is defined as the mean network degree and accounts for the total average of the degree accounted for all the nodes belonging to a network.</p>
	Strength	$s_i = \sum_{j \in \mathcal{N}} w_{ij}$ <p>Where s_i is the strength of a node by summing up the weights - w_{ij} (e.g., DTF amplitudes) of all the connections incoming or going out of that node.</p>
Integration	Average path length	$L = \frac{1}{N(N - 1)} \sum_{i, j \in \mathcal{N}, i \neq j} d_{ij}$ <p>Where d_{ij} is the length of the geodesic from the nodes $i \rightarrow j$.</p>
	Global efficiency	$E = \frac{1}{N(N - 1)} \sum_{i, j \in \mathcal{N}^2, i \neq j} \frac{1}{d_{ij}}$
Segregation	Clustering coefficient	$c_i = \frac{2e_i}{k_i(k_i - 1)} = \frac{\sum_{j, m} a_{ij} a_{jm} a_{mi}}{k_i(k_i - 1)}$

		$C = \langle c \rangle = \frac{1}{N} \sum_{i \in \mathcal{N}} c_i$ <p>Where e is the number of edges in the cluster of neighbors belonging G. The ratio $k_i(k_i - 1)/2$ is the maximum number of edges in G_i.</p>
	Local efficiency	$E_{\text{loc}} = \frac{1}{N} \sum_{i \in \mathcal{N}} E(G_i)$ <p>Where $E(G_i)$ is the global efficiency for the cluster of neighbors belonging G.</p>
Centrality	Betweenness	$b_i = \sum_{j, k \in \mathcal{N}, j \neq k} \frac{n_{jk}(i)}{n_{jk}}$ <p>Where n_{jk} is the number of shortest paths connecting j and k, and $n_{jk}(i)$ establishes the number of shortest paths that connect j and k that pass through i.</p>

In this way, 1% of the cost comprises the number of connections in the network that have a magnitude larger or equal to the 99% of the maximum DTF value found in the adjacency matrix. The same applies for the other percentages up to reaching 100% whose cost comprises all the significant connections regardless of the DTF magnitudes on the matrix.

A. Results on the graph theory indexes.

As a way to show the results obtained from the graph-based parameters calculation and for the sake of simplicity, let us consider the results of one of the windows. The window chosen for this purpose is the one corresponding to 20 seconds for the alpha band rhythm.

As explained above, the graph theory indexes quantify the important channels of a network by considering their roles over the evolution of the complex connections given the 62 nodes of this structure. That is why the cost of the network is considered and each of the graph-based parameters is estimated as a function of this cost. This independent variable varies from 1% to 100% being the lowest limit the one that represents the significant connections with the highest amplitudes and increasing the range towards 100% while the number of connections increases and hence considering all the intermediate DTF amplitudes up to the minimum.

Is in this way that the quantification of the integration, segregation, centrality, and basic measures is performed by calculating those parameters as a function of the density/cost of the network accounting for the network dynamics that changes over the number of connections considered and that are sorted from the highest to the lowest.

On Figure 55 there is depicted the mean value of the parameters of *degree* and *strength* estimated in the range of 0 – 100% of the cost variation. The graphs are shown for the eyes open and eyes closed conditions in the alpha band for the window of 20 seconds.

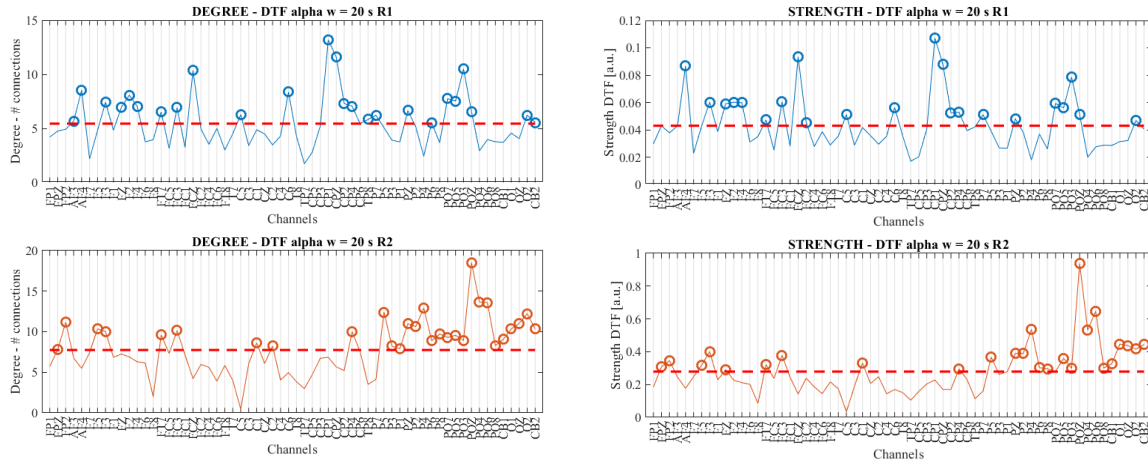


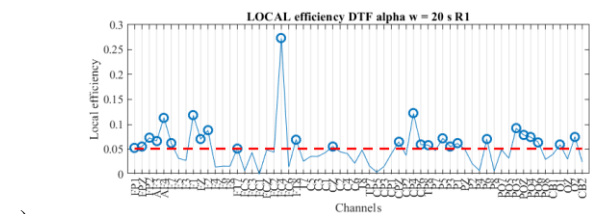
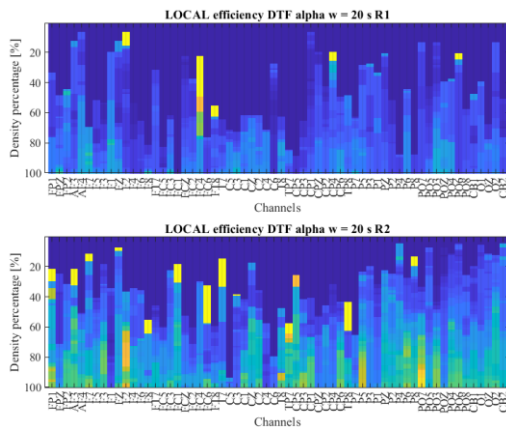
Figure 55. Average degree (left) and strength (right) of the effective connections estimated for the 62 channels composing the network.

Figure 55 shows the average value of the connections calculated for each of the channels that compose the network of 62 nodes, the red dotted line corresponds to the mean value of that average and corresponds to the threshold selected to choose the channels that have more connections (incoming + outgoing) and the nodes with higher weights according to the cost dynamics, i.e., the degree and strength, respectively.

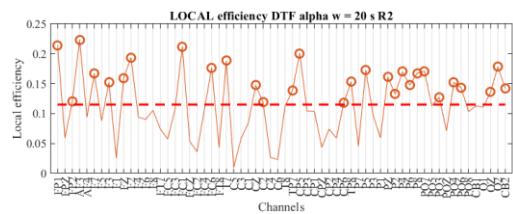
The mean of the average was used to establish a threshold from the distribution formed by the values calculated according to the cost. Since some distributions are skewed to the left (e.g., the degree of the channels is mostly low w.r.t the higher values) this threshold was employed to consider the channels that have higher graph parameters and that can be considered as central according to the flow of information in the network.

Only the channels that have strength and degrees higher than the threshold are picked and listed as central nodes relative to the parameter that are representing.

For the remaining nodal graph parameters (e.g., local efficiency, mean cluster coefficient and betweenness centrality), the same process applies, the average over the cost is performed and the threshold is set relative to each measure to find the central nodes, see Figure 56 below.



a)



b)

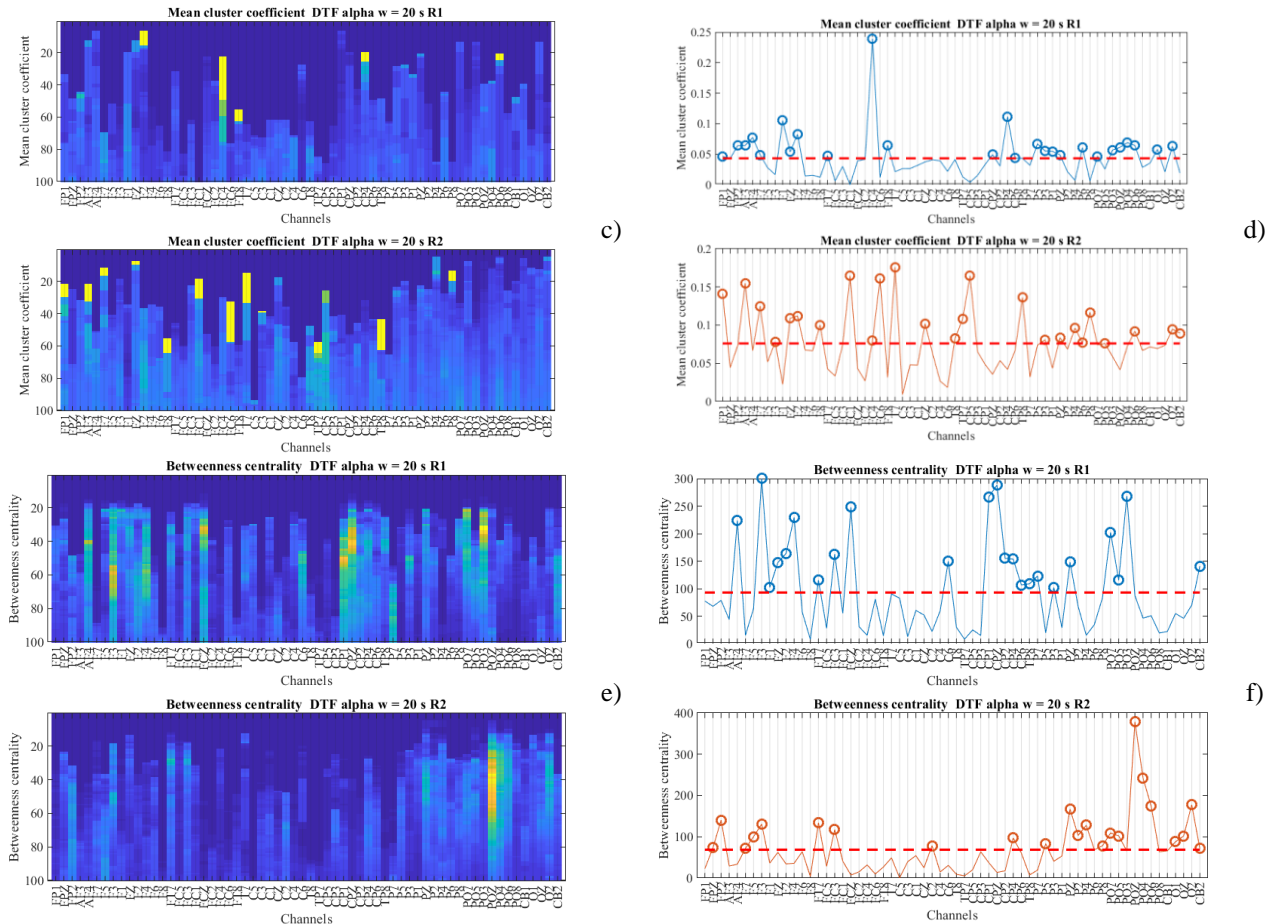


Figure 56. Graphs of mean local efficiency, mean cluster coefficient and betweenness centrality as a function of the cost for the channels of the network at each resting state condition (a, c, d). Averaged values of the nodal parameters, the thresholds and the channels selected represented by the marker 'O' (b, d, f). The colors in a, c, d represent the parameter amplitude at each cost percentage.

As can be observed from Figure 56 a, c, e, the graph parameters are not static and change in relation to the number of connections considered in the network (i.e., the cost, variable in the y-axis). This means that a node can be considered as important w.r.t what a graph measure represents in the network over a short range of cost values (see the yellow colors indicating the higher amplitudes for some channels in the graphs), however, as depicted in the figure this is not maintained when the network cost increases, and that indicates that its complexity grows. This is why the mean over the cost is calculated to highlight the channels with higher values in the overall range as shown in Figure 56 b, d, f.

The nodes that exhibited quantities higher than the threshold are grouped with the ones obtained from the basic features estimated earlier, and only the channels that were common for all the graph indexes are finally selected as the central electrodes at each resting state condition under evaluation. This means that it is possible to highlight the channels considered as central according to the causal relationships that occur inside the network and allows to have a better representation of the connectivity occurring among these channels testing the DTF amplitudes that converge on these central nodes.

Now, by combining the information of the DTF amplitudes given the adjacency matrices and the selected electrodes at each resting state condition for the window of 20 seconds for the alpha band, the connectivity diagrams shown in Figure 57 are generated.

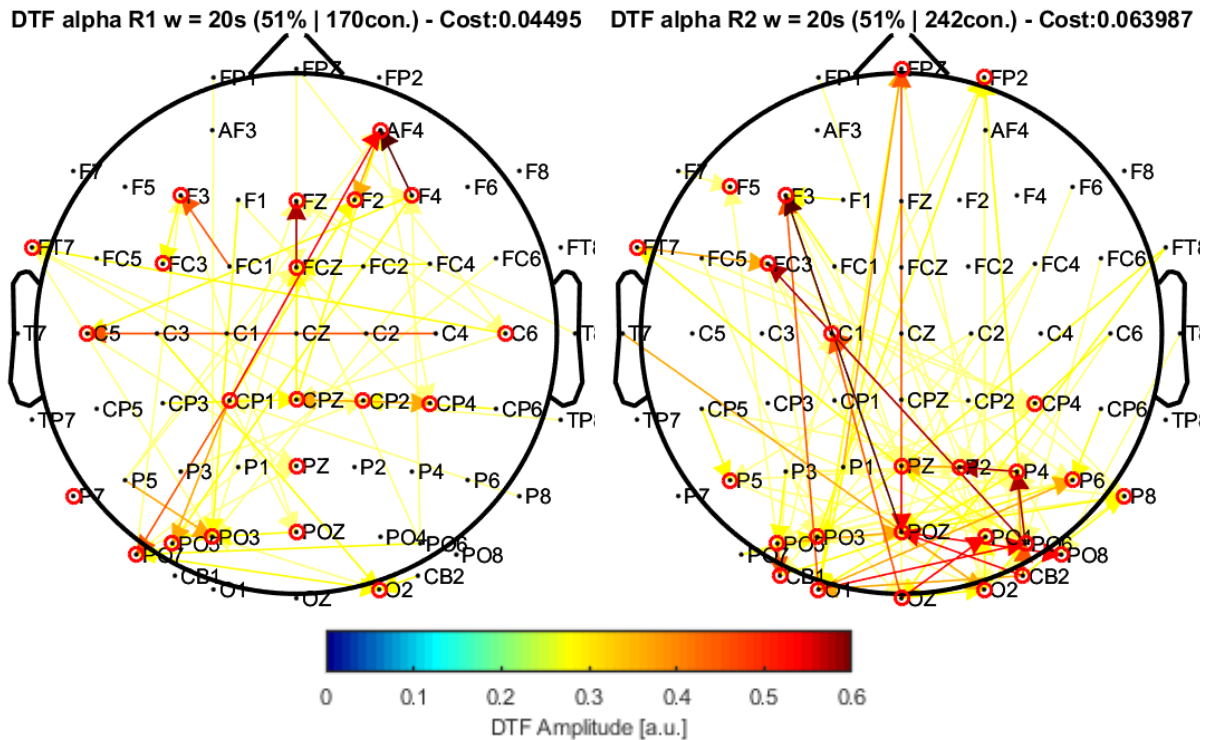


Figure 57. Connectivity diagrams of the window of 20 seconds. (left) Connectivity during eyes open (R1) condition. (right) Connectivity during eyes closed (R2) condition.

The connectivity diagrams on Figure 57 show the significant effective connections derived from the adjacency matrices at a cost of 51% of the maximum value of the DTF matrix, which means that only the connections that exhibited a DTF magnitude higher or equal 51% of the highest DTF element (~ 0.6 in both conditions) are being plotted in the graph. The connections are color coded so the strongest interactions can be identified.

The intersection of the selected channels from the graph measures provided a list of nodes that can be considered as central elements that participate actively in the network. These selected nodes are highlighted by the red circles around their topographic locations in the graphs (see Figure 57). Moreover, the directionalities are also depicted in the graph and show how the information is being directed to specific areas from different channels located given some identifiable clusters of channels observed in the connectivity diagrams.

The central channels can be grouped forming clusters which are used to identify the changes in the flow of information not only in the local level given the topographic location of individual electrodes but in a more general view considering complete regions that highlight the active areas in which the connectivity is being produced inside the group of nodes and between these areas. In this way, Figure 58 shows the clusters generated from the connectivity diagrams and the central electrodes that were obtained above for the window of 20 seconds in both resting state conditions for the alpha frequency band.

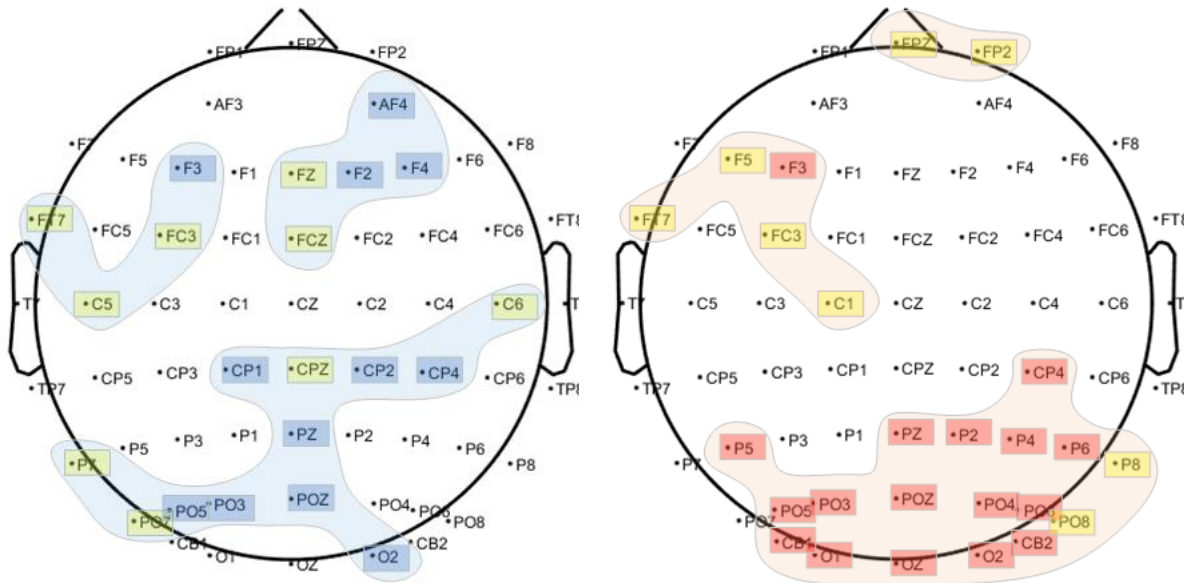


Figure 58. Connectivity diagrams of the window of 20 seconds. (left) Connectivity during eyes open (R1) condition. (right) Connectivity during eyes closed (R2) condition.

Considering the clusters in Figure 58, there are observed a set of channels that participate in the effective connectivity. Specifically, the channels grouped for the closed eyes condition show that the posterior region composed by channels located at the occipital and parietal areas (Ox, POx and Px channels) are more involved in the network for the information transmission. Moreover, the involvement of channels in the central, frontal, and prefrontal regions provide some insights of the network and how the distribution of channels and the information is flowing from or towards these areas.

In the case of the eyes open condition, the distribution of the channels is different and by observing its connectivity diagram (Figure 57 left), only a few channels show strong connections given the DTF amplitudes, which gives the idea that the connectivity in this case is more uniform among the clusters and tends to have more midrange connectivity amplitudes than the eyes closed case. In order to understand what happens at each resting state condition, it would be useful to observe what happens in the case where other windows are employed, and this will be shown in the section *Connectivity in the different windows*.

B. Connectivity in the different windows

One of the end goals of this thesis work is to provide a selection approach for the window size in order to perform the effective connectivity analysis of EEG data. This step was already done as explained before in the section *Window selection approach*. As result of this step, the windows of 400 milliseconds and 4 seconds were selected as the ones that exhibited most of the stationary characteristics given the EEG signals. This nonparametric step is designed as a tool to perform the selection of what is hypothesized to be a window length that is useful to capture most of the information given the assumption of stationarity needed to perform the effective connectivity analysis.

In order to evaluate the connectivity from the windows that were selected in this stage, some graph-based parameters were estimated and the connectivity diagrams that comprise the brain processes were generated and are now used to analyze the influences exerted among the channels that measure the neural activity in the form of electric potentials in the scalp.

As it was explained in the state-of-the-art section of this work, there is no consensus about a proper window duration that could be employed to analyze the connectivity information. There are some authors who even encourage the research of this issue since the results are heavily affected by this matter. In this way, this thesis work had as objective to provide a way to perform an informed decision regarding the window that could be employed for the connectivity analysis. It is based on the statistical characteristics of the EEG signals and is intended to be a pre-processing step on the connectivity framework which employs high order statistics to account for the stationary features so that they do not change drastically over time and be more uniform along with the signal that is being segmented piecewise into non-overlapping windows of the same size.

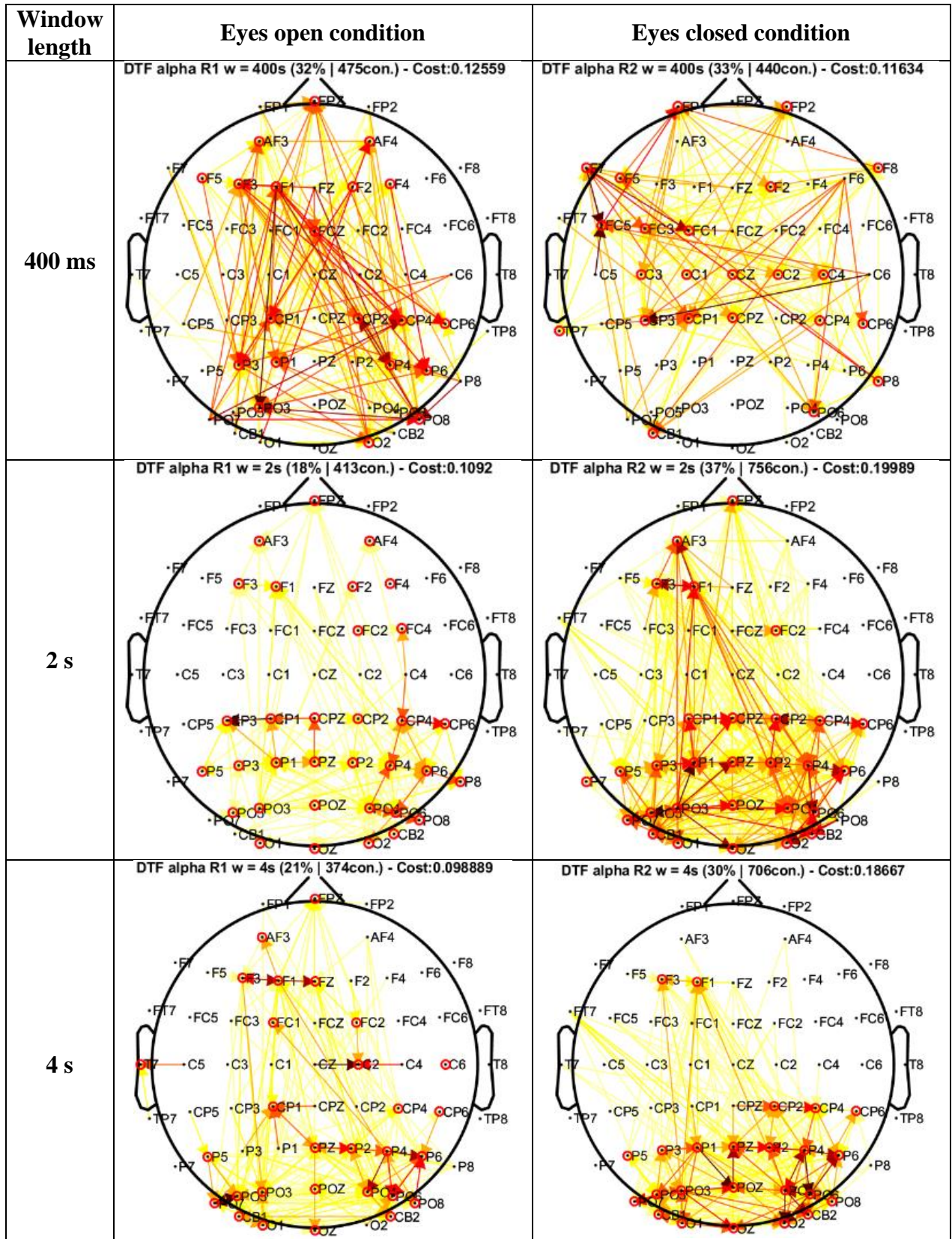
For the windows under consideration, the connectivity diagrams for the alpha and beta bands are summarized in Figure 59 and Figure 62 respectively. On the connectivity diagrams obtained from each of the window sizes of 400ms, 2s, 4s and 20s are shown for the eyes open and eyes closed condition for the alpha frequency band (7 – 13 Hz).

The figures displayed on Figure 61 and Figure 64 show the central electrodes found from the estimation of the graph-based measures as explained in the section *Connectivity in the sensor space: Graph Theory indexes*. The central electrodes highlighted by the red circle markers show the regions where there are more and stronger effective connections, as can be noted from the color-coded arrows which indicate the directionalities in a node-wise way.

From these graphs it is possible to note that there are regions formed by some of the electrodes which exhibit more internal connections. This is the case of the windows of 2s, 4s and 20s for the eyes closed condition. The electrodes located at the posterior part of the scalp formed by the occipital (Ox), parietal (Px) and central parietal (CPx) electrodes appear to be more involved in the connectivity process. In this region, the internal connections are very evident in terms of strength and number of connections. Also, the salient connections with other areas like the frontal region is shown as well. Considering the network and the connectivity estimated among the electrodes, it is observed a structure that is common for different windows. Excepting the 400 ms window, the connectivity diagrams for the closed eyes condition provide some insights about the directionalities of the connections as well as where they are being conducted.

In this way, besides the obvious internal connections occurring in the posterior area of the brain, during the eyes closed condition there is an influence from this region towards the frontal area, and each of the windows (excepting the 400ms one) were able to show such relationships.

In the case of the eyes open condition, the structures are less consistent, in other words they are not so structured as in the eyes closed condition where it was possible to observe similar connectivity across the windows (see the 2s and 4s windows) and the strengths from the central channels that participated more in the network were different as well. Finally, the window of 400 ms did not provide results comparable to the other segments, in fact, the connectivity diagrams show more spread connections that do not follow the observations from the state of the art [45], [46], [71], [74].



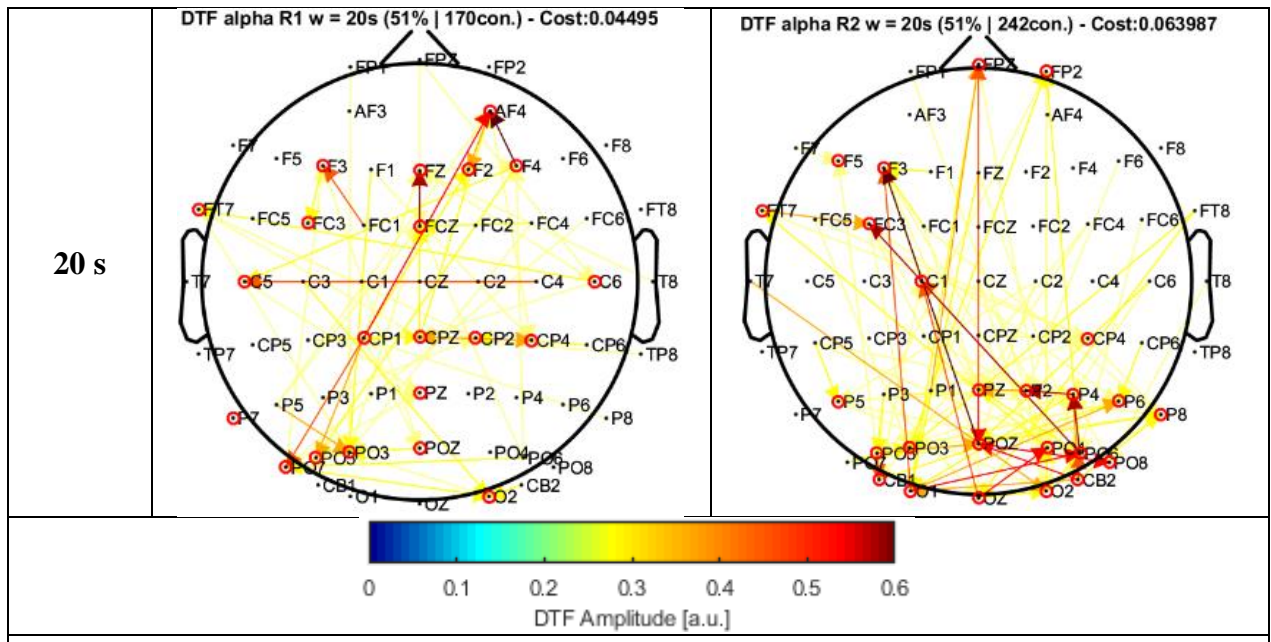
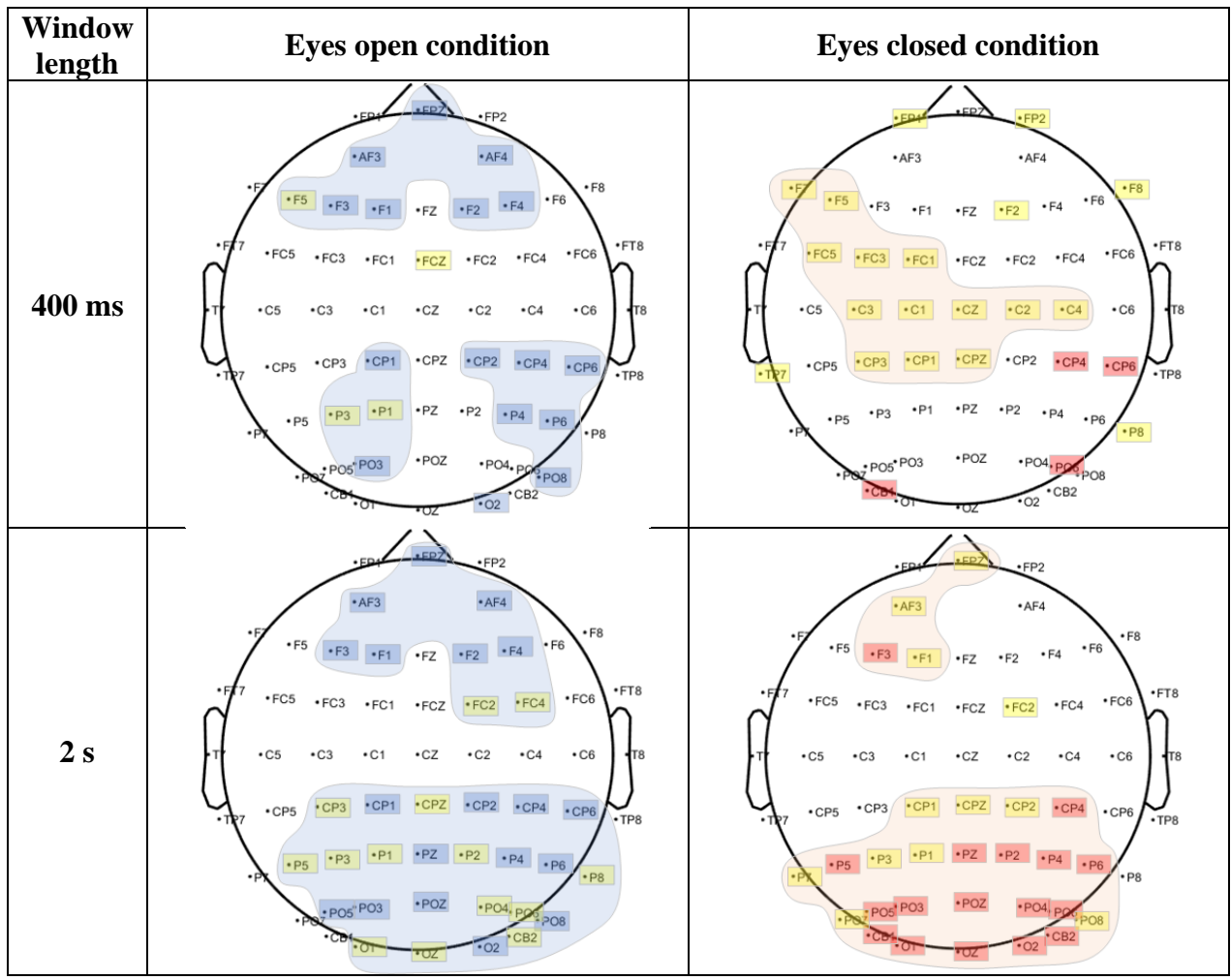


Figure 59. Connectivity diagrams for eyes open and eyes closed states during the alpha band for the selected windows.

In order to observe the channels that were involved in the process, the Figure 60 shows the cluster of electrodes composed by the central channels highlighted in the figures from Figure 59.



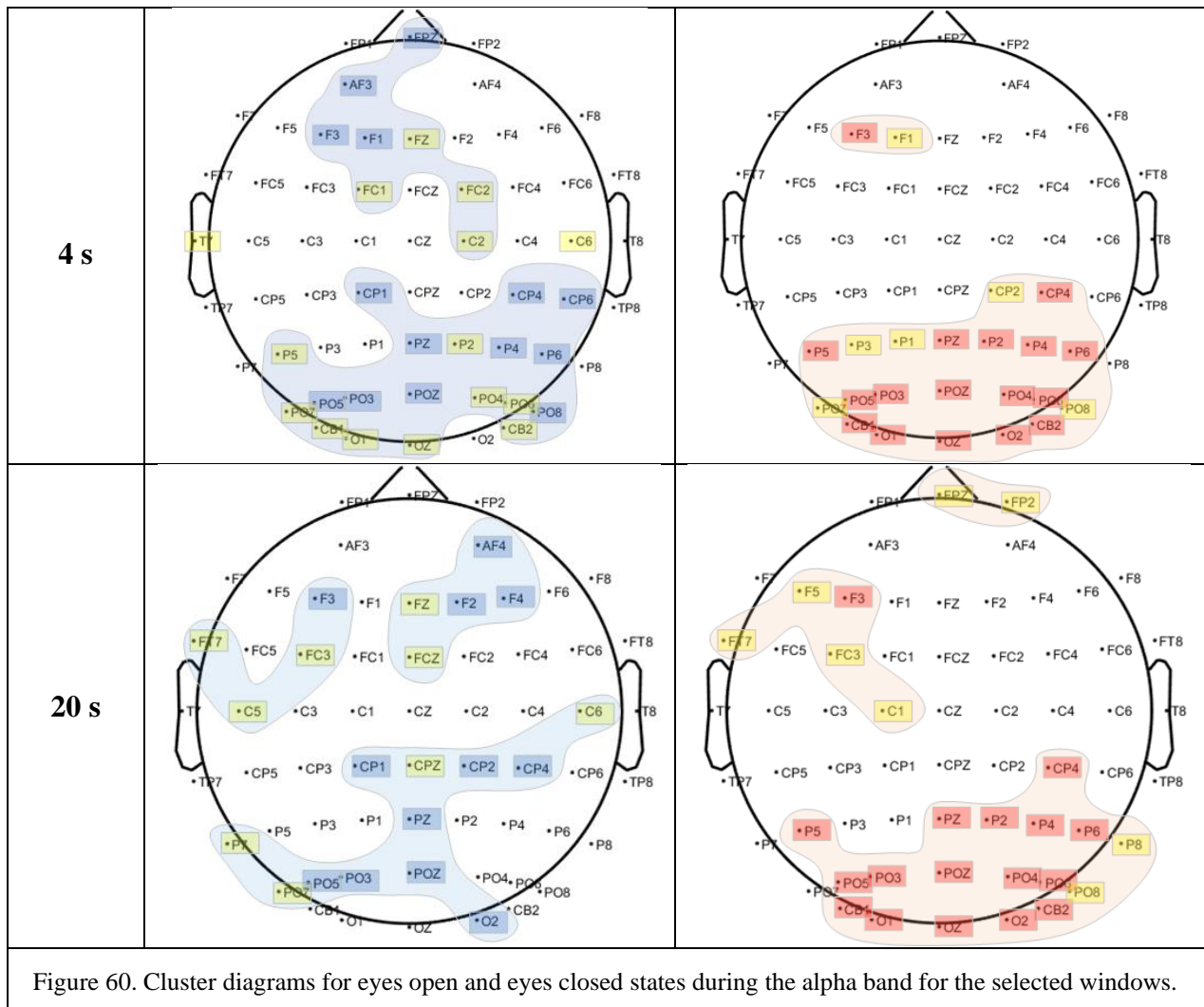


Figure 60. Cluster diagrams for eyes open and eyes closed states during the alpha band for the selected windows.

The cluster of electrodes on Figure 60 highlight the nodes from which more connections are being generated/directed. As it can be observed, these areas display most of the activity related to the effective connections from the windows that are being analyzed.

Let us focus on the clusters over the windows for the eyes closed condition. It is observed that these electrodes in the posterior part of the brain are the more active ones according to the connectivity diagrams in Figure 59

. The slight differences on these cases are evidenced by the slim variations of the channels located at the frontal regions, which vary at each window.

More interestingly, the variations on the eyes open condition are more evident, showing more spread clusters from the channels grouped at different window characteristics. These clusters can help to analyze what is happening in physiological terms and how they are connected to the areas of more influence that characterize the resting state conditions as the end goal of this analysis. The physiological analysis is performed in the discussion section.

As a final set of the useful results, in order to analyze what is happening in the network formed by the channels, let us consider some of the graph-based parameters introduced in Table 15. In this case, the parameters employed are: betweenness centrality, mean cluster coefficient, global efficiency, and local efficiency at each resting state condition of all the windows. The graph-

measures are shown as a function of the number of effective connections given the statistically significant relationships given the adjacency matrices generated for each window.

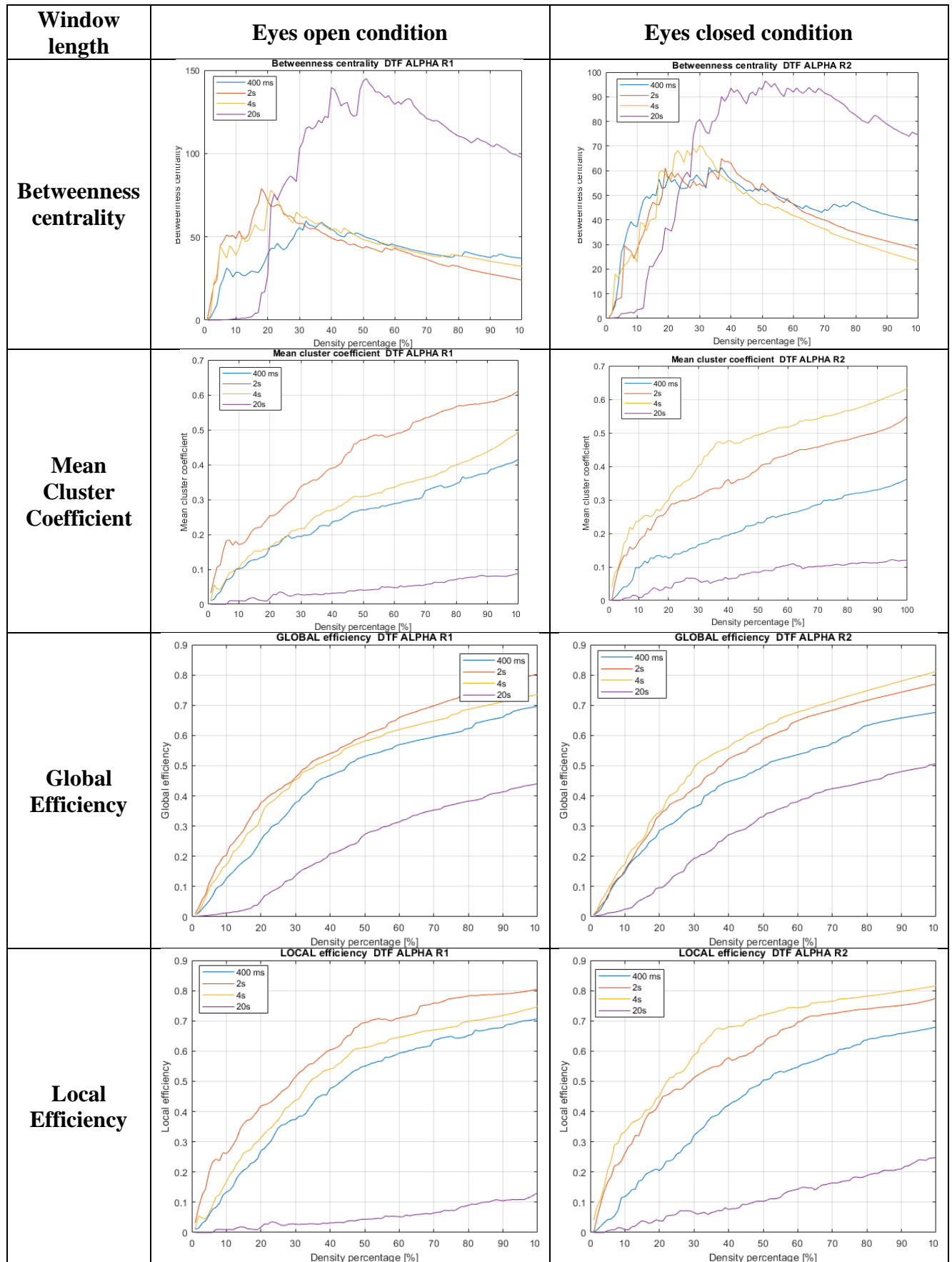


Figure 61. Graph based parameters estimated for R1 and R2 states during the alpha band for the selected windows.

According to the figures in Figure 61, when the graph-based parameters are calculated for the different window durations, there are observed evident differences across the segment durations on each resting state condition evaluated for the alpha band.

By considering the eyes open state (second column on the table), the betweenness centrality measure shows a significant increment for the window of 20 seconds. Its amplitudes increase up to reaching a maximum point that is almost the double in comparison to the other windows. While the trends exhibited for the windows of 400ms, 2s and 4 s, are similar to each other, evidencing a close correlation between the windows of 2s and 4s. The results of the betweenness centrality for the eyes open condition for the alpha band suggest that as long as the window length is increased, the values for this graph-based parameter increase as well, however, it would be needed to perform more tests considering intermediate window size to confirm this hypothesis.

In the case of the eyes closed condition, the previous observation is less obvious. The trend of the betweenness centrality in this case is more uniform for the short duration windows and the amplitudes for the segment of 20 seconds are smaller in comparison. Moreover, it is worth noting that the maximum points for the 400ms, 2s and 4s windows in both resting state conditions, is reached at a cost value of about 15% - 40% while for the window of 20 s such range is larger than 40%.

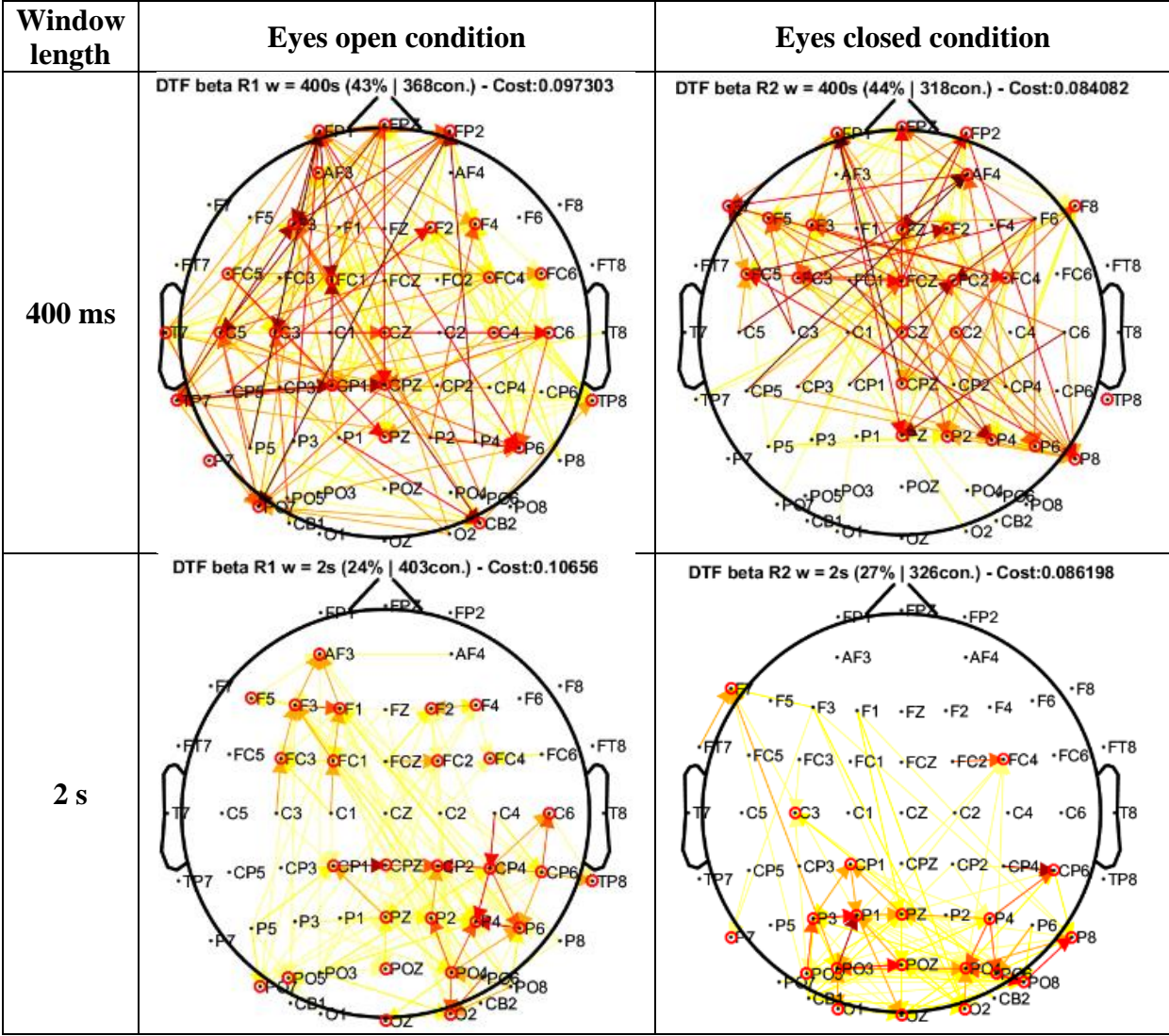
The betweenness centrality is a measure that quantifies how central a node is by considering the total of short-range connections that a node has in the network. By varying the proportion of effective connections in the network given the cost (i.e., density percentage), it is obtained a maximum value relative to the connections where all the central electrodes are found in the nodal structure, this means that at that maximum point all the main connections and the central electrodes can be displayed. Based on this, the connectivity diagrams from the Figure 59 are generated guaranteeing a proper visualization of the connectivity in the graphs.

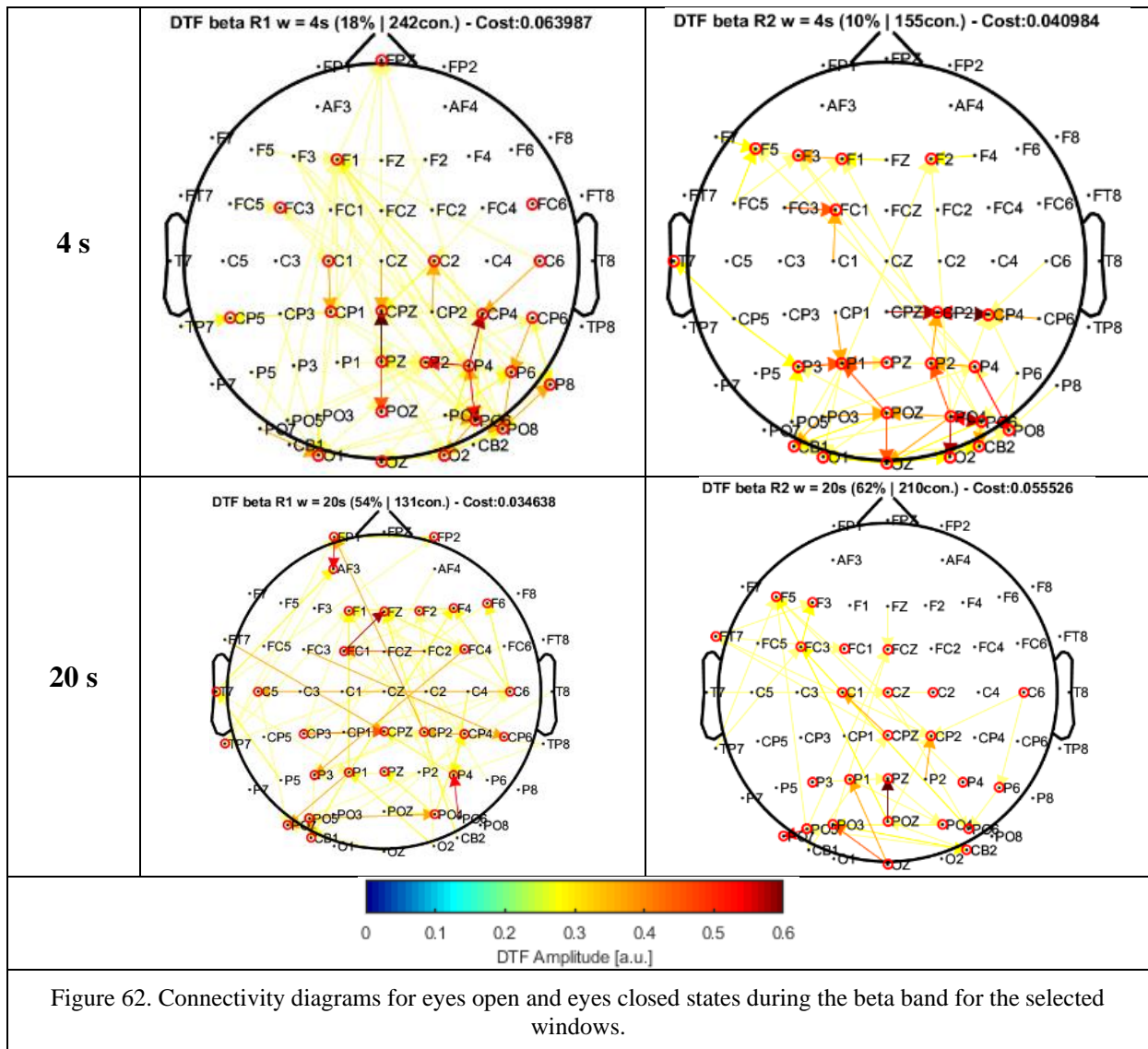
Following the other graph parameters, they all follow a logarithmic like function, in the case of the eyes open condition, the window of 2 seconds exhibits the higher values w.r.t the cost of the network, exhibiting a similar trend to the windows of 4s and 400 ms for the global and local efficiencies while for the mean cluster coefficient its values are significantly higher. In the case of the close eyes condition, the window of 4 seconds exhibits the higher graph-based values and present a similar behavior to the 2 seconds window as explained above.

Finally, the 20 seconds window presents the lowest variation of the segregation and integration measures for both resting state conditions.

Let us now consider the results over the beta band. Figure 62 shows the connectivity diagrams obtained for the resting state conditions evaluating each of the window lengths. As can be noted from these graphs, there is no evident structure on the connectivity that is being produced among the channels and that could be considered as common for the different windows, which is a difference w.r.t the alpha band where the effective connections that were captured in the processing established more connections with higher amplitudes that can be considered as common among the windows.

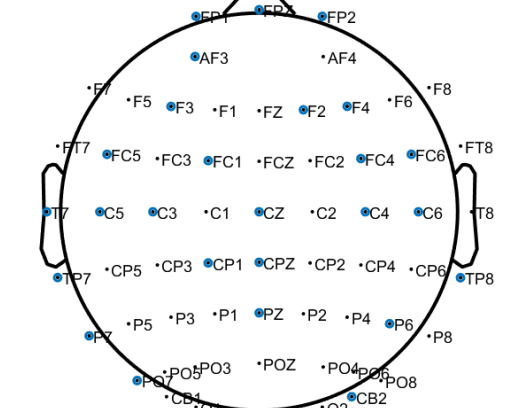
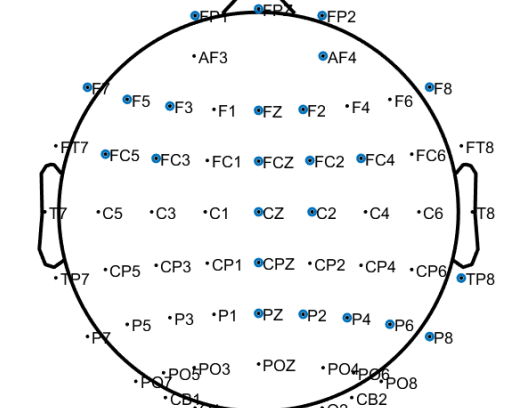
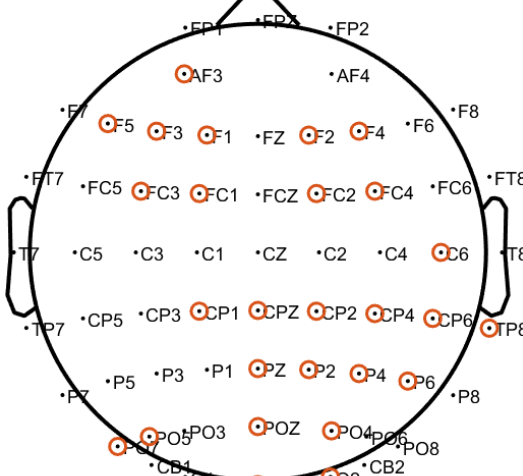
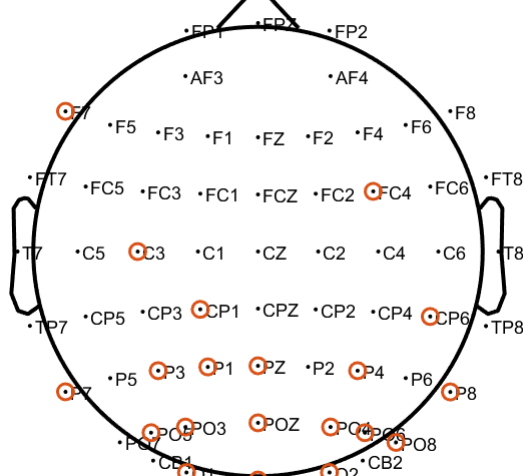
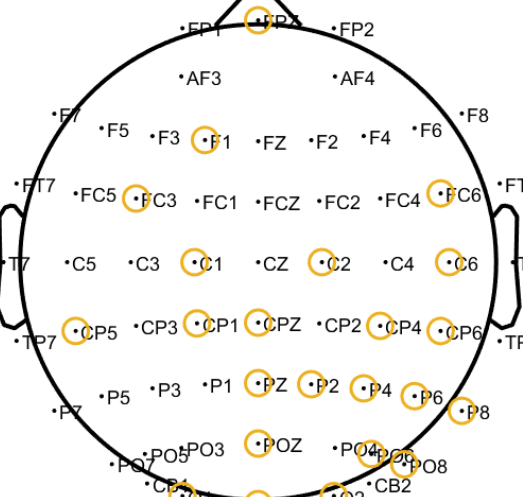
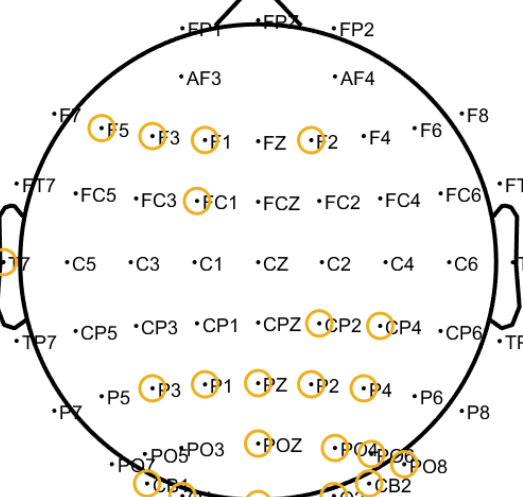
Excepting the 400 ms window, the connectivity diagrams show a broader distribution of connections including channels from different regions, not only from the posterior and frontal areas but including more temporal and central electrodes. In this case the connectivity evidenced by the 2 seconds and 4 seconds window are the most similar from the 4 segments evaluated it is found again a distribution of electrodes in the posterior part of the brain located in the right hemisphere that exerts influence in the central frontal areas, different from the alpha band where the central electrodes were found in a bilateral way in at the same area.





The results on Figure 63 explain the clusters of electrodes generated by the estimation of the central nodes in the network. As can be observed from the graphs, in general, for the opened eyes condition, the electrodes are more spread than in the closed eyes condition covering a larger number of electrodes that have significant connections. This is translated into having more areas involved in the connection which is more difficult to analyze since there are no focused areas that can explain the resting state process underlying. In contrast, for the eyes closed condition, the windows of 2 seconds and 4 seconds have some areas covered by the electrodes, however, the strength characteristics for these nodes are not so high.

By comparing the clustering of channels from the alpha and beta bands, it is observed that the closed eyes condition in both frequency ranges provides a better structure regarding the nodes where the connections are originated and where are being directed, which means that there can be identified the central nodes as well as the regions of greater connectivity. However, the connectivity of the beta band is characterized by being less strong in terms of the estimated magnitude (DTF amplitudes) and also because the quantity of effective connections is reduced as well. For the beta band the 2 seconds window provides more effective connections in comparison with the other segments from the group of long windows (i.e., $w_l \geq 1s$).

Window length	Eyes open condition	Eyes closed condition
400 ms	<p>DTF beta R1 w = 400s (43% 368con.) - Cost:0.097303</p> 	<p>DTF beta R2 w = 400s (44% 318con.) - Cost:0.084082</p> 
2 s	<p>DTF beta R1 w = 2s (24% 403con.) - Cost:0.10656</p> 	<p>DTF beta R2 w = 2s (27% 326con.) - Cost:0.086198</p> 
4 s	<p>DTF beta R1 w = 4s (18% 242con.) - Cost:0.063987</p> 	<p>DTF beta R2 w = 4s (10% 155con.) - Cost:0.040984</p> 

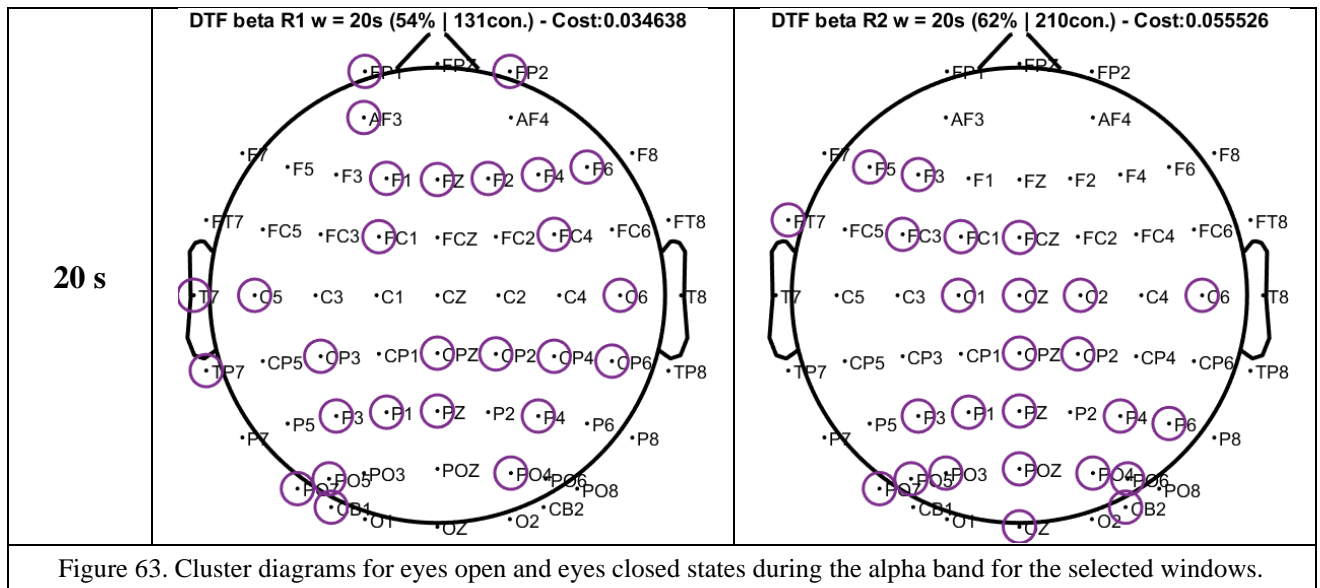
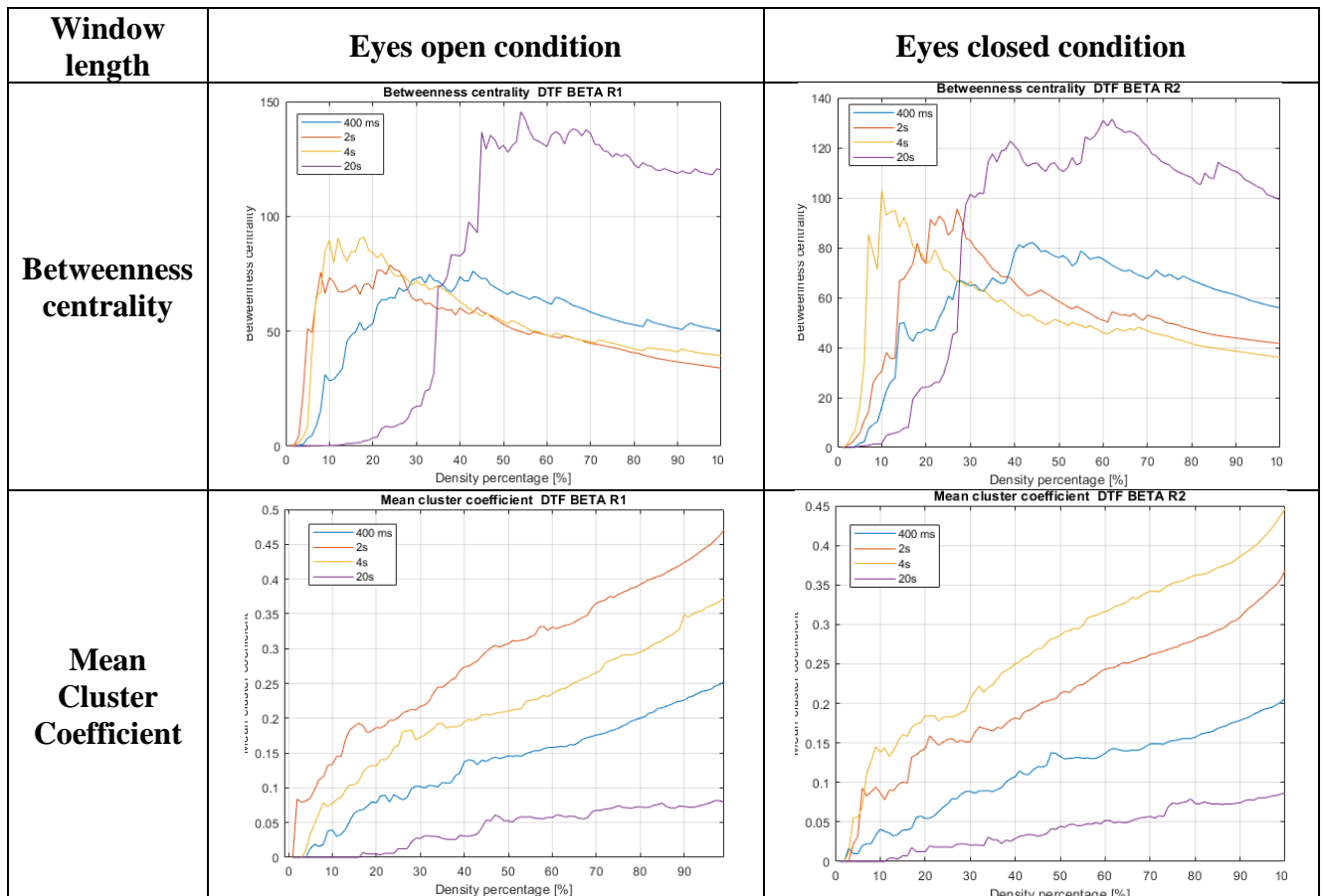


Figure 63. Cluster diagrams for eyes open and eyes closed states during the alpha band for the selected windows.

Figure 64 shows the graph-based parameters for the beta band in both resting state conditions. Similarly to the alpha rhythm case, there can be observed the same trend behavior for every window. The window of 2 seconds has the higher amplitudes with respect to the cost for the eyes open condition while the segment of 4 seconds provides the larger amplitudes for the eyes closed state. Again, the betweenness centrality for the 20 seconds window is significantly higher in comparison to the other windows and the ranges of centrality are similar as well, increasing the range of maximum value from 5% to 40%.



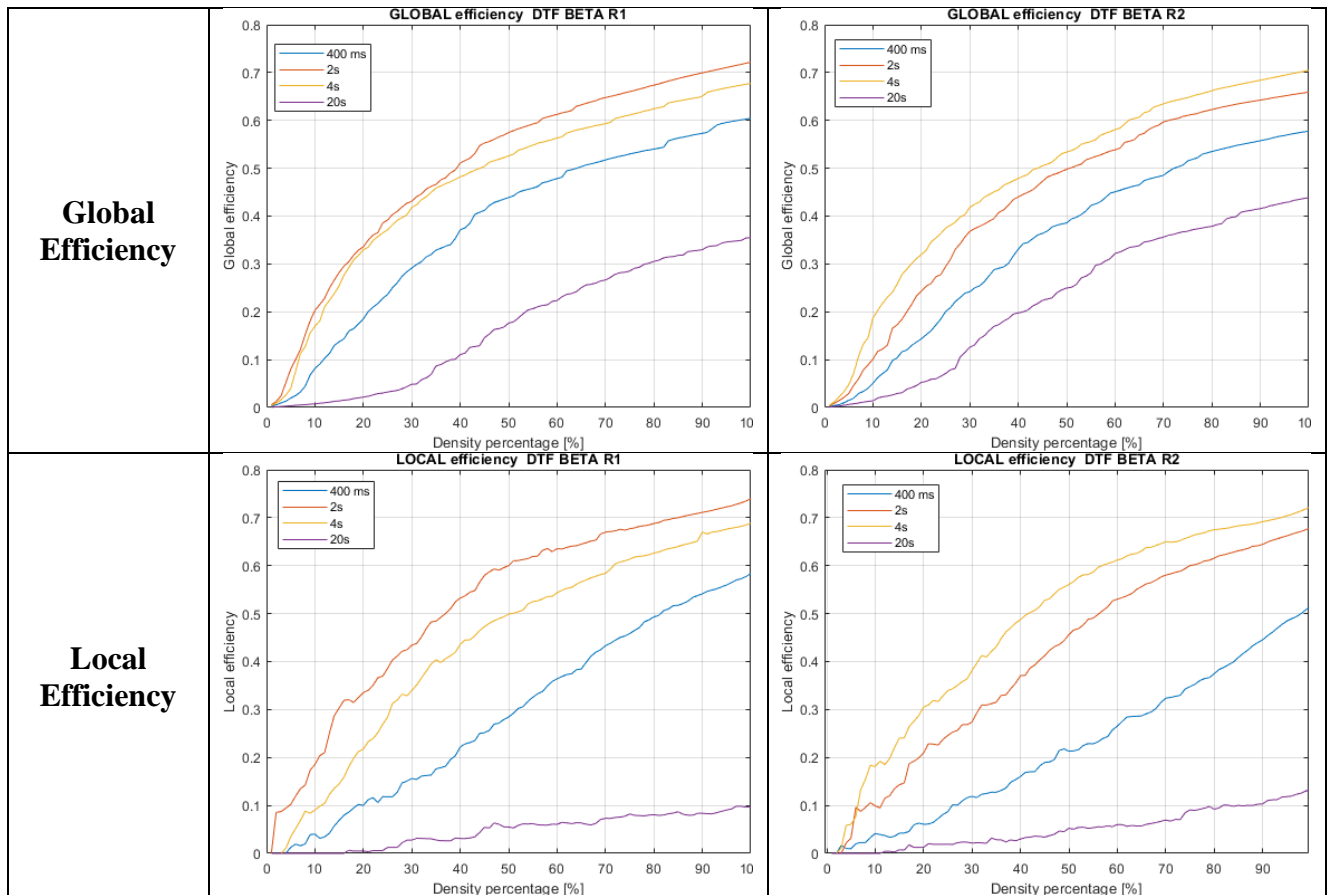


Figure 64. Graph based parameters estimated for R1 and R2 states during the beta band for the selected windows.

Regarding the connectivity measures, the variation across frequency bands do not provide significant differences that could help to discriminate alpha from beta frequency bands since the same trends are observed across windows and resting state conditions.

On the other hand, the graph metrics are different at each resting state which characterize the physiological processes and can be useful in discrimination tasks of the resting states.

7. Discussion

The connectivity results obtained in the sensor space and in the domain of the regions of interest show the causal relationships between the neural masses that are being analyzed and characterize the EEG process based on the window duration that has been selected.

As it was described above and depicted in the results, the connectivity diagrams change drastically according to the window duration employed for the MVAR fitting process. According to the theoretical considerations from some authors ([47],[48],[36],[17]), this is an issue that needs to be considered in order to guarantee consistent results in different experiment setups and inter-subject analysis. As a way to address this issue, within the framework of this thesis work it was defined an algorithm to look for a segment duration that maintains the stationarity of the EEG signals composing the recording for each of the subjects that were part of the resting state experiment.

This process considered the high-order statistics of the signals to account for the variability of their stationary features, and the most common window length across the dataset that exhibited the less variation of these statistic measures was selected as the window size for the connectivity analysis. As result, there were obtained 2 windows, a short one of 400 milliseconds and a long one of 4 seconds that were the most common windows among the subjects and resting states.

The connectivity results quantified by the DTF measures were estimated, and the adjacency matrices were obtained by performing statistical tests on the connectivity matrices that had the amplitudes and provided the causal relationships that were significant. As result, there were obtained non-fully connected networks that embedded only the significant values of the connections. These were then translated into connectivity diagrams and were analyzed through graph-based parameters to characterize the frequency bands and the resting state conditions.

The characterization from the connectivity allowed to find common observations with some other works that are closely related to the methodologies implemented, as it was explained from the work performed by Olejarczyk et. al., [40]. In this case, by applying their approach to our data and performing the connectivity analysis, the window of 20 seconds highlighted central nodes located in the posterior, left central-frontal joint and pre-frontal areas, which were not highlighted in their results. Moreover, the ANOVA analysis allowed to find a significant increment on the strength parameter on the alpha band by comparing the conditions of eyes closed and eyes open. Such increment was produced in the mainly in some of the regions of higher centrality (pre-frontal and central areas). This observation is one of the differences obtained by implementing their approach to our data.

Moreover, the work made by Tan and colleagues [46] also considered the analysis of graph-theory parameters, this time by performing the analysis on the variation of the network characteristics with respect to the number of significant connections. In this way, the connectivity patterns of these graph theory parameters were explored, and significant differences were found in relation to the characterization of the network. The local efficiency evaluated for the alpha band showed a significant increment for the eyes open condition w.r.t the closed eyes condition which states the opposite behavior from what Tan et. al., reported.

Moreover, the beta band characterized with the graph theory measures on our data exhibited significant differences for the global and local efficiencies, and, in a less extent for the mean cluster coefficients. This is totally opposite to what Tan and colleagues found. In this case, by

considering these results, it is possible to use these graph theory parameters as features of the resting state conditions in the beta band and opens the possibility to perform classification of the brain activity from graph measures. Of course, this is a possible implementation, and more data would be needed to validate this.

By implementing these approaches, it could be observed that the local connections were reduced in the bilateral posterior area for the alpha band in the eyes closed condition with respect to the opened eyes condition. Which is related to the fact that there is an increment of the alpha rhythm over the posterior areas during the eyes closed state. Also, there were observed more long-range connections coming from the posterior area during the eyes closed state.

After observing these results and analyzing what has been implemented in other works, the analysis of the window length was implemented, and it was provided an algorithm for the selection of the most stationary window according to the relative characteristics of the datasets. As result two windows were selected according to the short and long size analysis, one of 400 ms and one of 4 seconds. Two more windows were used for comparison, and hence, the windows of 400 ms, 2s, 4s and 20s were evaluated and provided significant differences in the connectivity patterns produced from the segmentation of the signals at each length.

First, an analysis in the domain of the regions of interest was performed and it provided some insights about main connections produced in the network. Specifically, the connections between the posterior to frontal areas, posterior to lateral regions and frontal to central areas were the most common ones across the windows. This characterized the flow of information in general terms, however, it was necessary to look into the details of the sensor space since the characterization of the connectivity was not possible to be done in such a general way by covering so large regions and averaging the connectivity amplitudes on the channels that belonged to those regions.

Is in this way that the sensor space was used, and the different connectivity patterns were identified at each window segment for both alpha and beta bands during eyes open and eyes closed conditions. In general, the 400 ms window did not present any connectivity pattern that followed any of the observations made by other authors which might suggest that this is not a proper segment length in order to perform the analysis of effective connectivity. This was observed for both alpha and beta bands, showing a very spread connectivity which did not characterize or highlight areas of centrality in comparison to the other windows.

The use of the 400ms segment length was derived from the results obtained by considering the signal segmentation into short segments (see *Window selection approach*), which was based on the assumption that stationary characteristics on physiological signals are mostly preserved in short periods of time [17], [75], [76]. In this way, under the short segment length processing framework the EEG signals were segmented into windows shorter than 1 second, and the 400ms was the one selected as the most stationary under this segmentation category, considering that it had enough samples to fulfill the sampling theorem requirement to cover the low frequency of 7 Hz (low level boundary of the alpha frequency band).

Then, the analysis of effective connectivity considering the 400ms window length was performed based on the results obtained from the algorithm applied to the 12 EEG recordings (6 subjects*2 conditions) that were employed for the stationary analysis.

In this way, when the effective connectivity results were obtained, it was expected to find outcomes in line with the observations made by other works in the state-of-the-art which in general considered rather different (longer) window lengths, however, it was not the case as explained before. The employment of this segment length was for exploratory reasons according to the hypothesis of the preservation of stationary characteristics in short segments. Unfortunately, the results were not positive, and this suggest that the term ‘short segment’ is relative and does not necessarily mean to use windows with periods in the order of milliseconds.

Conversely, other windows provided results that suggested similarities with the observations in previous research works. Specifically, the closed eyes condition for the alpha band was better represented by the connectivity patterns, showing similarities between the windows of 2 seconds and 4 seconds. These patterns confirmed the expected causal relationships between the posterior region directed to the frontal area, and also highlighted the intra connections that are mostly present in the posterior area of the scalp. The window of 20 seconds showed similar patterns as well for the closed eyes condition, however the strengths developed in these central areas are not as high as the ones represented in the other two windows.

The clusters generated from the central nodes show the areas of greater connection on each window, and as it could be observed on Figure 60, these cluster of electrodes were very similar for the closed eyes condition, only highlighting some differences on the channels located in the frontal area. However, what is more interesting to see are the patterns that are different and not the ones that do not present any changes. Thus, the cluster of channels for the alpha band in opened eyes state were analyzed to state those differences. By looking at the areas covered by the clusters, it can be seen that the electrodes that belong to the frontal region are organized differently, showing a symmetrical block of nodes for the windows of 2 seconds and 400 ms (not considered).

The 4 seconds window covers more areas and has some channels that participate more in the central region facilitating the communication flow in the network between the posterior area and the frontal region. This could explain the involvement of intermediate structures in the frontal-central joint with the central-posterior one, establishing the importance of such area in the influence of the posterior area exerted onto the frontal area.

The graph-based parameters evaluated as a function of the number of connections in the network showed greater values for the windows of 2 seconds and 4 seconds, being the results from the former higher for the eyes open condition, and the results from the latter higher for the closed eyes case in both alpha and beta bands. It is a way to characterize and identify the windows that convey more information according to the network characteristics derived from them and provide a starting point to account for the centrality of the nodes interconnected.

The connectivity diagrams in the beta band did not exhibited the same structural characteristics compared to the alpha band case. The connections are more spread and the strengths from the connections are smaller. For the closed eyes condition, the bilateral distribution of electrodes is observed for the windows of 2 seconds and 4 seconds, while central nodes located at the right central parietooccipital area exhibit higher connections in response to the opened eyes condition. For the case of the 20 seconds window such network structure is not noticeable and the directionalities in the connectivity patterns cannot be identified which could mean that at longer windows the connectivity structures are not so strong and might be necessary to lower the

strength threshold in order to address the connectivity directionalities and find such kind of structures.

According to the works described in [71], [46] and [45], it arises the hypothesis of the involvement of the central posterior and central frontal regions as the characteristic areas of the resting state conditions. According to these works, the Default Mode Network (DMN) that comprises the aforementioned regions are part of the synchronization over the alpha band. This hypothesis is reinforced by the results obtained in this thesis as it was shown in the last section. The posterior cingulate cortex that comprises the posterior central joint and the medial prefrontal cortex where the central frontal nodes are located, correspond to the areas of higher activation for the alpha band. It was indeed observed in the results for the 2 seconds, 4 seconds and 20 seconds windows, having a greater strength for the windows of 2 seconds and 4 seconds as shown in the results.

Considering this, it is possible to do a selection of an appropriate window according to these physiological characteristics. Despite that the window of 2 seconds presents more connections related to the DMN circuit, it did not have apparent significance on the degree for the alpha and beta bands, which according to [45] it should be present. In this way, the window of 4 seconds is the one that explains the most out of the attributes shown in the previous works, characterizing the network and explaining significantly the graph theoretical attributes.

8. Conclusions

This master's thesis work presented the design, implementation and evaluation of an algorithm that was devised as a tool for selecting an appropriate window size as a preliminary step under the effective connectivity framework. The algorithm provides a way to evaluate the stationary characteristics of EEG signals based on high-order statistics metrics, specifically based on kurtosis and the variation of this quantity over time according to the signals and the analysis of the window duration at test.

Based on available tools [61], [58], the approach presented here performs the data cleaning process of the signals and applies classical pre-processing steps (i.e., filtering, resampling, artifact rejection) to prepare the cleaned signals for their segmentation according to different non-overlapping windows which are then used as the smallest data blocks from which the statistical features are being estimated.

As it was shown, the application of the cleaning process reduced the total duration of the signals significantly, this supposed a limitation in the processing of the data, and the posterior connectivity analysis was affected since there were not enough samples to provide statistically significant results. A workaround was needed, and it was applied a less rigorous cleaning process by varying the parameters of the pre-processing stage to consider more data for the analysis. This situation is explained because some of the EEG recordings were heavily affected by external noise.

The statistical quantities characterize each of the segment durations and from them there are obtained a series of distributions employed by the algorithm to look for the most common segments across the EEG accounting for similar statistical values. In this way, according to the searching strategy the segments that had comparable statistical features from each signal were selected and grouped together. Then, the shortest segment that fulfilled these characteristics and that according to the theoretical constructions was the most stationary one was selected to perform the connectivity analysis.

The searching algorithm worked on the distribution domain of the variance of the kurtosis values according to the segmentation. This was an empirical way to look for the stationary segments according to the characteristics given the dispersion of the measures that evaluated the stationarity. This was devised as an iterative procedure that considered the model of the distribution, which was assumed to follow a gaussian like distribution of the kurtosis values and a chi-squared one for the kurtosis variance.

Based on this assumption the searching algorithm works and considers the maximum point of the distributions to perform the searching. In this way, the results can be affected since they depend on the local maxima of the distribution to perform the searching, however, as the iterative process considers this point as the point of maximum probability, the searching provides segments of similar stationary characteristics. In order to improve this, other modelling and searching procedures would be needed to be explored.

From the algorithm it was possible to select two windows for the overall group of subjects that were part of the experiment: one of 400 milliseconds for the short segment analysis and a second one of 4 seconds for the analysis at longer periods (i.e., larger than one second). However, as shown in Table 9 not all the subjects had the same window as choice. This diversity on the

results highlights the necessity of performing other evaluations on the selection, by performing conventional statistical tests of the quantities employed by the algorithm.

The effective connectivity analysis was based on the general processing scheme based on different works as shown in Figure 4. This diagram considers general steps, being one of them the employment of a connectivity measure. In the state of the art regarding the actual analysis of physiological data, the use of one measure or another is not usually compared and even though they are supposed to bring similar results, it is not always the case. The use of the Directed Transfer Function as the connectivity measure in this work was based on its implementation of other works, which according to the results reinforce the observations found in the state of the art.

The working domain definition in the channel space is a common practice performed in the analysis of resting state conditions, however, as it is explained by some authors [46], this is prone to errors and can provide erroneous descriptions of the connectivity analysis related to the topographical definitions of the channels. In this way, as a possible improvement, it would be useful to implement source localization schemes like LORETA in order to minimize the possible errors and provide a more accurate representation of the physiological processes in the brain.

The surrogate data approach is a complex step to perform, for the purposes of this thesis, it was implemented by using a MATLAB toolbox dedicated to this process, however, the performance was limited, and the surrogates took a long time to be produced; about 5 hours per each condition for each subject. Moreover, the data size was very large, producing files that were about 4 Gb on average. This reduced the overall performance of the processing and required to spend a lot of time in the data generation. As a way to improve the overall processing, as a future work, it could be implemented a custom program in charge of this process.

The analysis of connectivity provided a lot of insights regarding the nodes in the sensor space that generate and receive more influence from the other areas. As it was demonstrated by the results, the influence of the posterior part of the brain is increased and directed to the frontal area in a greater way when the closed eyes condition is produced.

In contrast, the open eyes condition reveals structures that are more spread in terms of the areas that are being covered by the electrodes in consideration, however, in this case the directionalities in the connectivity convey more information about the signals involved in the connectivity. The frontal area and specific nodes are more heterogeneous according to the windows employed which supports the hypothesis that the window length affects the results in connectivity.

In this sense, the use of graph-based parameters to select the electrodes of higher centrality according to the connectivity matrices derived from the windows employed, proved to be an appropriate way to highlight the regions of greater influence according to the significant connections. Moreover, the characterization in terms of the frequency bands demonstrated to provide features that characterize the resting state conditions, not only for the alpha band that was already found in previous works but in the beta band across multiple windows, being the segments of 2 seconds and 4 seconds, the ones of greater difference as shown in Figure 61 and Figure 64.

The generalization of the connectivity considering regions of interest did not provide meaningful results in the characterization of the information flow between the areas. As observed on Figure 55, the interaction across the regions shows that almost all of them are interconnected and are influenced reciprocally. This might be due to the large areas that are being covered by the electrodes that belong to them from which slight changes in the DTF amplitudes heavily affect the interactions and from them the connectivity might change. This is translated in the statistical results that were obtained which suggested that the interactions between the factors of window length, resting state condition and region of interest was not significant.

Moreover, the large areas covered by the electrodes do not allow to characterize the information flow and the effective connectivity from neurophysiological points of interest, which justifies the use of graph theory measures in the sensor space to perform such characterization.

The evaluation of the connectivity network considering the nodal information from the EEG electrodes highlighted specific connectivity influences as shown in the results. The connectivity results for the windows of 2s, 4s and 20s provided similar characteristics in the information influence pattern, while the 400ms provided information that cannot be validated considering the results from previous works. As it was discussed previously, the 400ms window was not appropriate and it was employed since it was an outcome from the window segmentation framework, however, after evaluating its results on effective connectivity it did not provide reproducible results considering other characteristic windows.

In this sense, due to the characteristics of the resting state conditions under analysis and the physiological observations from previous works, the results that are more in line with such characteristics are the ones derived from the windows of 2s and 4s, which as explained previously, show similarities with the DMN network which is hypothesized to characterize the resting state conditions in relaxation as measured by the data in our case.

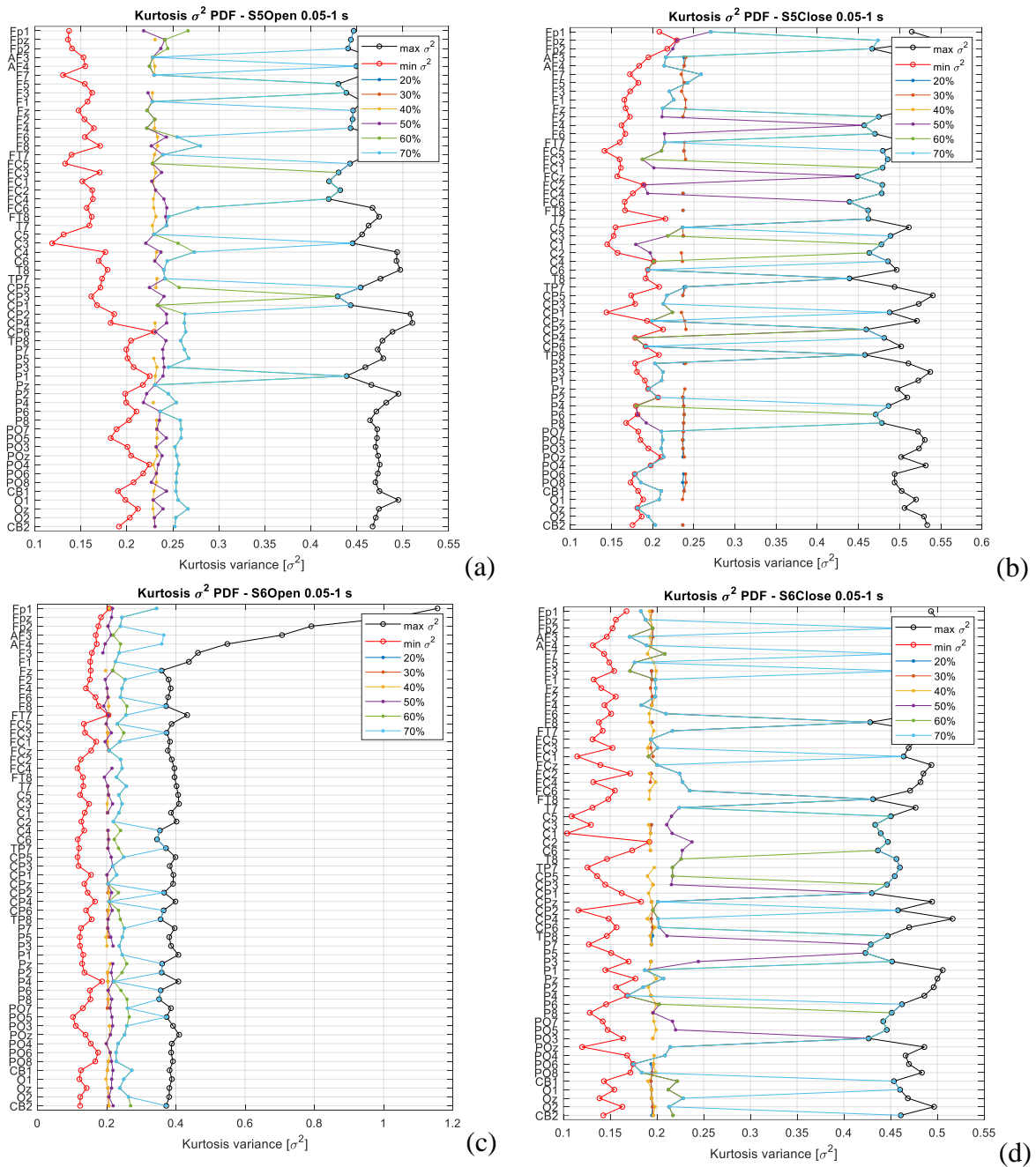
The algorithm for the window length selection based on the stationary characteristics of EEG signals according to this thesis work demonstrates to be a tool that could be employed in the effective connectivity framework as a preprocessing step used in the same way as it was described in this project.

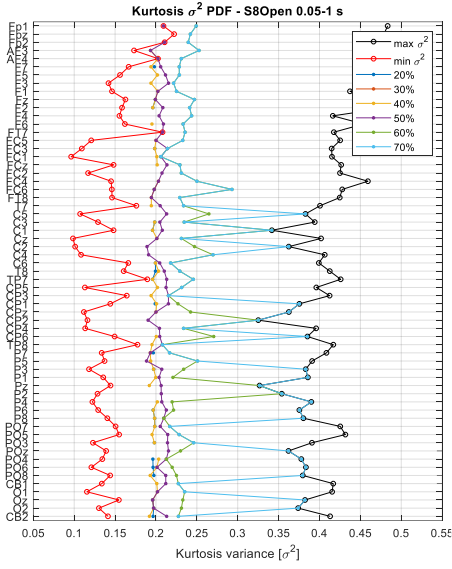
The advantage of the algorithm is that it is not restricted to be only used for signals that measure the resting state, after performing more tests and code optimization, it could be employed in any kind of EEG data (from any type of experiment setup), at different sampling rates and using any channel size. This could be employed as a tool that provides some insights about the stationary characteristics of such signals and help in the research practice considering EEG data.

Appendix A: Short-window duration analysis

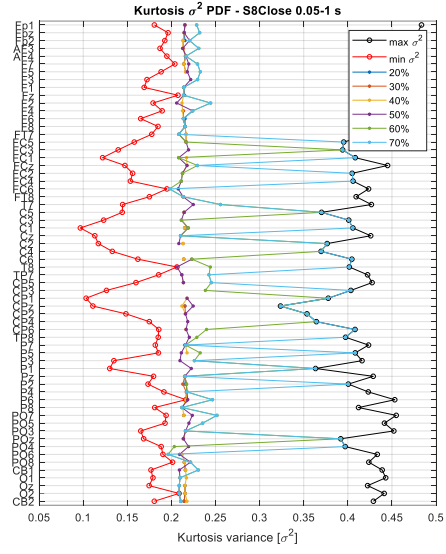
Following the structure of the long-window duration analysis that was presented in the previous section, let consider the analysis of shorter segments contemplating a basis window duration $W_L = 50\text{ms}$ and the number of windows $N_w = 20$. In this case, the stationary characteristics estimated from segment to segment reveal the modulation of rapid temporal dynamics exhibited by the signals if present.

In Figure 65 there are depicted the searching domains and the selected variances under specific percentage thresholds considering the subjects S5, S6, S8, S9, and S10 in R1, R2 under the short-window segmentation procedure.

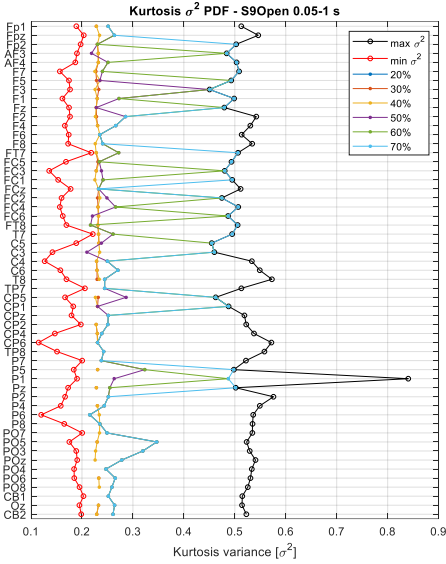




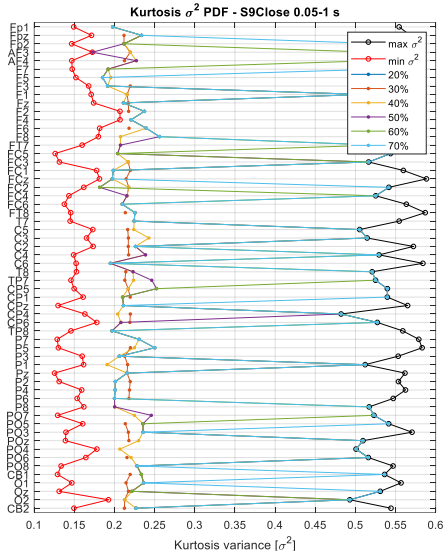
(e)



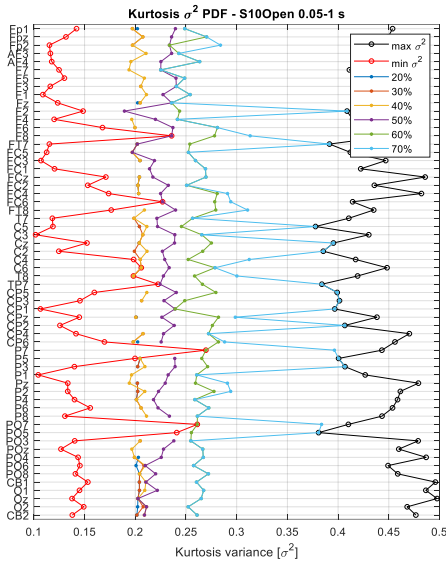
(f)



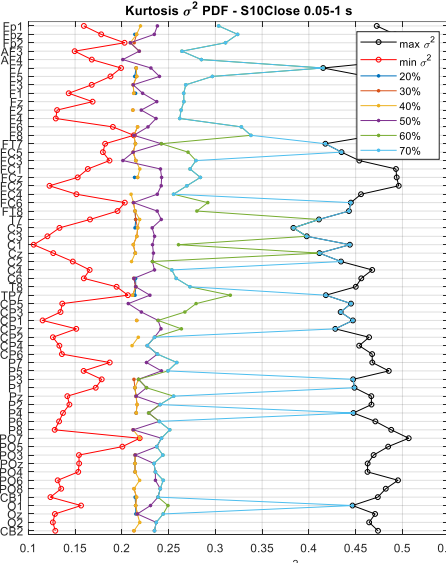
(g)



(g)



(i)



(j)

Figure 65. Kurtosis variance (K_{σ^2}) searching domains for segmentations from 50 ms to 1 second. Resting-state conditions depicted in pairs: a, b) S5 – R1, R2. c, d) S6 – R1, R2. e, f) S8 – R1, R2. g, h) S9 – R1, R2. i, j) S10 – R1, R2

All the searching domains depicted in Figure 65 can be considered part of the third category of the max and min kurtosis variance limits that was introduced earlier. In general, their limits are defined between $\min \sigma^2 \cong 0.2$ and $\max \sigma^2 \cong 0.4$, and the variability on each bound is considerably lower than the case for the long-window segmentation case. As explained before, this suggests that percentage thresholds could be found in between the interval limits, however, as the graphs show, this is not the case, and higher kurtosis variances are needed to obtain common segment durations.

In most of the searching domains, the algorithm is not able to find values restricted to percentage thresholds lower than the 40% of the largest variances, this shows that the minimum variances on each channel already exhibit magnitudes that are close to 0.4 times the maximum values. In general, it can be said that the kurtosis variances from shorter segments are higher in comparison to the longer ones from which it was possible to obtain values from the 20% proportion as can be observed in Figure 43.

From the searching domains, and the percentage thresholds the algorithm works using the kurtosis variance density to find the signals exhibiting similar characteristics. Such values restricted to such conditions are depicted in Figure 65 as the points in between the searching domain and the kurtosis variance densities in Figure AN 3.

The percentage threshold variance boundaries are summarized in Table 16 and Table 17. Among the variance lower and upper boundaries it can be noted that the percentage thresholds are found for magnitudes lower than 40% of the largest variances, however, they do not represent a significant number of channels sharing those characteristics as can be noted on Table AN 5- 14.

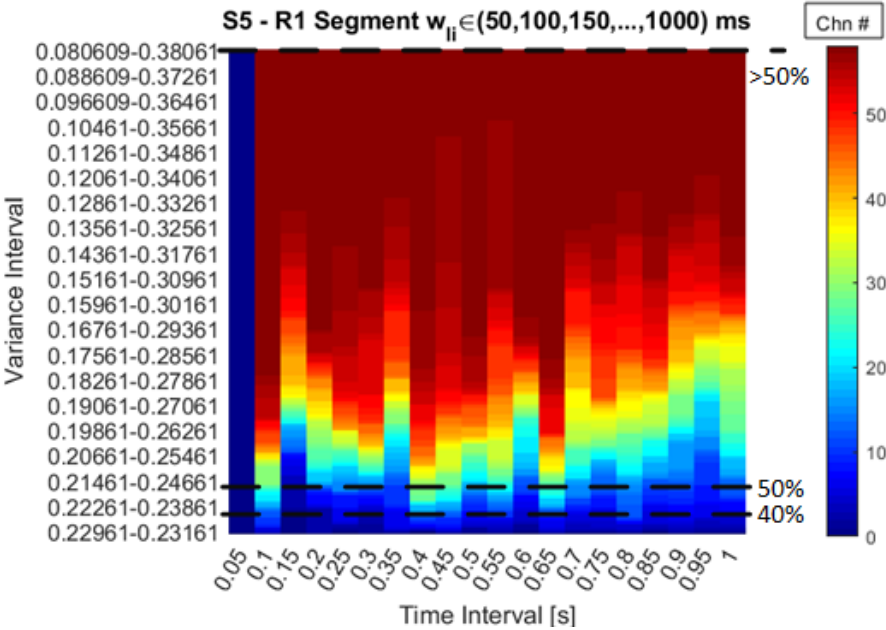
Table 16. Kurtosis variance range of different percentage thresholds, $w_l = 50,100, \dots, 1000$ milliseconds. Subjects S5, S6, S8, S9 and S10 in opened-eyes resting state condition R1

R1	Bound	10%	20%	30%	40%	50%	60%	70%	80%	90%	100%
S5	Lower	0	0	0	0.2276	0.2176	0.0216	0.0056	0	0	0
	Higher	0	0	0	0.2336	0.2436	0.4396	0.4556	0.4706	0.4766	0.5096
S6	Lower	0	0	0.2017	0.1967	0.1887	0.0627	0.0317	0.0197	0.0057	0
	Higher	0	0	0.2057	0.2107	0.2187	0.3447	0.3757	0.3877	0.4017	0
S8	Lower	0.1964	0.1954	0	0.1914	0.1794	0.0334	0.0044	0	0	0
	Higher	0.1984	0.1994	0	0.2034	0.2154	0.3614	0.3904	0.4154	0.4364	0.4994
S9	Lower	0	0	0.2273	0.2253	0.0063	0	0	0	0	0
	Higher	0	0	0.2333	0.2353	0.4543	0.4933	0.5113	0.5253	0.5373	1.2313
S10	Lower	0	0.2007	0.1967	0.1937	0.1647	0.1217	0	0	0	0
	Higher	0	0.2047	0.2087	0.2117	0.2407	0.2837	0.4097	0.4447	0.4597	1.2037

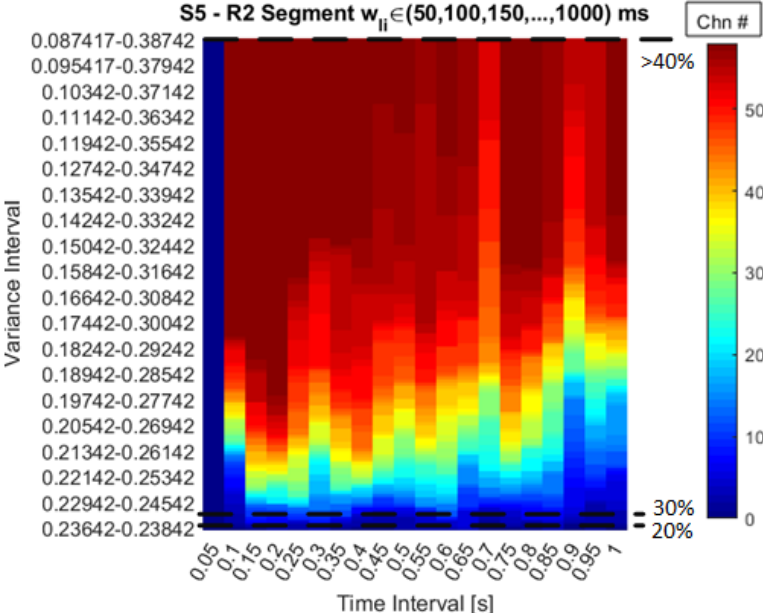
Table 17. Kurtosis variance range of different percentage thresholds, $w_l = 50,100, \dots, 1000$ milliseconds. Subjects S5, S6, S8, S9 and S10 in opened-eyes resting state condition R2

R2	Bound	10%	20%	30%	40%	50%	60%	70%	80%	90%	100%
S5	Lower	0	0.2364	0.2344	0	0.0124	0	0	0	0	0
	Higher	0	0.2384	0.2404	0	0.4624	0.4794	0.4934	0.5104	0.5224	1.2384
S6	Lower	0	0.1935	0.1925	0.1895	0	0	0	0	0	0
	Higher	0	0.1955	0.1965	0.1995	0.4325	0.4535	0.4655	0.4785	0.4935	0.5155
S8	Lower	0	0.2139	0.2129	0.2119	0.2049	0.0349	0.0209	0.0019	0	0
	Higher	0	0.2159	0.2169	0.2179	0.2249	0.3949	0.4089	0.4279	0.4519	0.4829
S9	Lower	0	0	0.2118	0.1858	0	0	0	0	0	0
	Higher	0	0	0.2198	0.2458	0.5168	0.5298	0.5438	0.5558	0.5688	0.5878
S10	Lower	0	0.2134	0.2114	0.2084	0.1854	0.0114	0	0	0	0
	Higher	0	0.2154	0.2174	0.2204	0.2434	0.4174	0.4494	0.4664	0.4804	1.2154

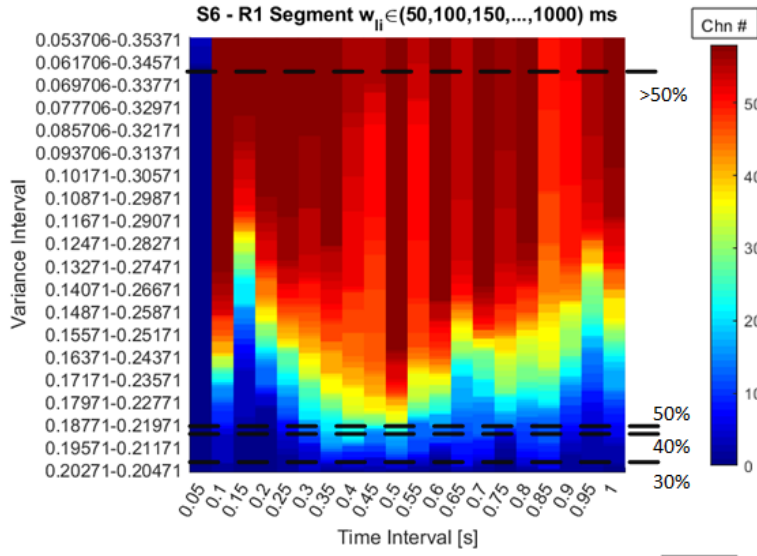
The boundaries of the percentage threshold intervals can be used to provide a graphical representation with respect to the number of channels that have comparable stationary characteristics. In this way, Figure 66 shows the heat plots of the number of channels as a function of the segment length and the variance interval provided by the searching strategy.



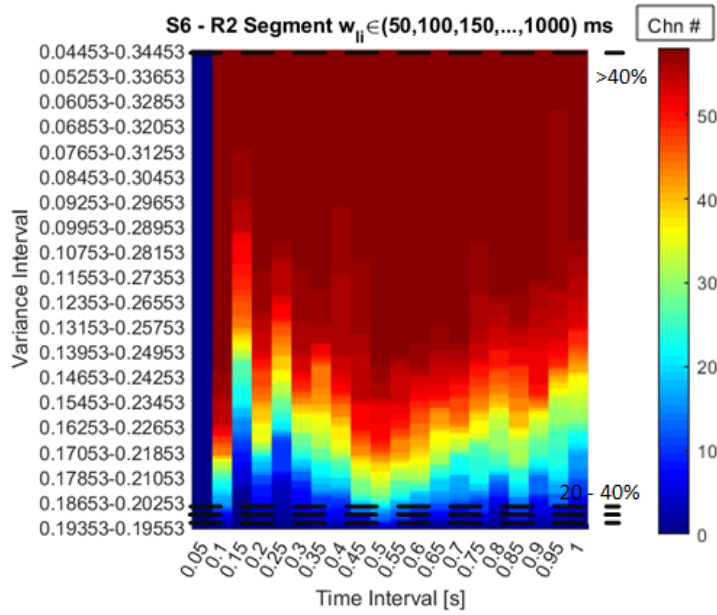
(a)



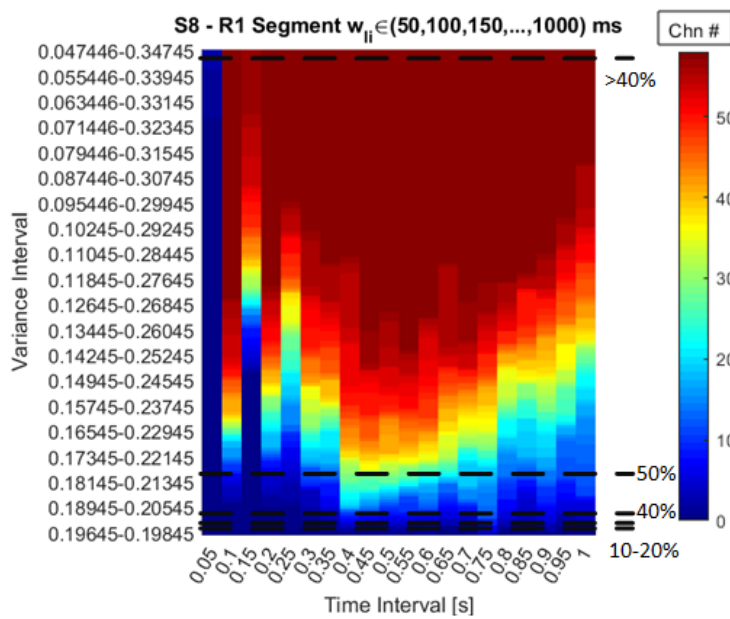
(b)



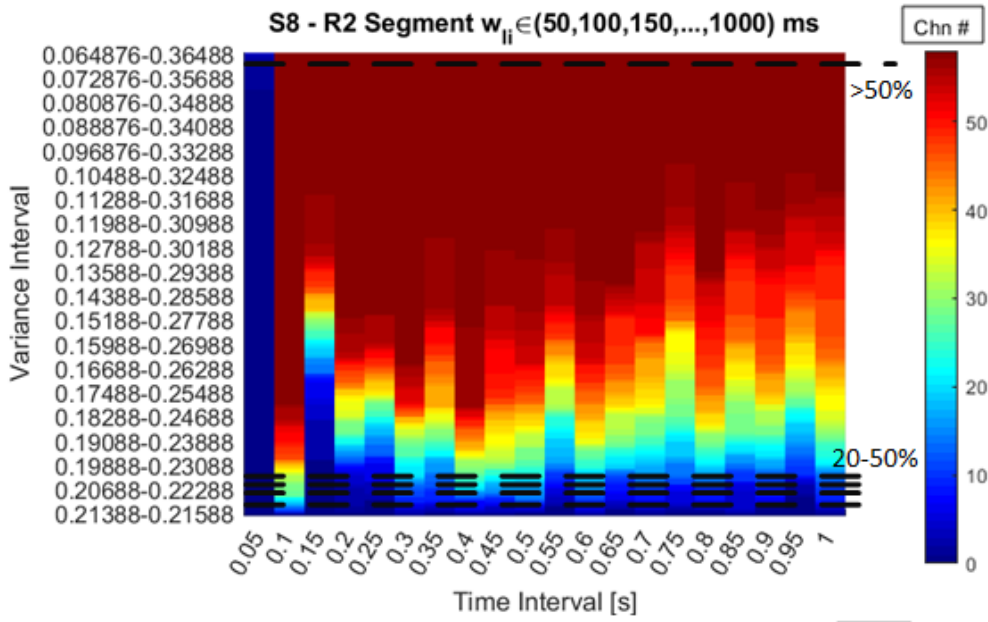
(c)



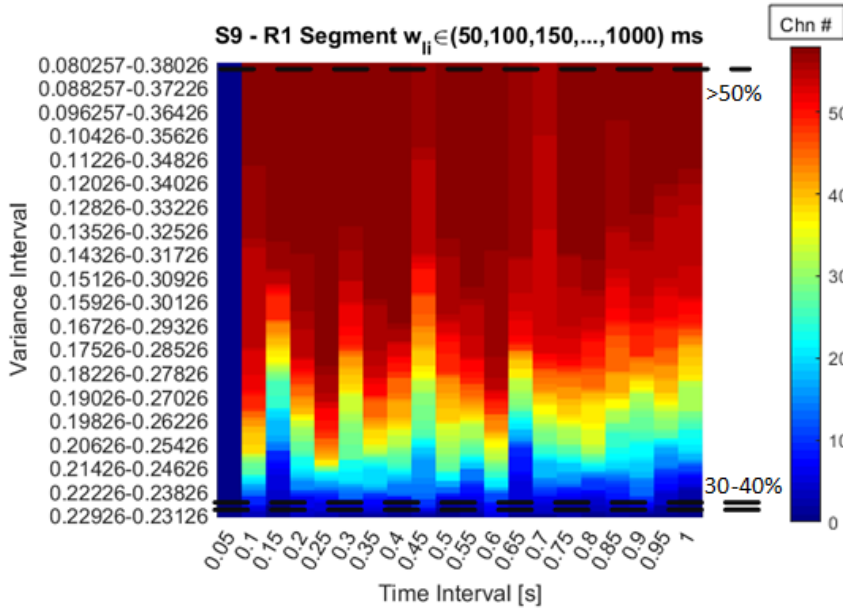
(d)



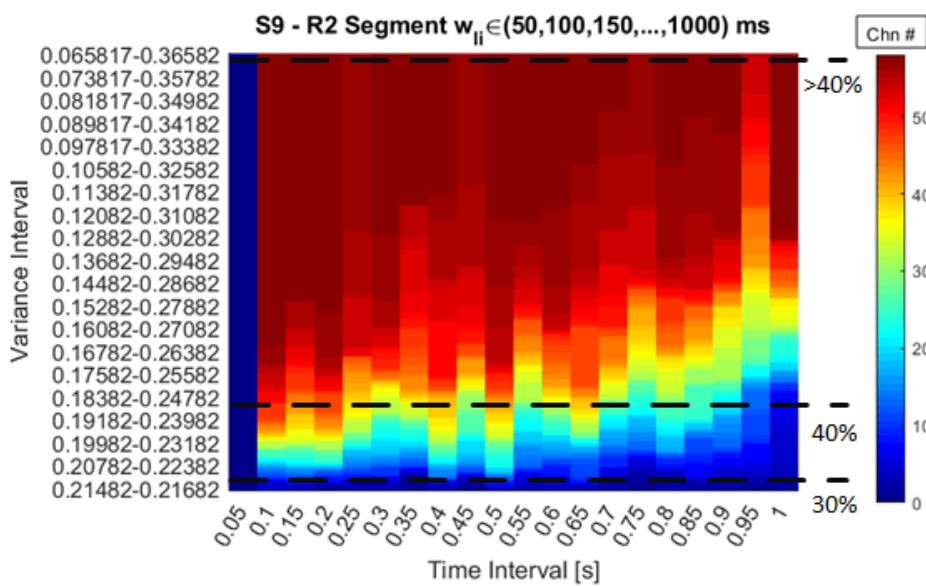
(e)



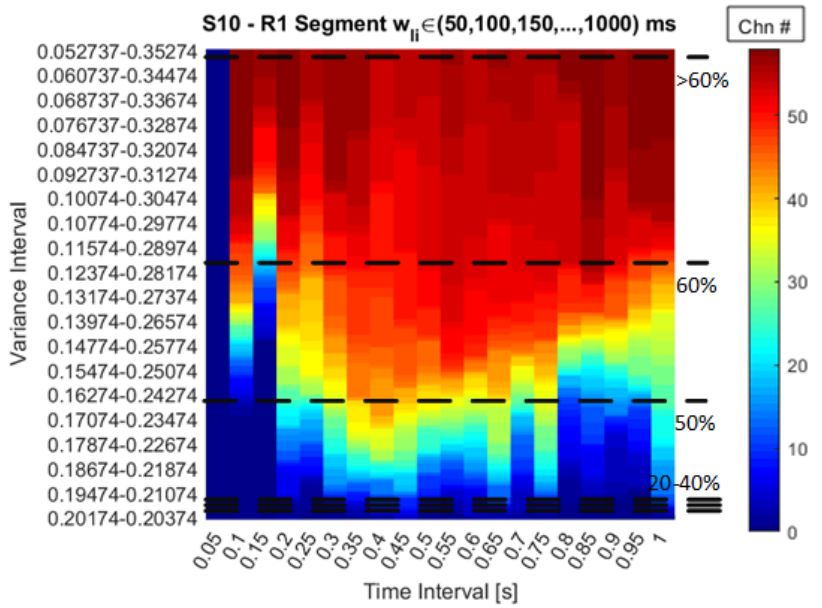
(f)



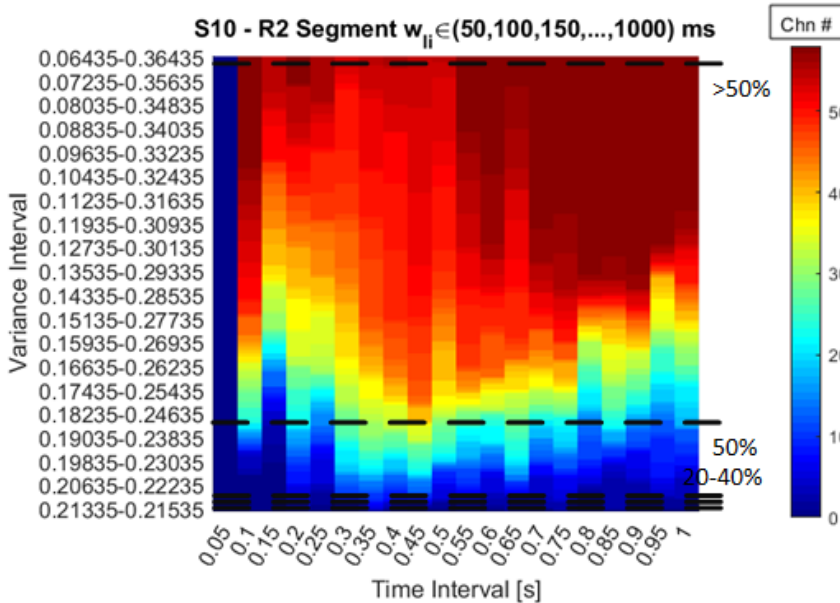
(g)



(h)



(i)



(j)

Figure 66. Number of channels as a function of the segment length and the searching interval in terms of the kurtosis variance – Short window segmentation.

a, b). S5 – R1, R2. c, d). S6 – R1, R2. e, f) S8 – R1, R2. g, h) S9 – R1, R2. i, j) S10 – R1, R2

The heat plots in Figure 66 show the number of channels (color-coded) on each of the 20 windows composing the segmentation matrix. As can be noted by comparing this graph with the long window segmentation, the distribution of the lower variances is more uniform and not exclusive to the longer segment durations. Considering this, the window selection can be performed by considering a window length whose variance interval is small enough and the number of channels within such interval is at least a half of the total number of channels from the EEG dataset.

Note that it is not possible to select segments with a duration lower than 0.143 s since it is the shortest duration to guarantee the observation of representative frequency components found in the alpha frequency band (that starts at 7 Hz).

By setting the percentage thresholds varying in the order of tens, it can be noted from the heat plots that in most of the cases the lower percentages do not cover any important number of

channels and when it is reached a value (around 40%), the interval coverage is so large that it would consider the whole domain of the distribution magnitudes. That is why for the short segment analysis a more subtle variation of the thresholds is needed, however, the thresholds shown in the heat plots as dashed lines are used for reference, and from them it is possible to check the variance intervals (y-axis) to look for the appropriate segment durations in the table of features generated by the algorithm.

The graphical representation is given in Figure 66 and the metrics derived from the algorithm provide the way to select the window durations for the short segmentation approach. As result, Table 18 shows the exact percentages of the windows that exhibit the lowest variance intervals from the densities with the shortest durations considering the limitations that have been discussed up to now.

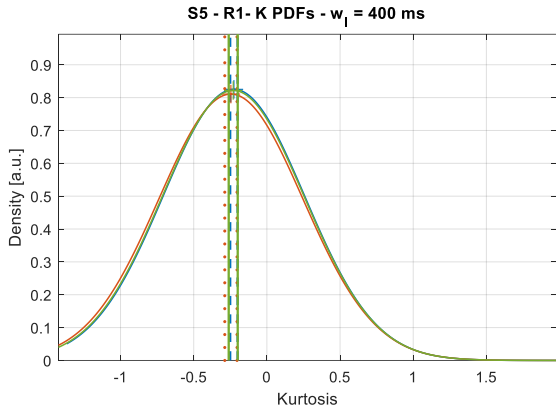
Table 18. Selected segment lengths (in green) for each subject and resting-state condition – Short window segmentation.

Subject	Condition	Lower	Upper	%	Win length	# Channels	Channel %
S5	R1	0.20560916	0.25560916	52%	400 ms	44	77%
	R2	0.21241667	0.26241667	47%	200 ms	47	80%
400 ms					45	--	
S6	R1	0.17070605	0.23670605	55%	500 ms	52	91%
	R2	0.17053044	0.21853044	43%	100 ms	46	--
					450 ms	45	75%
					500 ms	47	--
S8	R1	0.17244561	0.22244561	52%	400 ms	40	66%
					450 ms	41	--
					500 ms	40	--
	R2	0.18987643	0.23987643	52%	100 ms	54	--
					400 ms	46	74%
S9	R1	0.19625657	0.26425657	47%	250 ms	48	87%
					350 ms	43	--
	R2	0.184817	0.246817	40%	100 ms	51	--
					200 ms	47	--
					400 ms	40	69%
					500 ms	42	--
S10	R1	0.16273722	0.24273722	50%	400 ms	44	73%
	R2	0.17535043	0.25335043	52%	450 ms	48	79%
						Mean	77%

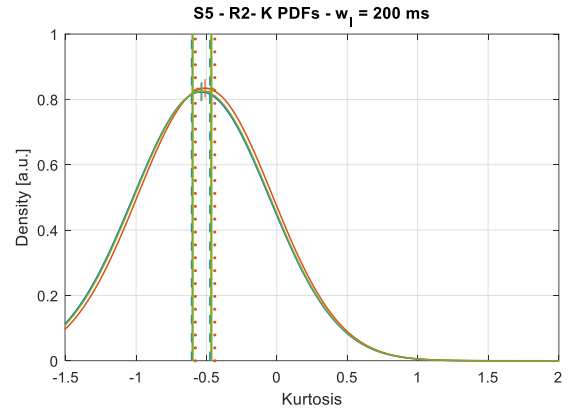
In this case, according to Table 18, the variance intervals according to the percentage thresholds of the selected windows are found at around 50% of the largest variances. As can be noted, the most common window across the EEG datasets correspond to the $w_l = 400$ ms (with 5 out of 10 as the mode). According to the selected lengths, the percentage of common channels is about 77% (higher than the 69% found for the long window segmentation approach).

From these data, it is observed that higher relative variances are considered for the window selection with an average of 49% for the percentage thresholds, which represents an increase of 13% w.r.t the 36% obtained for the case of longer window durations (Table 8).

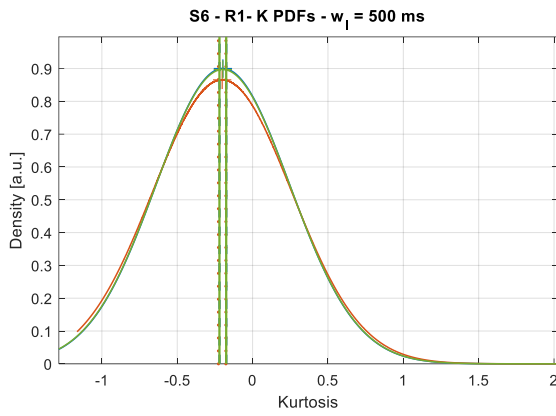
To check for the kurtosis distribution differences Figure 67 shows the estimated densities for the selected channels, the discarded channels, and the whole set of signals composing the EEG recordings under consideration.



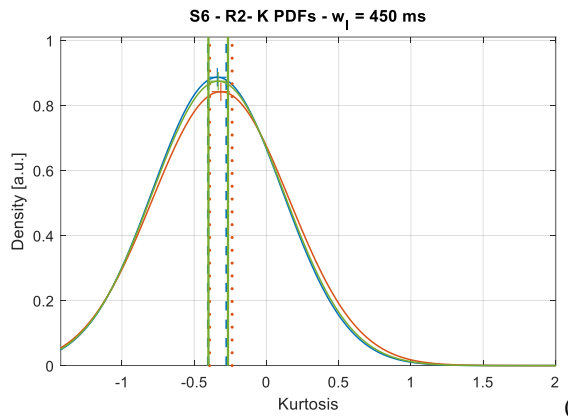
(a)



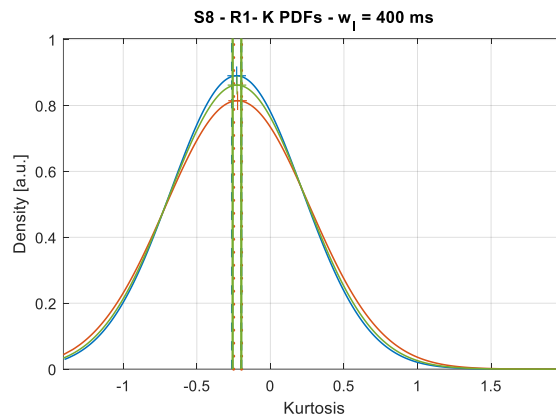
(b)



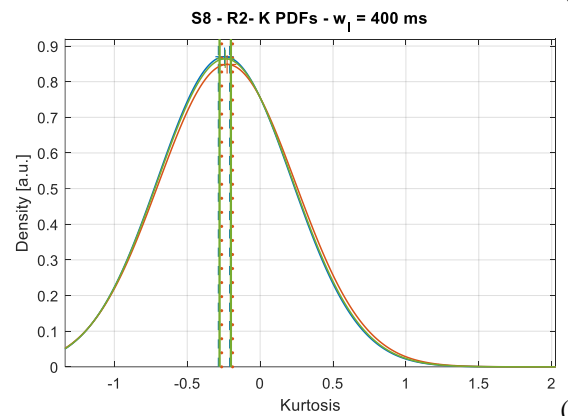
(c)



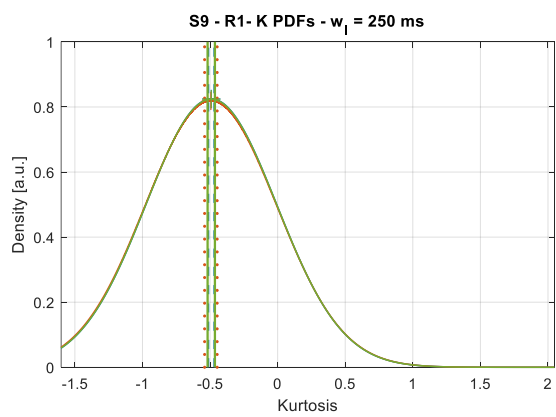
(d)



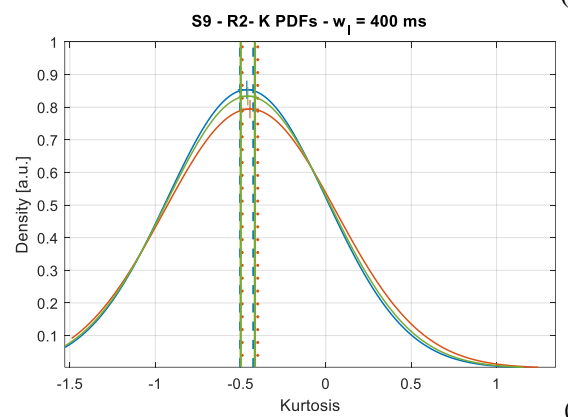
(e)



(f)



(g)



(h)

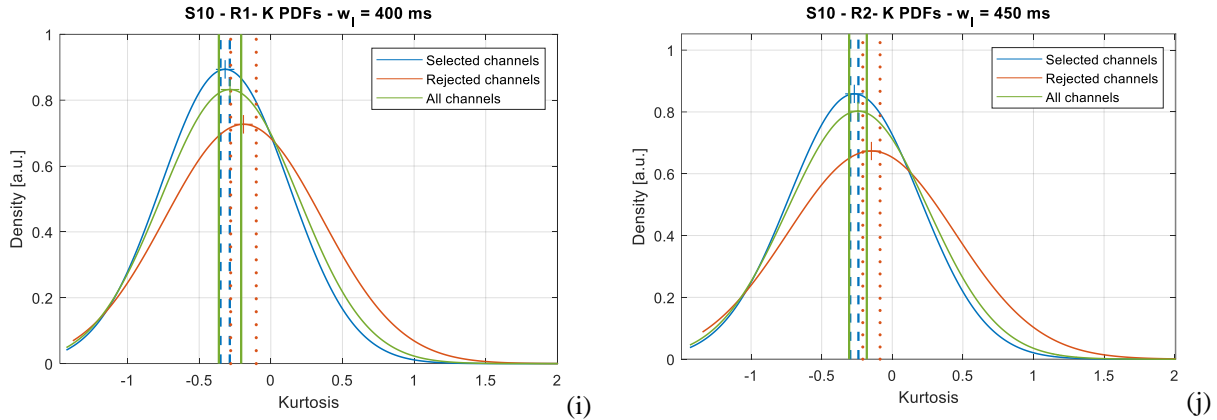


Figure 67. Kurtosis distributions considering the selected channels from the percentage thresholds. – Short window segmentation. Resting-state conditions depicted in pairs: a, b) S5 – R1, R2. c, d) S6 – R1, R2. e, f) S8 – R1, R2. g, h) S9 – R1, R2. i, j) S10 – R1, R2

In contrast to the previous case (Figure 46), here the resulted distributions obtained under the conditions for short segmentation show to have very similar characteristics, even the discarded segments have similar kurtosis expected values but slightly higher variances and that is why some of the channels are being discarded. Excepting the kurtosis distributions from Subject 10 in both resting-state conditions, the PDFs are almost identical, from this, could be generalized the use of the whole set of channels at the selected window length to perform the effective connectivity since the stationary characteristics are very related across the channels.

For the S10 – R1, R2 case, the kurtosis characteristics of the discarded channels have a large deviation from the ones of selected signals as well as from the overall distribution of the whole set of channels, this suggests that the discarded signals represent a very small portion of the total distribution, thereby they can be rejected for the further analysis, the very same happens on the cases from the long windows segmentation.

By considering all of the characteristics mentioned above, the window length selection is performed according to the characteristics derived from each of the EEG recordings, in this way, the analysis regarding the overall results is presented as follows.

Annex

- Figures

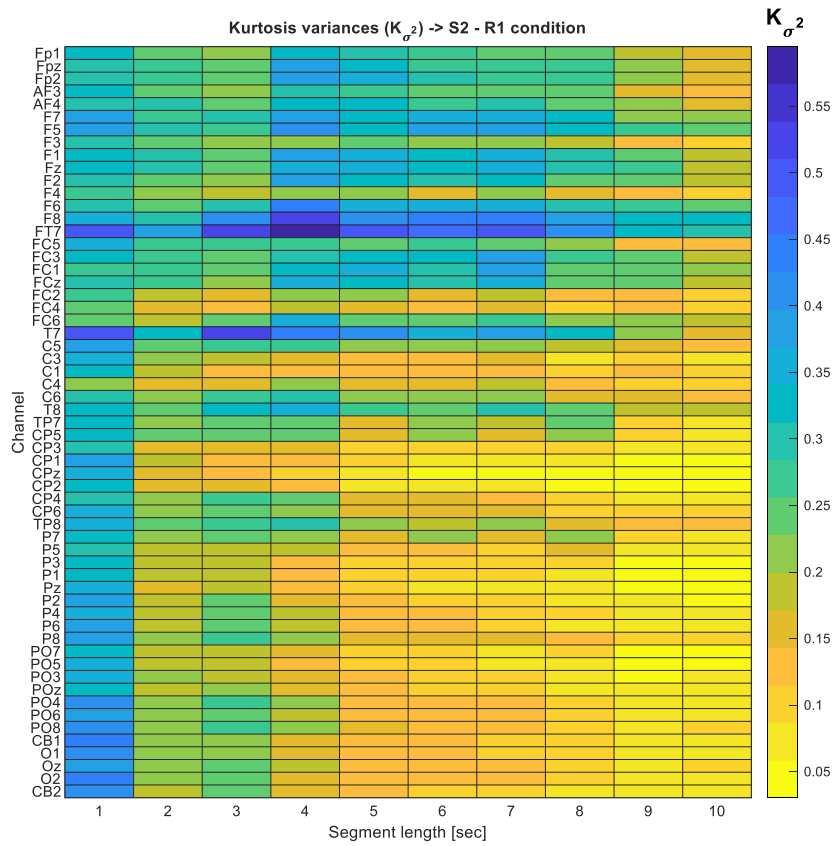
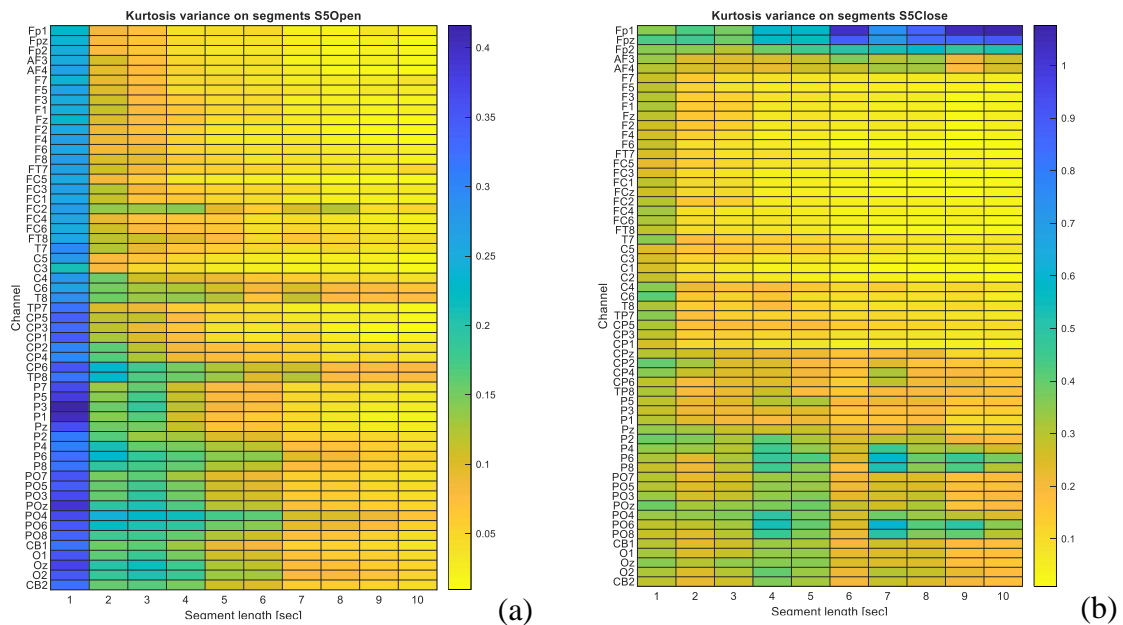
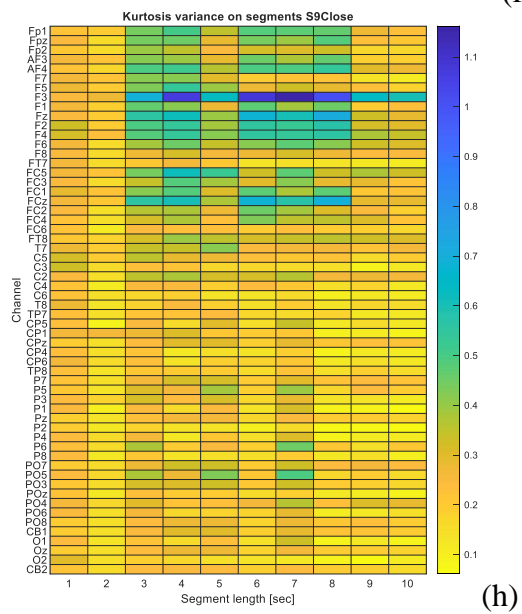
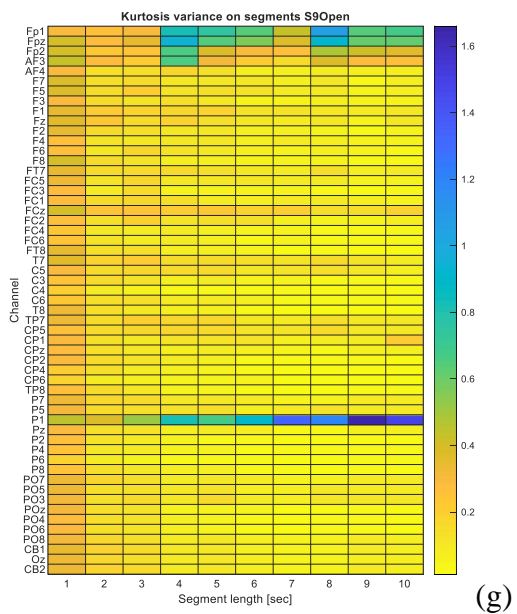
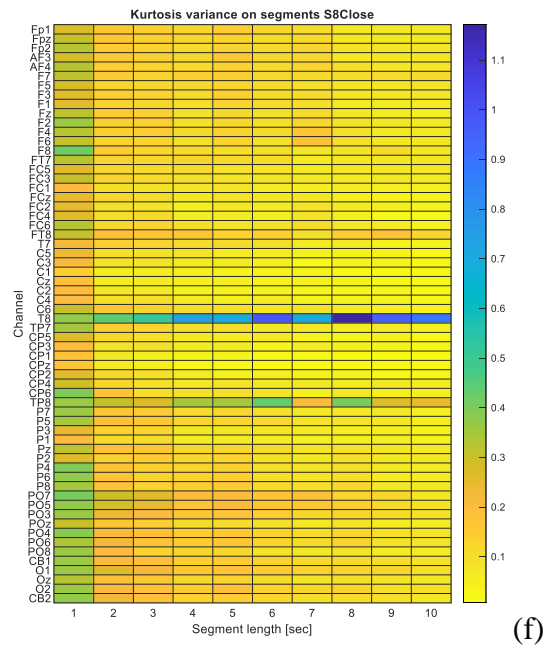
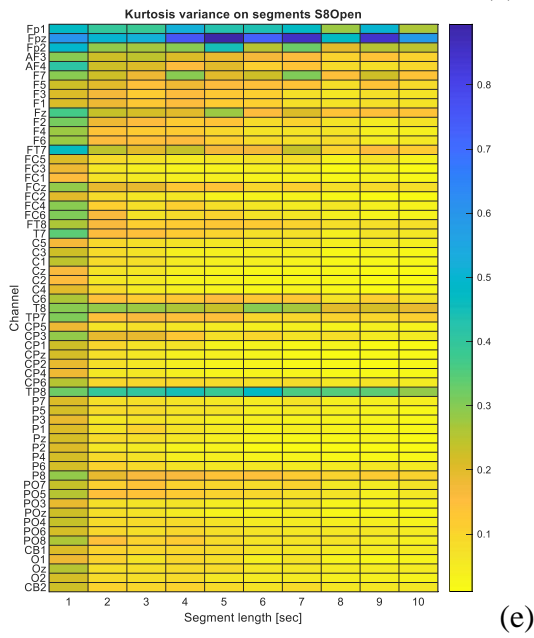
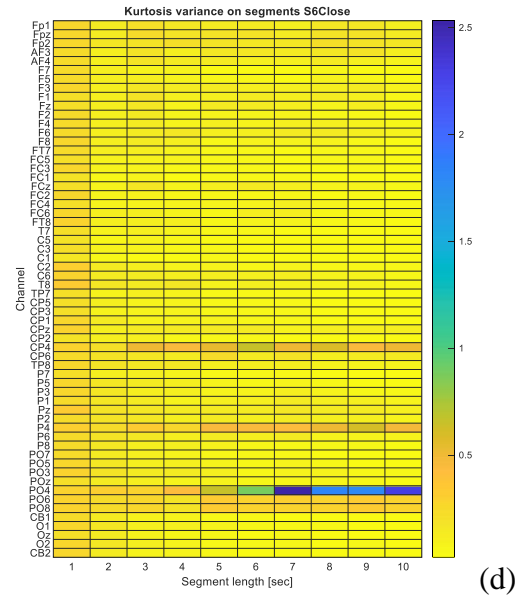
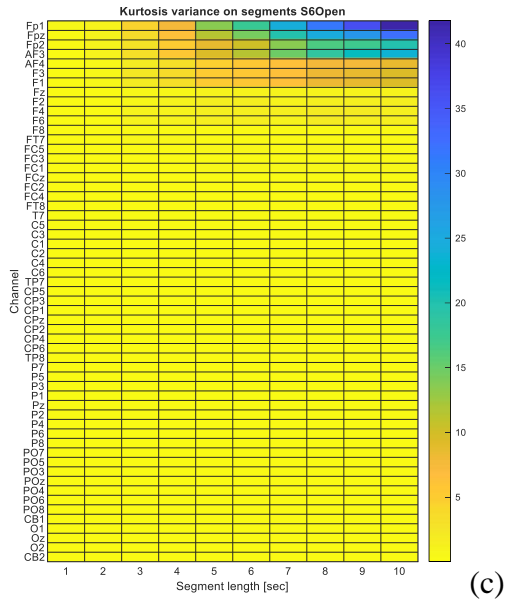


Figure AN 1. Heat plot of the K_{σ^2} values estimated from the recording of S2 in opened eyes resting-state condition.





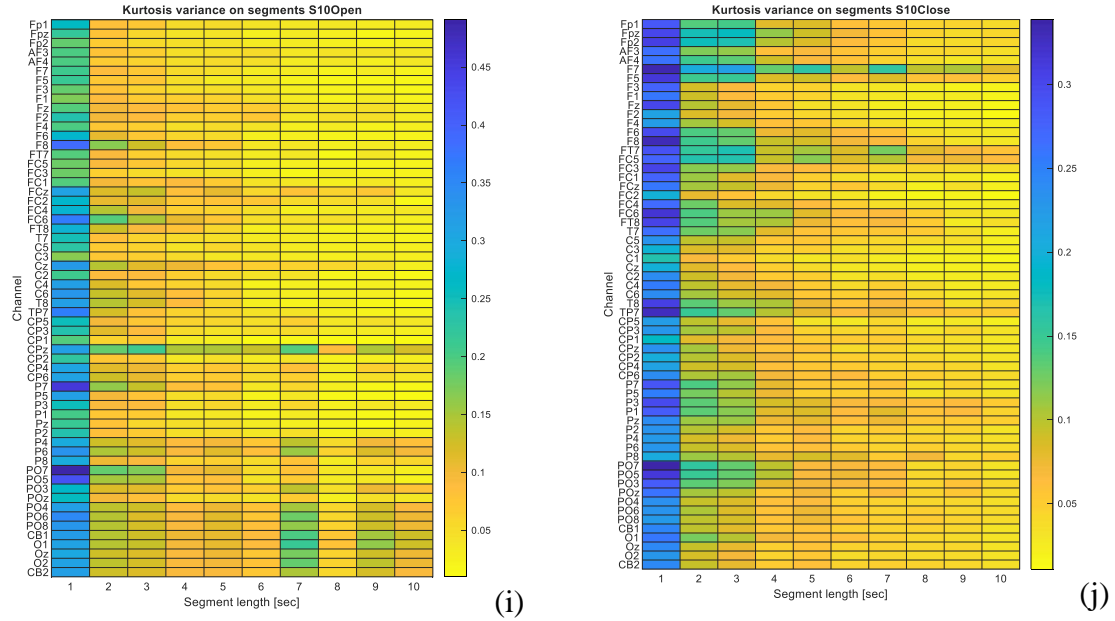
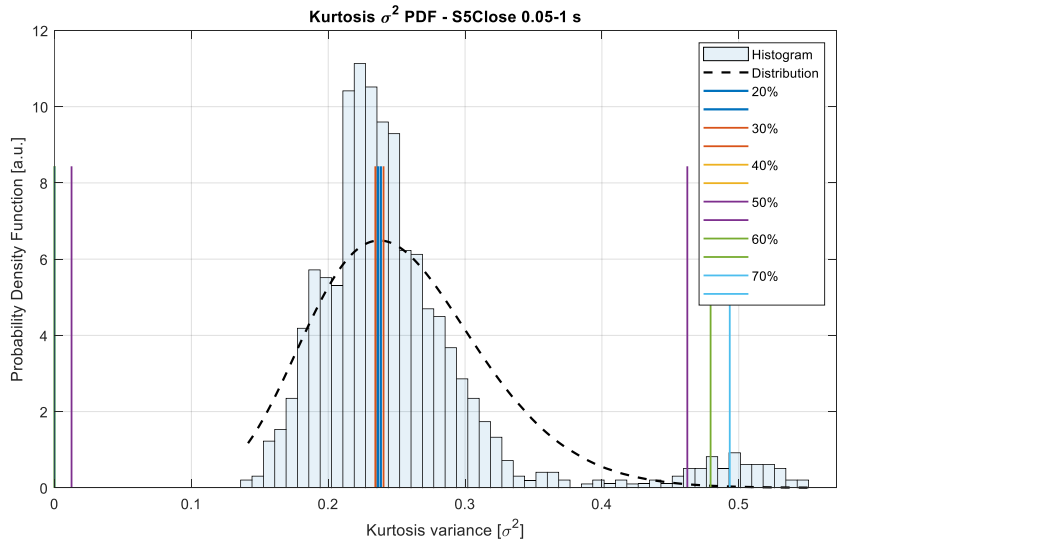
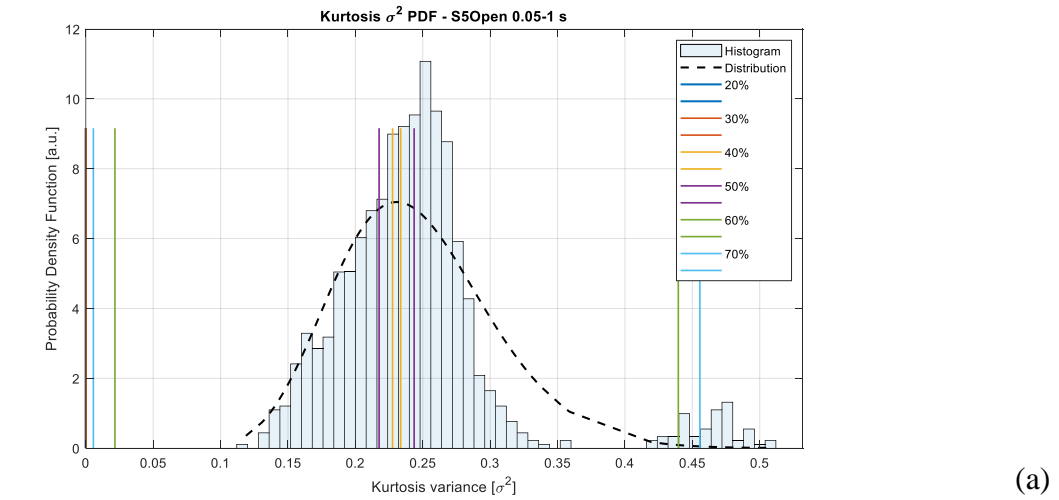
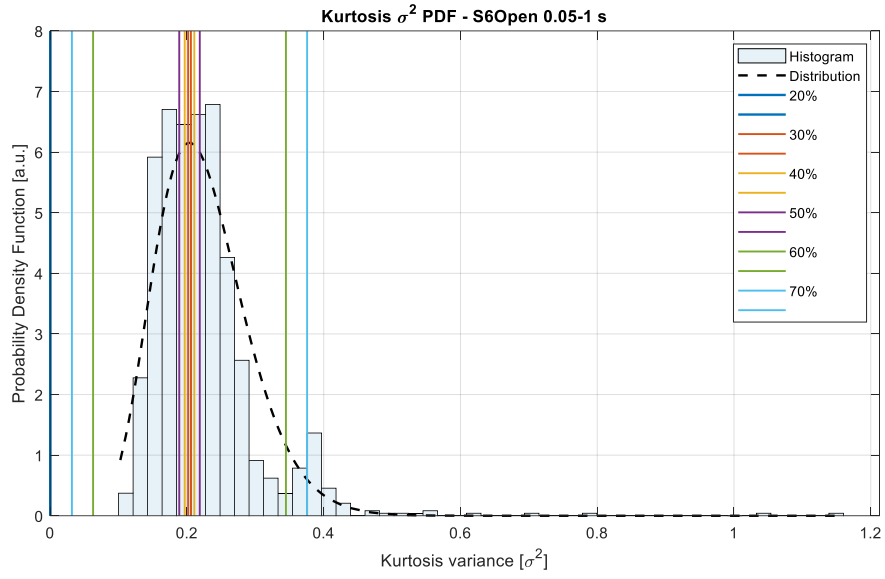
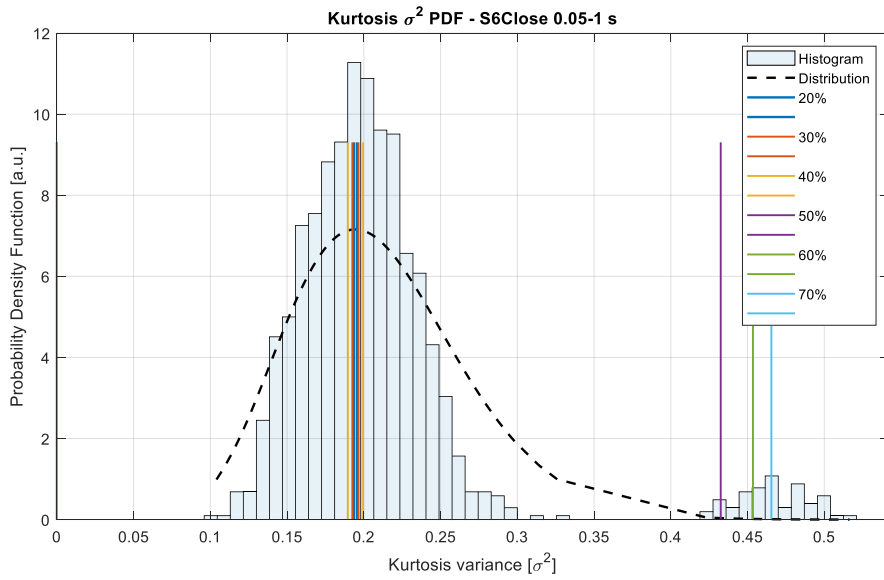


Figure AN 2. K_{σ^2} heat plot derived from 1 to 10 seconds segmentation. Resting state conditions depicted in pairs: a, b) S5 – R1, R2. c, d) S6 – R1, R2. e, f) S8 – R1, R2. g, h) S9 – R1, R2. i, j) S10 – R1, R2

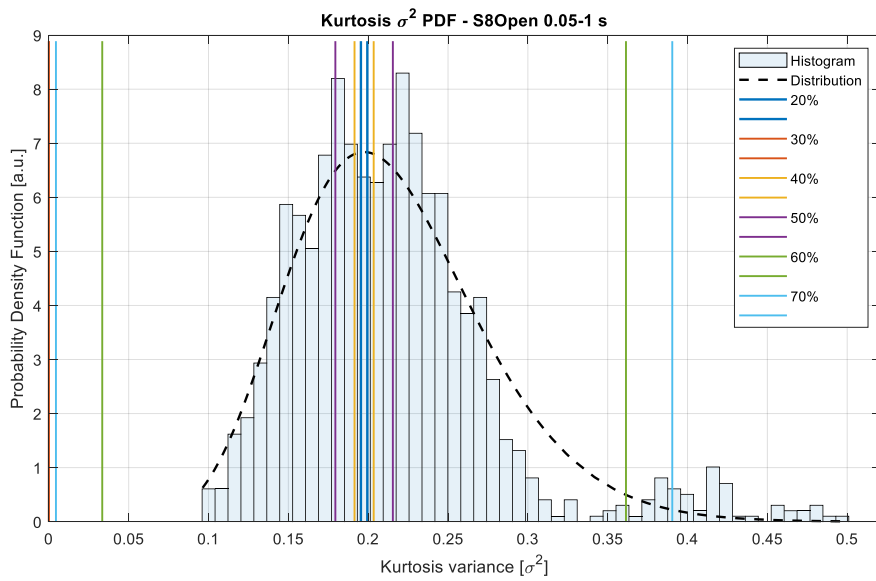




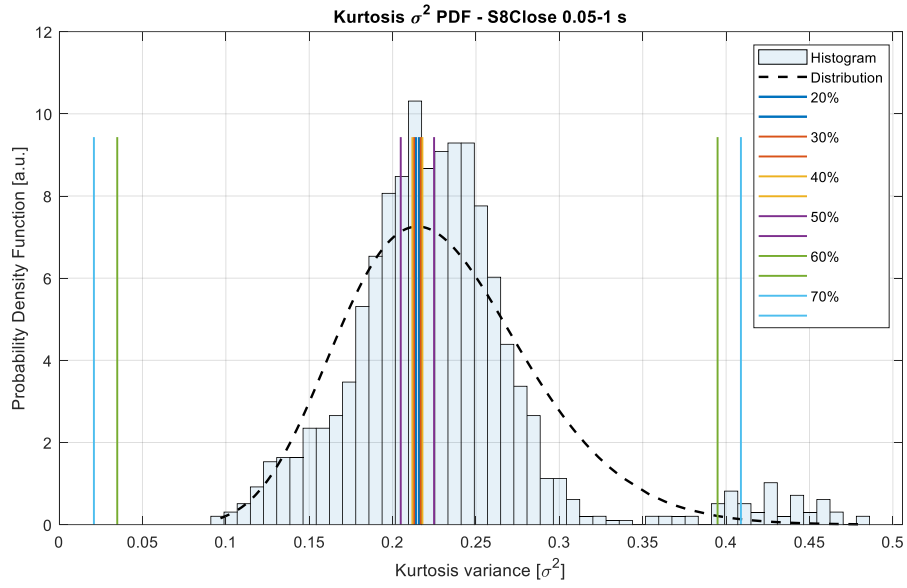
(c)



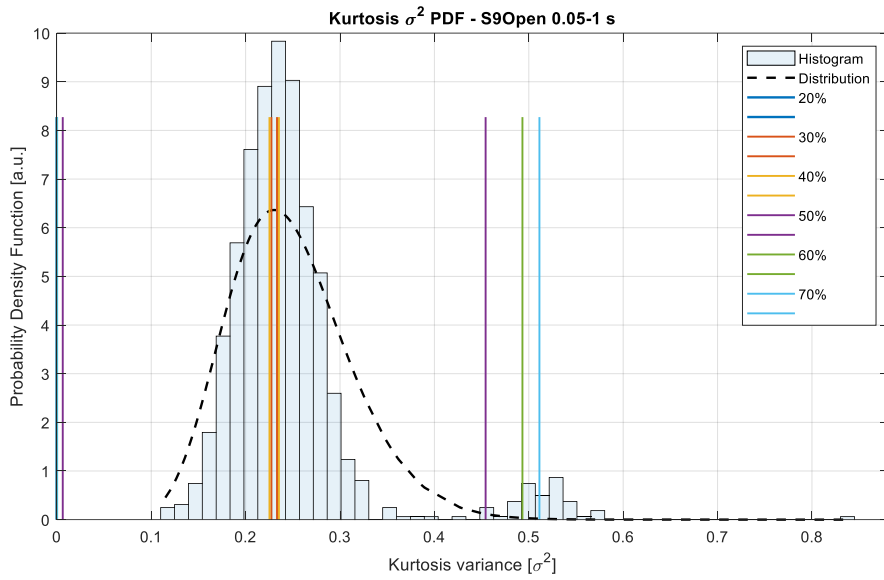
(d)



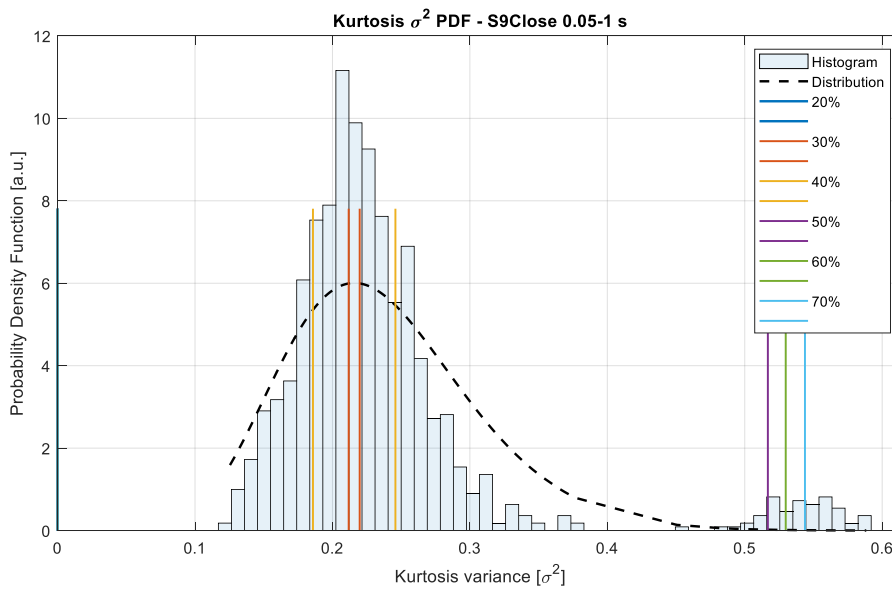
(e)



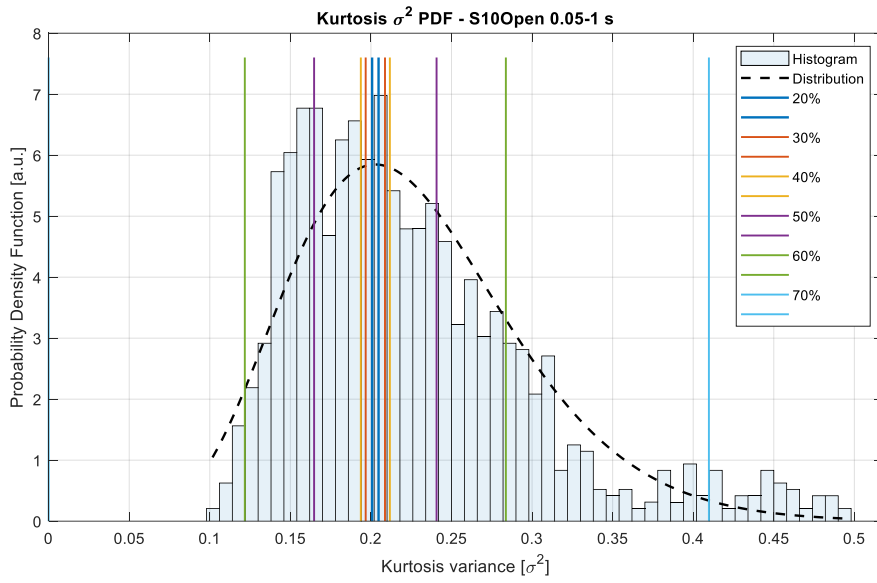
(f)



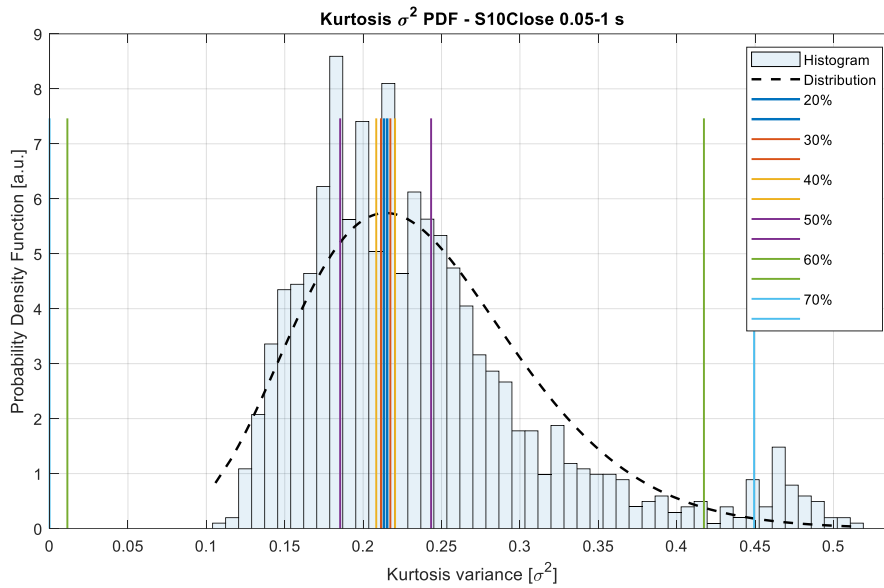
(g)



(h)



(i)



(j)

Figure AN 3. K_{σ^2} PDFs and the corresponding searching intervals with respect to max σ^2 proportion thresholds. Resting state conditions depicted in pairs – Short window segmentation:
a, b) S5 – R1, R2. c, d) S6 – R1, R2. e, f) S8 – R1, R2. g, h) S9 – R1, R2. i, j) S10 – R1, R2

Table AN 1. Number of channels, variance range and segment lengths, $w_t = 1, \dots, 10$ seconds. S2 – R1

	10%	20%	30%	40%	50%	60%	70%	80%	90%	100%
Lower limit	0.1096	0.1066	0.1006	0.0796	0.0496	0.0076	0	0	0	0
Upper limit	0.1156	0.1186	0.1246	0.1456	0.1756	0.2176	0.2636	0.3016	0.3416	1.1136
1 sec	0	0	0	0	1	7	22	35	49	59
2 sec	2	2	6	15	31	55	59	59	59	59
3 sec	1	2	3	16	36	48	53	55	57	59
4 sec	3	6	9	25	38	48	54	55	57	59
5 sec	3	6	13	30	47	51	54	55	57	59
6 sec	1	5	10	34	50	53	54	56	56	59
7 sec	1	5	10	31	50	52	55	57	57	59
8 sec	4	5	11	25	50	55	57	58	58	59
9 sec	1	2	5	19	46	53	55	56	57	59
10 sec	2	6	13	27	47	57	57	58	58	59

Table AN 2. Number of channels, variance range and segment lengths, $w_t = 1, \dots, 10$ seconds. S2 – R2

	10%	20%	30%	40%	50%	60%	70%	80%	90%	100%
Lower limit	0.17	0.168	0.165	0.163	0.131	0.065	0.025	-0.01	-0.05	-0.83
Upper limit	0.172	0.174	0.177	0.179	0.211	0.277	0.317	0.354	0.389	1.172
1 sec	0	0	0	0	0	6	19	32	46	60
2 sec	0	3	8	12	39	60	60	60	60	60
3 sec	1	4	7	9	33	59	60	60	60	60
4 sec	1	2	5	6	26	57	60	60	60	60
5 sec	2	4	10	11	44	59	60	60	60	60
6 sec	2	4	5	9	48	60	60	60	60	60
7 sec	1	3	4	6	40	60	60	60	60	60
8 sec	2	3	6	9	43	60	60	60	60	60
9 sec	0	1	1	2	13	49	60	60	60	60
10 sec	2	3	7	8	25	60	60	60	60	60

Table AN 3. Number of channels, variance range and segment lengths, $w_t = 0.05, \dots, 1$ seconds. S2 – R1

	10%	20%	30%	40%	50%	60%	70%	80%	90%	100%
Lower limit	0	0	0	0	0.24099	0.05799	0.04999	0.03599	0.02299	0
Upper limit	0	0	0	0	0.25299	0.43599	0.44399	0.45799	0.47099	1.24799
50 ms	0	0	0	0	0	6	19	33	47	59
100 ms	0	0	0	0	12	59	59	59	59	59
150 ms	0	0	0	0	7	59	59	59	59	59
200 ms	0	0	0	0	16	59	59	59	59	59
250 ms	0	0	0	0	23	59	59	59	59	59
300 ms	0	0	0	0	8	59	59	59	59	59
350 ms	0	0	0	0	4	59	59	59	59	59
400 ms	0	0	0	0	5	59	59	59	59	59
450 ms	0	0	0	0	10	59	59	59	59	59
500 ms	0	0	0	0	12	59	59	59	59	59
550 ms	0	0	0	0	8	59	59	59	59	59
600 ms	0	0	0	0	11	59	59	59	59	59
650 ms	0	0	0	0	10	59	59	59	59	59
700 ms	0	0	0	0	9	59	59	59	59	59
750 ms	0	0	0	0	5	59	59	59	59	59
800 ms	0	0	0	0	6	59	59	59	59	59
850 ms	0	0	0	0	8	59	59	59	59	59
900 ms	0	0	0	0	7	59	59	59	59	59
950 ms	0	0	0	0	6	57	58	58	58	59
1000 ms	0	0	0	0	3	59	59	59	59	59

Table AN 4. Number of channels, variance range and segment lengths, $w_l = 0.05, \dots, 1$ seconds. S2 – R2

	10%	20%	30%	40%	50%	60%	70%	80%	90%	100%
Lower limit	0	0	0	0.22811	0.02611	0.00111	0	0	0	0
Upper limit	0	0	0	0.23211	0.43411	0.45911	0.46611	0.47511	0.48511	0.51711
50 ms	0	0	0	0	1	12	24	35	47	59
100 ms	0	0	0	6	60	60	60	60	60	60
150 ms	0	0	0	4	60	60	60	60	60	60
200 ms	0	0	0	1	60	60	60	60	60	60
250 ms	0	0	0	5	60	60	60	60	60	60
300 ms	0	0	0	8	60	60	60	60	60	60
350 ms	0	0	0	7	60	60	60	60	60	60
400 ms	0	0	0	8	60	60	60	60	60	60
450 ms	0	0	0	0	60	60	60	60	60	60
500 ms	0	0	0	4	60	60	60	60	60	60
550 ms	0	0	0	0	60	60	60	60	60	60
600 ms	0	0	0	3	60	60	60	60	60	60
650 ms	0	0	0	5	60	60	60	60	60	60
700 ms	0	0	0	6	60	60	60	60	60	60
750 ms	0	0	0	6	60	60	60	60	60	60
800 ms	0	0	0	1	60	60	60	60	60	60
850 ms	0	0	0	4	60	60	60	60	60	60
900 ms	0	0	0	2	60	60	60	60	60	60
950 ms	0	0	0	2	60	60	60	60	60	60
1000 ms	0	0	0	1	60	60	60	60	60	60

50ms to 1 second segmentation

Table AN 5. Number of channels, variance range and segment lengths, $w_l = 0.05, \dots, 1$ seconds. S5 – R1

	10%	20%	30%	40%	50%	60%	70%	80%	90%	100%
Lower limit	0	0	0	0.22761	0.21761	0.02161	0.00561	-0.0094	-0.0154	-0.0484
Upper limit	0	0	0	0.23361	0.24361	0.43961	0.45561	0.47061	0.47661	0.50961
50 ms	0	0	0	0	0	8	19	32	44	56
100 ms	0	0	0	9	21	57	57	57	57	57
150 ms	0	0	0	0	2	57	57	57	57	57
200 ms	0	0	0	2	8	57	57	57	57	57
250 ms	0	0	0	2	11	57	57	57	57	57
300 ms	0	0	0	1	10	57	57	57	57	57
350 ms	0	0	0	6	10	57	57	57	57	57
400 ms	0	0	0	7	28	57	57	57	57	57
450 ms	0	0	0	8	23	57	57	57	57	57
500 ms	0	0	0	4	14	57	57	57	57	57
550 ms	0	0	0	4	19	57	57	57	57	57
600 ms	0	0	0	1	10	57	57	57	57	57
650 ms	0	0	0	6	23	57	57	57	57	57
700 ms	0	0	0	3	15	57	57	57	57	57
750 ms	0	0	0	4	11	57	57	57	57	57
800 ms	0	0	0	4	14	57	57	57	57	57
850 ms	0	0	0	3	10	57	57	57	57	57
900 ms	0	0	0	4	10	57	57	57	57	57
950 ms	0	0	0	3	8	57	57	57	57	57
1000 ms	0	0	0	3	12	57	57	57	57	57

Table AN 6. Number of channels, variance range and segment lengths, $w_l = 0.05, \dots, 1$ seconds. S5 – R2

	10%	20%	30%	40%	50%	60%	70%	80%	90%	100%
Lower limit	0	0.23642	0.23442	0	0.01242	-0.0046	-0.0186	-0.0356	-0.0476	-0.7636
Upper limit	0	0.23842	0.24042	0	0.46242	0.47942	0.49342	0.51042	0.52242	1.23842
50 ms	0	0	0	0	8	19	26	39	48	59
100 ms	0	0	2	0	59	59	59	59	59	59
150 ms	0	1	7	0	59	59	59	59	59	59
200 ms	0	3	6	0	59	59	59	59	59	59
250 ms	0	2	4	0	59	59	59	59	59	59
300 ms	0	4	8	0	59	59	59	59	59	59
350 ms	0	1	4	0	59	59	59	59	59	59
400 ms	0	0	2	0	59	59	59	59	59	59
450 ms	0	0	2	0	59	59	59	59	59	59
500 ms	0	2	2	0	59	59	59	59	59	59
550 ms	0	3	4	0	58	58	58	59	59	59
600 ms	0	3	4	0	59	59	59	59	59	59
650 ms	0	4	5	0	59	59	59	59	59	59
700 ms	0	0	1	0	57	59	59	59	59	59
750 ms	0	0	3	0	59	59	59	59	59	59
800 ms	0	1	2	0	59	59	59	59	59	59
850 ms	0	3	4	0	59	59	59	59	59	59
900 ms	0	0	2	0	57	57	57	58	58	59
950 ms	0	2	2	0	59	59	59	59	59	59
1000 ms	0	0	2	0	59	59	59	59	59	59

Table AN 7. Number of channels, variance range and segment lengths, $w_l = 0.05, \dots, 1$ seconds. S6 – R1

	10%	20%	30%	40%	50%	60%	70%	80%	90%	100%
Lower limit	0	0	0.20171	0.19671	0.18871	0.06271	0.03171	0.01971	0.00571	0
Upper limit	0	0	0.20571	0.21071	0.21871	0.34471	0.37571	0.38771	0.40171	0
50 ms	0	0	0	0	0	1	18	36	49	0
100 ms	0	0	1	3	5	57	57	57	57	0
150 ms	0	0	0	0	1	57	57	57	57	0
200 ms	0	0	0	0	0	57	57	57	57	0
250 ms	0	0	1	2	7	57	57	57	57	0
300 ms	0	0	4	4	13	57	57	57	57	0
350 ms	0	0	2	10	20	57	57	57	57	0
400 ms	0	0	3	8	22	55	56	56	57	0
450 ms	0	0	2	8	17	55	56	56	57	0
500 ms	0	0	4	13	23	57	57	57	57	0
550 ms	0	0	1	9	13	53	54	55	56	0
600 ms	0	0	1	3	13	57	57	57	57	0
650 ms	0	0	3	8	12	54	55	55	55	0
700 ms	0	0	1	7	13	57	57	57	57	0
750 ms	0	0	0	1	9	56	57	57	57	0
800 ms	0	0	2	7	11	57	57	57	57	0
850 ms	0	0	6	8	12	49	49	49	50	0
900 ms	0	0	1	2	7	51	52	52	52	0
950 ms	0	0	1	2	4	55	55	56	56	0
1000 ms	0	0	0	2	6	57	57	57	57	0

Table AN 8. Number of channels, variance range and segment lengths, $w_l = 0.05, \dots, 1$ seconds. S6 – R2

	10%	20%	30%	40%	50%	60%	70%	80%	90%	100%
Lower limit	0	0.19353	0.19253	0.18953	-0.0435	-0.0645	-0.0765	-0.0895	-0.1045	-0.1265
Upper limit	0	0.19553	0.19653	0.19953	0.43253	0.45353	0.46553	0.47853	0.49353	0.51553
50 ms	0	0	0	0	6	17	29	39	49	59
100 ms	0	2	4	8	60	60	60	60	60	60
150 ms	0	0	0	0	60	60	60	60	60	60
200 ms	0	1	2	5	60	60	60	60	60	60
250 ms	0	1	1	2	60	60	60	60	60	60
300 ms	0	1	2	7	60	60	60	60	60	60
350 ms	0	3	4	8	60	60	60	60	60	60
400 ms	0	2	3	8	60	60	60	60	60	60
450 ms	0	2	3	12	60	60	60	60	60	60
500 ms	0	4	7	15	60	60	60	60	60	60
550 ms	0	3	6	13	60	60	60	60	60	60
600 ms	0	2	3	8	60	60	60	60	60	60
650 ms	0	1	3	8	60	60	60	60	60	60
700 ms	0	3	3	6	60	60	60	60	60	60
750 ms	0	2	2	6	60	60	60	60	60	60
800 ms	0	1	1	3	60	60	60	60	60	60
850 ms	0	3	3	10	60	60	60	60	60	60
900 ms	0	2	3	5	60	60	60	60	60	60
950 ms	0	1	3	6	60	60	60	60	60	60
1000 ms	0	1	1	5	60	60	60	60	60	60

Table AN 9. Number of channels, variance range and segment lengths, $w_l = 0.05, \dots, 1$ seconds. S8 – R1

	10%	20%	30%	40%	50%	60%	70%	80%	90%	100%
Lower limit	0.19645	0.19545	0	0.19145	0.17945	0.03345	0.00445	-0.0206	-0.0416	-0.1046
Upper limit	0.19845	0.19945	0	0.20345	0.21545	0.36145	0.39045	0.41545	0.43645	0.49945
50 ms	0	0	0	0	0	4	20	35	48	60
100 ms	0	0	0	0	7	61	61	61	61	61
150 ms	0	0	0	0	0	60	61	61	61	61
200 ms	0	0	0	0	5	61	61	61	61	61
250 ms	0	0	0	1	4	61	61	61	61	61
300 ms	1	1	0	2	12	61	61	61	61	61
350 ms	1	3	0	4	13	61	61	61	61	61
400 ms	1	2	0	9	30	61	61	61	61	61
450 ms	0	2	0	8	29	61	61	61	61	61
500 ms	2	2	0	7	29	61	61	61	61	61
550 ms	1	2	0	8	27	61	61	61	61	61
600 ms	2	3	0	7	23	61	61	61	61	61
650 ms	0	0	0	6	20	61	61	61	61	61
700 ms	1	1	0	5	20	61	61	61	61	61
750 ms	4	8	0	13	19	61	61	61	61	61
800 ms	0	1	0	6	13	61	61	61	61	61
850 ms	0	0	0	4	12	61	61	61	61	61
900 ms	1	3	0	6	15	61	61	61	61	61
950 ms	0	0	0	3	12	60	61	61	61	61
1000 ms	0	0	0	5	13	60	60	61	61	61

Table AN 10. Number of channels, variance range and segment lengths, $w_l = 0.05, \dots, 1$ seconds. S8 – R2

	10%	20%	30%	40%	50%	60%	70%	80%	90%	100%
Lower limit	0	0.21388	0.21288	0.21188	0.20488	0.03488	0.02088	0.00188	-0.0221	-0.0531
Upper limit	0	0.21588	0.21688	0.21788	0.22488	0.39488	0.40888	0.42788	0.45188	0.48288
50 ms	0	0	0	0	0	10	24	37	49	61
100 ms	0	3	11	14	31	62	62	62	62	62
150 ms	0	0	0	0	0	62	62	62	62	62
200 ms	0	1	2	2	4	62	62	62	62	62
250 ms	0	0	0	1	4	62	62	62	62	62
300 ms	0	3	4	6	14	62	62	62	62	62
350 ms	0	0	3	4	13	62	62	62	62	62
400 ms	0	2	5	7	23	62	62	62	62	62
450 ms	0	2	4	4	18	62	62	62	62	62
500 ms	0	1	4	6	18	62	62	62	62	62
550 ms	0	1	1	1	8	62	62	62	62	62
600 ms	0	3	5	7	18	62	62	62	62	62
650 ms	0	1	1	3	9	62	62	62	62	62
700 ms	0	2	3	6	13	62	62	62	62	62
750 ms	0	1	2	3	8	62	62	62	62	62
800 ms	0	1	2	5	12	62	62	62	62	62
850 ms	0	2	4	5	6	62	62	62	62	62
900 ms	0	1	1	2	11	62	62	62	62	62
950 ms	0	0	0	0	3	62	62	62	62	62
1000 ms	0	2	3	5	12	62	62	62	62	62

Table AN 11. Number of channels, variance range and segment lengths, $w_l = 0.05, \dots, 1$ seconds. S9 – R1

	10%	20%	30%	40%	50%	60%	70%	80%	90%	100%
Lower limit	0	0	0.22726	0.22526	0.00626	-0.0327	-0.0507	-0.0647	-0.0767	-0.7707
Upper limit	0	0	0.23326	0.23526	0.45426	0.49326	0.51126	0.52526	0.53726	1.23126
50 ms	0	0	0	0	1	12	24	35	45	55
100 ms	0	0	5	9	55	55	55	55	55	55
150 ms	0	0	0	3	55	55	55	55	55	55
200 ms	0	0	4	6	55	55	55	55	55	55
250 ms	0	0	5	5	55	55	55	55	55	55
300 ms	0	0	4	7	55	55	55	55	55	55
350 ms	0	0	5	7	55	55	55	55	55	55
400 ms	0	0	2	6	55	55	55	55	55	55
450 ms	0	0	6	10	55	55	55	55	55	55
500 ms	0	0	1	3	55	55	55	55	55	55
550 ms	0	0	3	4	55	55	55	55	55	55
600 ms	0	0	7	8	55	55	55	55	55	55
650 ms	0	0	4	5	55	55	55	55	55	55
700 ms	0	0	4	5	54	54	54	54	54	55
750 ms	0	0	2	4	55	55	55	55	55	55
800 ms	0	0	3	4	55	55	55	55	55	55
850 ms	0	0	3	5	55	55	55	55	55	55
900 ms	0	0	4	7	55	55	55	55	55	55
950 ms	0	0	1	4	55	55	55	55	55	55
1000 ms	0	0	0	0	55	55	55	55	55	55

Table AN 12. Number of channels, variance range and segment lengths, $w_l = 0.05, \dots, 1$ seconds. S9 – R2

	10%	20%	30%	40%	50%	60%	70%	80%	90%	100%
Lower limit	0	0	0.21182	0.18582	-0.0852	-0.0982	-0.1122	-0.1242	-0.1372	-0.1562
Upper limit	0	0	0.21982	0.24582	0.51682	0.52982	0.54382	0.55582	0.56882	0.58782
50 ms	0	0	0	0	10	20	29	39	48	57
100 ms	0	0	6	48	58	58	58	58	58	58
150 ms	0	0	9	42	58	58	58	58	58	58
200 ms	0	0	8	47	58	58	58	58	58	58
250 ms	0	0	4	37	58	58	58	58	58	58
300 ms	0	0	5	32	58	58	58	58	58	58
350 ms	0	0	1	34	58	58	58	58	58	58
400 ms	0	0	9	40	58	58	58	58	58	58
450 ms	0	0	3	30	58	58	58	58	58	58
500 ms	0	0	11	42	58	58	58	58	58	58
550 ms	0	0	5	28	58	58	58	58	58	58
600 ms	0	0	6	35	58	58	58	58	58	58
650 ms	0	0	9	39	58	58	58	58	58	58
700 ms	0	0	3	28	58	58	58	58	58	58
750 ms	0	0	1	24	58	58	58	58	58	58
800 ms	0	0	2	27	58	58	58	58	58	58
850 ms	0	0	3	26	58	58	58	58	58	58
900 ms	0	0	3	21	58	58	58	58	58	58
950 ms	0	0	2	13	58	58	58	58	58	58
1000 ms	0	0	2	7	58	58	58	58	58	58

Table AN 13. Number of channels, variance range and segment lengths, $w_l = 0.05, \dots, 1$ seconds. S10 – R1

	10%	20%	30%	40%	50%	60%	70%	80%	90%	100%
Lower limit	0	0.20074	0.19674	0.19374	0.16474	0.12174	-0.0043	-0.0393	-0.0543	-0.7983
Upper limit	0	0.20474	0.20874	0.21174	0.24074	0.28374	0.40974	0.44474	0.45974	1.20374
50 ms	0	0	0	0	0	0	15	31	45	60
100 ms	0	0	0	0	4	48	60	60	60	60
150 ms	0	0	0	0	0	19	60	60	60	60
200 ms	0	2	3	7	26	50	60	60	60	60
250 ms	0	0	2	2	26	46	60	60	60	60
300 ms	0	2	8	12	36	52	60	60	60	60
350 ms	0	3	6	10	40	53	60	60	60	60
400 ms	0	5	11	15	44	52	59	60	60	60
450 ms	0	6	10	16	42	52	59	60	60	60
500 ms	0	2	7	10	39	54	59	60	60	60
550 ms	0	1	3	5	37	56	60	60	60	60
600 ms	0	5	5	7	35	55	60	60	60	60
650 ms	0	3	12	14	38	54	60	60	60	60
700 ms	0	2	4	5	29	55	60	60	60	60
750 ms	0	3	8	14	36	55	59	60	60	60
800 ms	0	1	2	2	12	54	60	60	60	60
850 ms	0	2	3	4	15	58	60	60	60	60
900 ms	0	1	1	3	17	53	60	60	60	60
950 ms	0	1	1	1	16	49	60	60	60	60
1000 ms	0	3	12	15	28	47	60	60	60	60

Table AN 14. Number of channels, variance range and segment lengths, $w_l = 0.05, \dots, 1$ seconds. S10 – R2

	10%	20%	30%	40%	50%	60%	70%	80%	90%	100%
Lower limit	0	0.21335	0.21135	0.20835	0.18535	0.01135	-0.0206	-0.0376	-0.0516	-0.7866
Upper limit	0	0.21535	0.21735	0.22035	0.24335	0.41735	0.44935	0.46635	0.48035	1.21535
50 ms	0	0	0	0	0	5	20	33	47	61
100 ms	0	0	0	1	22	61	61	61	61	61
150 ms	0	0	0	0	4	61	61	61	61	61
200 ms	0	3	6	6	23	61	61	61	61	61
250 ms	0	0	2	2	16	61	61	61	61	61
300 ms	0	1	6	11	29	61	61	61	61	61
350 ms	0	5	8	11	32	60	61	61	61	61
400 ms	0	2	5	9	35	61	61	61	61	61
450 ms	0	0	6	11	38	58	58	59	60	61
500 ms	0	0	2	6	30	59	60	61	61	61
550 ms	0	3	5	7	28	61	61	61	61	61
600 ms	0	1	3	4	25	61	61	61	61	61
650 ms	0	3	3	6	30	61	61	61	61	61
700 ms	0	1	3	5	22	61	61	61	61	61
750 ms	0	3	3	6	24	61	61	61	61	61
800 ms	0	0	0	1	16	61	61	61	61	61
850 ms	0	2	3	3	24	61	61	61	61	61
900 ms	0	0	2	3	17	61	61	61	61	61
950 ms	0	1	2	5	13	61	61	61	61	61
1000 ms	0	1	2	4	19	61	61	61	61	61

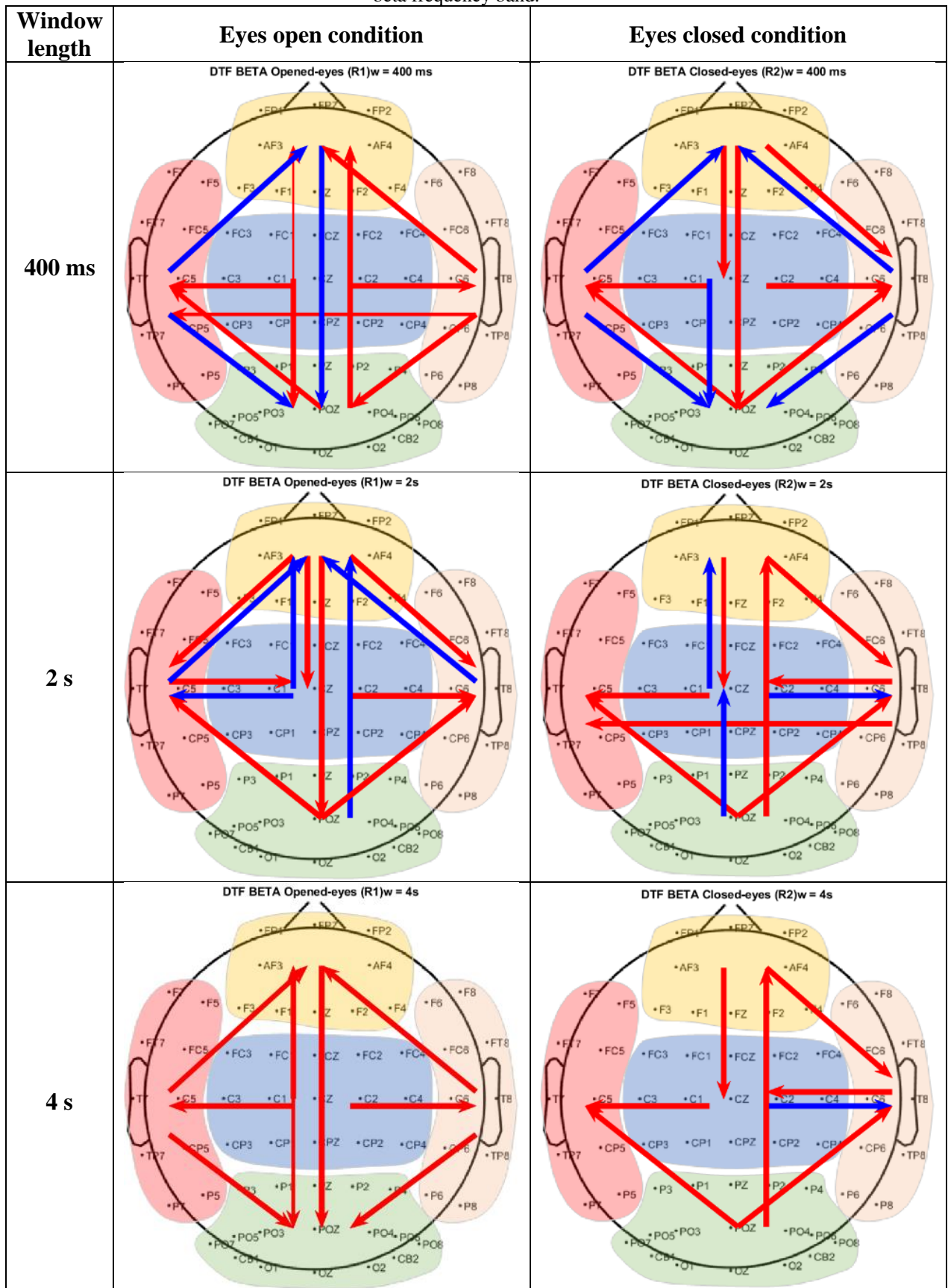
Table AN 15. Significance of interactions for the normalized density of the Beta band.

Row	SumSq	D	MeanSq	F	pValue	pValueG	pValueH	pValueL
(Intercept)	45.43532991	1	45.43532991	4519.96654	2.15443E-33	2.15443E-33	2.15443E-33	2.15443E-33
Error	0.291512018	29	0.010052139	1	0.5	0.5	0.5	0.5
Res_State	0.005013335	1	0.005013335	3.076786165	0.089981009	0.089981009	0.089981009	0.089981009
Error(Res_State)	0.047252784	29	0.001629406	1	0.5	0.5	0.5	0.5
Window	2.073837113	3	0.691279038	174.5138193	1.07974E-36	5.41781E-24	1.88394E-25	8.47695E-14
Error(Window)	0.344621856	87	0.003961171	1	0.5	0.5	0.5	0.5
ROI	2.486738601	4	0.62168465	248.4578562	6.87737E-56	3.73924E-29	3.92042E-31	9.2846E-16
Error(ROI)	0.29025212	116	0.002502173	1	0.5	0.5	0.5	0.5
Res_State:Window	0.018069819	3	0.006023273	3.584773301	0.016961997	0.023231894	0.019315042	0.068328254
Error(Res_State:Window)	0.146180721	87	0.001680238	1	0.5	0.5	0.5	0.5
Res_State:ROI	0.029834223	4	0.007458556	6.623020084	7.76193E-05	0.000714381	0.000415177	0.015444817
Error(Res_State:ROI)	0.130634129	116	0.001126156	1	0.5	0.5	0.5	0.5
Window:ROI	0.13729041	12	0.011440868	20.82103053	2.46031E-34	9.01308E-18	4.44002E-22	8.52993E-05
Error(Window:ROI)	0.191221174	348	0.000549486	1	0.5	0.5	0.5	0.5
Res_State:Window:ROI	0.012192842	12	0.00101607	1.6484924	0.076848776	0.146908003	0.128996469	0.209328057
Error(Res_State:Window:ROI)	0.214494417	348	0.000616363	1	0.5	0.5	0.5	0.5

Table AN 16. Significance of interactions for the average strength of the alpha band.

Row	SumSq	DF	MeanSq	F	pValue	pValueGG	pValueHF	pValueLB
(Intercept)	5559.851563	1	5559.851563	4285.458984	4.64202E-33	4.64202E-33	4.64202E-33	4.64202E-33
Error	37.62390137	29	1.297375917	1	0.5	0.5	0.5	0.5
(Intercept):Res_State	57.85322952	1	57.85322952	182.1325378	4.96133E-14	4.96133E-14	4.96133E-14	4.96133E-14
Error(Res_State)	9.2116642	29	0.317643583	1	0.5	0.5	0.5	0.5
(Intercept):Window	3432.019043	3	1144.006348	896.5610352	0	6.61871E-33	4.2158E-34	2.31929E-23
Error(Window)	111.0114594	87	1.275993824	1	0.5	0.5	0.5	0.5
(Intercept):ROI	0.61195755	4	0.152989388	2.553361416	0.042639766	0.048185941	0.042639766	0.120900318
Error(ROI)	6.950355053	116	0.059916854	1	0.5	0.5	0.5	0.5
(Intercept):Res_State:Window	13.34881115	3	4.449603558	9.344573021	2.02519E-05	0.002062998	0.001867456	0.004769025
Error(Res_State:Window)	41.42677307	87	0.476169795	1	0.5	0.5	0.5	0.5
(Intercept):Res_State:ROI	1.337808609	4	0.334452152	5.340751171	0.000553345	0.002083577	0.001280125	0.028139798
Error(Res_State:ROI)	7.264231205	116	0.062622681	1	0.5	0.5	0.5	0.5
(Intercept):Window:ROI	0.990084589	12	0.082507052	1.258646011	0.241647094	0.271934092	0.255803168	0.271111119
Error(Window:ROI)	22.81217575	348	0.065552227	1	0.5	0.5	0.5	0.5
(Intercept):Res_State:Window:ROI	0.377528459	12	0.031460706	0.492474943	0.918884456	0.829510272	0.87472868	0.488419563
Error(Res_State:Window:ROI)	22.2312355	348	0.063882858	1	0.5	0.5	0.5	0.5

Figure AN 4. ROI connectivity diagrams obtained for the eyes open and eyes closed conditions for the beta frequency band.



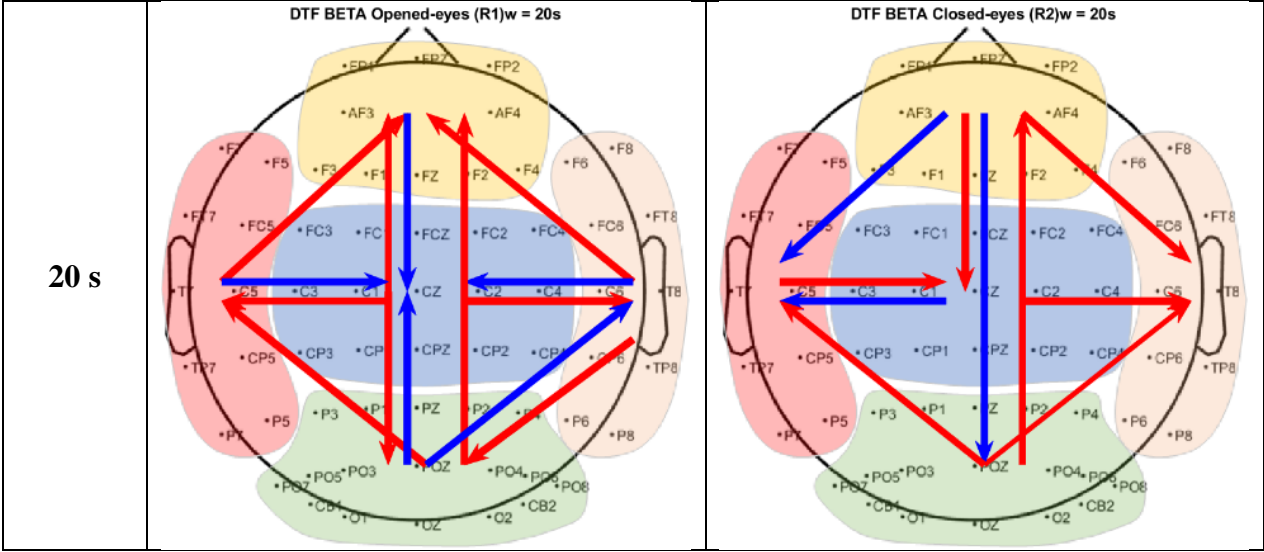


Table AN 17. P-values of all the windows for alpha and beta.

Alpha								Beta									
Res_State	Window	ROI_Origin	ROI_Destination	Difference	StdErr	pValue	Lower	Upper	Res_State	Window	ROI_Origin	ROI_Destination	Difference	StdErr	pValue	Lower	Upper
R1_w0.4	R01	R01	R02	0.0153	0.0067	0.3113	0.0358	0.0052	R1_w0.4	R01	R01	R03	-0.0140	0.0077	0.1949	0.0311	0.0021
R1_w0.4	R01	R01	R03	0.0339	0.0050	0.0000	0.0498	0.0181	R1_w0.4	R01	R01	R04	-0.0284	0.0060	0.0000	0.0468	0.0101
R1_w0.4	R01	R01	R04	0.0611	0.0050	0.0000	0.0458	0.0764	R1_w0.4	R01	R01	R05	0.0465	0.0052	0.0000	0.0306	0.0264
R1_w0.4	R01	R01	R05	0.0839	0.0065	0.0000	0.0644	0.1037	R1_w0.4	R01	R01	R06	0.0617	0.0068	0.0000	0.0424	0.0929
R1_w0.4	R02	R01	R02	0.0153	0.0067	0.3113	0.0358	0.0052	R1_w0.4	R01	R02	R01	0.0140	0.0057	0.1949	0.0332	0.0313
R1_w0.4	R02	R01	R03	0.0387	0.0070	0.0070	0.0339	0.0014	R1_w0.4	R01	R02	R02	0.0144	0.0047	0.0463	0.0287	0.0011
R1_w0.4	R02	R01	R04	0.0644	0.0070	0.0000	0.0551	0.0976	R1_w0.4	R01	R02	R03	0.0605	0.0060	0.0000	0.0422	0.0783
R1_w0.4	R02	R01	R05	0.0992	0.0050	0.0000	0.0841	0.1143	R1_w0.4	R01	R02	R04	0.0757	0.0048	0.0000	0.0612	0.0902
R1_w0.4	R02	R01	R06	0.0359	0.0050	0.0000	0.0181	0.0499	R1_w0.4	R01	R02	R05	0.0284	0.0060	0.0000	0.0401	0.0468
R1_w0.4	R03	R01	R02	0.0187	0.0057	0.0277	0.0014	0.0349	R1_w0.4	R01	R02	R06	0.0144	0.0047	0.0463	0.0287	0.0011
R1_w0.4	R03	R01	R03	0.0950	0.0050	0.0000	0.0799	0.1102	R1_w0.4	R01	R02	R07	0.0749	0.0047	0.0000	0.0607	0.0891
R1_w0.4	R03	R01	R04	0.1178	0.0067	0.0000	0.0974	0.1383	R1_w0.4	R01	R02	R08	0.0901	0.0057	0.0000	0.0729	0.1073
R1_w0.4	R03	R01	R05	0.1941	0.0050	0.0000	0.0764	0.2028	R1_w0.4	R01	R02	R09	0.0465	0.0052	0.0000	0.0424	0.0506
R1_w0.4	R03	R01	R06	0.0764	0.0070	0.0000	0.0976	0.0552	R1_w0.4	R01	R02	R10	0.0605	0.0060	0.0000	0.0788	0.0422
R1_w0.4	R04	R01	R02	0.0950	0.0050	0.0000	0.1102	0.0799	R1_w0.4	R01	R02	R11	0.0749	0.0047	0.0000	0.0891	0.0607
R1_w0.4	R04	R01	R03	0.0228	0.0050	0.0000	0.0041	0.0469	R1_w0.4	R01	R02	R12	0.0152	0.0048	0.0154	0.0020	0.0284
R1_w0.4	R04	R01	R04	0.0839	0.0065	0.0000	0.1037	0.0641	R1_w0.4	R01	R02	R13	0.0617	0.0063	0.0000	0.0809	0.0424
R1_w0.4	R04	R01	R05	0.0992	0.0050	0.0000	0.1143	0.0841	R1_w0.4	R01	R02	R14	0.0757	0.0048	0.0000	0.0902	0.0612
R1_w0.4	R04	R01	R06	0.1178	0.0067	0.0000	0.1383	0.0974	R1_w0.4	R01	R02	R15	0.0901	0.0057	0.0000	0.1073	0.0891
R1_w0.4	R04	R01	R07	0.1941	0.0050	0.0000	0.1383	0.0974	R1_w0.4	R01	R02	R16	0.0465	0.0052	0.0000	0.0424	0.0506
R1_w0.4	R05	R01	R02	0.0228	0.0059	0.0063	0.0409	0.0047	R1_w0.4	R01	R02	R17	0.0605	0.0060	0.0000	0.0788	0.0422
R1_w0.4	R05	R01	R03	0.0312	0.0091	0.0180	0.0588	0.0036	R1_w0.4	R01	R02	R18	0.0749	0.0047	0.0000	0.0891	0.0607
R1_w0.4	R05	R01	R04	0.0668	0.0112	0.0180	0.0891	0.0061	R1_w0.4	R01	R02	R19	0.0152	0.0048	0.0154	0.0020	0.0284
R1_w0.4	R05	R01	R05	0.0662	0.0065	0.0000	0.0463	0.0861	R1_w0.4	R01	R02	R20	0.0617	0.0063	0.0000	0.0809	0.0424
R1_w0.4	R05	R01	R06	0.0873	0.0068	0.0000	0.0667	0.1079	R1_w0.4	R01	R02	R21	0.0757	0.0048	0.0000	0.0902	0.0612
R1_w0.4	R05	R01	R07	0.1128	0.0057	0.0000	0.1031	0.1408	R1_w0.4	R01	R02	R22	0.0901	0.0057	0.0000	0.1073	0.0891
R1_w0.4	R05	R01	R08	0.0356	0.0106	0.0213	0.0378	0.0035	R1_w0.4	R01	R02	R23	0.0465	0.0052	0.0000	0.0424	0.0506
R1_w0.4	R05	R01	R09	0.0974	0.0078	0.0000	0.0788	0.1211	R1_w0.4	R01	R02	R24	0.0605	0.0060	0.0000	0.0788	0.0422
R1_w0.4	R05	R01	R10	0.1185	0.0078	0.0000	0.0915	0.1450	R1_w0.4	R01	R02	R25	0.0749	0.0047	0.0000	0.0891	0.0607
R1_w0.4	R05	R01	R11	0.0668	0.0112	0.0000	0.0329	0.1007	R1_w0.4	R01	R02	R26	0.0152	0.0048	0.0154	0.0020	0.0284
R1_w0.4	R05	R01	R12	0.0356	0.0106	0.0213	0.0378	0.0035	R1_w0.4	R01	R02	R27	0.0617	0.0063	0.0000	0.0809	0.0424
R1_w0.4	R05	R01	R13	0.1330	0.0091	0.0000	0.1608	0.1053	R1_w0.4	R01	R02	R28	0.0757	0.0048	0.0000	0.0902	0.0612
R1_w0.4	R05	R01	R14	0.1541	0.0093	0.0000	0.1257	0.1823	R1_w0.4	R01	R02	R29	0.0901	0.0057	0.0000	0.1073	0.0891
R1_w0.4	R05	R01	R15	0.0662	0.0065	0.0000	0.0861	0.0463	R1_w0.4	R01	R02	R30	0.0465	0.0052	0.0000	0.0424	0.0506
R1_w0.4	R05	R01	R16	0.0974	0.0078	0.0000	0.1211	0.0788	R1_w0.4	R01	R02	R31	0.0605	0.0060	0.0000	0.0788	0.0422
R1_w0.4	R05	R01	R17	0.1330	0.0091	0.0000	0.1608	0.1053	R1_w0.4	R01	R02	R32	0.0749	0.0047	0.0000	0.0891	0.0607
R1_w0.4	R05	R01	R18	0.0210	0.0068	0.0241	0.0018	0.0403	R1_w0.4	R01	R02	R33	0.0152	0.0048	0.0154	0.0020	0.0284
R1_w0.4	R05	R01	R19	0.0873	0.0068	0.0000	0.1079	0.0661	R1_w0.4	R01	R02	R34	0.0617	0.0063	0.0000	0.0809	0.0424
R1_w0.4	R05	R01	R20	0.1185	0.0089	0.0000	0.1455	0.0915	R1_w0.4	R01	R02	R35	0.0901	0.0057	0.0000	0.1073	0.0891
R1_w0.4	R05	R01	R21	0.1541	0.0093	0.0000	0.1823	0.1257	R1_w0.4	R01	R02	R36	0.0465	0.0052	0.0000	0.0424	0.0506
R1_w0.4	R05	R01	R22	0.0662	0.0065	0.0000	0.0861	0.0463	R1_w0.4	R01	R02	R37	0.0605	0.0060	0.0000	0.0788	0.0422
R1_w0.4	R05	R01	R23	0.0974	0.0078	0.0000	0.1211	0.0788	R1_w0.4	R01	R02	R38	0.0749	0.0047	0.0000	0.0891	0.0607
R1_w0.4	R05	R01	R24	0.1330	0.0091	0.0000	0.1608	0.1053	R1_w0.4	R01	R02	R39	0.0152	0.0048	0.0154	0.0020	0.0284
R1_w0.4	R05	R01	R25	0.0210	0.0068	0.0241	0.0018	0.0403	R1_w0.4	R01	R02	R40	0.0617	0.0063	0.0000	0.0809	0.0424
R1_w0.4	R05	R01	R26	0.0873	0.0068	0.0000	0.1079	0.0661	R1_w0.4	R01	R02	R41	0.0901	0.0057	0.0000	0.1073	0.0891
R1_w0.4	R05	R01	R27	0.1185	0.0089	0.0000	0.1455	0.0915	R1_w0.4	R01	R02	R42	0.0465	0.0052	0.0000	0.0424	0.0506
R1_w0.4	R05	R01	R28	0.1541	0.0093	0.0000	0.1823	0.1257	R1_w0.4	R01	R02	R43	0.0605	0.0060	0.0000	0.0788	0.0422
R1_w0.4	R05	R01	R29	0.0662	0.0065	0.0000	0.0861	0.0463	R1_w0.4	R01	R02	R44	0.0749	0.0047	0.0000	0.0891	0.0607
R1_w0.4	R05	R01	R30	0.0974	0.0078	0.0000	0.1211	0.0788	R1_w0.4	R01	R02	R45	0.0152	0.0048	0.0154	0.0020	0.0284
R1_w0.4	R05	R01	R31	0.1330	0.0091	0.0000	0.1608	0.1053	R1_w0.4	R01	R02	R46	0.0617	0.0063	0.0000	0.0809	0.0424
R1_w0.4	R05	R01	R32	0.0210	0.0068	0.0241	0.0018	0.0403	R1_w0.4	R01	R02	R47	0.0901	0.0057	0.0000	0.1073	0.0891
R1_w0.4	R05	R01	R33	0.0873	0.0068	0.0000	0.1079	0.0661	R1_w0.4	R01	R02	R48	0.0465	0.0052	0.0000	0.0424	0.0506
R1_w0.4	R05	R01	R34	0.1185	0.0089	0.0000	0.1455	0.0915	R1_w0.4	R01	R02	R49	0.0605	0.0060	0.0000	0.0788	0.0422
R1_w0.4	R05	R01	R35	0.1541	0.0093	0.0000	0.1823	0.1257	R1_w0.4	R01	R02	R50	0.0749	0.0047	0.0000	0.0891	0.0607
R1_w0.4	R05	R01	R36	0.0662	0.0065	0.0000	0.0861	0.0463	R1_w0.4	R01	R02	R51	0.0152	0.0048	0.0154	0.0020	0.0284
R1_w0.4	R05	R01	R37	0.0974	0.0078	0.0000	0.1211	0.0788	R1_w0.4	R01	R02	R52	0.0617	0.0063	0.0000	0.0809	0.0424
R1_w0.4	R05	R01	R38	0.1330	0.0091	0.0000	0.1608	0.1053	R1_w0.4	R01	R02	R53	0.0901	0.0057	0.0000	0.1073	0.0891
R1_w0.4	R05	R01	R39	0.0210	0.0068	0.0241	0.0018	0.0403	R1_w0.4	R01	R02	R54	0.0465	0.0052	0.0000	0.0424	0.0506
R1_w0.4	R05	R01	R40	0.0873	0.0068	0.0000	0.1079	0.0661	R1_w0.4	R01	R02	R55	0.0605	0.0060	0.0000	0.0788	0.0422
R1_w0.4	R05	R01	R41	0.1185	0.0089	0.0000	0.1455	0.0915	R1_w0.4	R01	R02	R56	0.0749	0.0047	0.0000	0.0891	0.0607
R1_w0.4	R05	R01	R42	0.1541	0.0093	0.0000	0.1823	0.1257	R1_w0.4	R01	R02	R57	0.0152	0.0048	0.0154	0.0020	0.0284
R1_w0.4	R05	R01	R43	0.0662	0.0065	0.0000	0.0861	0.0463									

References

- [1] R. Khandpur, *Biomedical Instrumentation: Technology and Applications*. McGraw-Hill Professiona, 2004.
- [2] R. M. Rangayyan, *Biomedical signal analysis: Second edition*. Hoboken, NJ, USA: John Wiley & Sons, Inc., 2015.
- [3] D. S. Tan and A. Nijholt, *Brain Computer Interfaces: Applying our Minds to Human-Computer Interaction*. Springer, 2010.
- [4] S. Saeid and J. A. Chambers, “Introduction to EEG,” in *EEG Signal Processing*, John Wiley & Sons, 2007, pp. 1–34.
- [5] B. J. Baars and N. M. Gage, “Fundamentals of Cognitive Neuroscience: A Beginner’s Guide,” in *Fundamentals of Cognitive Neuroscience: A Beginner’s Guide*, 2012, pp. 1–463.
- [6] “Rostral | The Science of Psychotherapy.” <https://www.thescienceofpsychotherapy.com/glossary/rostral/> (accessed Mar. 18, 2021).
- [7] “Brain anatomy, Anatomy of the human brain | Mayfield Brain & Spine Cincinnati, Ohio.” <https://mayfieldclinic.com/pe-anatbrain.htm> (accessed Mar. 18, 2021).
- [8] N. Pyatigorskaya *et al.*, “Medulla oblongata damage and cardiac autonomic dysfunction in Parkinson disease,” *Neurology*, vol. 87, no. 24, pp. 2540–2545, Dec. 2016, doi: 10.1212/WNL.0000000000003426.
- [9] W. Gerstner, W. M. Kistler, R. Naud, and L. Paninski, *Neuronal dynamics: From single neurons to networks and models of cognition*. Cambridge University Press, 2014.
- [10] A. P. Georgopoulos, J. F. Kalaska, R. Caminiti, and J. T. Massey, “On the relations between the direction of two-dimensional arm movements and cell discharge in primate motor cortex,” *J. Neurosci.*, vol. 2, no. 11, pp. 1527–1537, 1982, doi: 10.1523/jneurosci.02-11-01527.1982.
- [11] M. A. Maier, K. M. B. Bennett, M. C. Hepp-Reymond, and R. N. Lemon, “Contribution of the monkey corticomotoneuronal system to the control of force in precision grip,” *J. Neurophysiol.*, vol. 69, no. 3, pp. 772–785, 1993, doi: 10.1152/jn.1993.69.3.772.
- [12] W. Gerstner, R. Kempter, J. L. Van Hemmen, and H. Wagner, “A neuronal learning rule for sub-millisecond temporal coding,” *Nature*, vol. 383, no. 6595, pp. 76–78, 1996, doi: 10.1038/383076a0.
- [13] R. M. Rangayyan, “Introduction to Biomedical Signals,” in *Biomedical Signal Analysis*, John Wiley & Sons, Inc., 2015, pp. 1–69.
- [14] J. Rogala, E. Kublik, R. Krauz, and A. Wróbel, “Resting-state EEG activity predicts frontoparietal network reconfiguration and improved attentional performance,” *Sci. Rep.*, vol. 10, no. 1, Dec. 2020, doi: 10.1038/s41598-020-61866-7.
- [15] X. Pei, D. L. Barbour, E. C. Leuthardt, and G. Schalk, “Decoding vowels and consonants in spoken and imagined words using electrocorticographic signals in

- humans.,” *J. Neural Eng.*, vol. 8, no. 4, p. 046028, Aug. 2011, doi: 10.1088/1741-2560/8/4/046028.
- [16] C. M. Michel and M. M. Murray, “Towards the utilization of EEG as a brain imaging tool,” *NeuroImage*, vol. 61, no. 2. Academic Press, pp. 371–385, Jun. 01, 2012, doi: 10.1016/j.neuroimage.2011.12.039.
- [17] V. Sakkalis, “Review of advanced techniques for the estimation of brain connectivity measured with EEG/MEG,” *Comput. Biol. Med.*, vol. 41, no. 12, pp. 1110–1117, Dec. 2011, doi: 10.1016/j.combiomed.2011.06.020.
- [18] A. A. Braitenberg, *Information Processing in the Cortex*. Springer Berlin Heidelberg, 1992.
- [19] K. J. Friston, “Functional and Effective Connectivity: A Review,” *Brain Connect.*, vol. 1, no. 1, pp. 13–36, Jun. 2011, doi: 10.1089/brain.2011.0008.
- [20] B. He *et al.*, “Electrophysiological Brain Connectivity: Theory and Implementation,” *IEEE Trans. Biomed. Eng.*, vol. 66, no. 7, pp. 2115–2137, Jul. 2019, doi: 10.1109/TBME.2019.2913928.
- [21] N. Wiener, *The theory of prediction*. New York: McGraw-Hil, 1956.
- [22] M. J. Kaminski and K. J. Blinowska, “A new method of the description of the information flow in the brain structures,” *Biol. Cybern.*, vol. 65, no. 3, pp. 203–210, Jul. 1991, doi: 10.1007/BF00198091.
- [23] L. Astolfi *et al.*, “Comparison of different cortical connectivity estimators for high-resolution EEG recordings,” *Hum. Brain Mapp.*, vol. 28, no. 2, pp. 143–157, Feb. 2007, doi: 10.1002/hbm.20263.
- [24] L. A. Baccala, K. Sameshima, and D. Y. Takahashi, “Generalized partial directed coherence,” in *2007 15th International Conference on Digital Signal Processing, DSP 2007*, 2007, pp. 163–166, doi: 10.1109/ICDSP.2007.4288544.
- [25] M. Killmann, L. Sommerlade, W. Mader, J. Timmer, and B. Schelter, “Inference of time-dependent causal influences in Networks,” *Biomed. Tech.*, vol. 57, no. SUPPL. 1 TRACK-F, pp. 387–390, Aug. 2012, doi: 10.1515/bmt-2012-4263.
- [26] A. Korzeniewska, M. Mańczak, M. Kamiński, K. J. Blinowska, and S. Kasicki, “Determination of information flow direction among brain structures by a modified directed transfer function (dDTF) method,” *J. Neurosci. Methods*, vol. 125, no. 1–2, pp. 195–207, May 2003, doi: 10.1016/S0165-0270(03)00052-9.
- [27] K. J. Friston, L. Harrison, and W. Penny, “Dynamic causal modelling,” *Neuroimage*, vol. 19, no. 4, pp. 1273–1302, Aug. 2003, doi: 10.1016/S1053-8119(03)00202-7.
- [28] C. W. J. Granger, “Investigating Causal Relations by Econometric Models and Cross-spectral Methods,” *Econometrica*, vol. 37, no. 3, p. 424, Aug. 1969, doi: 10.2307/1912791.
- [29] J. S. Johnson, B. Kundu, A. G. Casali, and B. R. Postle, “Task-dependent changes in cortical excitability and effective connectivity: A combined TMS-EEG study,” *J. Neurophysiol.*, vol. 107, no. 9, pp. 2383–2392, May 2012, doi: 10.1152/jn.00707.2011.
- [30] M. Rahimi, M. H. Moradi, and F. Ghassemi, “Comparison of brain effective connectivity in different states of attention and consciousness based on EEG signals,”

- Biomed. Signal Process. Control*, vol. 51, pp. 393–400, May 2019, doi: 10.1016/j.bspc.2019.02.002.
- [31] H. Bakhshayesh, S. P. Fitzgibbon, A. S. Janani, T. S. Grummett, and K. J. Pope, “Detecting connectivity in EEG: A comparative study of data-driven effective connectivity measures,” *Comput. Biol. Med.*, vol. 111, p. 103329, Aug. 2019, doi: 10.1016/j.compbiomed.2019.103329.
- [32] M. Eichler, “A graphical approach for evaluating effective connectivity in neural systems,” *Philos. Trans. R. Soc. B Biol. Sci.*, vol. 360, no. 1457, pp. 953–967, May 2005, doi: 10.1098/rstb.2005.1641.
- [33] G. Varotto *et al.*, “Altered resting state effective connectivity in long-standing vegetative state patients: An EEG study,” *Clin. Neurophysiol.*, vol. 125, no. 1, pp. 63–68, Jan. 2014, doi: 10.1016/j.clinph.2013.06.016.
- [34] M. De Tommaso, S. Stramaglia, D. Marinazzo, G. Trotta, and M. Pellicoro, “Functional and effective connectivity in EEG alpha and beta bands during intermittent flash stimulation in migraine with and without aura,” *Cephalalgia*, vol. 33, no. 11, pp. 938–947, Aug. 2013, doi: 10.1177/0333102413477741.
- [35] M. Wada *et al.*, “Resting-State Isolated Effective Connectivity of the Cingulate Cortex as a Neurophysiological Biomarker in Patients with Severe Treatment-Resistant Schizophrenia,” *J. Pers. Med.*, vol. 10, no. 3, p. 89, Aug. 2020, doi: 10.3390/jpm10030089.
- [36] F. Rotondi, S. Franceschetti, G. Avanzini, and F. Panzica, “Altered EEG resting-state effective connectivity in drug-naïve childhood absence epilepsy,” *Clin. Neurophysiol.*, vol. 127, no. 2, pp. 1130–1137, Feb. 2016, doi: 10.1016/j.clinph.2015.09.003.
- [37] B. Maharathi, J. A. Loeb, and J. Patton, “Estimation of resting state effective connectivity in epilepsy using direct-directed transfer function,” in *Proceedings of the Annual International Conference of the IEEE Engineering in Medicine and Biology Society, EMBS*, Oct. 2016, vol. 2016-October, pp. 716–719, doi: 10.1109/EMBC.2016.7590802.
- [38] B. Hu, Q. Dong, Y. Hao, Q. Zhao, J. Shen, and F. Zheng, “Effective brain network analysis with resting-state EEG data: A comparison between heroin abstinent and non-addicted subjects,” *J. Neural Eng.*, vol. 14, no. 4, p. 046002, May 2017, doi: 10.1088/1741-2552/aa6c6f.
- [39] S. A. Valizadeh, R. Riener, S. Elmer, and L. Jäncke, “Decrypting the electrophysiological individuality of the human brain: Identification of individuals based on resting-state EEG activity,” *Neuroimage*, vol. 197, pp. 470–481, Aug. 2019, doi: 10.1016/j.neuroimage.2019.04.005.
- [40] M. Muthuraman *et al.*, “EEG-MEG Integration Enhances the Characterization of Functional and Effective Connectivity in the Resting State Network,” *PLoS One*, vol. 10, no. 10, p. e0140832, Oct. 2015, doi: 10.1371/journal.pone.0140832.
- [41] H. Shahabi and S. Moghimi, “Toward automatic detection of brain responses to emotional music through analysis of EEG effective connectivity,” *Comput. Human Behav.*, vol. 58, pp. 231–239, May 2016, doi: 10.1016/j.chb.2016.01.005.
- [42] M. Lee, J.-G. Yoon, and S.-W. Lee, “Predicting Motor Imagery Performance From

- Resting-State EEG Using Dynamic Causal Modeling,” *Front. Hum. Neurosci.*, vol. 14, p. 321, Aug. 2020, doi: 10.3389/fnhum.2020.00321.
- [43] T. F. Tafreshi, M. R. Daliri, and M. Ghodousi, “Functional and effective connectivity based features of EEG signals for object recognition,” *Cogn. Neurodyn.*, vol. 13, no. 6, pp. 555–566, Dec. 2019, doi: 10.1007/s11571-019-09556-7.
- [44] D. Tan and A. Nijholt, “Brain-Computer Interfaces and Human-Computer Interaction,” 2010, pp. 3–19.
- [45] E. Olejarczyk, L. Marzetti, V. Pizzella, and F. Zappasodi, “Comparison of connectivity analyses for resting state EEG data,” *J. Neural Eng.*, vol. 14, no. 3, p. 036017, Mar. 2017, doi: 10.1088/1741-2552/aa6401.
- [46] B. Tan, X. Kong, P. Yang, Z. Jin, and L. Li, “The difference of brain functional connectivity between eyes-closed and eyes-open using graph theoretical analysis,” *Comput. Math. Methods Med.*, vol. 2013, 2013, doi: 10.1155/2013/976365.
- [47] F. Van de Steen, H. Almgren, A. Razi, K. Friston, and D. Marinazzo, “Dynamic causal modelling of fluctuating connectivity in resting-state EEG,” *Neuroimage*, vol. 189, pp. 476–484, Apr. 2019, doi: 10.1016/j.neuroimage.2019.01.055.
- [48] K. Sameshima and L. A. Baccalá, *Methods in brain connectivity inference through multivariate time series analysis*. CRC Press, 2014.
- [49] S. Sanei and J. A. Chambers, *EEG Signal Processing*. West Sussex, England: John Wiley & Sons Ltd, 2013.
- [50] Gü. Bodenstern and H. M. Praetorius, “Feature Extraction from the Electroencephalogram by Adaptive Segmentation,” *Proc. IEEE*, vol. 65, no. 5, pp. 642–652, 1977, doi: 10.1109/PROC.1977.10543.
- [51] K. M. Davis, J. L. Ryan, V. D. Aaron, and J. B. Sims, “PET and SPECT Imaging of the Brain: History, Technical Considerations, Applications, and Radiotracers,” *Semin. Ultrasound, CT MRI*, Aug. 2020, doi: 10.1053/j.sult.2020.08.006.
- [52] G. XUE, C. CHEN, Z.-L. LU, and Q. DONG, “Brain Imaging Techniques and Their Applications in Decision-Making Research,” *Acta Psychol. Sin.*, vol. 42, no. 1, pp. 120–137, Feb. 2010, doi: 10.3724/sp.j.1041.2010.00120.
- [53] T. M. Lau, J. T. Gwin, and D. P. Ferris, “How Many Electrodes Are Really Needed for EEG-Based Mobile Brain Imaging?,” *J. Behav. Brain Sci.*, vol. 02, no. 03, pp. 387–393, Aug. 2012, doi: 10.4236/jbbs.2012.23044.
- [54] P. Trujillo *et al.*, “Quantitative EEG for predicting upper limb motor recovery in chronic stroke robot-Assisted rehabilitation,” *IEEE Trans. Neural Syst. Rehabil. Eng.*, vol. 27, no. 5, pp. 1058–1067, Jul. 2017, doi: 10.1109/TNSRE.2017.2678161.
- [55] A. Mastropietro *et al.*, “Quantitative EEG and virtual reality to support post-stroke rehabilitation at home,” in *Smart Innovation, Systems and Technologies*, 2016, vol. 60, pp. 147–157, doi: 10.1007/978-3-319-39687-3_15.
- [56] “SynAmps RT 64-channel Amplifier – Compumedics Neuroscan.” <https://compumedicsneuroscan.com/product/synamps-rt-64-channel-ee-erp-amplifier/> (accessed Sep. 21, 2020).
- [57] I. Pisarenco, M. Caporro, C. Prosperetti, and M. Manconi, “High-density

- electroencephalography as an innovative tool to explore sleep physiology and sleep related disorders,” *Int. J. Psychophysiol.*, vol. 92, no. 1, pp. 8–15, Apr. 2014, doi: 10.1016/j.ijpsycho.2014.01.002.
- [58] A. Delorme and S. Makeig, “EEGLAB: an open source toolbox for analysis of single-trial EEG dynamics including independent component analysis.,” *J. Neurosci. Methods*, vol. 134, no. 1, pp. 9–21, Mar. 2004, doi: 10.1016/j.jneumeth.2003.10.009.
- [59] H. J. Scheer, T. Sander, and L. Trahms, “The influence of amplifier, interface and biological noise on signal quality in high-resolution EEG recordings,” *Physiol. Meas.*, vol. 27, no. 2, pp. 109–117, Feb. 2006, doi: 10.1088/0967-3334/27/2/002.
- [60] M. K. Islam, A. Rastegarnia, and Z. Yang, “Methods for artifact detection and removal from scalp EEG: A review,” *Neurophysiol. Clin. Neurophysiol.*, vol. 46, no. 4–5, pp. 287–305, Nov. 2016, doi: 10.1016/j.neucli.2016.07.002.
- [61] A. Delorme, J. Palmer, J. Onton, R. Oostenveld, and S. Makeig, “Independent EEG sources are dipolar,” *PLoS One*, vol. 7, no. 2, p. 30135, Feb. 2012, doi: 10.1371/journal.pone.0030135.
- [62] C. Andreas Edgar Kothe, “Artifact removal techniques with signal reconstruction,” Jun. 03, 2014.
- [63] M. Plechawska-Wojcik, M. Kaczorowska, and D. Zapala, “The artifact subspace reconstruction (ASR) for EEG signal correction. A comparative study,” in *Advances in Intelligent Systems and Computing*, Sep. 2019, vol. 853, pp. 125–135, doi: 10.1007/978-3-319-99996-8_12.
- [64] I. Winkler, S. Brandl, F. Horn, E. Waldburger, C. Allefeld, and M. Tangermann, “Robust artifactual independent component classification for BCI practitioners,” *J. Neural Eng.*, vol. 11, no. 3, p. 035013, May 2014, doi: 10.1088/1741-2560/11/3/035013.
- [65] I. Winkler, S. Haufe, and M. Tangermann, “Automatic Classification of Artifactual ICA-Components for Artifact Removal in EEG Signals,” *Behav. Brain Funct.*, vol. 7, no. 1, p. 30, Aug. 2011, doi: 10.1186/1744-9081-7-30.
- [66] C. Y. Chang, S. H. Hsu, L. Pion-Tonachini, and T. P. Jung, “Evaluation of Artifact Subspace Reconstruction for Automatic Artifact Components Removal in Multi-Channel EEG Recordings,” *IEEE Trans. Biomed. Eng.*, vol. 67, no. 4, pp. 1114–1121, Apr. 2020, doi: 10.1109/TBME.2019.2930186.
- [67] I. Winkler, “MARA Tutorial.” pp. 1–15, 2014, [Online]. Available: <https://irene.github.io/artifacts/>.
- [68] T. R. Mullen *et al.*, “The Dynamic Brain: Modeling Neural Dynamics and Interactions From Human Electrophysiological Recordings,” 2014.
- [69] A. Delorme *et al.*, “EEGLAB, SIFT, NFT, BCILAB, and ERICA: New tools for advanced EEG processing,” *Comput. Intell. Neurosci.*, vol. 2011, 2011, doi: 10.1155/2011/130714.
- [70] J. Theiler, S. Eubank, A. Longtin, B. Galdrikian, and J. Doyne Farmer, “Testing for nonlinearity in time series: the method of surrogate data,” *Phys. D Nonlinear Phenom.*, vol. 58, no. 1–4, pp. 77–94, Sep. 1992, doi: 10.1016/0167-2789(92)90102-S.

- [71] J. L. Chen, T. Ros, and J. H. Gruzelier, "Dynamic changes of ICA-derived EEG functional connectivity in the resting state," *Hum. Brain Mapp.*, vol. 34, no. 4, pp. 852–868, Apr. 2013, doi: 10.1002/hbm.21475.
- [72] J. Ito, A. R. Nikolaev, and C. Van Leeuwen, "Spatial and temporal structure of phase synchronization of spontaneous alpha EEG activity," *Biol. Cybern.*, vol. 92, no. 1, pp. 54–60, Jan. 2005, doi: 10.1007/s00422-004-0533-z.
- [73] S. Boccaletti, V. Latora, Y. Moreno, M. Chavez, and D. U. Hwang, "Complex networks: Structure and dynamics," *Physics Reports*, vol. 424, no. 4–5. North-Holland, pp. 175–308, Feb. 01, 2006, doi: 10.1016/j.physrep.2005.10.009.
- [74] K. J. Blinowska and M. Kaminski, "Functional Brain Networks: Random, 'Small World' or Deterministic?," *PLoS One*, vol. 8, no. 10, p. e78763, Oct. 2013, doi: 10.1371/journal.pone.0078763.
- [75] D. Ludvig and E. J. Perreault, "System identification of physiological systems using short data segments," *IEEE Trans. Biomed. Eng.*, vol. 59, no. 12, pp. 3541–3549, 2012, doi: 10.1109/TBME.2012.2220767.
- [76] M. Ding, S. L. Bressler, W. Yang, and H. Liang, "Short-window spectral analysis of cortical event-related potentials by adaptive multivariate autoregressive modeling: Data preprocessing, model validation, and variability assessment," *Biol. Cybern.*, vol. 83, no. 1, pp. 35–45, 2000, doi: 10.1007/s004229900137.
- [77] A. Delorme and S. Makeig, "EEGLAB: An open source toolbox for analysis of single-trial EEG dynamics including independent component analysis," *J. Neurosci. Methods*, vol. 134, no. 1, pp. 9–21, Mar. 2004, doi: 10.1016/j.jneumeth.2003.10.009.